Searching for Quantum Gravity with Neutrinos, Optical Module Beam Test at Fermilab and Hadronization Model studies for IceCube

by

Shivesh Mandalia

Submitted in partial fullfilment of the requirements
for the award of the degree of

Doctor of Philosophy

Submitted: November 1, 2019

at

Queen Mary University of London
Particle Physics Research Centre,
School of Physics and Astronomy,
Faculty of Science and Engineering

Declaration

I, Shivesh Mandalia, confirm that the research included within this thesis is my own work or that where it has been carried out in collaboration with, or supported by others, that this is duly acknowledged below and my contribution indicated. Previously published material is also acknowledged below.

I attest that I have exercised reasonable care to ensure that the work is original, and does not to the best of my knowledge break any UK law, infringe any third party copyright or other Intellectual Property Right, or contain any confidential material.

I accept that the College has the right to use plagiarism detection software to check the electronic version of the thesis.

I confirm that this thesis has not been previously submitted for the award of a degree by this or any other university.

Signature:

Shivesh Mandalia

Date: November 1, 2019

Abstract

Neutrinos are elementary particles of nature, and they are composed of three flavours; electron, muon, and tau neutrinos. Neutrino telescopes, such as the IceCube Neutrino Observatory, detect high-energy neutrinos produced from cosmic ray interactions in the atmosphere and distant astrophysical objects. Such high-energy neutrinos can be used as a probe to search for violations of fundamental spacetime symmetries as new spacetime structure can drive non-standard flavour mixings of neutrinos. Firstly, a search using atmospherically produced neutrinos detected at IceCube is presented. This allows us to set limits on higher-dimensional operators in this framework. Secondly, a search using very-high-energy astrophysically produced neutrinos is presented, searching for modifications in the measured astrophysical neutrino flavour composition for the very first time. Although the current statistics and detector sensitivity allows for searches for only rather special new physics effects, it is demonstrated that the sensitivity of this new approach reaches for the first time the necessary precision to look for new physics within the Planck scale expectation.

Future neutrino telescopes such as the IceCube-Upgrade will focus on oscillation physics down to $\sim$few GeV. Here, photomultiplier tubes (PMTs) are used to cover large volumes, however instrumentation is relatively coarse, and particle identification (PID) is done through the morphology of PMT hits. Here, the principle of pulse shape PID using a single 10-inch hemispherical PMT is studied. The Fermilab Test Beam Facility MTest beam line is used to demonstrate that with pulse shape PID, it is possible to distinguish 2 GeV electrons from 8 GeV pions, where the total charge deposition is $\sim$20 PE. Furthermore, among the physics of hadronic systems in neutrino interactions, the hadronization model controls multiplicities of final state hadrons. Here, the possibility of implementing the PYTHIA 8 program in the GENIE neutrino interaction generator is studied, showing comparisons of PYTHIA 8 predictions with neutrino-hadron multiplicity data from bubble chamber experiments.

Acknowledgements

First thanks goes to my supervisor, Teppei Katori (香取哲平). You made this PhD a lot more fun than I had imagined it to be! For every page in this thesis, there is a story which we shared in the last 5 years I have had you as my supervisor. Your dedication and passion for physics (among many other things...) is something I have and always will admire.

This PhD may bear my name, but there are so many people I have had the delight to get to know who also deserve recognition for their support and friendship, for not only making me a better physicist, but also a better person. I hope to see you all again in the future! I extend a special thank you to: Rodrigo, Andres, Antony, Billy, Kareem, Pierre, Paul, Stephanie, Susy, Carlos (Abrazos!), Tianlu, Donglian, Qinrui, Ty, Kevin, Elim, Liz, Ward, Joakim, Steven, Thomas, Justin, Hector, Gleb, Sebastian, Rowan, Jorge, Yosuke, Aaron and Kim. Extra special thanks to Kareem for also reading this thesis!

Back at home I also want to thank James G, James M and Louis for the many poker/movie nights and for the many more to come!

Finally I want to thank my parents, my aunt and uncle and my sisters. It is your continuous and unconditional support that have allowed me to become the person I am today.

This work was supported by the Science and Technology Facilities Council.

Contents

Abstract i

Acknowledgements iii

List of Figures ix

List of Tables xxi

I Neutrinos at IceCube 1

1 Neutrino Physics 3

1.1 History . . . 3
1.2 Neutrino Mixing . . . 6
1.2.1 Two neutrino mixing . . . 9
1.2.2 Matter interactions . . . 11
1.2.3 Wave packet treatment . . . 13
1.2.4 CPT transformations . . . 15
1.3 Neutrino Production . . . 16
1.3.1 Atmospheric neutrinos . . . 16
1.3.2 Astrophysical neutrinos . . . 19
1.4 Neutrino Detection . . . 25
1.4.1 Neutrino interactions with matter . . . 25
1.4.2 Propagation of leptons . . . 28
1.4.3 Propagation of hadrons . . . 31

2 The IceCube Neutrino Observatory 33

2.1 Digital Optical Module . . . 34
2.1.1 Data Acquisition . . . 35
2.2 Event Signatures . . . 38
2.2.1 Tracks . . . 38
2.2.2 Cascades . . . 39
2.2.3 Taus . . . 39
2.3 The IceCube-Upgrade . . . 41

II Search for Quantum Gravity **43**

3 Search for Lorentz Violation with Atmospheric Neutrinos **45**

3.1 Phenomenology . . . 46
3.1.1 Standard model extension . . . 47
3.1.2 Lorentz violating neutrino oscillations . . . 48
3.2 Analysis Method . . . 51
3.2.1 Data selection . . . 51
3.2.2 Simulation . . . 53
3.2.3 Systematics . . . 56
3.2.4 Classical statistics . . . 59
3.2.5 Bayesian statistics . . . 62
3.2.6 Sampling . . . 65
3.3 Results . . . 67
3.3.1 Discussion . . . 72
3.3.2 Bayesian approach . . . 73
3.3.3 Other checks . . . 78
3.3.4 Conclusion . . . 79

4 Search for Quantum Gravity with Astrophysical Neutrinos **81**

4.1 Phenomenology . . . 82
4.1.1 New physics framework . . . 82
4.1.2 New physics in the astrophysical neutrino flavour . . . 83
4.1.3 New physics texture . . . 85
4.2 Analysis Method . . . 87
4.2.1 Data selection . . . 87
4.2.2 Simulation . . . 89
4.2.3 Systematics . . . 92
4.2.4 Statistics . . . 96
4.2.5 Anarchic sampling . . . 96
4.3 Results . . . 98
4.3.1 Discussion . . . 102
4.3.2 Other checks . . . 103
4.3.3 Conclusion . . . 108

III IceCube DOM Beam Test at the Fermilab Test Beam Facility 109

5 IceCube DOM Beam Test at the Fermilab Test Beam Facility 111

5.1 The Fermilab Test Beam Facility . . . 112
5.1.1 FTBF MTest beam line . . . 112
5.1.2 FTBF beam structure . . . 113
5.1.3 FTBF instrumentation . . . 113
5.1.4 Beam trigger . . . 115
5.1.5 Beam performance . . . 117
5.2 Experimental Setup . . . 119
5.2.1 PMT unit specification . . . 119
5.2.2 Tank specification . . . 120
5.2.3 DAQ specification . . . 122
5.2.4 Calibration . . . 124
5.3 Results . . . 126
5.3.1 PMT waveforms . . . 126
5.3.2 Primary pulse . . . 129
5.3.3 Secondary pulse . . . 129
5.3.4 Saturation . . . 132
5.3.5 Beam spread . . . 133
5.3.6 Pulse shape analysis . . . 134
5.4 Simulation . . . 135
5.4.1 GEANT4 . . . 135
5.4.2 Hit distribution . . . 137
5.5 Conclusion . . . 139

IV Hadronization processes in neutrino interactions 141

6 Hadronization processes in neutrino interactions 143

6.1 Hadronization Modelling . . . 143
6.1.1 GENIE neutrino interaction generator . . . 143
6.1.2 KNO hadronization model . . . 145
6.1.3 PYTHIA hadronization model . . . 146
6.2 Approaches . . . 148
6.2.1 Direct translation . . . 148
6.2.2 Further features . . . 150
6.3 Conclusion . . . 152

V Conclusion **153**

7 Conclusion **155**

A Appendix **157**

A.1 Gain calculation from LED charge distribution 157

A.2 Atmospheric neutrino LV exclusion regions 159

A.3 Astrophysical flavour exclusion regions 172

A.4 Neutrino interferometry for high-precision tests of Lorentz symmetry with IceCube 178

A.6 PYTHIA hadronization process tuning in the GENIE neutrino interaction generator 187

Bibliography **201**

List of Figures

1.1 Historical evolution of the size and type of neutrino detection technology. Detectors are categorised into one of the following detection technologies: Cherenkov, radiochemical, segmented tracker, time projection chamber (TPC), unsegmented scintillator or bubble chamber, as indicated by the shape (and colour). Active volume mass of each detector is plotted against the year in which the detector became operational. This plot was made as part of INSS 2017 [16]. 5

1.2 Graphical representation of the relationship between the neutrino flavour and mass eigenstates. The three mass eigenstates are depicted as three boxes, coloured such that the relative area gives the probability of finding the corresponding flavour neutrino in that given mass state. Normal ordering of the neutrino masses is assumed and mixing elements reflect neutrino propagation in a vacuum. Normal ordering and inverted ordering correspond to the case where the mass of ν_3 is greater than the mass of ν_1 or the mass of ν_1 is greater than the mass of ν_3, respectively. 7

1.3 Neutrino survival probability in the two neutrino scheme for $\sin^2 2\theta = 1$ as a function of $L/E\,[\mathrm{km/GeV}]\,\Delta m^2\,[\mathrm{eV}^2]$. 10

1.4 Neutrino oscillation probabilities when treating the neutrino as a wave packet. A neutrino of flavour ν_α is produced on the left. In colour, the probability of detecting a neutrino with flavour ν_α (blue) and ν_β (green). In black, the probability of the neutrino being of a particular mass eigenstate ν_1 (dashed) and ν_2 (dashed-dotted). The top figure shows the probabilities as a function of time after production for three fixed detector locations, $L_0 < L_1 < L_2$. The bottom figure shows the probabilities as a function of the distance to the source for three fixed detection times, $t_0 < t_1 < t_2$. . . . 14

1.5 Scheme of CPT, CP and T transformations that relate different flavour transition channels [21]. 15

1.6 Simplified schematic of an air shower generated by a cosmic ray. The decay of light mesons in the shower produces a flux of neutrinos, more specifically the conventional atmospheric neutrino flux. Adapted from [31]. 17
1.7 Atmospheric neutrino fluxes for $\nu_\mu + \bar{\nu}_\mu$ (blue) and $\nu_e + \bar{\nu}_e$ (red), calculated using the MCEQ package [32]. Dashed line shows the conventional components, dotted line shows the prompt components and solid line shows the total. Note the prompt neutrino flux has not yet been experimentally observed. 18
1.8 Neutrinos as messengers of astrophysical objects. Exotic astrophysical objects produce high-energy cosmic rays, photons and neutrinos, which can be detected on Earth. Credit: IceCube, NSF. 20
1.9 Estimated rate of ν_μ events (blue) and ν_e events (red) for a kilometre-scale detector. Solid line is for the atmospheric neutrino component and dashed for the astrophysical component. Recreated from [29]. 21
1.10 Astrophysical neutrino flavour composition ternary plot. Axes show the fraction of each neutrino flavour. Coloured shapes show 3 models for the source flavour composition. The arrows indicate the effect of neutrino mixing during propagation and the unfilled shapes show the corresponding measured flavour compositions. The hatched area shows the region in measured flavour space in which all standard astrophysical models live. 24
1.11 Feynman diagrams for neutrino-electron scattering. Neutral-current interaction channel shown on the left, and charged-current interaction shown on the right. 25
1.12 Muon neutrino cross-section on a water target, shown as a function of the neutrino energy. Also shown are the contributions from quasi-elastic scattering (dashed, red), resonance production (dash-dotted, blue) and deep inelastic scattering (dotted, green). Cross-sections were generated using GENIE [43]. 26
1.13 Feynman diagram for deep inelastic scattering on a target nucleon (left) shown with the kinematical quantities defining this interaction (right). . . . 27
1.14 High-energy neutrino (solid) and antineutrino (dashed) cross-sections on an isoscalar target for charged-current and neutral-current scattering, calculated by CSMS [46]. 28

1.15 Cherenkov radiation produced by a particle travelling faster than the speed of light in the same medium. 29
1.16 Stopping power ($\mathrm{d}E/\mathrm{d}x$) for a muon in ice as a function of the muon momentum (solid, black). Its contributions are also shown from ionization (dashed, blue), pair production (dotted, red), bremsstrahlung (dash-dotted, green) and photonuclear (dash-dash-dotted, pink). Data taken from PDG [48]. 30

2.1 The IceCube neutrino observatory with the In-Ice array, its subarray DeepCore and the cosmic ray shower array IceTop. 33
2.2 The Digital Optical Module, the photon detection unit at IceCube [50]. . . . 34
2.3 The same signal sampled in the ATWD (top) and the fADC (bottom): the ATWD recording duration is 427 ns whereas the fADC recording duration is 6.4 μs [52]. 35
2.4 Average of 10,000 SPE waveforms for a PMT at a gain of 10^7 [52]. 36
2.5 Typical SPE charge distribution at a gain of 5×10^7 including pedestal peak [52]. 36
2.6 Distribution (histogram) of the timing of SPE hits at a gain of 10^7 in reference to an illumination by a narrow pulse from a diode laser. A small fraction of late pulses are due to laser afterglow plus the random background rate (dashed). [52]. 36
2.7 Position dependence of the response of a DOM [50]. The x–y coordinates measure distance from the centre of the DOM. 37
2.8 Examples of neutrino event signatures in IceCube from [56]. Main panel shows the event view with spheres representing hit DOMs whose volume is proportional to the collected charge. Timing of hits is represented by the colour, with red being earlier hits and blue being later hits. Smaller panels on the right show projections of the detector along the z, x and y axes, respectively. 40
2.9 Schematic drawing of the IceCube-Upgrade strings (red), embedded in the IceCube/DeepCore array (blue/green respectively) [59]. 41
2.10 Current measurements of the rate of ν_τ appearance relative to the standard expectation, compared with the projected IceCube-Upgrade 1 year sensitivity [59]. 42

3.1 Diagram showing two types of Lorentz rotation on a particle in the presence of a background field. On the left is shown an observer Lorentz rotation and on the right is shown a particle Lorentz rotation. 46
3.2 Test of LV with atmospheric neutrinos. The LV field, indicated by the arrows, permeates space and could induce an anomalous neutrino oscillation to tau neutrinos. Note, here only the isotropic component is tested. 49
3.3 The distribution of reconstructed muon energy proxy for events in the final sample, compared to expected distributions [39]. Only statistical errors are shown. The shaded regions show data which is excluded in this analysis. Note the binning shown here is not the one used in this analysis (see text). . 52
3.4 The distribution of reconstructed zenith angles in the final sample, compared to expected distributions [39]. Only statistical errors are shown, though in almost all bins they are small enough to be hidden by the data markers. The shaded region shows data which is excluded in this analysis. Note the binning shown here is not the one used in this analysis (see text). 52
3.5 The effective area of the detector for a flux of neutrinos after all data selection criteria have been applied [54]. The area is shown for five zenith angle bands, and the average of all zenith angles is overlaid in green. 53
3.6 The ratio of vertical to horizontal neutrino transition probabilities. Here, vertical events are defined by $\cos\theta \leq -0.6$ and the horizontal events are defined as $\cos\theta \geq -0.6$. The transition probability ratio with 1σ statistical errors, extracted from the data, is compared to the prediction for various dimension-six operator values. The range of uncorrelated systematic uncertainties is shown as a light gray band. This is constructed from ensembles of many simulations where the nuisance parameters are varied within their uncertainties (see Section 3.3.2). 55
3.7 Effect of the systematic parameters used in this analysis on the event distribution in muon energy proxy space. Black (solid) histogram shows the baseline expectation, blue (dashed) shows an upward fluctuation and red (dotted) shows a downward fluctuation. 58
3.8 Spherical representation of the SME paremeters. 68

3.9 Exclusion region assuming only off-diagonal parameters are non-zero. The dimension of the operator d increases from 3 to 8 in these plots, from left to right, and top to bottom. The red (blue) regions are excluded with 90% (99%) confidence. 69

3.10 Exclusion regions in the space of two parameters: ρ_d and either $\mathring{c}^{(d)}_{\mu\mu}/\rho_d$ (odd d) or $\mathring{a}^{(d)}_{\mu\mu}/\rho_d$ (even d), which are a combination of the three SME operators. The dimension of the operator d increases from 3 to 8 in these plots, from left to right, and top to bottom. The red (blue) regions are excluded with 90% (99%) confidence. 71

3.11 Dimension-six operator results from the Bayesian approach for the dimension-six operator elements. The light green area represents the excluded region with a 99% credibility. The yellow area shows the case in which the posterior is profiled over the nuisance parameters instead of marginalised. The dark green area corresponds to a region with a very strong strength-of-evidence for the null hypothesis, Bayes factor $B \geq 10^{3/2}$. 75

3.12 Joint posterior distributions for the various nuisance parameters and SME elements for the dimension-six operator. Here, the non-diagonal plots show joint distributions between two parameters, labelled on the x- and y-axis and the diagonal plots show the marginalised distributions for each parameter, as labelled on the x-axis. The blue (light blue) shows the 90% (99%) credibility intervals. 76

3.13 Joint posterior distributions for the various nuisance parameters in the case of no LV effects. Here, the non-diagonal plots show joint distributions between two parameters, labelled on the x- and y-axis and the diagonal plots show the marginalised distributions for each parameter, as labelled on the x-axis. The blue (light blue) shows the 90% (99%) credibility intervals. . . . 77

3.14 Exclusion region for the dimension-six SME operator using a subset of data with a maximum muon proxy energy of 2×10^3. 78

3.15 Distribution of $-2\ln\lambda$ where λ is the test statistic. Also shown are χ^2 distributions for $k = 2$ degrees of freedom and $k = 3$ degrees of freedom. . . 79

4.1 The neutrino landscape up to ultra-high-energy scales [116]. 81

4.2 Astrophysical neutrinos are emitted from distant high-energy objects. Neutrino propagation may be affected by new spacetime effects, or more specifically any additional interactions which exist in the vacuum modifies neutrino mixings from the standard case. 84

4.3 Unitary bounds of astrophysical neutrino flavours for three source flavour compositions indicated by the filled shapes [145]. Coloured points represent the posterior probability density for each respective source flavour composition [146]. Flavour composition 68% and 90% credibility intervals from IceCube HESE 7.5yr are shown as the grey-shaded regions. 85

4.4 Demonstration of the HESE veto. Outer layers of the IceCube array act as an active veto against atmospheric backgrounds as shown on the left. Only events which do not trigger the veto are selected as shown on the right [152]. 87

4.5 The distribution of events in reconstructed deposited energy shown as crosses, compared to the best-fit expectation distributions for a given flux component. The events below 60 TeV (light blue) are ignored in the fit [147]. 88

4.6 The distribution of events above 60 TeV in the cosine of the reconstructed zenith angle $\cos(\theta_z)$ shown as crosses, compared to the best-fit expectation distributions for a given flux component [147]. 88

4.7 Effect of new physics on the astrophysical neutrino flavour for the dimension six operator. For a source composition of $(0:1:0)_{\rm S}$ with a $\mathcal{O}_{e\tau}$ texture, as the new physics scale Λ_6^{-1} becomes large, the observed flavour composition tends to the ν_μ corner. For a source composition of $(1:0:0)_{\rm S}$ with a $\mathcal{O}_{\mu\tau}$ texture, as the new physics scale Λ_6^{-1} becomes large, the observed flavour composition tends to the ν_e corner. Credibility intervals at 68% and 90% for the HESE 7.5yr are shown in grey. The hatched area shows the region in which all standard astrophysical models live. The grey shaded area shows the region accessible by new physics phenomena studied here, with the red shaded area restricting only to consider a source composition of $(1:2:0)_{\rm S}$ [145]. 91

4.8 Effect of the flux related systematic parameters used in this analysis on the event distribution in deposited energy. Black (solid) histogram shows the baseline expectation, blue (dashed) shows an upward fluctuation and red (dotted) shows a downward fluctuation. Note the peak seen at $\sim$6 PeV is due to the Glashow resonance [159]. 94

4.9 Exclusion regions for the dimension-six new physics operator. Limits are obtained for the new physics scale (vertical axis) as a function of the source flavour composition (horizontal axis) for certain new physics flavour textures. Green and blue shaded regions are excluded with a strong strength-of-evidence for the null hypothesis (Bayes factor, $B_{0/1} > 10$) according to Jeffreys' scale [101]. New physics scale is shown normalised to the Planck scale expectation, with the purple line indicating the point below which Planck scale physics is being probed. The hashed region shows the previous IceCube limit [72]. 99

4.10 Exclusion limits obtained for the new physics scale (horizontal axis) for dimension-three to dimension-eight new physics operators. Limits are obtained for each dimension (left vertical axis) corresponding to certain assumptions on the source flavour composition and also on the new physics flavour texture (right vertical axis). Green and blue shaded regions are excluded with a strong strength-of-evidence for the null hypothesis (Bayes factor, $B_{0/1} > 10$) according to Jeffreys' scale [101]. The purple line indicates the point at which Planck scale physics is being probed. The hashed region shows the previous IceCube limit [72]. 100

4.11 Bayes factor $B_{0/1}$ for two scenarios, shown as a function of the new physics scale for the dimension-six operator. Excluded region is defined with a strong strength-of-evidence for the null hypothesis according to Jeffreys' scale [101], $B_{0/1} > 10$, as indicated by the dashed horizontal line. 103

4.12 Joint posterior distributions for the various nuisance parameters and the new physics scale for the dimension-six operator here with a source composition $(0:1:0)_{\mathrm{S}}$ and texture $\mathcal{O}_{e\tau}$. 105

4.13 Joint posterior distributions for the various nuisance parameters and the new physics scale for the dimension-six operator here with a source composition $(1:0:0)_{\mathrm{S}}$ and texture $\mathcal{O}_{\mu\tau}$. 106

4.14 Joint posterior distributions for the various nuisance parameters and the measured flavour composition in terms of the flavour angles $\sin^4\phi_{\oplus}$, $\cos(2\psi_{\oplus})$ (see text). 107

5.1 Schematic diagram of the beam preparation of the MTest beam at the FTBF [166]. 120 GeV protons are extracted from the Main Injector and through the SY120 switchyard they are directed to form the MTest and MCenter primary beam lines. 112

5.2 Plan view of the MTest area highlighting the various instrumentation available [166]. The beam enters from the left. Upstream and highlighted in purple, are the two Cherenkov counters which are used for PID. four scintillators, SC1, SC2, SC3 and SC4 are placed throughout the beam line as can be seen in light blue, with SC4 being the most downstream. MWPCs, shown in yellow are also distributed throughout the beam line for monitoring of the beam. The tank used in this beam test was placed in the location shown in the diagram. 114

5.3 Pictures of the FTBF instrumentation used for this beam test. Left two images show the scintillation counters, SC1 and SC4 respectively. Upper right image shows one of the Multi Wire Proportional Chambers (MWPC) and bottom right image shows a Cherenkov counter. 116

5.4 Beam composition of the MTest beam line using a negative beam as a function of the beam energy in GeV [166]. 116

5.5 Spatial variation of particles detected in the X-Y plane of the MWPCs. Left plots show the variation in the X-plane and right plots show variation in the Y-plane. 117

5.6 Gain extrapolation using two lab measurements of the PMT used in this beam test [169]. Measurements are shown as the blue dots. Gain is specified to have a power law relationship to the input voltage [170], which is used to fit to these data points as is shown as the black line. For reference the R7081 Hamamatsu PMT profile is shown in orange [171]. 119

5.7 Diagram showing the layout of the tank with the PMT placed inside. DAQ and calibration components are labelled. The LED is connected to an optical fibre thread passed into the tank to the underside of the PMT. The beam is shown by the green arrow and the propagation of the Cherenkov photons is represented by the red arrow. 121
5.8 Picture of tank placed inside the MT6.2 enclosure (left) and picture of the PMT floating inside the tank which is filled with distilled water (right). . . 123
5.9 Photograph of the DDC2 (Digitizer Daughter Card, revision 2) which is the waveform digitiser used in this beam test. Highlighted in red are 2 capacitors, C4 and C13, which form the low pass filter with resistors R11 and R18. These two capacitors were removed to disable the low pass filter. . 123
5.10 Charge distribution of data in nanovolt-seconds collected with the PMT on 20$^{\text{th}}$ June 2017 of a flashing LED pulse. Fitted to this distribution is a Gaussian distribution with normalization A, mean μ and standard deviation σ. 125
5.11 On the left, a plot showing the variability of the average number of effective PE liberated from the photocathode per waveform as a function of the date and on the right a plot showing the variability of the effective gain as a function of the date, with a 10% error shaded in grey. For the dates June 15–June 18, the LED was found to be malfunctioning. 125
5.12 PMT waveforms for a 2 GeV electron triggered beam, split up into respective charge bins labelled on the top right of each plot. 127
5.13 PMT waveforms for an 8 GeV pion triggered beam, split up into respective charge bins labelled on the top right of each plot. 128
5.14 Primary pulse extracted with a Gaussian fit for a 2 GeV electron beam, split up into respective charge bins labelled on the top right of each plots. 130
5.15 Primary pulse extracted with a Gaussian fit for an 8 GeV pion beam, split up into respective charge bins labelled on the top right of each plots. 131
5.16 Charge of the secondary pulse plotted as a function of the charge of the waveform. In red circles show data points for a 2 GeV electron beam and in blue triangles show data points for an 8 GeV pion beam. For both configurations, it can be seen that the second pulse grows linearly with the total waveform. 132

5.17 Left figure shows the average spread of the beam as a function of the beam energy for an electron trigger and pion trigger. Spread was computed from beam profile data which was taken using 3 multi-wire proportional chambers (see Figure 5.5). The right figure shows the average of the primary peak width as a function of the beam energy. In both figures electron and pion triggered data are shown in red and blue, respectively. 133

5.18 Scatter plot showing the spread of the primary pulse σ_p vs the deposited charge. Each red circle corresponds to a waveform from the 2 GeV electron beam and each blue triangle corresponds to a waveform from the 8 GeV pion beam. The red and blue bands show the one sigma containment region for the 2 GeV electron and 8 GeV pion beams, respectively. On the right is shown a histogram of the primary pulse σ_p for the respective waveform data. 136

5.19 GEANT4 simulation [178] geometry of the beam test. The underside of the halfway immersed PMT is defined to be the sensitive detector. PMT hits are logged when the electron/pion penetrates the tank and hits the downstream SC4 scintillator. 137

5.20 Hit distribution of the number of photons hitting the PMT for both electron and pion events. Data points taken from this beam test are compared to GEANT4 simulations. The presence of saturation can be seen to have a large affect for very high charge data, such as for the 2 GeV data with electron triggering. 138

6.1 W distribution of ν_μ-water target interaction in GENIE. Left red hatched region is quasi-elastic scattering, middle hatched region is resonance interaction, and right green hatched region is from DIS. The W distribution can be split into three regions, KNO scaling-based model only region, PYTHIA 6 only region, and the transition region [190] 144

6.2 Illustrative depiction of the massless relativistic string in the Lund string fragmentation model. New $q\bar{q}$ pairs are created by breakups in the string from an intiaited quark-antiquark pair $q_0\bar{q}_0$ [196]. 146

6.3 Averaged charged hadron multiplicity as a function of W^2. Here, two predictions from GENIE are compared with bubble chamber neutrino hadron production data from ν_μ-proton (left) and ν_μ-neutron (right) interactions [193, 194]. The upper red line represents default GENIE which uses PYTHIA 6 and the blue line represents GENIE with PYTHIA 8. 149

6.4 Averaged charged hadron multiplicity as a function of W^2. Here, two predictions from GENIE are compared with bubble chamber neutrino hadron production data from ν_μ-proton (left) and ν_μ-neutron (right) interactions [193, 194]. The red line represents default GENIE which uses PYTHIA 6, the blue line represents GENIE with a direct translation of the PYTHIA 6 routines into PYTHIA 8 and the green line represents an implementation of PYTHIA 8 in GENIE in which the beam remnant structure is also handled by PYTHIA 8 (see text for details). 152

A.1 SME exclusion regions at 90% (99%) confidence in red (blue) for dimension $d = 3$. 160

A.2 SME exclusion regions at 90% (99%) confidence in red (blue) for dimension $d = 4$. 161

A.3 SME exclusion regions at 90% (99%) confidence in red (blue) for dimension $d = 5$. 162

A.4 SME exclusion regions at 90% (99%) confidence in red (blue) for dimension $d = 6$. 163

A.5 SME exclusion regions at 90% (99%) confidence in red (blue) for dimension $d = 7$. 164

A.6 SME exclusion regions at 90% (99%) confidence in red (blue) for dimension $d = 8$. 165

A.7 SME exclusion regions at 90% (99%) confidence in red (blue) for dimension $d = 3$. 166

A.8 SME exclusion regions at 90% (99%) confidence in red (blue) for dimension $d = 4$. 167

A.9 SME exclusion regions at 90% (99%) confidence in red (blue) for dimension $d = 5$. 168

A.10 SME exclusion regions at 90% (99%) confidence in red (blue) for dimension $d = 6$. 169

A.11 SME exclusion regions at 90% (99%) confidence in red (blue) for dimension $d = 7$. 170
A.12 SME exclusion regions at 90% (99%) confidence in red (blue) for dimension $d = 8$. 171
A.13 Exclusion regions for the dimension-three new physics operator. 173
A.14 Exclusion regions for the dimension-four new physics operator. 174
A.15 Exclusion regions for the dimension-five new physics operator. 175
A.16 Exclusion regions for the dimension-seven new physics operator. 176
A.17 Exclusion regions for the dimension-eight new physics operator. 177

List of Tables

1.1 Three neutrino flavour oscillation parameters from a fit to global data [23]. Δm^2_{3l} refers to Δm^2_{31} for normal ordering and Δm^2_{32} for inverted ordering. See Reference [24] for more up-to-date values. 9

3.1 Systematic parameters used in this analysis, showing the prior imposed on each parameter. Note the conventional flux normalisation prior is also constrained such that it cannot go below a value of 0.1. See text for more details. 59

3.2 List of Bayes factors and their inference convention according to Jeffreys' scale [101]. 64

3.3 Comparison of attainable best limits of SME operators in various fields shown with limits in this work at 90%/99% confidence level (CL). 70

3.4 Priors used for each parameter in the Bayesian approach for the dimension-six operator. 73

4.1 Parameters used in this analysis, showing the prior imposed on each parameter. 95

4.2 Comparison of attainable best limits of SME operators in various fields. Note, astrophysical neutrino limits are applied under the assumption of a produced neutrino flavour composition of either $(0:1:0)_\mathrm{S}$ or $(1:0:0)_\mathrm{S}$ at the source. 101

6.1 Driving PYTHIA 6 from GENIE. "Some amount of monkey business in making quark+diquark assignments most certainly due to our own unfamiliarity with PYTHIA. Luckily, overall generation outcomes not sensitive to choices made" [201]. 151

Part I

Neutrinos at IceCube

1 Neutrino Physics

1.1 History

The name "neutrino" was coined to describe a then hypothetical particle suggested by Wolfgang Pauli in the 1930's [1]. Pauli's idea was that of a neutral, weakly interacting particle having a very small mass. He proposed this particle could be used to explain the spectrum of electrons emitted by β-decays of atomic nuclei, which was of considerable controversy at the time. The observed spectrum of these electrons is continuous [2], which is incompatible with the two-body decay description successfully used to describe discrete spectral lines in α- and γ- decay of atomic nuclei. As Pauli observed, by describing β-decay as a three-body decay instead, releasing both an electron and his proposed particle, one can explain the continuous β-decay spectrum while still imposing the laws of conservation of energy and spin. Soon after discovery of the neutron [3], Enrico Fermi used Pauli's light neutral particle as an essential ingredient in his successful theory of β-decay, giving the neutrino it's name as a play on words of "little neutron" in Italian and predicting that it should have a very small or zero mass [4]. It was not until some 20 years later that the discovery of the neutrino was realised. Nuclear reactors provide a large flux of neutrinos and this was exploited by Cowan and Reines who were successfully able to detect inverse β-decay interactions occurring when a neutrino interacts with a proton [5]. With a further understanding of the weak force, these neutrinos induced from β-decay were identified to be not just neutrinos but electron antineutrinos. It was eventually understood that neutrinos came in three distinct *flavours* (ν_e, ν_μ, ν_τ) along with their associated antiparticles ($\bar{\nu}_e, \bar{\nu}_\mu, \bar{\nu}_\tau$), in a similar paradigm to that of the charged leptons.

The Sun also produces a large flux of neutrinos and so efforts to detect such solar neutrinos were undertaken by Ray Davis and his team, giving birth to the field of neutrino astrophysics [6]. In 1968, Davis constructed a detector filled with a chlorine compound at the Homestake mine. Here, ν_e incident on ^{37}Cl would interact, causing a conversion of ^{37}Cl into ^{37}Ar, which could be counted and then used to make an inference on the rate of

ν_e interactions. Whilst the presence of these neutrino interactions was confirmed in this experiment, the observed rate was less than that predicted by the standard solar models. This discrepancy is known as the *solar neutrino problem*. One solution came from the hypothesis that the neutrino may transform to a neutrino of a different flavour, in analogy to that of neutral meson oscillations [7, 8] but this solution was not confirmed until further observations had been made. A series of neutrino experiments were carried out to understand this, and it was during this time in which neutrinos were, for the first time, detected from a source from outside our galaxy. In 1987, a burst of neutrino events were observed preceding the optical detection of a supernova in the Large Magellanic Cloud [9–12].

Neutrinos are also produced when cosmic rays interact with the Earth's atmosphere. The flux of these atmospheric neutrinos is roughly isotropic across the Earth and this makes them interesting to study as it provides detectors with a 4π flux of atmospheric neutrinos. The neutrinos which travel from the other side of the Earth will have a much larger baseline to travel than those produced above a detector, giving more time for the phenomena of neutrino oscillations to occur. This was observed by the Super-Kamiokande experiment which was able to measure the zenith angle dependence of the flux of atmospheric ν_μ and then show that the observations made were consistent with the neutrino oscillation hypothesis [13]. The next step in our understanding came from the Sudbury Neutrino Observatory (SNO) experiment which detected solar neutrinos. SNO had the ability to both observe charged current ν_e interactions and also the total neutral-current interactions from all three neutrino flavours [14, 15]. Again it saw a deficit in the number of charged-current ν_e interactions but it was critically able to show that the total neutral-current flux was consistent with solar models, provding the first convincing evidence of flavour transitions from ν_e to ν_μ, ν_τ.

Figure 1.1 shows the evolution of neutrino experiment technologies and size. It gives a glimpse into the rich and ongoing field of neutrino physics, and the great potential neutrinos have to probe the unknowns in the Universe and discover physics beyond the Standard Model.

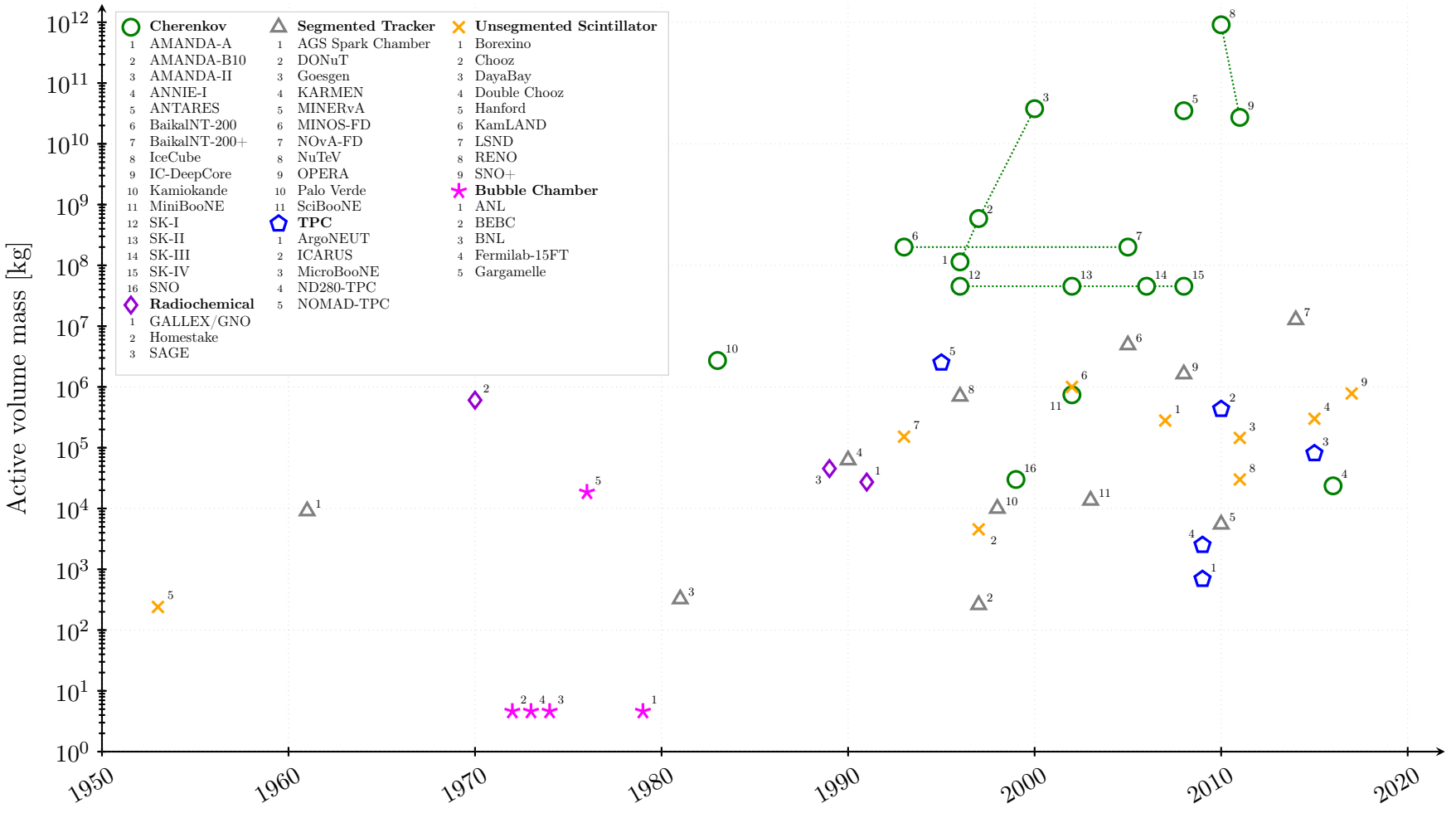

Figure 1.1: Historical evolution of the size and type of neutrino detection technology. Detectors are categorised into one of the following detection technologies: Cherenkov, radiochemical, segmented tracker, time projection chamber (TPC), unsegmented scintillator or bubble chamber, as indicated by the shape (and colour). Active volume mass of each detector is plotted against the year in which the detector became operational. This plot was made as part of INSS 2017 [16].

1.2 Neutrino Mixing

For the three massive neutrinos, the flavour eigenstates of the neutrino $|\nu_\alpha\rangle$, $\alpha \in \{e, \mu, \tau\}$, are related to the mass eigenstates $|\nu_i\rangle$, $i \in \{1, 2, 3\}$ via a unitary mixing matrix $U_{\alpha i}$ known as the PMNS matrix [7, 8]:

$$|\nu_\alpha\rangle = \sum_{i=1}^{3} U^*_{\alpha i} |\nu_i\rangle \tag{1.1}$$

This relationship between them can be better visualised in Figure 1.2. The time evolution of the flavour eigenstate as the neutrino propagates is given by:

$$|\nu_\alpha(t)\rangle = \sum_{i=1}^{3} U^*_{\alpha i} |\nu_i(t)\rangle \tag{1.2}$$

There are various mathematical approaches on the theory of neutrino mixing such the plane wave approximation [17], quantum mechanical wave packet treatments [18, 19] or through a Quantum Field Theory framework [20]. Despite the subtleties between the approaches, the final expression for the oscillation probability is robust. This section will focus on describing the mixing a neutrino undergoes in a vacuum. As shall be seen, in this case the neutrino mixing occurs in an oscillatory fashion and so can be described more specifically as *neutrino oscillations*. This section will also follow the derivation given in [21] in which the neutrino is described as a plane wave. Here, the time evolution of the neutrino in a vacuum can be described by the Schrödinger equation:

$$i\frac{\partial}{\partial t} |\nu_i(t)\rangle = H |\nu_i(0)\rangle \tag{1.3}$$

$$|\nu_i(t)\rangle = e^{-i(E_i t - \vec{\boldsymbol{p}}_i \cdot \vec{\boldsymbol{x}})} |\nu_i(0)\rangle \tag{1.4}$$

where the Hamiltonian, H, eigenstates are the mass eigenstates with $E_i = \sqrt{|\vec{\boldsymbol{p}}_i|^2 + m_i^2}$, where E_i and $\vec{\boldsymbol{p}}_i$ are the energy and momentum associated to each mass eigenstate, respectively. The case in which the neutrino momenta are aligned along $\vec{\boldsymbol{x}}$ such that $\vec{\boldsymbol{p_i}} \cdot \vec{\boldsymbol{x}} = p_i L$ where $p_i = |\vec{\boldsymbol{p_i}}|$ and $L = |\vec{\boldsymbol{x}}|$ is considered[1].

[1] This is sometimes referred to as the *equal momentum approximation* and it can be shown that this approximation is appropriate as long as the dependence of the production and detection probabilities on the neutrino masses is negligible [21].

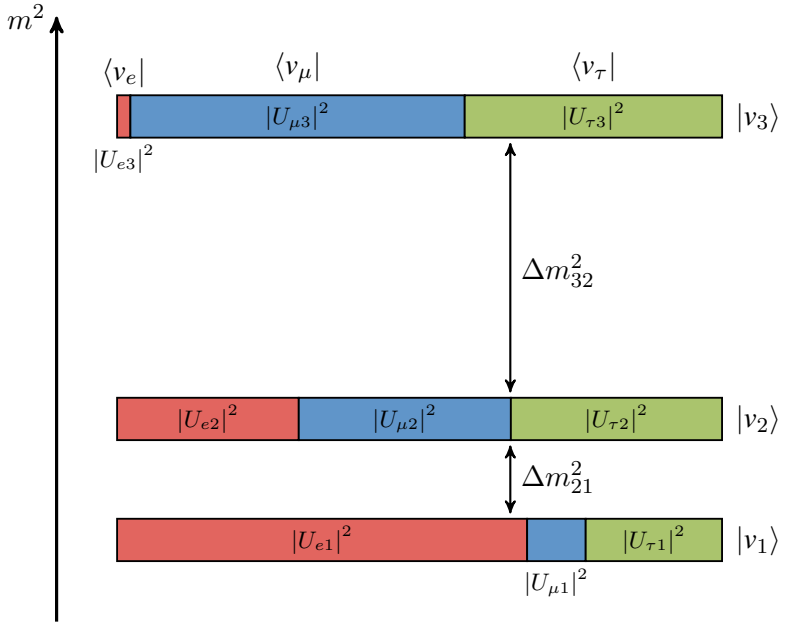

Figure 1.2: Graphical representation of the relationship between the neutrino flavour and mass eigenstates. The three mass eigenstates are depicted as three boxes, coloured such that the relative area gives the probability of finding the corresponding flavour neutrino in that given mass state. Normal ordering of the neutrino masses is assumed and mixing elements reflect neutrino propagation in a vacuum. Normal ordering and inverted ordering correspond to the case where the mass of ν_3 is greater than the mass of ν_1 or the mass of ν_1 is greater than the mass of ν_3, respectively.

In the ultrarelativistic limit, the dispersion relation can be approximated:

$$E_i = \sqrt{p_i^2 + m_i^2} \approx p_i + \frac{m_i^2}{2p_i} \approx p_i + \frac{m_i^2}{2E} \tag{1.5}$$

where E is neutrino energy neglecting mass contributions. Then in natural units, $t \approx L$ which is the distance travelled by the neutrino and this relation is sometimes called the *light-ray approximation* (more on this in Section 1.2.3).

$$E_i t - \vec{\boldsymbol{p}}_i \cdot \vec{\boldsymbol{x}} \approx E_i t - p_i L \tag{1.6}$$

$$\approx (E_i - p_i) L \tag{1.7}$$

$$\approx \frac{m_i^2}{2E} L \tag{1.8}$$

$$|\nu_i\,(L)\rangle = e^{-i\frac{m_i^2 L}{2E}}\,|\nu_i\,(0)\rangle \tag{1.9}$$

The oscillation probability gives the probability that a neutrino produced in a flavour state α is then detected in a flavour state β after a propagation distance L:

$$P_{\nu_\alpha \to \nu_\beta}(L) = |\langle \nu_\beta(L) | \nu_\alpha(0) \rangle|^2 \tag{1.10}$$

$$= \left| \sum_{i=1}^{3} \sum_{j=1}^{3} \langle \nu_j(L) | U_{\beta j} U^*_{\alpha i} | \nu_i(0) \rangle \right|^2 \tag{1.11}$$

$$= \left| \sum_{i=1}^{3} \sum_{j=1}^{3} U_{\beta j} U^*_{\alpha i} \langle \nu_j(0) | e^{-i\frac{m_j^2 L}{2E}} e^{-i\frac{m_i^2 0}{2E}} | \nu_i(0) \rangle \right|^2 \tag{1.12}$$

$$= \left| \sum_{i=1}^{3} U_{\beta i} U^*_{\alpha i} e^{-i\frac{m_i^2 L}{2E}} \right|^2 \tag{1.13}$$

where the relation $\langle \nu_i | \nu_j \rangle = \delta_{ij}$ was used. Expanding this expression gives [21]:

$$P_{\nu_\alpha \to \nu_\beta}(L, E) = \delta_{\alpha\beta} - 4 \sum_{i>j} \mathrm{Re}\left(U^*_{\alpha i} U_{\beta i} U_{\alpha j} U^*_{\beta j}\right) \sin^2\left(\frac{\Delta m^2_{ij} L}{4E}\right) + 2 \sum_{i>j} \mathrm{Im}\left(U^*_{\alpha i} U_{\beta i} U_{\alpha j} U^*_{\beta j}\right) \sin\left(\frac{\Delta m^2_{ij} L}{2E}\right) \tag{1.14}$$

where $\Delta m^2_{ij} = m^2_i - m^2_j$. First note that for neutrino oscillations to occur, there must be at least one non-zero Δm^2_{ij} and therefore there must exist at least one non-zero neutrino mass state. Second is that the oscillation probability is Lorentz invariant, meaning that neutrino flavour at detection is seen as being the same by any inertial observer. The approximation $t \approx L$ was made, which means that L transforms as t, which subsequently transforms as E as they are both time-like components. Therefore the ratio L/E is Lorentz invariant. Note that L here is generally not the instantaneous source-detector distance at the time of neutrino detection, which is subject to length contraction, but is in fact the spatial difference between the two spacetime events of neutrino production and detection.

The mixing matrix can be parameterised using the standard factorisation [22]:

$$U = \begin{pmatrix} 1 & 0 & 0 \\ 0 & c_{23} & s_{23} \\ 0 & -s_{23} & c_{23} \end{pmatrix} \begin{pmatrix} c_{13} & 0 & s_{13} e^{-i\delta} \\ 0 & 1 & 0 \\ -s_{13} e^{i\delta} & 0 & c_{13} \end{pmatrix} \begin{pmatrix} c_{12} & s_{12} & 0 \\ -s_{12} & c_{12} & 0 \\ 0 & 0 & 1 \end{pmatrix} \tag{1.15}$$

where $s_{ij} \equiv \sin\theta_{ij}$, $c_{ij} \equiv \cos\theta_{ij}$, θ_{ij} are the three mixing angles and δ is the CP violating phase. Overall phases in the mixing matrix do not affect neutrino oscillations, which only

Parameter	Normal Ordering	Inverted Ordering
$\sin^2\theta_{12}$	$0.307^{+0.013}_{-0.012}$	$0.307^{+0.013}_{-0.012}$
$\sin^2\theta_{23}$	$0.538^{+0.033}_{-0.069}$	$0.554^{+0.023}_{-0.033}$
$\sin^2\theta_{13}\,[10^{-2}]$	$2.206^{+0.075}_{-0.075}$	$2.227^{+0.074}_{-0.074}$
$\Delta m^2_{21}\,[10^{-5}\,\mathrm{eV}^2]$	$7.40^{+0.21}_{-0.20}$	$7.40^{+0.21}_{-0.20}$
$\Delta m^2_{3l}\,[10^{-3}\,\mathrm{eV}^2]$	$+2.494^{+0.033}_{-0.031}$	$-2.465^{+0.034}_{-0.031}$
$\delta\,[^\circ]$	234^{+43}_{-31}	278^{+26}_{-29}

Table 1.1: Three neutrino flavour oscillation parameters from a fit to global data [23]. Δm^2_{3l} refers to Δm^2_{31} for normal ordering and Δm^2_{32} for inverted ordering. See Reference [24] for more up-to-date values.

depend on quartic products as can be seen in Equation 1.14, and so they have been omitted[2]. Therefore, this gives a total of six independent free parameters describing neutrino oscillations for three neutrino flavours in a vacuum. Table 1.1 outlines the current knowledge of these parameters determined by a fit to global data [23]. This table shows two columns of values, *normal ordering* and *inverted ordering* corresponding to the case where the mass of ν_3 is greater than the mass of ν_1 or the mass of ν_1 is greater than the mass of ν_3, respectively. The experimental determination of this mass ordering is ongoing.

1.2.1 Two neutrino mixing

Two neutrino mixing is the approximation in which only two neutrino states are considered, and the third one is ignored. Here, the mixing matrix is given by the 2×2 rotational matrix with a mixing angle θ:

$$U = \begin{pmatrix} \cos\theta & \sin\theta \\ -\sin\theta & \cos\theta \end{pmatrix} \tag{1.16}$$

Then, there exists a single mass splitting $\Delta m^2 \equiv m_2^2 - m_1^2$. From Equation 1.14, the oscillation probability can be seen as being:

$$P_{\nu_\alpha\to\nu_\beta}(L,E) = \begin{cases} 1 - \sin^2 2\theta \sin^2\left(\frac{\Delta m^2 L}{4E}\right) & \text{for } \alpha = \beta \\ \sin^2 2\theta \sin^2\left(\frac{\Delta m^2 L}{4E}\right) & \text{for } \alpha \neq \beta \end{cases} \tag{1.17}$$

[2]For a more detailed look into the properties of the mixing matrix see [21]

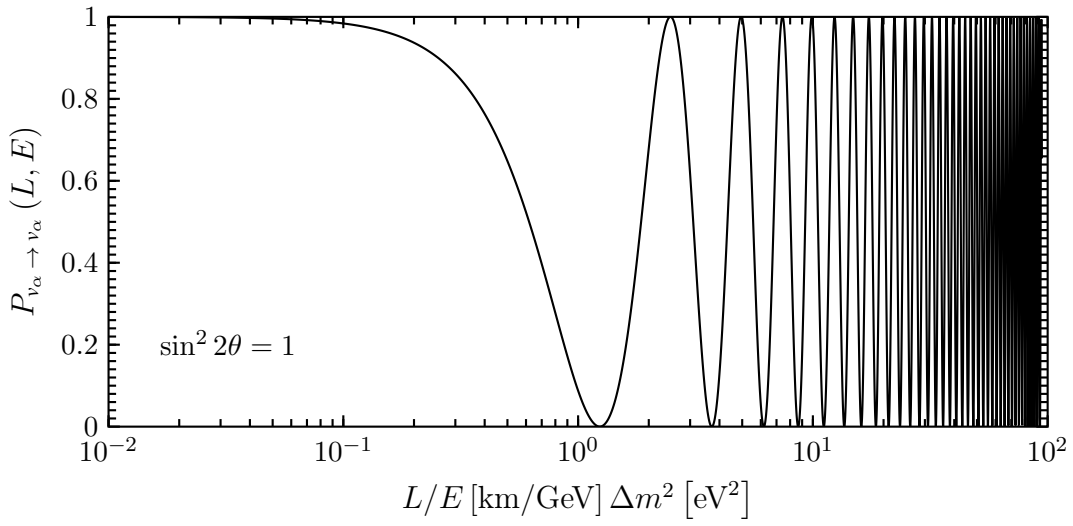

Figure 1.3: Neutrino survival probability in the two neutrino scheme for $\sin^2 2\theta = 1$ as a function of $L/E\,[\mathrm{km/GeV}]\,\Delta m^2\,[\mathrm{eV}^2]$.

Here the sinusoidal behaviour can be seen to have an amplitude driven by the mixing angle and a frequency proportional to Δm^2. This approximation is extremely useful for describing atmospheric neutrino oscillations as they are dominated by transitions between the two neutrino flavours, ν_μ and ν_τ. The neutrino survival probability ($\alpha = \beta$) can be visualised in Figure 1.3. There are three regions in which the phenomenology can be split into. First when $\sin^2\left(\Delta m^2 L/4E\right) \to 0$, the survival probability is 1 so no flavour transition occurs. The region when $\sin^2\left(\Delta m^2 L/4E\right) = 1$, represents the *first oscillation maximum* and corresponds to the first maximum conversion between neutrino flavours. Here, neutrino oscillations are observable and so oscillation experiments are traditionally designed to lie in this region. The baseline at which a complete period of the oscillation cycle has been completed is referred to as the *oscillation length*,

$$L_{\mathrm{osc}} = \frac{4\pi E}{\Delta m^2} \tag{1.18}$$

Lastly, at $\Delta m^2 L/4E \gg 1$, one encounters fast oscillations which cannot be resolved by experiments. Here the oscillation probability averages to $P_{\nu_\alpha \to \nu_\beta}(L, E) \sim \frac{1}{2}\sin^2 2\theta$ therefore only information on $\sin^2 2\theta$ is observable.

1.2.2 Matter interactions

So far, the description given of neutrinos only considers them propagating in a vacuum, however neutrinos travelling through a dense region will experience modifications to the neutrino oscillation probability [25, 26]. When travelling through matter containing electrons, the ν_e have contributions coming from elastic forward scattering interactions $\nu + e \to \ell + \nu_e$ which are not present for the ν_μ and ν_τ flavours (see Section 1.4.1). These extra interactions can be expressed as a potential energy term for ν_e given by [25]:

$$V_e = \sqrt{2} G_F n_e \tag{1.19}$$

where G_F is the Fermi coupling constant and n_e is the electron number density in the medium. The Hamiltonian is then modified as:

$$H_m^\alpha = H_0^\alpha + H_{\text{int}}^\alpha \tag{1.20}$$

where α denotes the flavour representation, H_m^α is the effective Hamiltonian which takes into account both the vacuum Hamiltonian, H_0^α, and the Hamiltonian which accounts for neutrino-matter interactions, H_{int}^α, which can be written as simply[3]:

$$H_{\text{int}}^\alpha = \text{diag}\left(\sqrt{2} G_F n_e, 0, 0\right) \tag{1.21}$$

This has the effect of modifying the dispersion relations such that the modified ν_e mass can be written as:

$$m_{ee,m}^2 = m_{ee}^2 + 2E\sqrt{2} G_F n_e \tag{1.22}$$

This can be transformed back into the vacuum mass eigenstate representation ν_i. In the two neutrino flavour scheme:

$$H_m^i = H^i + \frac{1}{2E} U^\dagger \,\text{diag}\,(A, 0)\, U \tag{1.23}$$

$$= \frac{1}{2E} \begin{pmatrix} m_1^2 + A\cos^2\theta & A\cos\theta\sin\theta \\ A\cos\theta\sin\theta & m_2^2 + A\cos^2\theta \end{pmatrix} \tag{1.24}$$

[3]Note that there is also a matter effect coming from neutral current interactions however this takes place for all neutrino flavours and so does not affect the oscillation probability.

where $A \equiv 2\sqrt{2}G_F E n_e$. The effective Hamiltonian H_m^i now has non-diagonal terms, which means that the vacuum mass eigenstates are no longer eigenstates of H_m^i. Equation 1.24 can subsequently be diagonalised in order to obtain the effective mass eigenvalues, $m_{i,m}^2$ (effective masses):

$$m_{1m,2m}^2 = \frac{1}{2}\left[\left(m_1^2 + m_2^2 + A\right) \mp \sqrt{\left(A - \Delta m^2 \cos 2\theta\right)^2 + \left(\Delta m^2\right)^2 \sin^2 2\theta}\right] \tag{1.25}$$

Now the effective mixing matrix U_m can connect the effective mass eigenstates with the flavour eigenstates through a mixing angle θ_m. The oscillation probability can then be written down in the same form as in Equation 1.17 with the modified parameters:

$$P_{\nu_\alpha \to \nu_\beta,\, m}\left(L, E\right) = \begin{cases} 1 - \sin^2 2\theta_m \sin^2\left(\frac{\Delta m_m^2 L}{4E}\right) & \text{for } \alpha = \beta \\ \sin^2 2\theta_m \sin^2\left(\frac{\Delta m_m^2 L}{4E}\right) & \text{for } \alpha \neq \beta \end{cases} \tag{1.26}$$

where

$$\sin 2\theta_m = \frac{\sin 2\theta}{\sqrt{\left(\frac{A}{\Delta m^2} - \cos 2\theta\right)^2 + \sin^2 2\theta}} \tag{1.27}$$

$$\Delta m_m^2 = \Delta m^2 \sqrt{\left(\frac{A}{\Delta m^2} - \cos 2\theta\right)^2 + \sin^2 2\theta} \tag{1.28}$$

For the case when $A \to 0$, which corresponds to the vacuum case, $\theta_m \to \theta$ and $\Delta m_m^2 \to \Delta m^2$ as expected. The oscillation probability can be seen to undergo a resonance when the condition $A = \Delta m^2 \cos 2\theta$ is met, where the probability equals 1 for any vacuum mixing angle. Another interesting case to note is when $A \gg \Delta m^2$, i.e. when the density of matter becomes very large. Here the probability is very suppressed so flavour transitions no longer occur and the neutrino becomes frozen in its flavour state. The mixing angle $\theta_m \to 0$, diagonalising the effective mixing matrix meaning that the flavour and mass eigenstates coincide. Similar behaviour can be observed from solar neutrinos which are produced in the Sun's core. The density in the Sun, however, decreases slowly going from the solar core to the surface, meaning that the effective mixing matrix becomes a function of the density, causing non-oscillatory flavour conversion known as *adiabatic flavour conversion* or the MSW effect [27]. It was this phenomena that was accepted as the solution to the *solar neutrino problem* discussed in Section 1.1.

1.2.3 Wave packet treatment

So far, neutrinos have been described as plane waves, however this approach has inconsistencies, one example being the application of the *light-ray approximation* $t = L$, which is unjustified as plane waves extend over all of spacetime with the same amplitude. Also, neutrino production and detection are spatially localised in a region with finite energy and momentum uncertainties, which the plane wave picture fails to describe. While the results obtained are nonetheless robust, it can be instructive to describe neutrinos as wave packets instead[4]. In this picture, a neutrino mass state is described as a superposition of plane waves known as a wave packet, which in quantum mechanics describes real localised particles with a momentum spread at production, σ_p^{prod}, and detection, σ_p^{det}. The wave packet can be approximated as a Gaussian and it can be shown that the effect of the source and detector due to this spread is symmetric, allowing the wave packet to be described by a combined effective spread, σ_p. Figure 1.4 shows an illustration of the dynamics at play for a two-neutrino system with a mixing angle of $\theta = 45°$. The top figure shows the neutrino oscillation probabilities as a function of the time after production. At a detector distance of $L_0 = 0$, the momentum spread at the production can be seen in the time axis. From the Heisenberg uncertainty principle, $\sigma_p \sim \sigma_t^{-1}$, the neutrino is not produced at a single point in spacetime and a distribution can be seen, even though the detector has been placed at the production point. As the detector distance is increased, $L_1 > L_0$, two effects can be noted. There is a shift in the wave packets of the two mass eigenstates due to the difference in group velocities between them. The lighter mass eigenstate ν_1 can be seen to arrive at the detector before the heavier ν_2. The second effect is that oscillations between the two neutrino flavours only occur when the mass eigenstates are overlapping. Indeed, the effect of oscillations is caused by a coherent interference of different mass states. Lastly at detector distances $L_2 > L_1$, the mass eigenstates have decoupled and oscillations can no longer be observed. The distance above which coherence is lost is called the *coherence length* and can be written as:

$$L_{coh} = \sigma_x \frac{2E^2}{\Delta m^2} \tag{1.29}$$

Note the dependence on σ_x, implying that coherence is also a function of the detector resolution. Similar logic can also be applied in the spatial plane (bottom figure).

[4] A full derivation will not be demonstrated and can be found instead in [19].

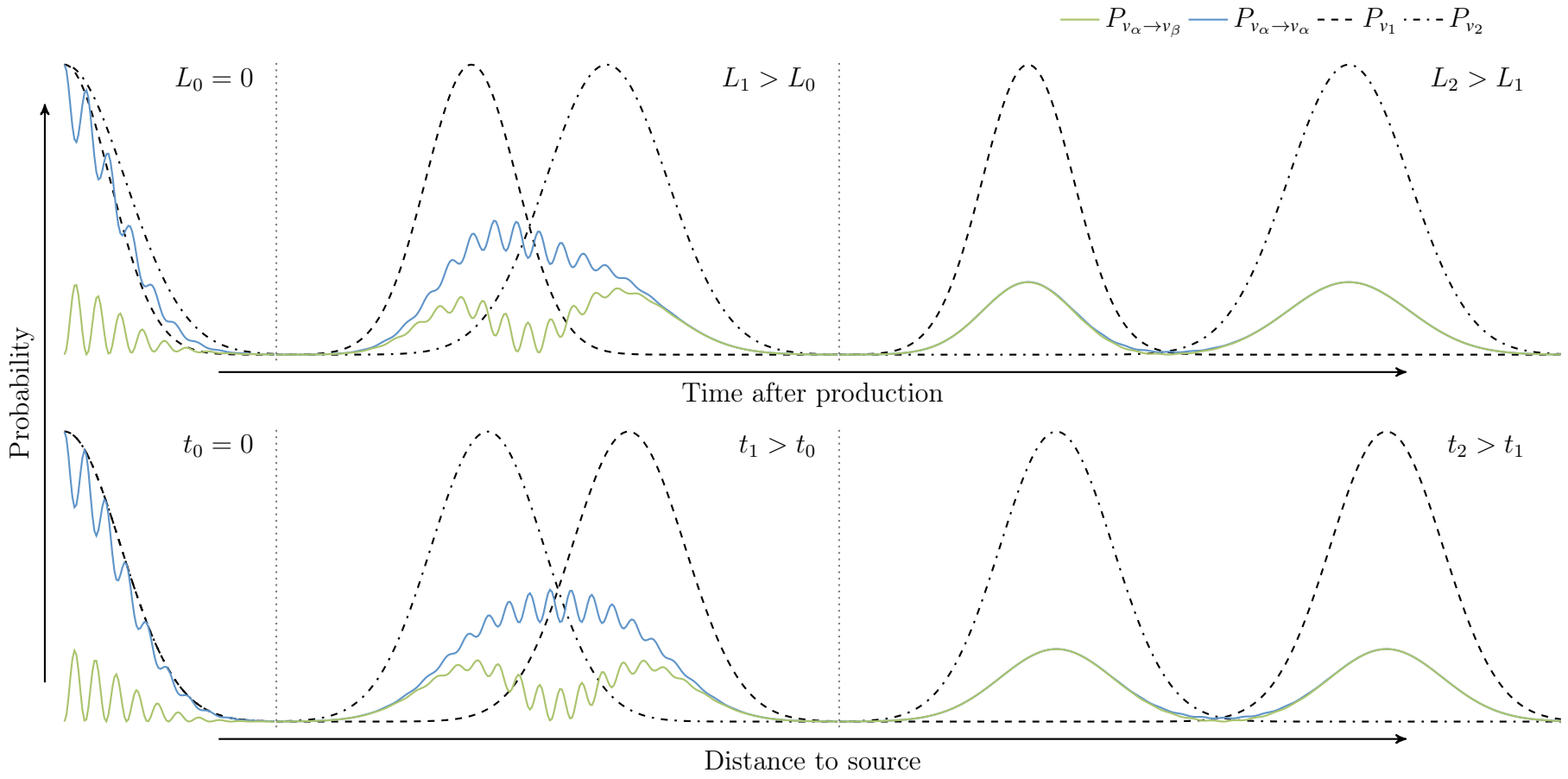

Figure 1.4: Neutrino oscillation probabilities when treating the neutrino as a wave packet. A neutrino of flavour ν_α is produced on the left. In colour, the probability of detecting a neutrino with flavour ν_α (blue) and ν_β (green). In black, the probability of the neutrino being of a particular mass eigenstate ν_1 (dashed) and ν_2 (dashed-dotted). The top figure shows the probabilities as a function of time after production for three fixed detector locations, $L_0 < L_1 < L_2$. The bottom figure shows the probabilities as a function of the distance to the source for three fixed detection times, $t_0 < t_1 < t_2$.

1.2.4 CPT transformations

The simultaneous transformation of *charge*, *parity* and *time reversal* (CPT) has so far been observed to be an exact symmetry of nature. CPT theorem is based on *causality* and *Lorentz invariance* (LI), therefore making CPT symmetry a fundamental probe in our understanding of particle physics [28]. Figure 1.5 shows how these transformations relate the different flavour transition channels in neutrino mixing. CP transformation interchanges neutrinos with antineutrinos and reverses the helicity, giving the relation $\nu_\alpha \overset{CP}{\longleftrightarrow} \bar{\nu}_\alpha$. A T transformation interchanges the incoming and outgoing states, from the $\nu_\alpha \to \nu_\beta$ channel to $\nu_\beta \to \nu_\alpha$ and finally CPT interchanges $\nu_\alpha \to \nu_\beta$ to $\bar{\nu}_\beta \to \bar{\nu}_\alpha$.

Quantum Field Theory (QFT) and *general relativity* (GR) are the two theoretical and mathematical foundations of modern physics, however physicists have so far been unable to reconcile the two paradigms to produce a coherent theory of *quantum gravity* (QG), able to describe physics at the Planck scale ($\sim 10^{19}$ GeV), where effects quantum effects from gravity are expected to dominate. As will be discussed more in Chapter 3, many approaches to QG imply the breaking of LI and CPT symmetries, and so tests of these symmetries provide a powerful probe into theories of QG.

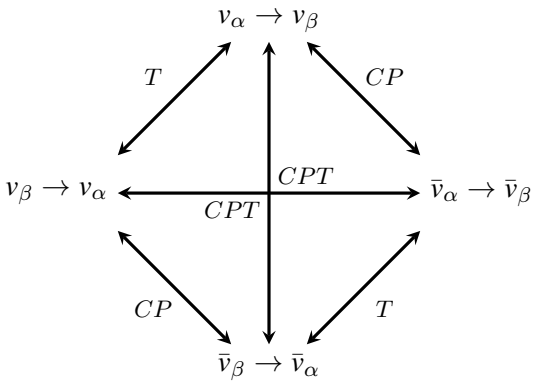

Figure 1.5: Scheme of CPT, CP and T transformations that relate different flavour transition channels [21].

1.3 Neutrino Production

1.3.1 Atmospheric neutrinos

The study of atmospheric neutrinos was and still is one of the most important fields in neutrino physics. These are produced when cosmic rays interact in the Earth's upper atmosphere. Cosmic rays are composed of ionised nuclei, about 90% protons, 9% alpha particles and the rest heavier nuclei [29]. They are mostly relativistic, having energies similar to or greater than their masses. The field of cosmic ray physics is an area of very active research and in particular the fundamental question of the origins and acceleration mechanisms of the very highest energy cosmic rays - extending to 10^{20} eV - still remains unanswered.

An air shower is induced when cosmic rays interact in the atmosphere, having electromagnetic, muonic and hadronic components. The hadronic showers are rich in light mesons, whose cascades can be linked to the production of atmospheric neutrinos. The most important channels are through the following pion and kaon decays, given here with their branching ratio:

$$\pi^{\pm} \to \mu^{\pm} + \nu_{\mu}\,(\bar{\nu}_{\mu}) \;\; (\sim 100\%) \tag{1.30}$$

$$K^{\pm} \to \mu^{\pm} + \nu_{\mu}\,(\bar{\nu}_{\mu}) \;\; (\sim 63.5\%) \tag{1.31}$$

The decay of the muon here must also be considered:

$$\mu^{\pm} \to e^{\pm} + \nu_{e}\,(\bar{\nu}_{e}) + \bar{\nu}_{\mu}\,(\nu_{\mu}) \tag{1.32}$$

The flux of neutrinos produced through this mechanism makes up the *conventional* atmospheric neutrino component and an illustration of this can be seen in Figure 1.6. If all particles decay, we can expect $(\nu_e + \bar{\nu}_e)\,/\,(\nu_\mu + \bar{\nu}_\mu) \sim \frac{1}{2}$. In fact, it was the observation by Kamiokande [30] that the ν_e/ν_μ ratio averages to $\sim$1 for upgoing neutrinos that eventually led to the discovery of neutrino oscillations (see Section 1.2 for more). For muon energies above $\sim$2.5 GeV, the Lorentz boost is high enough that the muon decay length surpasses the typical production height ($\sim$15 km), and so the ν_e/ν_μ ratio quickly decreases whereby the only source of ν_e comes from contributions from $K^0_L \to \pi\, e\, \nu_e$ and $K^{\pm} \to \pi^0\, e\, \nu_e$. This

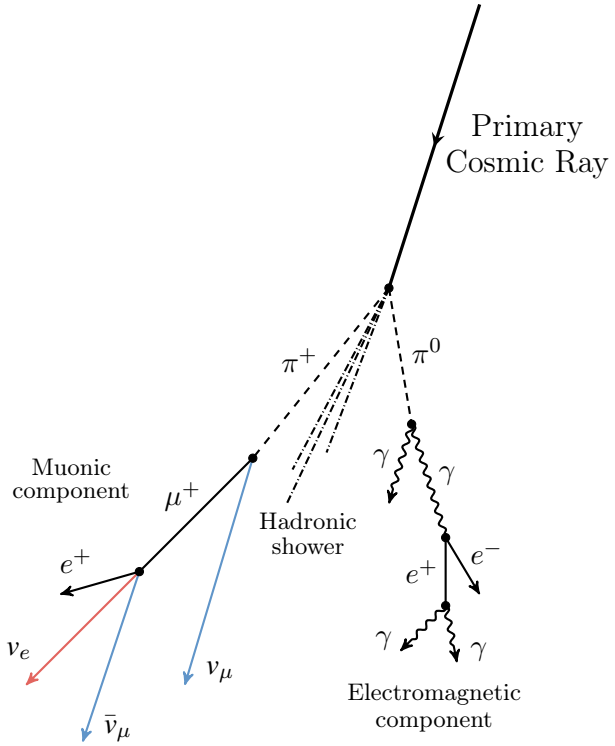

Figure 1.6: Simplified schematic of an air shower generated by a cosmic ray. The decay of light mesons in the shower produces a flux of neutrinos, more specifically the conventional atmospheric neutrino flux. Adapted from [31].

is called the *critical energy* and is the energy at which the decay and interaction lengths of a particle in an air shower are equal. This is an important feature of the conventional component, resulting in a softer (steeper) energy spectrum ($\sim E^{-3.7}$) than that of the cosmic rays ($\sim E^{-2.7}$). The effective critical energy is also a function of zenith due to the varying propagation lengths. The shorter lifetime of the kaons means their critical energy is less dependent on the zenith than for the muons. However, both components see an enhancement of the neutrino flux at the horizon compared to the vertical, where the effective critical energy is maximal as the particles are more likely to have enough distance to decay.

The conventional flux dominates up to ~18 TeV. At even greater energies, the flux of atmospheric neutrinos is dominated by the decays of charmed particles. These particles are substantially heavier and have livetimes so short that they almost always decay before interacting, i.e. they decay promptly and thus the name of this component of the atmospheric neutrino flux is called the *prompt* flux. The prompt flux is not as well understood as the conventional flux, as they have not yet been observed experimentally. However, it is

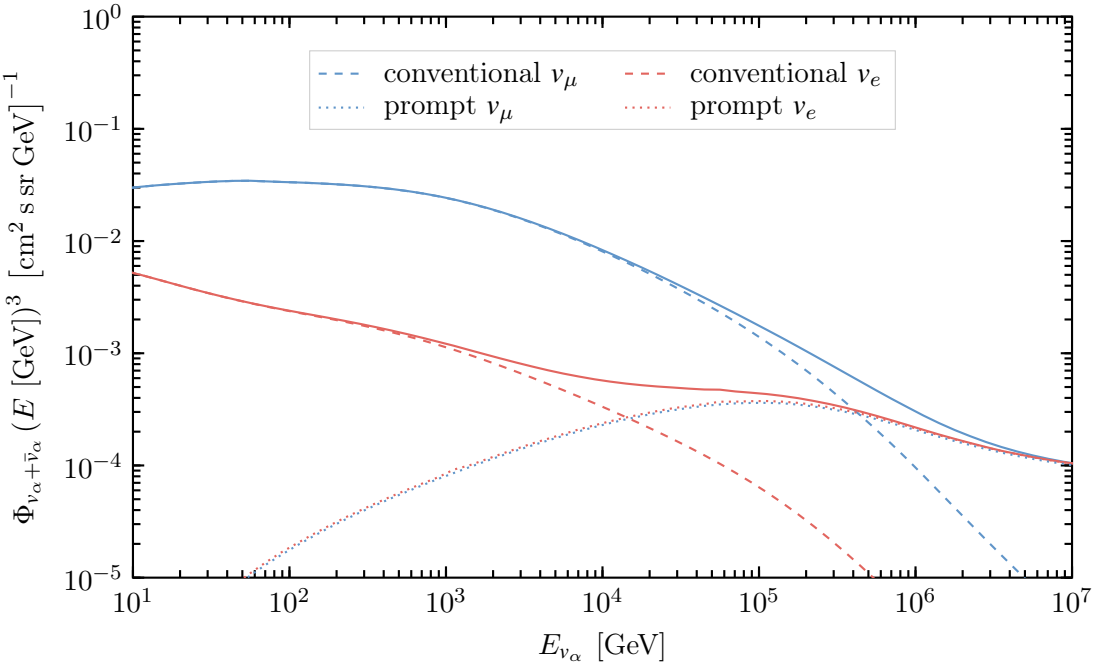

Figure 1.7: Atmospheric neutrino fluxes for $\nu_\mu + \bar{\nu}_\mu$ (blue) and $\nu_e + \bar{\nu}_e$ (red), calculated using the MCEQ package [32]. Dashed line shows the conventional components, dotted line shows the prompt components and solid line shows the total. Note the prompt neutrino flux has not yet been experimentally observed.

expected to produce a quantitatively different flux than the conventional flux in two ways. First, the energy spectrum will be similar to the spectrum of the primary cosmic rays as the charmed particles have much higher critical energies ($\sim 4 \times 10^7$ GeV for the $D^\pm$ [29], which would produce the next largest flux). The harder (flatter) spectrum compared to the conventional component is why, despite the much lower rate of production, they are expected to eventually dominate the neutrino flux. Second the angular distribution is isotropic, again because of the high critical energies. The decay of the charmed particles to electrons (with ν_e) is not suppressed as it is for the light mesons, so the prompt ν_e flux is expected to be very similar to the prompt flux of ν_μ.

Figure 1.7 shows the conventional and prompt atmospheric neutrino flux as a function of the neutrino energy. The modelling of the atmospheric neutrino flux requires three main ingredients; the primary cosmic ray spectrum, the hadronic interaction model and the atmospheric density profile over which the shower develops. The primary cosmic ray spectrum is approximately proportional to an $E^{-\gamma}$ power law with $\gamma \sim 2.7$ up to proton energies of $\sim 10^6$ GeV. Above this, the spectrum exhibits discrete features discussed above (called the *knee*) causing the spectrum to soften. Here, we use the Honda-Gaisser model

with the Gaisser-Hillas H3a correction [33]. The next ingredient is the hadronic interaction model, which simulates the secondary hadron production from the primary cosmic ray. These models are based on data from fixed target and collider experiments with extrapolations for the highest energy cosmic rays which are beyond the reach of man-made accelerators. Here we use the SIBYLL 2.3c hadronic interaction model [34, 35]. Lastly, the atmospheric density profile is built by using atmospheric data from satellites to create detailed numerical models. The seasonal variation of the atmospheric density also leads to seasonal variations of the atmospheric neutrino flux. Here we use the NRLMSISE-00 model taken at the South Pole, averaging the seasonal effects over the month of January [36]. Under these assumptions, the atmospheric neutrino flux is computed by numerically solving the coupled cascade equation describing the evolution of the flux of particles in a cosmic ray shower. Here, the package MCEQ [32] is used to solve these to obtain the atmospheric neutrino flux shown.

1.3.2 Astrophysical neutrinos

The origin and acceleration mechanism of ultra-high-energy cosmic rays is still unknown. The difficulty comes from the fact that the cosmic rays are bent by interstellar magnetic fields, and so their arrival direction on Earth does not point back to their sources. The observation of these ultra-high-energy cosmic rays supports the existence of neutrino production at the sources of a similar energy range - an astrophysical neutrino flux. Neutrinos are electrically neutral, so are not perturbed by interstellar magnetic fields, and they also have a small enough interaction cross-section to escape from dense regions. This makes them ideal messengers to help identify the sources of cosmic rays, see Figure 1.8.

Ultra-high-energy cosmic rays detected on Earth manifestly succeed in escaping their sources, therefore these sources must be optically thin compared to the Earth's atmosphere. Thus, the following interactions of the accelerated protons are expected to be more important than lengthy shower processes. High-energy protons can interact with photons as such:

$$p + \gamma \to \Delta^+ \to \begin{cases} p + \pi^0 \\ n + \pi^+ \end{cases} \tag{1.33}$$

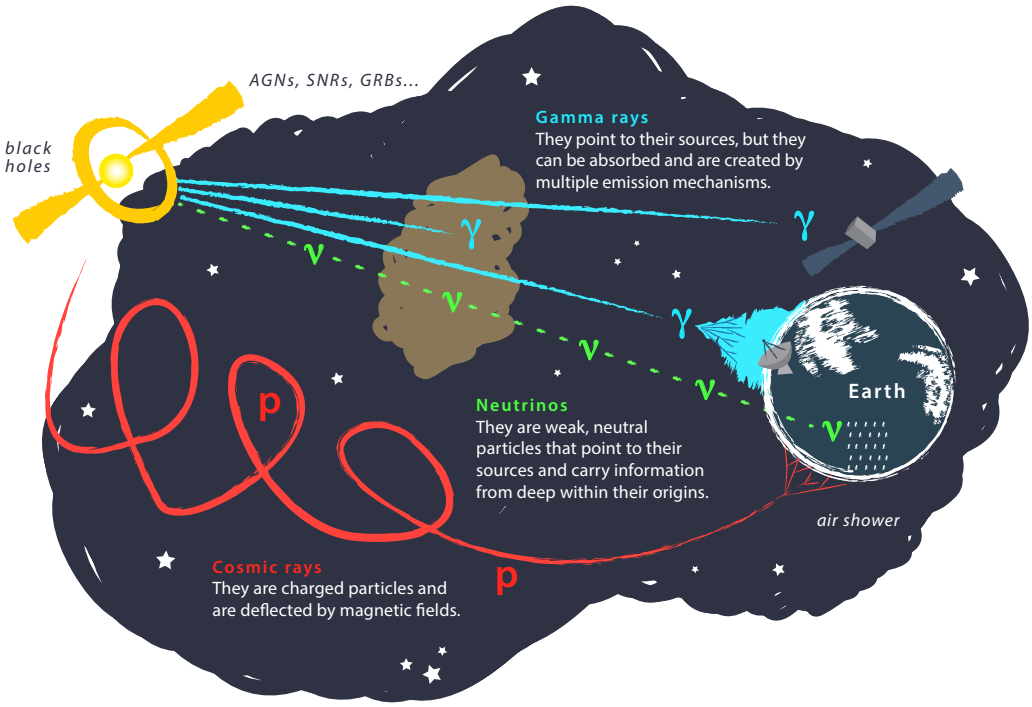

Figure 1.8: Neutrinos as messengers of astrophysical objects. Exotic astrophysical objects produce high-energy cosmic rays, photons and neutrinos, which can be detected on Earth. Credit: IceCube, NSF.

They can also interact with other hadrons:

$$p + p \rightarrow \begin{cases} p + p + \pi^0 \\ p + n + \pi^+ \end{cases} \tag{1.34}$$

$$p + n \rightarrow \begin{cases} p + n + \pi^0 \\ p + p + \pi^- \end{cases} \tag{1.35}$$

Importantly, final states here tend to produce pions which decay into either photons if neutral, $\pi^0 \rightarrow \gamma\gamma$, or if they are charged they decay into charged leptons and neutrinos (see Equation 1.30) - a process very similar to the production of conventional atmospheric neutrinos. The neutral and charged pions are produced in similar amounts, meaning that the neutrino and photon fluxes are related. Indeed the diffuse astrophysical neutrino flux can be estimated through γ-ray astronomy [37]. It can also be measured directly as an excess of high-energy neutrinos from the whole sky above the softer background of atmospheric neutrinos. Figure 1.9 illustrates this by showing the differences in the atmospheric

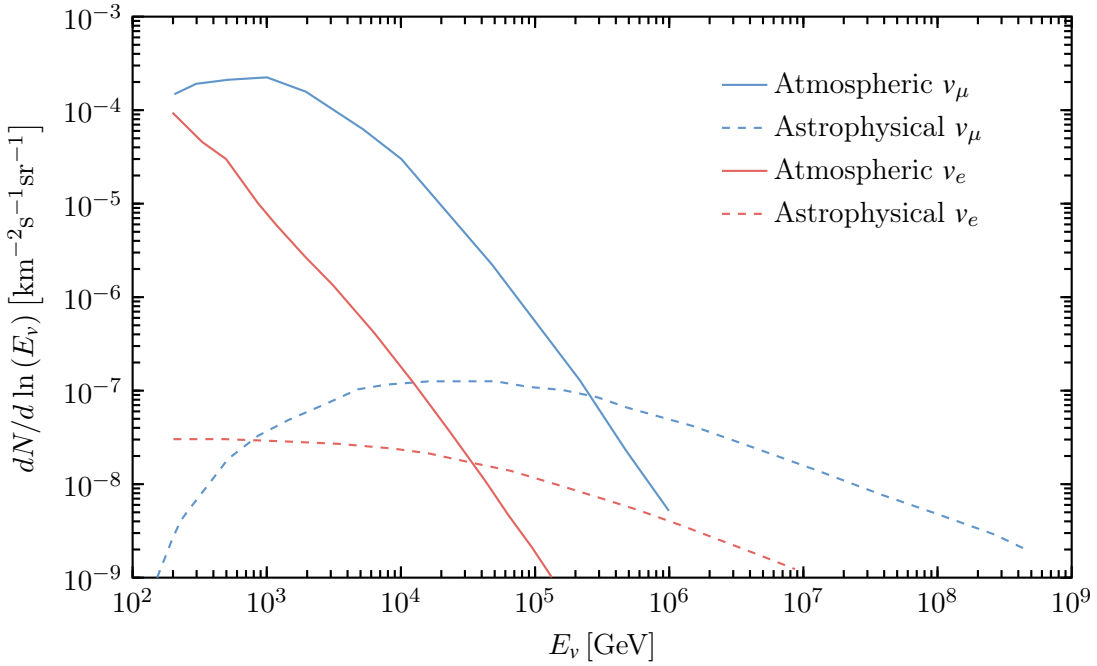

Figure 1.9: Estimated rate of ν_μ events (blue) and ν_e events (red) for a kilometre-scale detector. Solid line is for the atmospheric neutrino component and dashed for the astrophysical component. Recreated from [29].

and astrophysical neutrino spectrum. Here the rate of atmospheric and astrophysical neutrino events is plotted against the neutrino energy for a kilometre-scale detector [29]. For astrophysical neutrinos, a generic E^{-2} spectrum is taken, normalised to IceCube data and for atmospheric neutrinos a spectral index of $E^{-3.7}$ is taken. IceCube was able to measure this excess in high-energy neutrinos and so provide the first evidence of the existence of a diffuse flux of astrophysical neutrinos [38, 39].

Point source searches of neutrinos are also being pursued. In 2017, a multi-messenger approach which searched for γ-ray observations in coincidence with neutrinos coming from a particular source has successfully been able to identify for the very first time, a source of high-energy astrophysical neutrinos [40, 41].

Of particular interest is the composition of flavours produced at the source. In the simple pion decay model described above, the *neutrino flavour composition* (sometimes referred to as the *neutrino flavour ratio*) produced at the source is:

$$\pi \text{ decay} \qquad (f_e : f_\mu : f_\tau)_S = (1 : 2 : 0)_S \tag{1.36}$$

For all discussions on the astrophysical neutrino flavour composition, the neutrino and

antineutrino fluxes will been summed over as it is not yet experimentally possible to distinguish between the two. In the case that the muon interacts in the source before it has a chance to decay, e.g. losing energy rapidly in strong magnetic fields or being absorbed in matter, only the ν_μ from the initial pion decay escapes and so the source flavour composition is simply:

$$\mu \text{ suppressed} \qquad (f_e : f_\mu : f_\tau)_{\mathrm{S}} = (0 : 1 : 0)_{\mathrm{S}} \tag{1.37}$$

Another popular model is one in which the produced flux is dominated by neutron decay, $n \to p + e^- + \bar{\nu}_e$, which gives rise to a purely ν_e component:

$$n \text{ decay} \qquad (f_e : f_\mu : f_\tau)_{\mathrm{S}} = (1 : 0 : 0)_{\mathrm{S}} \tag{1.38}$$

Production of ν_τ at the source is not expected in standard astrophysics models. However, even in the standard construction, the composition could vary between any of the three idealised models above, which can be represented as a source flavour composition of $(x : 1 - x : 0)$, where x is the fraction of ν_e and can vary between $0 \to 1$.

Once the neutrinos escape the source, they are free to propagate in the vacuum. As discussed in detail in Section 1.2, neutrinos can transform from one flavour to another. Astrophysical neutrinos have $\mathcal{O}$(Mpc) or higher baselines, large enough that the mass eigenstates completely decouple. This can be seen by considering L_{coh}, the coherence length, as shown in Equation 1.29. Using the values $E \sim 10^6$ GeV, $\Delta m^2 \sim 10^{-23}$ GeV^2 and $\sigma_x \sim 10^{-13}$ m [27], one finds $L_{coh} \sim 0.6$ Mpc. The mass state wave packets are also seen to spread as they propagate, as discussed in Section 1.2.3. The ratio of the spread σ_{spread} and separation Δx_{shift} is given by [27]:

$$\frac{\sigma_{\text{spread}}}{\Delta x_{\text{shift}}} = 2\left(\frac{m^2}{\Delta m^2}\right)\left(\frac{\sigma_E}{E}\right) \tag{1.39}$$

where $\sigma_E \sim 1/\sigma_x \sim \mathcal{O}\,(\text{MeV})$ is the initial size of the wave packet in energy-momentum space and we can take $m^2/\Delta m^2 \sim 1$. Note that this ratio does not depend on the baseline. Since the energies here are large, $\sigma_E/E \ll 1$ meaning that $\sigma_{\text{spread}}/\Delta x_{\text{shift}} \ll 1$, and the separation is much larger than the spread. Indeed, the astrophysical neutrinos detected on Earth are decoherent and are propagating in pure mass eigenstates. Taking this assumption greatly simplifies the transition probability as all the interference terms between the three

mass eigenstates can be dropped, and all that is left is to convert from the propagating mass state to the flavour states (see Equation 1.1):

$$\phi_{i,\oplus} = \sum_{\alpha} \phi_{\alpha,\mathrm{S}} |U_{\alpha i}|^2 \tag{1.40}$$

$$\phi_{\alpha,\oplus} = \sum_{i,\beta} |U_{\alpha i}|^2 |U_{\beta i}|^2 \phi_{\beta,\mathrm{S}} \tag{1.41}$$

where ϕ_α is the flux for a neutrino flavour ν_α and ϕ_i is the flux for a neutrino mass state ν_i. The subscript "S" denotes the source and "$\oplus$" denotes as measured on Earth. The same result can be obtained in the plane wave picture of the neutrino using Equation 1.14 by taking the limit $L \to \infty$, thus this type of decoherent mixing is also known as oscillation-averaged neutrino mixing (as is even more evident in Figure 1.3). From this, the flavour composition on Earth is defined as $f_{\alpha,\oplus} = \phi_{\alpha,\oplus} / \sum_\alpha \phi_{\alpha,\oplus}$ and this can be calculated using the mixing matrix parameters in Table 1.1. For the three source models discussed above:

$$(1:2:0)_{\mathrm{S}} \to (0.31:0.35:0.34)_{\oplus} \tag{1.42}$$

$$(0:1:0)_{\mathrm{S}} \to (0.18:0.44:0.38)_{\oplus} \tag{1.43}$$

$$(1:0:0)_{\mathrm{S}} \to (0.55:0.18:0.27)_{\oplus} \tag{1.44}$$

This can be visualised in a ternary plot [42], with axes being the fraction of each neutrino flavour as shown in Figure 1.10. The coloured circle, square and triangle show the source flavour compositions. The arrows show the effect of neutrino mixing on the flavour composition. The unfilled circle, square and triangle show the corresponding measured flavour composition. Neutrino mixing during propagation has the effect of averaging out the flavour contributions, which is why the arrows point towards the centre of the triangle. This effect is more pronounced for $\nu_\mu \leftrightarrow \nu_\tau$ due to the their larger mixings, see Table 1.1. Also shown on this figure in the hatched "Standard Model" area, is the region of measured flavour compositions containing all source models of $(x : 1-x : 0)$, using Gaussian priors on the standard mixing angles as outlined in Table 1.1. Therefore, this hatched area is the region in which all standard astrophysical models live.

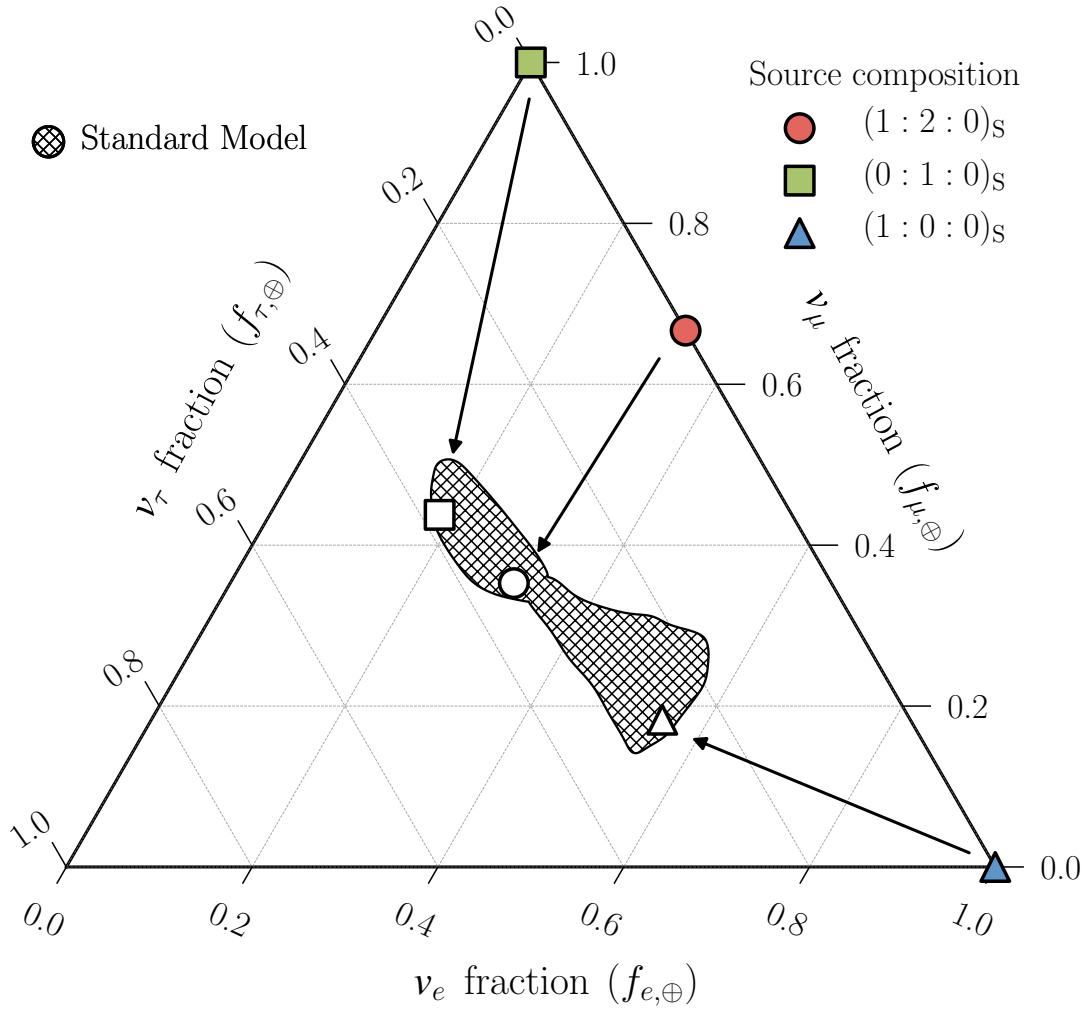

Figure 1.10: Astrophysical neutrino flavour composition ternary plot. Axes show the fraction of each neutrino flavour. Coloured shapes show 3 models for the source flavour composition. The arrows indicate the effect of neutrino mixing during propagation and the unfilled shapes show the corresponding measured flavour compositions. The hatched area shows the region in measured flavour space in which all standard astrophysical models live.

1.4 Neutrino Detection

1.4.1 Neutrino interactions with matter

As electrically neutral fermions, neutrinos only interaction mode is via the weak force. As a consequence, neutrinos have very small cross-sections compared to particles which interact through the strong nuclear force or electromagnetic force. One of the simplest neutrino interactions is the case of a two-body *elastic scattering* (ES) between a neutrino and an electron. This interaction can mediated by either a Z^0 boson in *neutral-current* (NC) interactions or a $W^{\pm}$ boson in *charged-current* (CC) interactions as shown in Figure 1.11. Both NC and CC can occur for all neutrino flavours. However in the case of CC ES, there must be sufficient energy to produce the final charged lepton. As mentioned in Section 1.2.2, ES interactions play an important role in neutrino mixing when they propagate through electron dense matter, owing to the fact that CC ES exclusively produces ν_e.

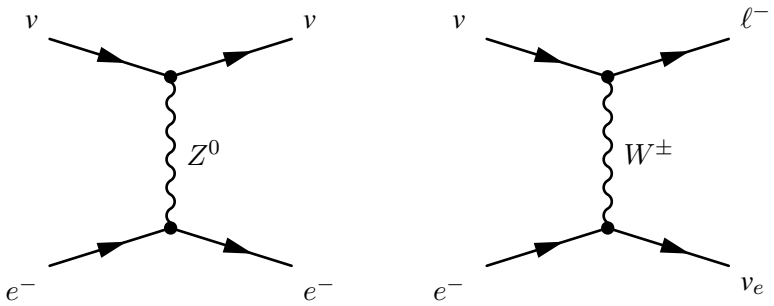

Figure 1.11: Feynman diagrams for neutrino-electron scattering. Neutral-current interaction channel shown on the left, and charged-current interaction shown on the right.

From a theoretical standpoint, ES is ideal for analysis as they are the most well understood. However in practice, neutrino interactions with nucleons are preferred. Firstly, neutrino-nucleon collisions are much easier to instrument and secondly, they provide much higher cross-sections compared to collisions with elementary particles. Neutrino-nucleon interactions typically fall within three main categories; *quasi-elastic* (QE) scattering, *resonance production* and *deep elastic scattering* (DIS) processes, as can be seen in Figure 1.12. QE interactions are dominant at the lowest energies of $\sim$1–10 GeV. These interactions are ones in which the nucleon remains intact. The NC process is simply when the neutrino scatters of the target nucleon $\nu + N \rightarrow \nu + N$, and in the CCQE process the nucleon is modified and a lepton is produced, for example in the process $\nu_\mu + n \rightarrow \mu^- + p$, the target neutron

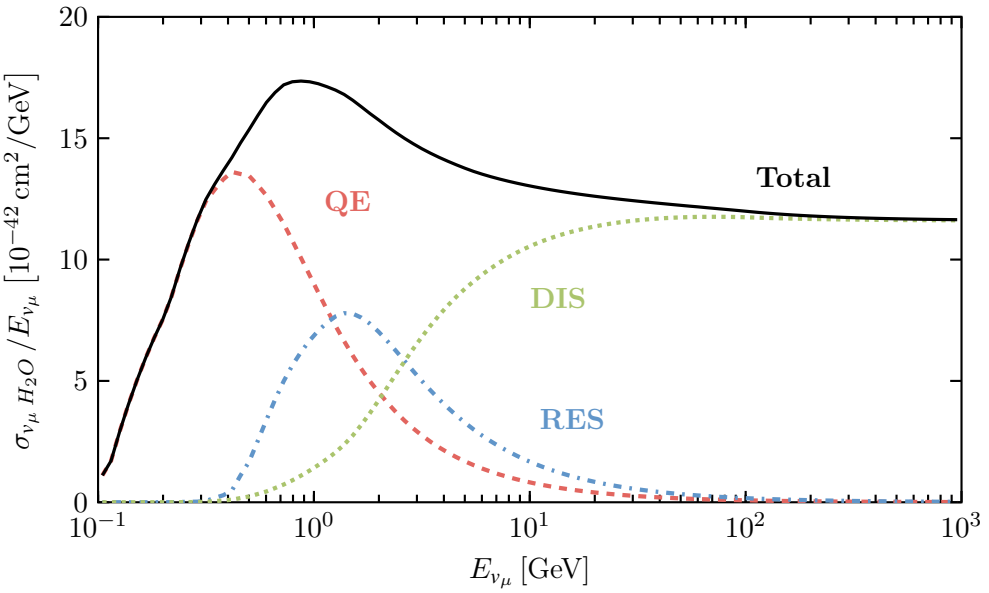

Figure 1.12: Muon neutrino cross-section on a water target, shown as a function of the neutrino energy. Also shown are the contributions from quasi-elastic scattering (dashed, red), resonance production (dash-dotted, blue) and deep inelastic scattering (dotted, green). Cross-sections were generated using GENIE [43].

is converted to a proton. At higher energies, the contribution from inelastic processes increases and so we start to see fragmentation of the nucleon. In the transition region between QE and DIS processes at $\sim$0.5–10 GeV, there is a resonance region in which the neutrino excites a nucleon into an excited state, for example $\nu_\mu + p \to \mu^- + \Delta^{++}$. These then decay quickly back into a stable nucleon, most often accompanied with a single pion, $\Delta^{++} \to p + \pi^+$. At neutrino energies greater than 10 GeV, the neutrino is able to resolve the internal structure of the nucleon. Nucleons are bound states consisting of *valence* quarks, which determine the overall properties of the nucleon, and a *sea* of quarks and gluons. Collectively these are known as *partons* and the process by which a neutrino interacts with these is known as deep inelastic scattering (DIS) and is shown in Figure 1.13. The stuck parton recoils and a process called *hadronization* occurs, in which the struck parton produces hadrons as it cannot exist singularly due to colour confinement. The particles created by the hadronization process can hadronize themselves until they reach a stable state. This creates a tight cone of hadrons, referred to as a jet or a *hadronic cascade*. Also shown in Figure 1.13 are definitions of the Lorentz invariant quantities used to describe neutrino-nucleon scattering kinematics. Here, $k = (E, \vec{\mathbf{k}})$ and $k' = (E', \vec{\mathbf{k}'})$ are the four vectors for the incoming neutrino and outgoing lepton, P is the target nucleon four vector with mass M, q is the four momentum transfer and W is the mass of the final hadronic

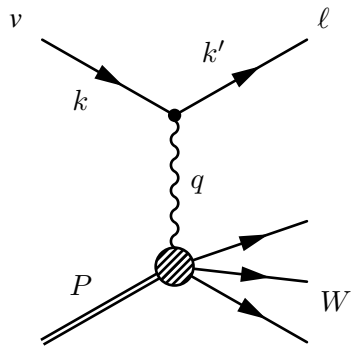

$$s \equiv (P+k)^2 \qquad t \equiv q^2 \equiv -Q^2 \equiv -\left(k-k'\right)^2$$

$$M^2 \equiv P^2 \qquad W^2 \equiv (P+q)^2$$

$$x \equiv \frac{Q^2}{2\,q\cdot P} \text{ (Bjorken-x)} \qquad y \equiv \frac{q\cdot P}{k\cdot P} \text{ (inelasticity)}$$

$$Q \gg M \text{ (deep)} \qquad W \gg M \text{ (inelastic)}$$

Figure 1.13: Feynman diagram for deep inelastic scattering on a target nucleon (left) shown with the kinematical quantities defining this interaction (right).

system. s and t are Mandelstam variables. In the lab frame where the nucleus is at rest, the two Lorentz scalars Bjorken-x and y can be expressed as $x \overset{lab}{=} Q^2/2Mv$ and $y \overset{lab}{=} v/E$ where $v \overset{lab}{=} E - E'$. These quantities are particularly useful as they can be measured experimentally by looking only at the scattered lepton and the total hadronic state, without needing to know the details of each partonic process. This can then compared to the neutrino nucleon differential cross-section written in terms of Bjorken-x and y [44], given here for a ν_μ CC interaction on an *isoscalar target*, which is a target normalised such that it is composed of an equal amount of up and down quarks, so that the cross-section is an average such as $\sigma_{\nu N} \approx (\sigma_{\nu p} + \sigma_{\nu n})/2$:

$$\left.\frac{\mathrm{d}^2\sigma}{\mathrm{d}x\,\mathrm{d}y}\right|_{\nu_\mu N\to\mu X} = \frac{2\,G_F^2\,M\,E_\nu}{\pi}\left(\frac{M_W^2}{Q^2+M_W^2}\right)^2\left[xq\left(x,Q^2\right)+x\bar{q}\left(x,Q^2\right)(1-y)^2\right] \quad (1.45)$$

where G_F is the Fermi constant, M_W is the W mass and q and $\bar{q}$ are the *parton distribution functions* (PDFs) for quarks and antiquarks. These PDFs describe the relative contributions of any sea or valence parton species as a function of the Bjorken-x and Q^2. While this equation does provide a tidy picture of DIS, additional effects must be included in any realistic description. The total interaction cross-section can be obtained by integration of the result shown in Figure 1.12. Here, the calculation uses the GRV98 leading order (LO) PDF with modifications to describe scattering at low Q^2, most appropriate for neutrino experiments in the few GeV region [45]. At the higher energies, more contemporary PDFs are used to calculate the cross-section, as is the one shown Figure 1.14, which is a calculation by CSMS using HERAPDF1.5 at next to leading order (NLO) [46]. The energies are large enough such that the massless lepton limit can be used, and so the cross-section given

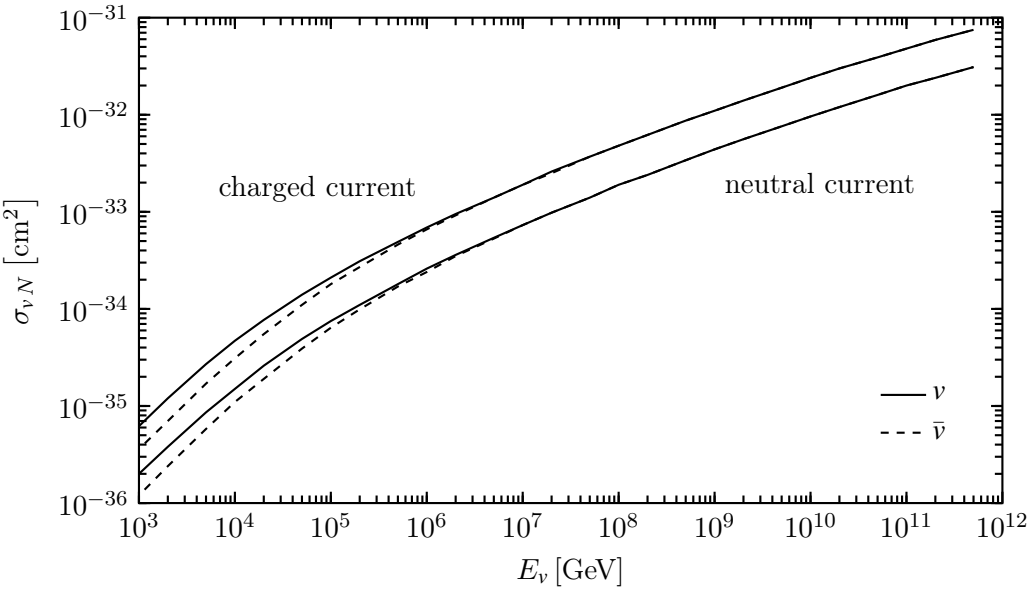

Figure 1.14: High-energy neutrino (solid) and antineutrino (dashed) cross-sections on an isoscalar target for charged-current and neutral-current scattering, calculated by CSMS [46].

here is the same for all neutrino flavours, i.e. *lepton flavour universality*. As expected the neutrino cross-section increases as a function of the neutrino energy, which partially makes up for the falling flux at high energies (Figure 1.9). On the other hand, at sufficiently high energies $\sim 10^6$ GeV, the Earth becomes opaque to neutrinos, making experiments blind to high-energy neutrinos in the direction of Earth's core.

1.4.2 Propagation of leptons

Understanding the behaviour of charged leptons is key in the study of neutrinos. While detection through neutral-current channels is possible, by far the observable that almost all neutrino experiments look for is the energy deposition from the charged lepton produced in CC interactions. By understanding the energy deposition of the charged lepton well enough, estimations of the properties of the mother neutrino can be made, such its energy or the direction it came from. For IceCube, the energies and medium of the charged leptons of concern are energies above a few GeV in a medium of ice (water). Energy loss can occur in a variety of different ways here, depending on the lepton flavour and energy. However, the most important mechanism for detection is the emission of *Cherenkov radiation*. This occurs for any charged particle whose energy is high enough such that its speed is greater than the speed of light in that medium. This threshold is given by $v > c/n$, where n is the

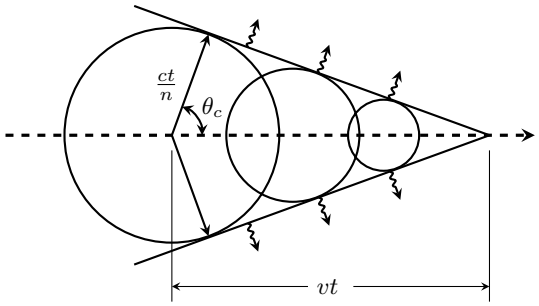

Figure 1.15: Cherenkov radiation produced by a particle travelling faster than the speed of light in the same medium.

index of refraction. In such a case, an electromagnetic shock wave is created as shown in Figure 1.15, with the coherent wave front emitted at an angle:

$$\cos\theta_c = \frac{1}{n\beta} \tag{1.46}$$

where $\beta = v/c$. For ice $n \sim 1.33$, giving a Cherenkov angle of $\theta_c \sim 41°$ for relativistic particles. The spectrum of radiation emitted is given by the Frank-Tamm formula [47]:

$$\frac{\mathrm{d}^2N}{\mathrm{d}x\,\mathrm{d}\lambda} = \frac{2\pi\alpha z^2}{\lambda^2}\left(1 - \frac{1}{\beta^2 n^2(\lambda)}\right) \tag{1.47}$$

Here x is the distance travelled, λ is the wavelength of the produced Cherenkov photon, α is the fine structure constant and z is the charge of the particle. The dependence on $1/\lambda^2$ means that high frequency photons dominate. In fact, the energy loss from Cherenkov radiation is minimal but due to its characteristic emission angle and spectrum, it is the principal observable in optical detectors such as IceCube (see Section 2.1).

In general, the average energy loss per unit path length, or *stopping power*, of a charged particle through matter can be described by summing up contributions from four different sources:

$$\frac{\mathrm{d}E}{\mathrm{d}x} = \left(\frac{\mathrm{d}E}{\mathrm{d}x}\right)_i + \left(\frac{\mathrm{d}E}{\mathrm{d}x}\right)_p + \left(\frac{\mathrm{d}E}{\mathrm{d}x}\right)_b + \left(\frac{\mathrm{d}E}{\mathrm{d}x}\right)_n \tag{1.48}$$

where i denotes *ionization*, b *bremsstrahlung*, p *pair production* and n *photonuclear* interactions. Ionization describes the electronic collision loss and as will be seen it is typically important at lower energies. Pair production describes the creation of a particle antiparticle pair at high energies, such as e^+e^-. Bremsstrahlung describes the radiation produced when a charged particle decelerates or is deflected by another charged particle. Lastly,

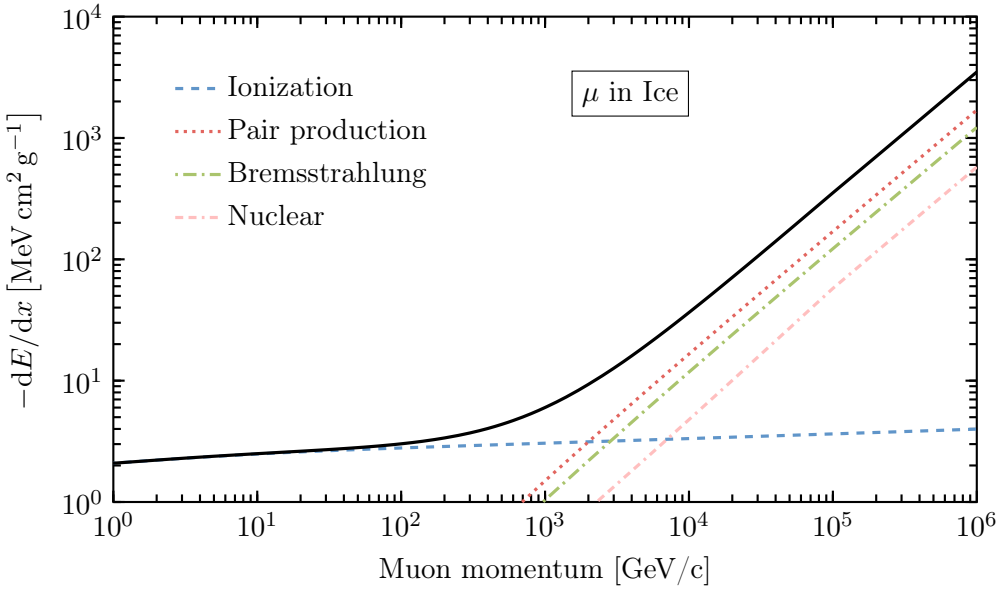

Figure 1.16: Stopping power ($\mathrm{d}E/\mathrm{d}x$) for a muon in ice as a function of the muon momentum (solid, black). Its contributions are also shown from ionization (dashed, blue), pair production (dotted, red), bremsstrahlung (dash-dotted, green) and photonuclear (dash-dash-dotted, pink). Data taken from PDG [48].

photonuclear interactions describe coherent interactions with nuclei. The $\mathrm{d}E/\mathrm{d}x$ is given separately for two different classes of charged particles; electrons and positrons, and heavier particles such as muons, pions, protons and other light nuclei.

Figure 1.16 shows the $\mathrm{d}E/\mathrm{d}x$ for a muon in ice as a function of the muon's momentum. Also shown are the individual contributions from the four sources mentioned above. At muon momenta up to ~ 1 TeV, the ionization energy loss is seen to dominate and the muon is described to be in the *minimum ionization* region. This is described by the Bethe formula (see [49]) and the most striking feature here is that, for all practical purposes, the average $\mathrm{d}E/\mathrm{d}x$ in any given material is a function of β alone. For the energies of interest here the muons are well into the relativistic regime so by fixing $\beta \approx 1$, the ionization losses are effectively independent of the energy of the muon. Therefore, particles in the minimum ionization region or *minimum ionizing particles* (MIPs) have a fixed amount of energy loss in any particular medium. Reading from the figure, it can be seen that for ice/water with density $\rho \sim 1\ \mathrm{g\,cm^{-3}}$, the average energy loss of a muon is ~ 2 MeV/cm. Above muon momenta of ~ 1 TeV, the contributions from pair production, bremsstrahlung and photonuclear dominate. Collectively these are known as *radiative* losses and they grow in direct proportion with the energy of the muon (see [48] for details).

High-energy electrons predominantly lose energy in matter by bremsstrahlung due to their small mass (emission probability is inversely proportional to the squared mass). As in the case of muons, the $\mathrm{d}E/\mathrm{d}x$ is proportional to the energy of the electron. The photons created, in turn, can pair produce back into e^+e^- so their dynamics also need to be considered. At high enough energies, an *electromagnetic* (EM) *cascade* is initiated as pair production and bremsstrahlung generate more electrons and photons. The characteristic quantity to describe this behaviour is the *radiation length* which is the mean distance over which the electron losses $1/e$ of its energy due to radiation loss. For ice/water the radiation length is 38 $\mathrm{g\,cm^{-2}}$. Compared to muons or other light nuclei of similar energies, the electron energy deposition is more rapid and localised, with larger fluctuations.

1.4.3 Propagation of hadrons

While the study of the charged lepton in CC neutrino interactions is preferred, the presence of a hadronic emission is characteristic in every type of neutrino-nucleon interaction. As discussed in Section 1.4.1, DIS interactions cause a break up of the nucleon, leading to hadronization in the recoiling hadronic system, called a hadronic cascade. In a similar way to EM cascades, the characteristic quantity used to describe the energy losses is the *nuclear interaction length*, which for ice/water is 83.3 $\mathrm{g\,cm^{-2}}$. Compared to EM cascades, the overall deposition is even more localised and subject to stochastic variations. In fact, the production of neutral pions in the hadronic cascade can directly feed into an EM component, meaning that hadronic cascades are often supplemented by EM cascades.

2 The IceCube Neutrino Observatory

The study of astrophysical neutrinos is a relatively new yet quickly growing field in high-energy particle physics. The challenges here are the steeply falling flux at higher energy (see Figure 1.9), along with the weakly interacting nature of the neutrino, which has pushed the need for larger and larger detectors. The IceCube neutrino observatory is a cubic kilometre photomultiplier array embedded in the extremely thick and clear glacial ice located near the geographic South Pole in Antarctica [50]. A schematic layout of IceCube is shown in Figure 2.1. The IceCube *In-Ice* array is made up of 5160 purpose built *Digital Optical Modules* (DOMs) which are deployed on 86 *strings* (or cables) between 1450 and 2450 m below the ground. The inner string separation is 125 m with a vertical DOM separation of 17 m. Eight of the centrally located strings make up the subarray *DeepCore* [51] which are sensitive to lower energy neutrinos. It achieves this through denser instrumentation, having an inner string separation of 60 m and a vertical DOM separation of 7 m. A surface air shower array, IceTop, is instrumented on the surface and consists of a set of frozen water tanks which act as a veto against the background cosmic rays.

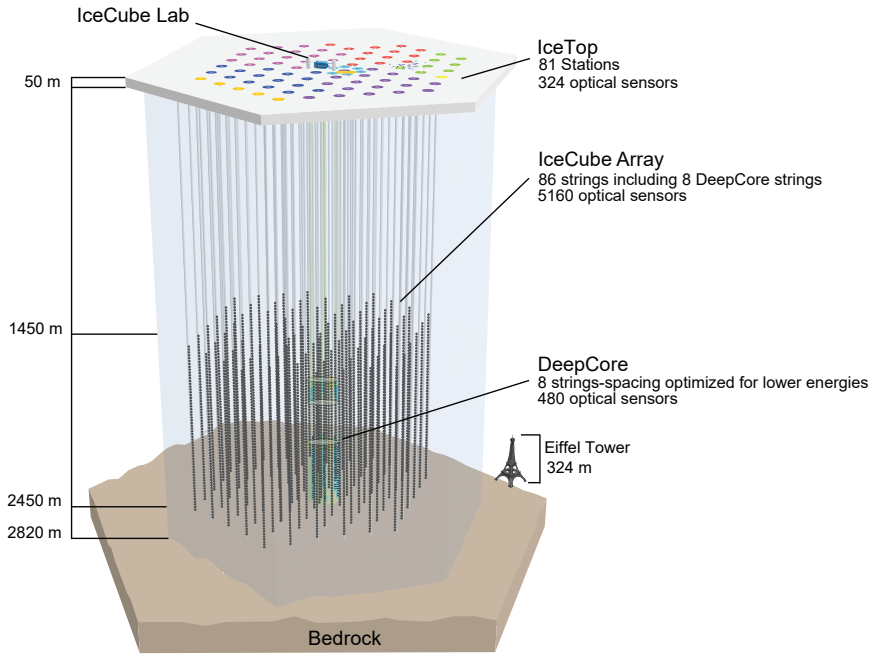

Figure 2.1: The IceCube neutrino observatory with the In-Ice array, its subarray DeepCore and the cosmic ray shower array IceTop.

2.1 Digital Optical Module

The sole photon detection and *digitisation* unit in IceCube is the DOM [52]. A diagram of the DOM with the main components labelled is shown in Figure 2.2. Each In-Ice module contains a Hamamatsu R7081-02 10″ downward facing *photomultiplier tube* (PMT), which has a spectral response between 300 nm to 650 nm with a peak quantum efficiency around 25% near 390 nm. The DeepCore array DOMs contain the Hamamatsu R7081-MOD PMT, which has a higher quantum efficiency but it is otherwise identical to the In-Ice DOM. Each features a box-and-line dynode chain with 10 stages operated at a gain of 10^7. The DOM houses a high voltage generator, various circuit boards for digitisation and calibration all inside a 35 cm diameter pressurised borosilicate glass sphere. Analog and digital signal processing and calibration electronics are integrated onto the mainboard along with an LED flasher board. A total of 12 LEDs are pointed in different directions and are used for calibration. The PMT and surrounding electronics are secured in a high-strength silicon gel that optically couples components to the glass sphere. This particular glass material is chosen as it has a wide transparency window down to 350 nm and very little radioactive trace elements in order to minimise dark noise. The underside is surrounded by a mu-metal cage to shield from geomagnetic effects at the South Pole. Once digitised, the signal is transmitted to the *DOMHub*, located in the surface IceCube Lab, which is responsible for controlling and processing of all DOMs on a single string.

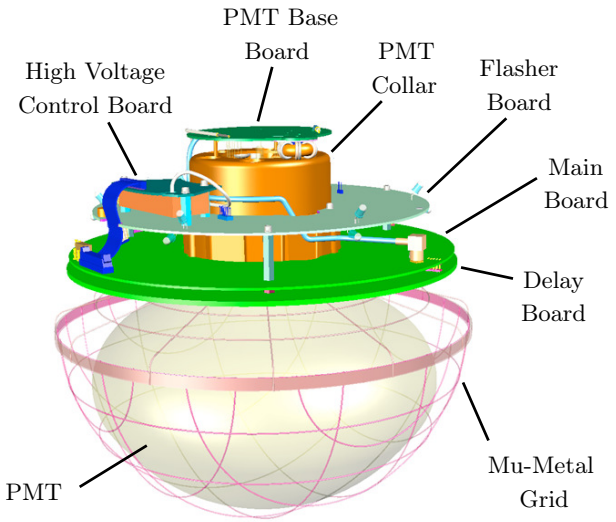

Figure 2.2: The Digital Optical Module, the photon detection unit at IceCube [50].

2.1.1 Data Acquisition

Each DOM instruments two methods of digitisation; a rapid continuously running, low frequency digitiser called the *fast analogue to digital converter* (fADC) and the more precise *analog transient waveform digitiser* (ATWD). An example of these is shown in Figure 2.3. They are both 10-bit digitisers. The fADC operates at 40 MHz (one sample per 25 ns) and when requested, the onboard *field programmable gate array* (FPGA) is programmed to save at intervals of 6.4 μs. The ATWD is triggered by a discriminator set to a voltage threshold of 0.25 *photo-electrons* (PE). It is provided with waveforms of three different amplifier gains of 16, 2 and 0.25 to cover up to a dynamic range of 400 PE/ns and operates at 300 MHz (one sample per 3.3 ns) for a sampling window of 427 ns. Each DOM is equipped with 2 ATWDs to reduce dead time during digitisation.

Once the waveform has been digitised, the two most important pieces of information that are extracted are the number of photons hitting the PMT and their arrival times, which subsequently are fed into reconstruction algorithms. The PMT response is compared to a *single photo-electron* (SPE) template, which has been measured on a sample of DOMs before they were deployed. Figures 2.4–2.6 show such lab measurements. A dim 375 nm UV LED was used to generate pulses of light, dim enough to initiate only SPE signals and Figure 2.4 shows an average of 10,000 of these waveforms. SPE pulses can be seen

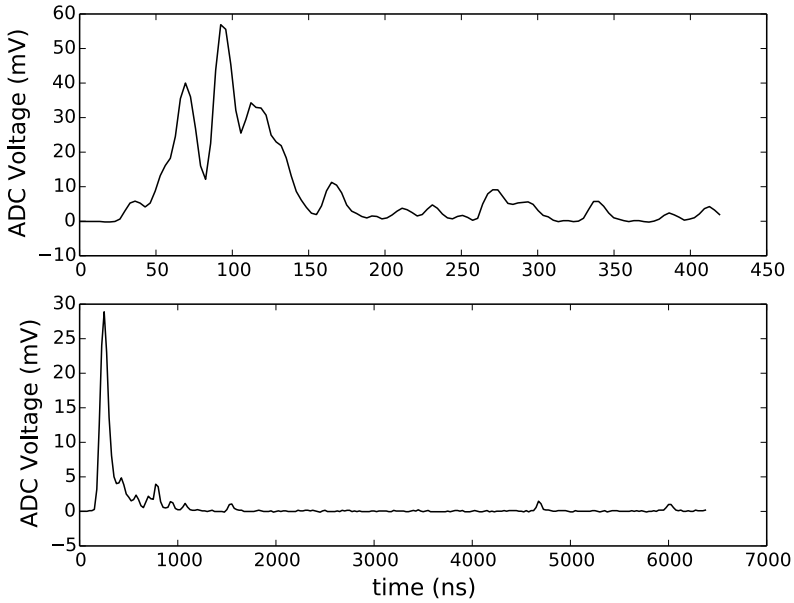

Figure 2.3: The same signal sampled in the ATWD (top) and the fADC (bottom): the ATWD recording duration is 427 ns whereas the fADC recording duration is 6.4 μs [52].

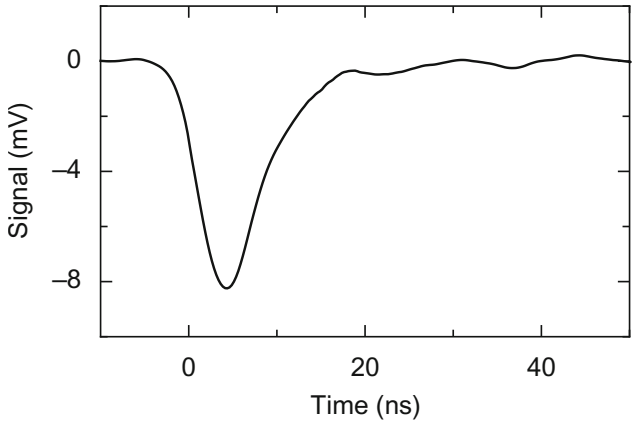

Figure 2.4: Average of 10,000 SPE waveforms for a PMT at a gain of 10^7 [52].

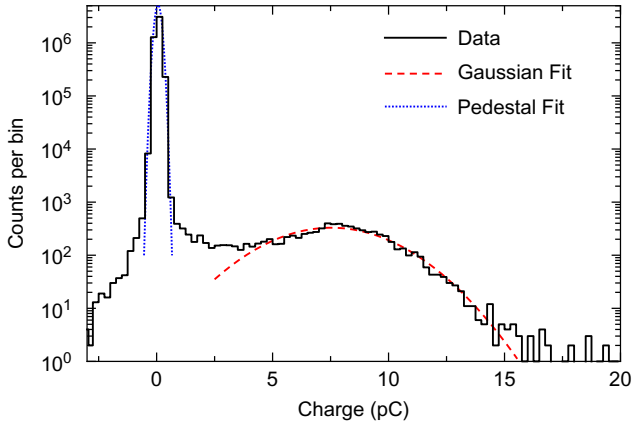

Figure 2.5: Typical SPE charge distribution at a gain of 5×10^7 including pedestal peak [52].

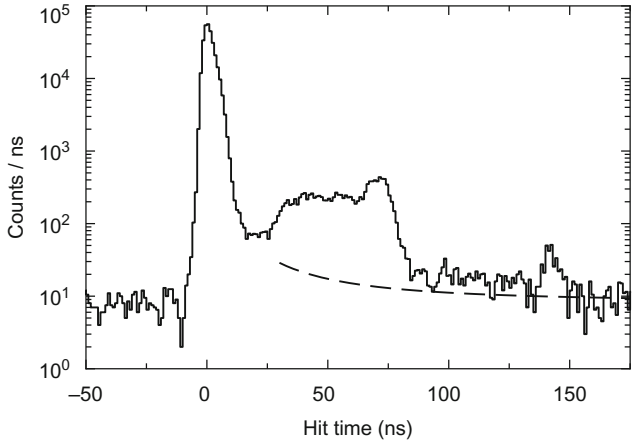

Figure 2.6: Distribution (histogram) of the timing of SPE hits at a gain of 10^7 in reference to an illumination by a narrow pulse from a diode laser. A small fraction of late pulses are due to laser afterglow plus the random background rate (dashed). [52].

to be around 8 mV for a gain of 10^7, which is well above the digitiser precision and other electronic noise (~ 0.1 mV). Figure 2.5 shows the SPE charge distribution, which exhibits a clear SPE peak to the right of the pedestal. This data gives us a charge probability distribution, characterising the variability in the SPE waveform. Therefore the response of each photon can be approximated using the average SPE waveform, scaled randomly according to this charge probability distribution. By fitting to these templates, the number of photons hitting the PMT can be estimated from more realistic waveforms such as the ones shown in Figure 2.3, which contain overlapping contributions from multiple PE hits.

The timing resolution of an SPE, relative to the photon arrival time is shown in Figure 2.6. The arrival time distribution has a peak at ~ 2 ns after the laser turns on, which is then followed by secondary pulses. The estimated contribution due to laser afterglow effects and random background noise is shown as the dashed line. Excess above the dashed line is due to *late pulses*, which is due to backscattering of photo-electrons off the first dynode (see Section 5.3.3 for more). Dispersion in the timing resolution of the PMT of the scale of 2 ns is not a limiting factor compared to the time delay due to scattering in ice at the length scales of concern at IceCube. Photon scattering over a comparatively very short distance of 10 m, causes 40% of the photons to be delayed by more than 5 ns, which is already larger than the corresponding timing delay effects from the PMT [52].

The optical efficiency of the DOM is not constant across its surface, nor is it the same for every DOM. This includes effects from the photocathode quantum efficiency, collection efficiency, dynode multiplication and DOM glass and gel absorption. The position dependence was systematically measured for 16 fully integrated DOMs and an example is shown in Figure 2.7.

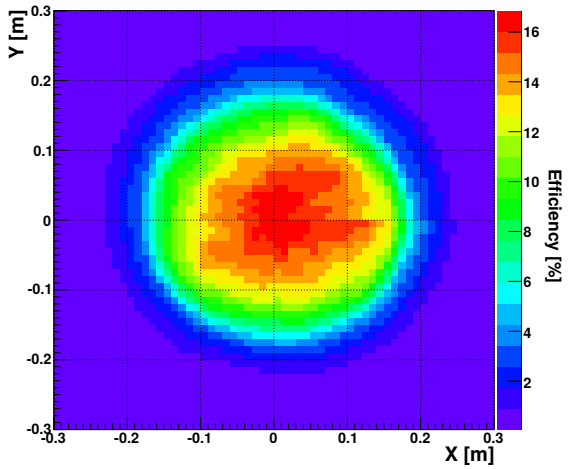

Figure 2.7: Position dependence of the response of a DOM [50]. The x–y coordinates measure distance from the centre of the DOM.

2.2 Event Signatures

Cherenkov telescope arrays such as IceCube are able to classify the properties of a neutrino event by looking at the morphology of photon hits across its PMT array. There are two main types of neutrino event signatures at IceCube - *tracks* and *cascades*.

2.2.1 Tracks

Tracks are predominantly made by muons which are directly produced by neutrinos in the CC ν_μ interaction channel. Muons have a long lifetime, ~ 2 μs at rest, and in ice they have relatively low energy losses (see Section 1.4.2). Therefore, as shown in Figure 2.8a, a high-energy muon travelling through the IceCube array will leave a long trail of hits. These features, along with the timing information of hits across the DOMs, help in determining the directionality of the muon, giving an angular resolution typically around 0.5–1° [53]. At energies of concern here, there is little deviation between the direction of the neutrino and the induced muon as they are both heavily boosted. Therefore, this pointing ability of tracks makes them the most attractive events to use for point source searches. Energy reconstruction is more complicated, however. At the lower energies ($\lesssim$ 100 GeV), the muon's range is short enough that it is able to deposit all its energy inside the detector. This is the ideal situation for a good energy reconstruction as the IceCube array acts as a calorimeter, so the total deposited charge is proportional to the energy of the muon. At higher energies, the range of the muon is typically greater than the length of the detector. Therefore the energy of muon must be extrapolated from the portion of energy deposited inside the detector. This is particularly challenging for muons which are not produced inside the detector, for which only a lower bound can be made. The typical approach taken to reconstruct the muon is to segment the reconstruction along the track. In this way, biases from stochastic variations of the energy loss can be minimised by applying some averaging over each segment. In each segment, the mean $\mathrm{d}E/\mathrm{d}x$ is determined, which is then roughly proportional to the muon momentum (see Figure 1.16). The energy resolution improves with the muon energy up to an uncertainty of a factor of 2 [54]. For more details on this see the IceCube energy reconstruction methods publication [55].

2.2.2 Cascades

Cascades are created as a result of hadronic cascades and/or EM cascades (see Sections 1.4.2–1.4.3). NC interactions and CC ν_e interactions are the channels in which a pure cascade is created, and an example of one is shown in Figure 2.8b. However, this does not mean that neutrino events produce exclusively one type of signature, in fact all high-energy neutrino-nucleon events produce at least a hadronic cascade at the interaction vertex. Characteristic of a cascade is the isotropic deposition of energy in a localised region near the neutrino vertex. Contrary to tracks, cascade events have much shorter typical lengths and so the entire energy deposition is easily contained within the detector array. This is ideal for energy reconstruction giving a deposited energy resolution of $\sim 15\%$ at neutrino energies above 10 TeV [55]. Inferring the true neutrino energy is more difficult, however, as IceCube is not capable of resolving the difference between EM showers and hadronic showers, which potentially have a large amount of missing energy, leading to $\sim 15\%$ lower light yield compared to an equivalent EM shower. Deposited energy is reconstructed using an EM shower hypothesis, and therefore this quantity gives the lower limit of the neutrino energy. Directional reconstruction is more challenging than for tracks and is done by looking for timing/light intensity anisotropies around the interaction vertex. The deviations are small, but it is expected that the light deposition in the forward direction is greater. Typical angular resolutions are 10–15° [56].

2.2.3 Taus

Not mentioned so far are the CC ν_τ interactions, which for energies $\gtrsim 1$ PeV, can produce τ which travels a detectable distance before decaying. This provides a unique signature for such events. The initial ν_τ interaction produces a hadronic cascade, followed by a track by the τ itself, in turn followed by either a track from the τ's muonic decay ($\tau^- \to \mu^- \bar{\nu}_\mu \nu_\tau$ with branching ratio $\sim 17\%$), or a cascade from its other decays. Because of their distinctive signatures, such events are called *double bangs* or *double cascades*. See Section 4.2.1 or References [57, 58] for more.

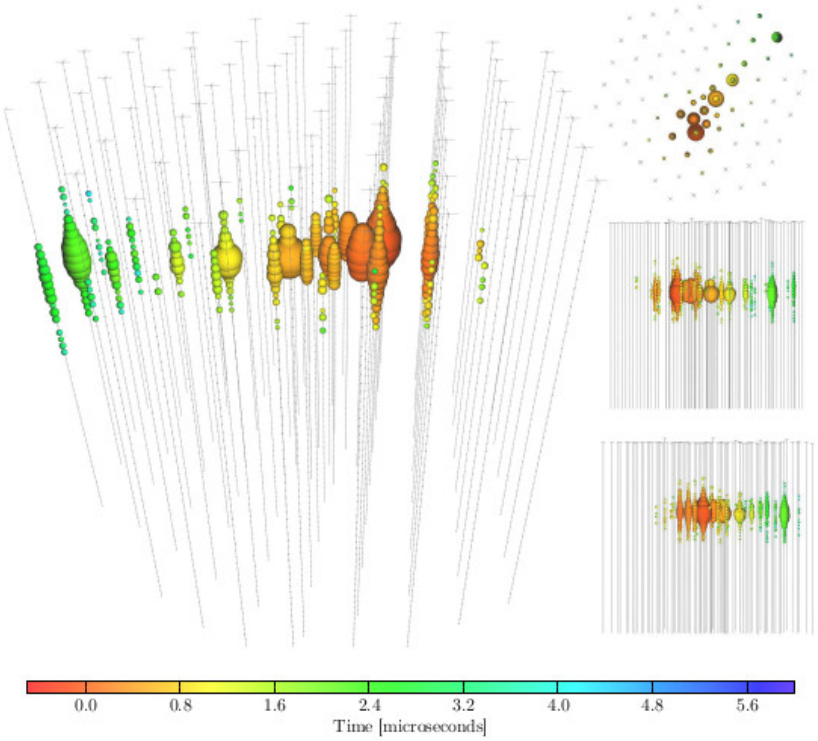

(a) A track event initiated by a CC muon neutrino interaction in the detector. The muon deposits 74 TeV before escaping.

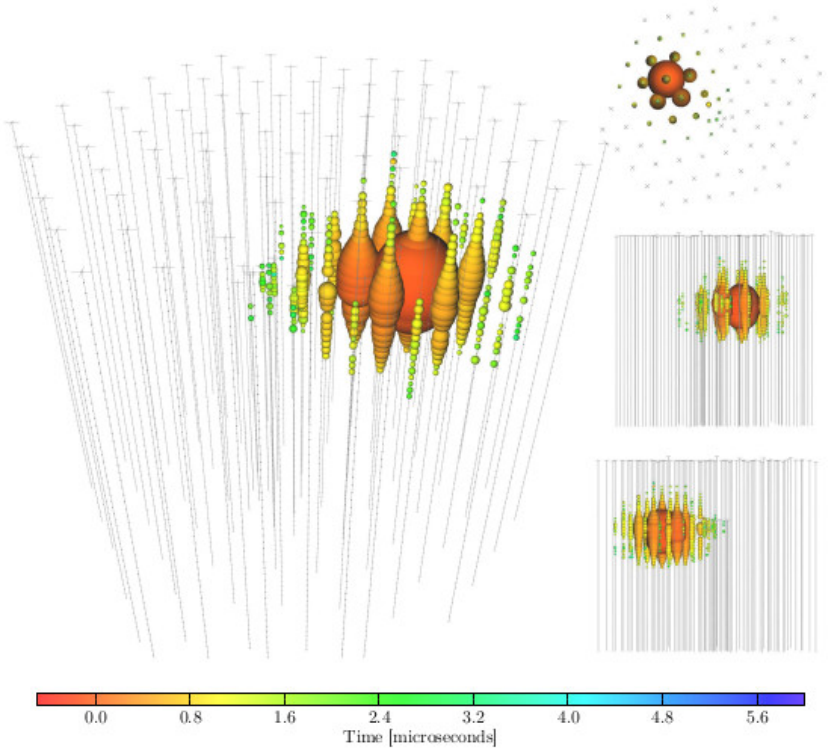

(b) A cascade event initiated by a neutrino interaction in the detector. The cascade deposits 1070 TeV in the detector.

Figure 2.8: Examples of neutrino event signatures in IceCube from [56]. Main panel shows the event view with spheres representing hit DOMs whose volume is proportional to the collected charge. Timing of hits is represented by the colour, with red being earlier hits and blue being later hits. Smaller panels on the right show projections of the detector along the z, x and y axes, respectively.

2.3 The IceCube-Upgrade

Desgin and development of the next generation of IceCube is well under way [59–61]. The first of these incremental upgrades is the *IceCube-Upgrade* (ICU), which is planned for deployment in the season of 2022/23. The ICU will improve on the existing DeepCore array through the addition of seven additional strings of photosensors with novel, denser instrumentation as shown in Figure 2.9. The DOM design will be updated, taking advantage of contemporary ADCs (see Section 5.2.3). New photosensors have also been developed each providing better photocathode coverage per module, such as the DEgg (Dual optical sensors in an Ellipsoid Glass for Gen2) which uses two back-to-back 8 inch PMTs [62], or the mDOMs (Multi-PMT Digital Optical Module) which houses 24 3 inch PMTs pointed in all directions [63]. Further instrumentation will include advanced LED calibration devices such as the POCAM, to study the ice properties and sensor characteristics [64].

One of the primary goals of the ICU is to enhance the sensitivity of the low energy program of IceCube. The denser array and improved optical modules will reduce the energy threshold of neutrinos down to the GeV scale and also improve the ability to reconstruct these

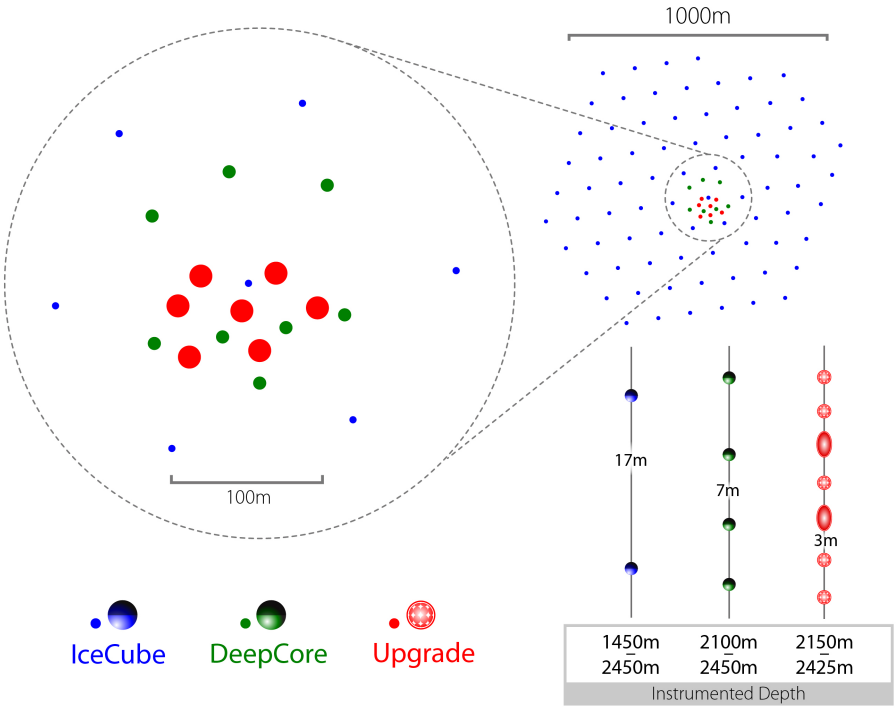

Figure 2.9: Schematic drawing of the IceCube-Upgrade strings (red), embedded in the IceCube/DeepCore array (blue/green respectively) [59].

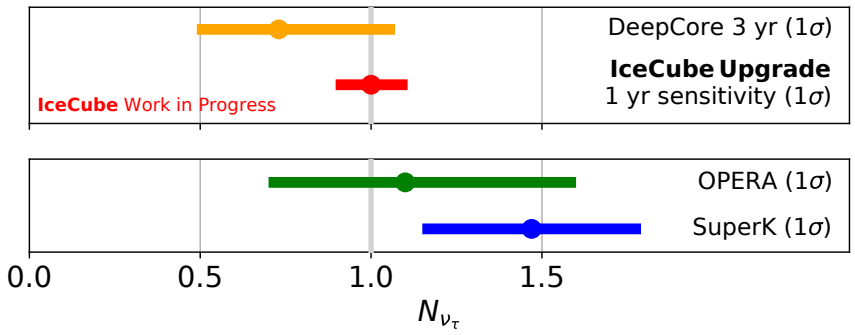

Figure 2.10: Current measurements of the rate of ν_τ appearance relative to the standard expectation, compared with the projected IceCube-Upgrade 1 year sensitivity [59].

events. This will enable for a more precise measurement of the neutrino mixing parameters using atmopsherically produced neutrinos. In particular, as shown in Figure 2.10, the ICU will achieve unprecedented sensitivity for the atmospheric ν_τ appearance channel, providing strong constraints on the unitarity of the neutrino mixing matrix (see Section 1.2).

The calibration instrumentation also provides an opportunity to greatly improve reconstruction of high-energy astrophysical neutrino events, which are currently limited by systematic uncertainties of the ice and DOM responses. The refined calibration can be applied not just for future events but can be used in order to reanalyse all events contained in more than ten years of archival data. The high-energy cascade events account for the majority of detected astrophysical neutrinos, and these events in particular will benefit from an improved angular resolution, shown to reach an accuracy of 5–10°, compared to the current 10–15° [59]. It is also a realistic hope to achieve an angular resolution of 0.1° for high-energy track events. The improved angular resolution will also help in identification of astrophysical neutrino cascade events, potentially leading to additional signals upon reanalysis of archival data. This performance will greatly improve the prospects for neutrino astronomy with IceCube, allowing for all-flavour point source searches.

Part II

Search for Quantum Gravity

3 Search for Lorentz Violation with Atmospheric Neutrinos

Very small violations of Lorentz symmetry, or *Lorentz violation* (LV), are allowed in many ultra-high-energy quantum gravity (QG) theories [65–67]. Localisation of these theories is set by the strength of gravity, therefore these violations are expected to occur at Planck scale regimes ($M_P \sim 10^{19}$ GeV). The discovery of LV could be the first indication of a theory of QG. World-wide efforts are therefore underway to search for evidence of LV [68, 69]. So far all searches of LV have obtained null results.

Neutrinos are a particularly interesting sector to search for such effects as they are neutral, relativistic particles and so one expects deviations to occur at around M_P[1]. In the past, the cause of neutrino oscillations was not precisely known, and LV was suggested as a possible source of neutrino flavour anomalies [70]. Subsequently, the L/E dependence of standard neutrino oscillations was measured [71] (see Section 1.2 for more on neutrino mixing). Because the neutrino mass term in the effective Hamiltonian has a $1/E$ energy dependence, it was a strong indication that a nonzero neutrino mass is in fact the cause of neutrino oscillations, not LV. Then, the focus of the community shifted to consider LV to be a second order effect in neutrino oscillations. Here, experiments measure the number of neutrinos of different flavours, observed as a function of the neutrino energy E, and the distance the beam has travelled L. The microscopic neutrino masses are directly tied to the macroscopic neutrino oscillation length and so neutrino oscillation data has been used to look for small deviations due to LV from the standard neutrino mass oscillations. In this sense, neutrino oscillations are similar to photon interference experiments in their ability to probe very small scales in nature. The focus here is to present the most precise test of LV in the atmospheric neutrino sector by using $\nu_\mu \to \nu_\tau$ neutrino oscillations as a natural interferometer with a size equal to the diameter of Earth. This work has been published in Reference [72].

[1] For non-relativistic massive particles, LV effects are expected to occur at scales even greater than M_P

3.1 Phenomenology

There are a few different possibilities of Lorentz symmetry in QG theories [73]. The first is simply an unmodified symmetry in which inertial observers, O and O', are related by the familiar relation $L' = \sqrt{1 - v^2/c^2}\, L$ and the dispersion relation takes the form $E^2 = c^2p^2 + c^4m^2$.

Another possibility is the presence of a background field which selects a preferred inertial observer. This situation is demonstrated in Figure 3.1. There is a relevant distinction to be made between two types of Lorentz transformations here. The first are *observer Lorentz transformations*, shown on the left, which involve a transform of the coordinate system. In this thesis, the system is unaffected and observer Lorentz symmetry is preserved, or in other words the Lorentz symmetry is covariant. The figure on the right demonstrates a *particle Lorentz transformation*, which is a Lorentz transformation of a particle but not on the background fields. Here, there is lack of invariance as the laws of transformation are not applied to the background field, therefore the particle Lorentz symmetry is broken. In particular, the dispersion relation of a particle depends on the background [74].

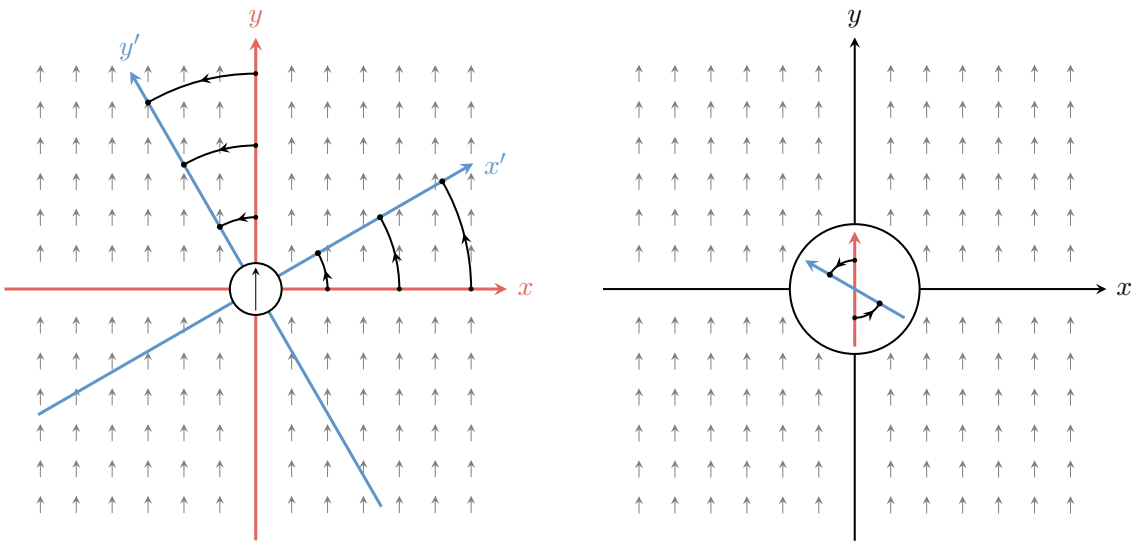

Figure 3.1: Diagram showing two types of Lorentz rotation on a particle in the presence of a background field. On the left is shown an observer Lorentz rotation and on the right is shown a particle Lorentz rotation.

3.1.1 Standard model extension

One approach to look for LV is to use a model-independent effective field theory, such as the *standard model extension* (SME) [75, 76]. The SME can provide a framework to compare results of LV searches from many different fields such as photons [77–80], nucleons [81–83], charged leptons [84–86], and gravity [87]. This formalism incorporates various fundamental features of quantum field theories, such as energy-momentum conservation, observer Lorentz transformations, and spin-statistics; however, it also includes all possible types of violations of particle Lorentz transformations. Past searches of LV have mainly focused on the directional effect in the Sun-centered celestial-equatorial frame by looking at the time dependence of physics observables as direction-dependent physics appears as a function of the Earth's rotation [68]. However, in this case, no time dependence is assumed, and instead what is looked at are the energy distribution distortions caused by direction- and time-independent isotropic LV, by assuming that the new physics is isotropic in the cosmic microwave background (CMB) frame. It would be most optimal to simultaneously look for both effects, but the limited statistics in the analysis does not allow for this.

Starting from an effective Hamiltonian derived from the SME [88, 89], which can be written as a series expansion:

$$H_{\text{eff}} \approx \frac{m^2}{2E} + \sum_{d=3,5,\ldots} E^{\,d-3}\, \mathring{a}^{(d)} - \sum_{d=4,6,\ldots} E^{\,d-3}\, \mathring{c}^{(d)} \tag{3.1}$$

The first term here is the from standard two-neutrino Hamiltonian (see Section 1.2) and notably it decreases with energy. The remaining terms ($\mathring{a}^{(3)}$, $\mathring{c}^{(4)}$, $\mathring{a}^{(5)}$, and so on) arise from the SME and describe isotropic LV effects. The circle symbol on the top indicates isotropic coefficients, and the number in the bracket is the dimension of the operator. Their terms are typically classified by CPT symmetry; CPT-odd/-violating ($\mathring{a}^{(d)}$) and CPT-even/-conserving ($\mathring{c}^{(d)}$), highlighting the reliance of CPT symmetry on Lorentz invariance as discussed in Section 1.2.4. Focusing on muon neutrino to tau neutrino ($\nu_\mu \to \nu_\tau$) oscillations, all SME terms here can be expressed as 2×2 matrices, such as:

$$\mathring{c}^{(6)} = \begin{pmatrix} \mathring{c}^{(6)}_{\mu\mu} & \mathring{c}^{(6)}_{\mu\tau} \\ \mathring{c}^{(6)*}_{\mu\tau} & \mathring{c}^{(6)}_{\tau\tau} \end{pmatrix} \tag{3.2}$$

Without loss of generality, the matrices are defined so that they are traceless, $\mathring{c}^{(6)}_{\mu\mu} + \mathring{c}^{(6)}_{\tau\tau} = 0$, leaving three independent elements, in this case: $\mathring{c}^{(6)}_{\mu\mu}$, $\mathrm{Re}(\mathring{c}^{(6)}_{\mu\tau})$ and $\mathrm{Im}(\mathring{c}^{(6)}_{\mu\tau})$. The off-diagonal LV term $\mathring{c}^{(6)}_{\mu\tau}$ dominates neutrino oscillations at high-energy, which is the main interest in this analysis. In this formalism, LV can be described by an infinite series, but higher-order terms are expected to be suppressed by powers of M_P. Therefore, most terrestrial experiments focus on searching for effects of dimension-three and -four operators; $\mathring{a}^{(3)}$ and $E\,\mathring{c}^{(4)}$ respectively, also called the minimal SME. However, this analysis extends to dimension-eight; that is $E^2\,\mathring{a}^{(5)}$, $E^3\,\mathring{c}^{(6)}$, $E^4\,\mathring{a}^{(7)}$ and $E^5\,\mathring{c}^{(8)}$. Such higher orders are accessible by IceCube, which observes high-energy neutrinos where an enhancement is expected from the terms with dimension greater than four. As an example, dimension-six new physics operators of order $\frac{1}{M_P^2} \sim 10^{-38}$ GeV^{-2} are expected. Only one dimensional operator is assumed to be important at any given energy scale, because the strength of LV is expected to be different at different orders.

3.1.2 Lorentz violating neutrino oscillations

As discussed in Section 1.2, for conventional vacuum neutrino mixing, the oscillation probability $P_{\nu_\alpha \to \nu_\beta}$ is determined by the energy independent mixing angles; θ_{12}, θ_{13}, θ_{23}, δ and mass squared differences; Δm^2_{21}, Δm^2_{3l}, with the energy dependence entering through the oscillation length $L_{\mathrm{osc}} \propto E/\Delta m^2$. Once LV is introduced through the SME as in Equation 3.1, each of the LV SME operators introduces an energy dependence differing from the standard case. For example, the case of the $\mathring{c}^{(4)}$ operator with an effective mass difference of $\Delta\mathring{c}^{(4)}$ would lead to an oscillation length with dependence $L^{(4)}_{\mathrm{osc}} \propto \left(E\Delta\mathring{c}^{(4)}\right)^{-1}$. Therefore, detection of neutrino oscillation spectral anomalies differing from the usual $\propto E$ dependence or energy dependence in the vacuum mixing angles would constitute a clear signal of LV. Figure 3.2 shows a depiction of how this is applied to search for LV in this analysis. By utilising the flux of atmospheric muon neutrinos, the LV field in the background could induce an anomalous neutrino oscillation into tau neutrinos. Therefore, a potential signal of LV is the anomalous disappearance of muon neutrinos.

The $\nu_\mu \to \nu_\tau$ two flavour new physics oscillation scheme following from References [70, 90] is used. This is appropriate as the matter potential of ν_e is much bigger than that due to LV effects, the size of LV that is considered here hardly induces any $\nu_\mu \to \nu_e$ transition.

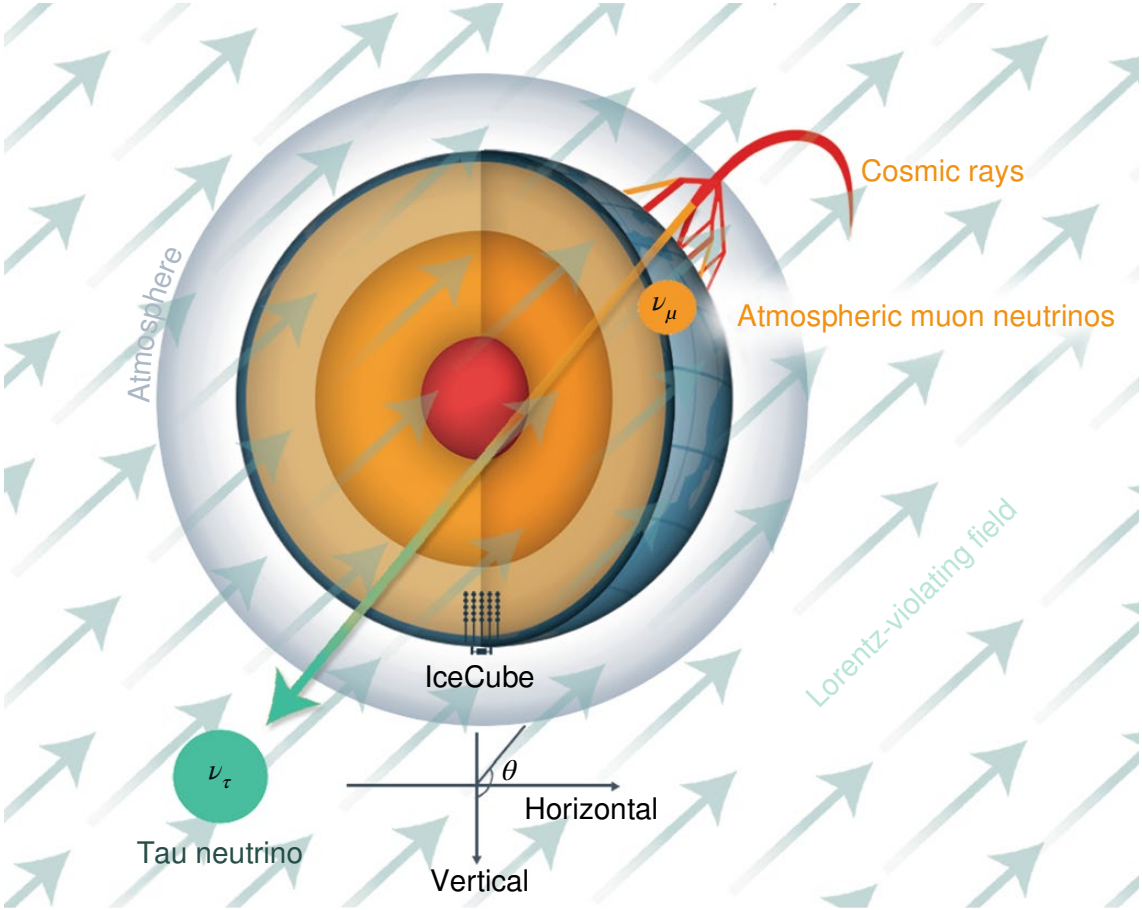

Figure 3.2: Test of LV with atmospheric neutrinos. The LV field, indicated by the arrows, permeates space and could induce an anomalous neutrino oscillation to tau neutrinos. Note, here only the isotropic component is tested.

The oscillation probability can then be calculated from the SME effective Hamiltonian given in Equation 3.1, in a similar way as that shown in Section 1.2.2:

$$P^{(d)}_{\nu_\mu \to \nu_\tau} = \frac{\left|2A_2^{(d)}\right|^2}{\left(\lambda_2^{(d)} - \lambda_1^{(d)}\right)^2} \sin^2\left(\frac{\lambda_2^{(d)} - \lambda_1^{(d)}}{2} L\right) \tag{3.3}$$

where

$$\lambda_1^{(d)} = 12\left[\left(A_1^{(d)} + A_3^{(d)}\right) - \sqrt{\left|A_1^{(d)} - A_3^{(d)}\right|^2 + \left|2A_2^{(d)}\right|^2}\right] \tag{3.4}$$

$$\lambda_2^{(d)} = 12\left[\left(A_1^{(d)} + A_3^{(d)}\right) + \sqrt{\left|A_1^{(d)} - A_3^{(d)}\right|^2 + \left|2A_2^{(d)}\right|^2}\right] \tag{3.5}$$

$$A_1^{(d)} = \frac{1}{2E}\left(m_2^2 \cos^2\theta_{23} + m_3^2 \sin^2\theta_{23}\right) + E^{d-3}\left(\mathring{a}^{(d)}_{\mu\mu} - \mathring{c}^{(d)}_{\mu\mu}\right) \tag{3.6}$$

$$A_2^{(d)} = \frac{1}{2E}\cos\theta_{23}\sin\theta_{23}\left(m_2^2 - m_3^2\right) + E^{d-3}\left(\mathring{a}^{(d)}_{\mu\tau} - \mathring{c}^{(d)}_{\mu\tau}\right) \tag{3.7}$$

$$A_3^{(d)} = \frac{1}{2E}\left(m_2^2 \cos^2\theta_{23} + m_3^2 \sin^2\theta_{23}\right) - E^{d-3}\left(\mathring{a}^{(d)}_{\mu\mu} - \mathring{c}^{(d)}_{\mu\mu}\right) \tag{3.8}$$

Here, the SME effective Hamiltonian is diagonalised with eigenvalues $\lambda_1^{(d)}$ and $\lambda_2^{(d)}$, where $\lambda_2^{(d)} > \lambda_1^{(d)}$. The equivalent antineutrino oscillation probability can be obtained by switching the sign of the CPT-odd terms, $\mathring{a}^{(d)} \to -\mathring{a}^{(d)}$. This gives the oscillation probability as it is used in this analysis.

In the high-energy limit, the neutrino mass effect is negligible in comparison to LV effects and so the oscillation probability can be simplified:

$$P^{(d)}_{\nu_\mu \to \nu_\tau} \sim \left(1 - \frac{\left|\mathring{a}^{(d)}_{\mu\mu} - \mathring{c}^{(d)}_{\mu\mu}\right|^2}{\rho_d^2}\right) \sin^2\left(L\,\rho_d\,E^{d-3}\right) \tag{3.9}$$

$$= \frac{\left|\mathring{a}^{(d)}_{\mu\tau} - \mathring{c}^{(d)}_{\mu\tau}\right|}{\rho_d^2} \sin^2\left(L\,\rho_d\,E^{d-3}\right) \tag{3.10}$$

Here, $\rho_d \equiv \sqrt{(\mathring{a}^{(d)}_{\mu\mu})^2 + \mathrm{Re}(\mathring{a}^{(d)}_{\mu\tau})^2 + \mathrm{Im}(\mathring{a}^{(d)}_{\mu\tau})^2}$ or $\sqrt{(\mathring{c}^{(d)}_{\mu\mu})^2 + \mathrm{Re}(\mathring{c}^{(d)}_{\mu\tau})^2 + \mathrm{Im}(\mathring{c}^{(d)}_{\mu\tau})^2}$ which represents the strength of LV. Then, $\mathring{a}^{(d)}_{\mu\mu}/\rho_d$ and $\mathring{c}^{(d)}_{\mu\mu}/\rho_d$ become fractions of diagonal terms that are bounded between -1 and $+1$. This suggests that there are no LV neutrino oscillations without off-diagonal terms and that the LV oscillations are symmetric between the real and imaginary parts of the off-diagonal SME operators.

3.2 Analysis Method

3.2.1 Data selection

The analysis presented here uses a public data set released by IceCube [39]. This data set was developed to search for diffuse astrophysical neutrinos and consists of a high purity muon data set representing 34,975 ν_μ from the northern sky with 0.1% atmospheric muon contamination, extracted from data taken during 659.5 days of live time recorded between May 2010 and May 2012. A short summary will be given here but for more details see the publication or thesis by Weaver [39, 54].

This data set takes advantage of the long tracks produced by muons in IceCube (see Section 2.2.1). In order to ensure that the observed muons are likely produced by neutrinos and are not from cosmic ray air showers, only muons whose directions imply that they have passed through substantially more material that the maximum range of the muon are selected. This approach cannot distinguish neutrinos by origin (atmospheric or astrophysical), indeed the majority of the data set originates from atmospheric neutrinos, with the diffuse astrophysical component populating only the highest energy tail. Therefore, this data set provides a high purity sample of high-energy atmospheric muon neutrinos which will be used here in order to search for LV as described in the previous section.

As discussed in Section 2.2.1, the energy reconstruction of non-contained tracks is challenging. Reconstruction is split into segments in which the mean $\mathrm{d}E/\mathrm{d}x$ is determined by fitting the amount of light expected to be observed. This gives a proxy for the muon energy, limited by the relatively short section of the muon's total track which is observed and is only loosely connected to the energy of the interacting neutrino. The energy proxy does not have a linear relationship to the actual muon energy, but values above $\sim 3 \times 10^3$ are roughly equivalent to the same quantity in GeV.

Figures 3.3-3.4 show the reconstructed muon energy proxy distribution and reconstructed zenith angle, respectively, compared to expected distributions of the conventional, prompt and astrophysical neutrino spectrum (see Section 1.3 for more on neutrino production). The conventional flux dominates at proxy energies less than 18×10^3 ($\sim$ 18 TeV muon energy) above which the harder prompt and astrophysical components become relevant. To minimize contamination from prompt or astrophysical neutrinos, events with proxy

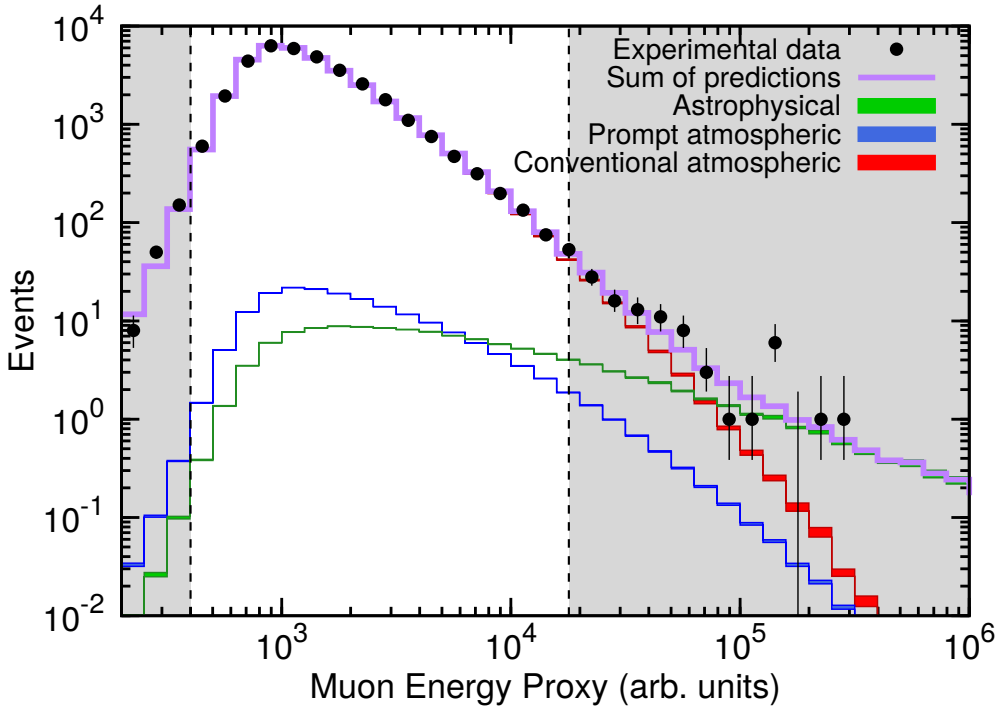

Figure 3.3: The distribution of reconstructed muon energy proxy for events in the final sample, compared to expected distributions [39]. Only statistical errors are shown. The shaded regions show data which is excluded in this analysis. Note the binning shown here is not the one used in this analysis (see text).

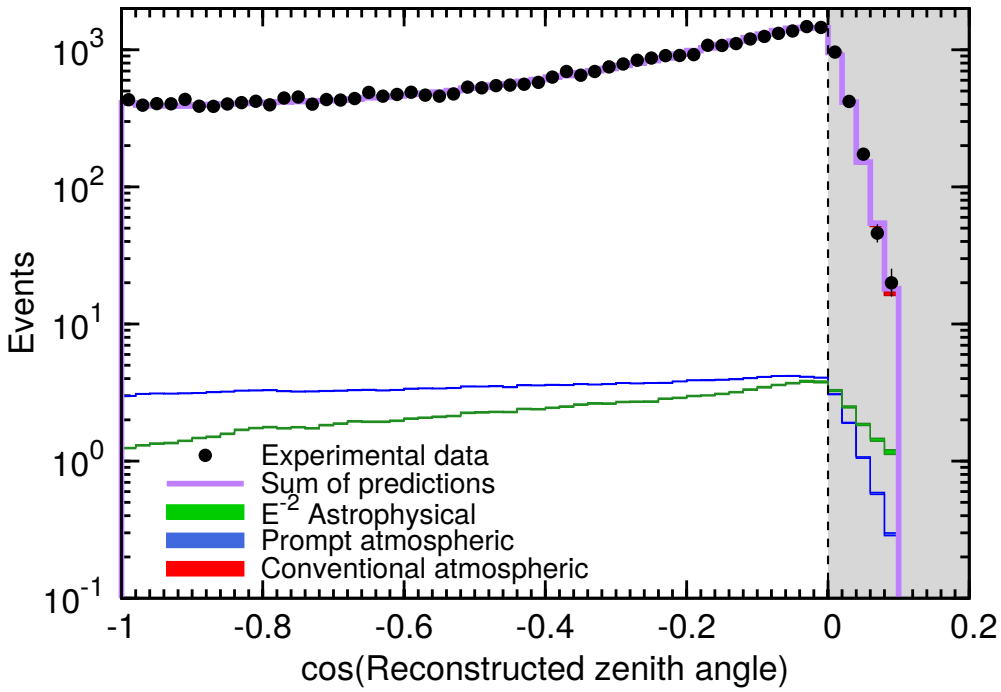

Figure 3.4: The distribution of reconstructed zenith angles in the final sample, compared to expected distributions [39]. Only statistical errors are shown, though in almost all bins they are small enough to be hidden by the data markers. The shaded region shows data which is excluded in this analysis. Note the binning shown here is not the one used in this analysis (see text).

energies above 18×10^3 are not used in this analysis. Furthermore, we introduce a lower energy boundary at a proxy energy of 400, as the correlation between proxy energy and incident muon energy is lost below this point [54]. For this analysis, we use 10 linearly spaced bins in cosine of the zenith angle from -1.0 (vertical) to 0.0 (horizontal) and 17 logarithmically spaced bins in reconstructed muon energy proxy ranging from 400 to 18×10^3.

3.2.2 Simulation

The data release includes the tools necessary to compute expected event rates for any given theoretical neutrino flux in the form of an *effective area* release [39]. The effective area gives the area of a hypothetical detector with perfect efficiency which would be required to collect neutrino interactions at the same rate, therefore it accounts for the propagation of neutrinos through the Earth, interaction to produce secondaries, detection of the secondaries by IceCube, and the data selection criteria. They are provided as eight tables labelled by year (2010, 2011) and particle type (ν_μ, $\bar{\nu}_\mu$, ν_τ, $\bar{\nu}_\tau$) with each binned in three dimensions; true neutrino energy, true/reconstructed neutrino zenith angle, and reconstructed muon energy proxy. Figure 3.5 shows the effective area of this data selection as a function of true neutrino energy for several different ranges of zenith angles, averaged to all other

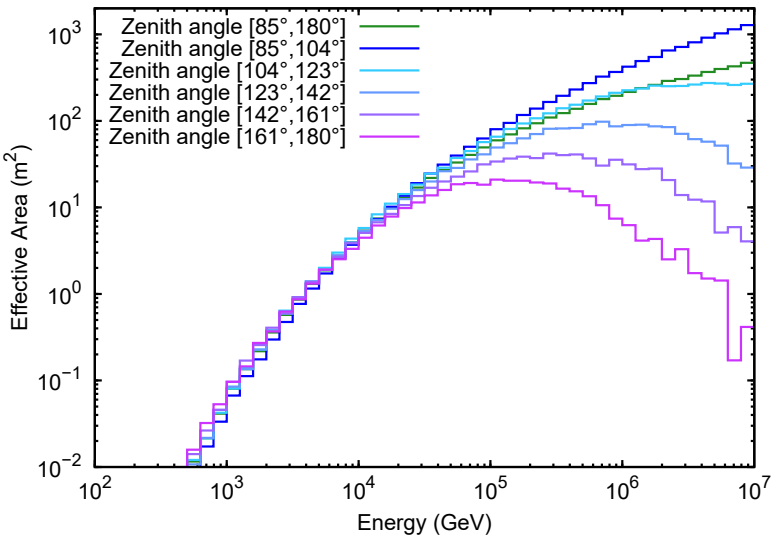

Figure 3.5: The effective area of the detector for a flux of neutrinos after all data selection criteria have been applied [54]. The area is shown for five zenith angle bands, and the average of all zenith angles is overlaid in green.

event properties. A notable feature here is the attenuation due to Earth absorption at the largest zenith angles, where the amount of material traversed is greatest, and also at the highest energies, where the cross-section is larger. The Earth model used in the calculation of these effective areas is the Preliminary Earth Reference Model (PREM) [91] and for the neutrino cross-section model, the CSMS calculation is used [46] which is discussed in detail in Section 1.4.1 and shown in Figure 1.14.

The number of expected events in analysis space $(\cos\theta, E_{\text{proxy}})$, can then be computed for a given differential neutrino flux at the detector $\Phi(E_\nu, \cos\theta)$:

$$N(\cos\theta, E_{\text{proxy}}) = \int \mathrm{d}E_\nu \cdot \mathrm{d}t \cdot \Phi(E_\nu, \cos\theta) \cdot A^\nu_{\text{eff}}(E_\nu, \cos\theta, E_{\text{proxy}}) \tag{3.11}$$

where t is the total livetime. In this way, the effects of LV can be probed in analysis space as a deviation in the neutrino flux at the detector $\Phi(E_\nu, \cos\theta) \to \Phi^{(d)}\left(E_\nu, \cos\theta, \mathring{c}^{(d)}_{\mu\tau}\right)$. This flux is calculated in the following way. The predicted conventional atmospheric neutrino fluxes[2] are calculated using the matrix cascade equation using the MCEQ package [32], as described in Section 1.3.1. The prompt neutrino flux is calculated with the ERS [92] model. The astrophysical neutrino flux, while small in the energy range of consideration here, is modelled as a power law with normalisation and spectral index, $\sim \Phi E^{-\gamma}$. Finally, $\nu_\mu \to \nu_\tau$ neutrino oscillations are taken into account in the presence of an LV field using the SME effective Hamiltonian prescription given by Equation 3.3.

The short distance of travel for horizontal neutrinos $(\cos\theta = 0)$ leads to negligible spectral distortion due to LV, whereas the long path length for vertical neutrinos $(\cos\theta = -1)$ leads to modifications. By comparing the ratio between between the vertical and horizontal transition probabilities, one can visualise the effect of LV as is shown in Figure 3.6. The data transition probability is defined by the ratio of observed events to expected events, and the simulation transition probability is defined by the expected events in the presence of LV to the number of events in the absence of LV. In the absence of LV, this ratio equals 1. Here several predictions from simulations with different dimension-six LV parameters $\left|\mathring{c}^{(6)}_{\mu\tau}\right|$ are shown. In general, higher order terms are more important at higher energies.

[2] The components of the conventional flux coming from pions and kaons is calculated separately and then summed. This enables us to account for systematic uncertainties between the two components, as will be seen in Section 3.2.3.

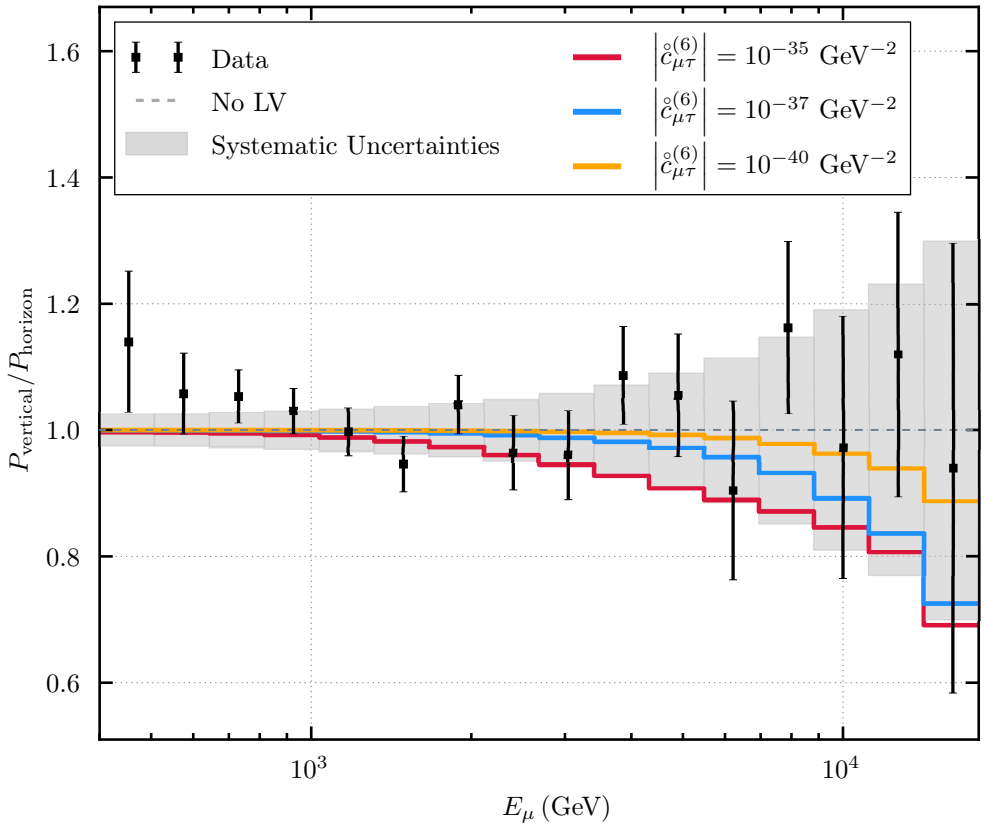

Figure 3.6: The ratio of vertical to horizontal neutrino transition probabilities. Here, vertical events are defined by $\cos\theta \leq -0.6$ and the horizontal events are defined as $\cos\theta \geq -0.6$. The transition probability ratio with 1σ statistical errors, extracted from the data, is compared to the prediction for various dimension-six operator values. The range of uncorrelated systematic uncertainties is shown as a light gray band. This is constructed from ensembles of many simulations where the nuisance parameters are varied within their uncertainties (see Section 3.3.2).

3.2.3 Systematics

The dominant systematic uncertainties in this analysis are related to the atmospheric and astrophysical neutrino fluxes. This analysis is particularly sensitive to the highest energies neutrinos, where an enhancement is expected for higher dimensional SME coefficients (see Section 3.1). Therefore, the uncertainties concerning the neutrino flux predictions must be taken into account. A description of the parameters used to quantify this uncertainty will be introduced and discussed here and, as will be expanded on in Section 3.2.4, these will then define the *nuisance parameters* of this analysis.

The systematic uncertainties of the data set being used for this analysis has been studied in great detail, both in the diffuse astrophysical flux analysis, for which this data set was curated, and also in an analysis searching for anomalous neutrino oscillations of atmospheric neutrinos due to a sterile neutrino flavour [39, 54, 93–95]. In order to describe the uncertainties in the neutrino flux predictions, a similar approach will be taken as in these analyses. The atmospheric ν_μ flux can be written as:

$$\Phi_{\text{atm}} = N_{\text{conv}} \cdot \Phi_{\text{conv}} \cdot \left(\frac{E_\nu}{2020\,\text{GeV}}\right)^{-\Delta\gamma_{\text{CR}}} + N_{\text{prompt}} \cdot \Phi_{\text{prompt}} \cdot \left(\frac{E_\nu}{7877\,\text{GeV}}\right)^{-\Delta\gamma_{\text{CR}}} \tag{3.12}$$

$$\Phi_{\text{conv}} = \Phi_K + R_{\pi/K}\,\Phi_\pi \tag{3.13}$$

where Φ_{conv} is the conventional ν_μ flux, Φ_{prompt} is the prompt ν_μ flux, Φ_K is the conventional ν_μ flux component coming from kaon decays, and Φ_π is the conventional ν_μ flux component coming from muon decays. These various components of the atmospheric flux are discussed in detail in Section 1.3.1. The four systematic parameters introduced here are the overall conventional flux normalisation N_{conv}, the ratio of the conventional flux coming from pions or kaons $R_{\pi/K}$, the spectral index of the primary cosmic ray flux $\Delta\gamma_{\text{CR}}$, and the overall prompt flux normalisation N_{prompt}.

The conventional ν_μ flux normalisation has fairly large uncertainty, primarily due to QCD uncertainties in the air shower development in the energy range of interest here. A theoretical uncertainty on this normalisation derived from variations of the hadronic interaction model is presented in [96]. It finds an $\sim 40\%$ uncertainty, which will be used here to define

a Gaussian prior on N_{conv}. Note the prior is modified slightly such that N_{conv} is always greater than 0.1. On top of this normalisation, hadronic interaction models also exhibit a spectral uncertainty based on the ratio of the pion- and kaon-induced neutrinos due to their different critical energies (see Section 1.3.1). The parameter $R_{\pi/K}$ accounts for this and in this analysis it will be included with a Gaussian prior with a 10% uncertainty [93, 95]. As for the prompt flux normalisation, it has never been conclusively observed and so the only constraint made on its value is that it never go below 0. Finally, both these fluxes depend directly on the flux of cosmic rays. The overall normalisation uncertainty is already accounted for in the individual normalisations; however, there is also an uncertainty in the shape. For the energies of interest here, measurements of the cosmic ray spectral index show some disagreement, at the level of ± 0.05 [33]. Here, we implement this with a Gaussian prior for $\Delta\gamma_{\text{CR}}$. Note here, the spectral index is implemented around a pivot of the approximate median energy of the spectrum to minimise degeneracy with the normalisation parameters. Figures 3.7a-d demonstrate the effect of each of these systematic parameters in proxy energy space.

The astrophysical neutrino flux can equivalently be written as:

$$\Phi_{\text{astro}} = N_{\text{astro}} \cdot \phi_{\text{astro}} \cdot \left(\frac{E_\nu}{100\ \text{TeV}} \right)^{-2+\Delta\gamma_{\text{astro}}} \tag{3.14}$$

where ϕ_{astro} is the astrophysical neutrino flux normalisation, N_{astro} is an overall normalisation systematic parameter and $\Delta\gamma_{\text{astro}}$ is the modification to astrophysical neutrino spectral index. As per conventions, the pivot is chosen here to be at 100 TeV and the systematic parameter is fashioned to be the change from an E^{-2} power spectrum. In this analysis, we assume ignorance on the normalisation, only that it never go below 0. From measurements of this spectral index from various other IceCube analyses, a flat prior is used for $\Delta\gamma_{\text{astro}}$ with ranges $-0.5 \rightarrow 0.5$ [38]. Figures 3.7e-f demonstrate the effect of these two systematic parameters in proxy energy space.

Also to be considered are detector and ice related uncertainties. While the absolute DOM optical efficiency is measured in lab, shadowing caused by the DOM cable and unknown local optical conditions after deployment introduce an uncertainty in the detected energy and angular event reconstruction. This was accounted for in the diffuse astrophysical analysis with extensive simulations of various DOM configurations, fitting to the effective

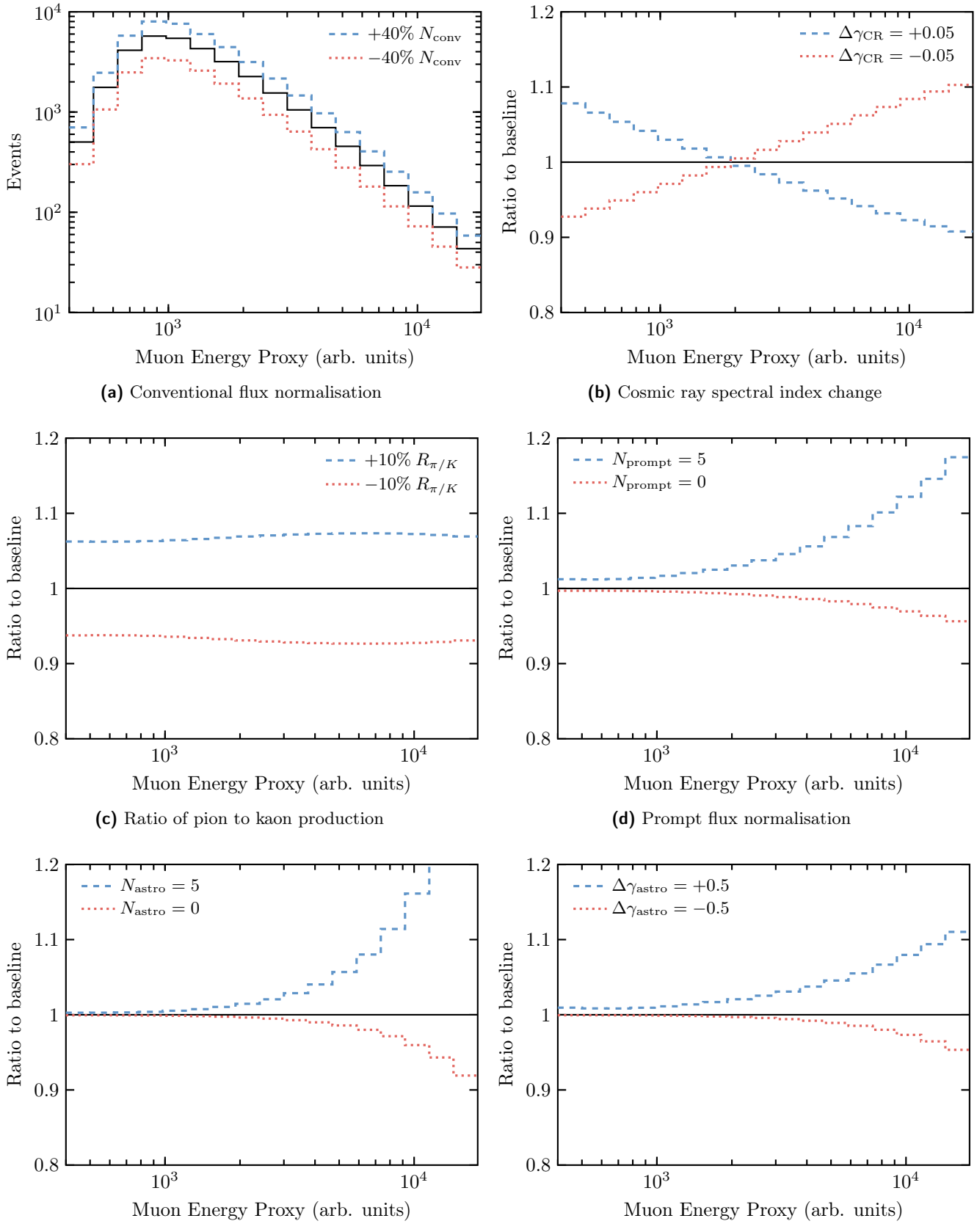

(a) Conventional flux normalisation

(b) Cosmic ray spectral index change

(c) Ratio of pion to kaon production

(d) Prompt flux normalisation

(e) Astrophysical flux normalisation

(f) Astrophysical spectral index change

Figure 3.7: Effect of the systematic parameters used in this analysis on the event distribution in muon energy proxy space. Black (solid) histogram shows the baseline expectation, blue (dashed) shows an upward fluctuation and red (dotted) shows a downward fluctuation.

Parameter	Symbol	Central value	Prior
Conventional flux normalisation	N_{conv}	1	Gaussian: $1 \pm 40\%$
Prompt flux normalisation	N_{prompt}	1	Flat: $0 \rightarrow \infty$
Astrophysical flux normalisation	N_{astro}	1	Flat: $0 \rightarrow \infty$
Ratio of pion to kaon production	$R_{\pi/K}$	1	Gaussian: $1 \pm 10\%$
Cosmic ray spectral index change	$\Delta\gamma_{\text{CR}}$	0	Gaussian: 0 ± 0.05
Astrophysical spectral index change	$\Delta\gamma_{\text{astro}}$	0	Flat: $-0.5 \rightarrow +0.5$

Table 3.1: Systematic parameters used in this analysis, showing the prior imposed on each parameter. Note the conventional flux normalisation prior is also constrained such that it cannot go below a value of 0.1. See text for more details.

DOM optical efficiency. The data was seen to tightly constrain the DOM efficiency, with a 0.5% error on the best fit value [39]. The DOM efficiency is set with good precision with the position of the peak of the energy distribution at $\sim$TeV, as was also observed in the sterile neutrino analysis [93]. The analysis here, however, is most sensitive to the highest energies, therefore the DOM efficiency is expected to have a small effect on constraints of LV. Light propagation uncertainties may also arise from uncertainties in the ice scattering and absorption models; however, it was found in the sterile analysis that the uncertainty is not significant and is comparable to the statistical error [93]. Also investigated in the sterile neutrino analysis but found to be small effects were neutrino propagation and interaction uncertainties. Table 3.1 provides a summary of the systematic parameters used in this analysis.

3.2.4 Classical statistics

Data is stochastic in nature, so an experimenter uses statistical methods on a data sample $\mathbf{x}$ to make inferences about unknown parameters $\boldsymbol{\theta}$ of a probabilistic model of the data $f(\mathbf{x}|\boldsymbol{\theta})$. The *likelihood principle* describes a function of the parameters $\boldsymbol{\theta}$, determined by the observed sample, that contains all the information about $\boldsymbol{\theta}$ that is available from the sample. Given $\mathbf{x}$ is observed and is distributed according to a joint *probability distribution function* (PDF), $f(\mathbf{x}|\boldsymbol{\theta})$, the function of $\boldsymbol{\theta}$ which is defined by

$$L(\boldsymbol{\theta}|\mathbf{x}) \equiv f(\mathbf{x}|\boldsymbol{\theta}) \tag{3.15}$$

is called the *likelihood function* [97]. If the data $\mathbf{x}$ consists of independent and identically distributed values, then:

$$L\left(\boldsymbol{\theta}|\mathbf{x}\right) = L\left(\theta_1, \ldots, \theta_k | x_1, \ldots, x_n\right) = \prod_{i=1}^{n} f\left(x_i|\theta_1, \ldots, \theta_k\right) \tag{3.16}$$

The *maximum likelihood estimators* (MLE) of the parameters $\boldsymbol{\theta}$, denoted by $\hat{\boldsymbol{\theta}}(\mathbf{x})$, are attained by maximising $L\left(\boldsymbol{\theta}|\mathbf{x}\right)$. When working with large data samples, it can be convenient to bin the values into a histogram with N bins, so one obtains a vector of binned values $\mathbf{n} = (n_1, \ldots, n_N)$. If n_i are regraded as independent and Poisson distributed, then the likelihood can be written as:

$$L\left(\boldsymbol{\theta}|\mathbf{n}\right) = \prod_{i=1}^{N} \frac{\mu_i\left(\boldsymbol{\theta}\right)^{n_i}}{n_i!} e^{-\mu_i(\boldsymbol{\theta})} \tag{3.17}$$

where the mean values μ_i are functions of $\boldsymbol{\theta}$. This is the form of the likelihood that will be used in this analysis. Often, not all the model parameters are of direct inferential interest however they are included as they may reduce the effect of systematic bias. These are called the nuisance parameters, $\boldsymbol{\theta}_v$. To reduce the impact of the nuisance parameters, prior knowledge based on past measurements $\mathbf{y}$ may be included in the likelihood:

$$L\left(\boldsymbol{\theta}_I, \boldsymbol{\theta}_v|\mathbf{x}, \mathbf{y}\right) = \prod_{i=1}^{N} f_I\left(x_i|\boldsymbol{\theta}_I\right) \cdot f_v\left(\mathbf{y}|\boldsymbol{\theta}_v\right) \tag{3.18}$$

By finding the MLE for the nuisance parameters, $\hat{\boldsymbol{\theta}}_v(\mathbf{y})$, the *profile likelihood* can be written in terms independent of $\boldsymbol{\theta}_v$:

$$L_P\left(\boldsymbol{\theta}_I|\mathbf{x}, \mathbf{y}\right) = L\left(\boldsymbol{\theta}_I, \hat{\boldsymbol{\theta}}_v\left(\mathbf{y}\right)\middle|\mathbf{x}, \mathbf{y}\right) \tag{3.19}$$

For this analysis, the parameters of interest will be the three independent parameters making up an SME term for a given dimension d (see Section 3.1.1). In addition, Table 3.1 provides a summary of the six nuisance parameters along with the respective prior.

The key method of inference in physics is *hypothesis testing*. The two complementary hypotheses in a hypothesis testing problem are called the *null hypothesis* and the *alternative hypothesis*. The goal of a hypothesis test is to decide, based on a sample of data, which of the two complementary hypotheses is preferred. The general format of the null and

alternative hypothesis is $H_0 : \boldsymbol{\theta} \in \Theta_0$ and $H_1 : \boldsymbol{\theta} \in \Theta_0^c$, where Θ_0 is some subset of the parameter space and Θ_0^c is its complement. In this analysis, the null hypothesis will be the no LV hypothesis, where each SME term is equal to 0, and the alternative hypothesis will be a non-zero LV hypothesis, where any SME term is non-zero. Typically, a hypothesis test is specified in terms of a *test statistic* (TS) which is used to define the *rejection region*, which is the region in which the null hypothesis can be rejected. The Neyman-Pearson lemma [98] then states that the *likelihood ratio test* (LRT) statistic is the most powerful test statistic:

$$\lambda(\mathbf{x}) = \frac{L\left(\hat{\boldsymbol{\theta}}_0 \middle| \mathbf{x}\right)}{L\left(\hat{\boldsymbol{\theta}} \middle| \mathbf{x}\right)} \tag{3.20}$$

where $\hat{\boldsymbol{\theta}}$ is a MLE of $\boldsymbol{\theta}$ and $\hat{\boldsymbol{\theta}}_0$ is a MLE of θ obtained by doing a restricted maximisation, assuming Θ_0 is the parameter space. The effect of nuisance parameters can be included by substituting the likelihood with the profile likelihood $L \to L_P$, as shown in Equation 3.19. The rejection region then has the form $R(\boldsymbol{\theta}_0) = \{\mathbf{x} : \lambda(\mathbf{x}) \leq c(\alpha)\}$, such that $P_{\boldsymbol{\theta}_0}(\mathbf{x} \in R(\boldsymbol{\theta}_0)) \leq \alpha$, where α satisfies $0 \leq \alpha \leq 1$ and is called the *size* or *significance level* of the test and is specified prior to the experiment. Typically in high-energy physics the level of significance where an effect is said to qualify as a discovery is at the 5σ level, corresponding to an α of 2.87×10^{-7}. In a binned analysis, the distribution of $\lambda(\mathbf{n})$ can be approximated by generating mock data or *realisations* of the null hypothesis. However, this can be computationally difficult to perform. Instead, according to Wilks' theorem [99], for sufficiently large $\mathbf{x}$ and provided certain regularity conditions are met (MLE exists and is unique), $-2\ln\lambda(\mathbf{x})$ can be approximated to follow a χ^2 distribution. The χ^2 distribution is parameterised by k, the *number of degrees of freedom*, which is defined as the number of independent normally distributed variables that were summed together. When the profile likelihood is used to account for n nuisance parameters, the effective number of degrees of freedom will be reduced to $k - n$, due to additional constraints placed via profiling. From this, $c(\alpha)$ can be easily obtained from χ^2 *cumulative distribution function* (CDF) lookup tables.

As shown so far, the LRT informs on the best fit point of parameters $\boldsymbol{\theta}$. In addition to this point estimator, some sort of *interval* estimator is also useful to report to reflect its statistical precision. Interval estimators together with a measure of confidence are also

known as *confidence intervals* which has the important property of *coverage*. The purpose of using an interval estimator is to have some guarantee of capturing the parameter of interest, quantified by the coverage coefficient, $1-\alpha$. In this classical approach, one needs to keep in mind that the interval is the random quantity, not the parameter - which is fixed. Since we do not know the value of θ, we can only guarantee a coverage probability equal to the *confidence coefficient*. There is a strong correspondence between hypothesis testing and interval estimation. The hypothesis test fixes the parameter and asks what sample values (the acceptance region) are consistent with that fixed value. The interval estimation fixes the sample value and asks what parameter values (the confidence interval) make this sample value most plausible. This can be written in terms of the LRT statistic:

$$\lambda(\boldsymbol{\theta}) = \frac{L(\boldsymbol{\theta}|\mathbf{x})}{L\left(\hat{\boldsymbol{\theta}}\middle|\mathbf{x}\right)} \tag{3.21}$$

The confidence interval is then formed as $C(\mathbf{x}) = \{\boldsymbol{\theta} : \lambda(\boldsymbol{\theta}) \geq c(1-\alpha)\}$, such that $P_{\boldsymbol{\theta}}(\boldsymbol{\theta} \in C(\mathbf{x})) \geq 1-\alpha$. Assuming Wilks' theorem holds, this can be written more specifically as $C(\mathbf{x}) = \left\{\boldsymbol{\theta} : -2\ln\lambda(\boldsymbol{\theta}) \leq \mathrm{CDF}_{\chi^2}^{-1}(k, 1-\alpha)\right\}$, where $\mathrm{CDF}_{\chi^2}^{-1}$ is the inverse CDF for a χ^2 distribution. One again, the effect of nuisance parameters can be accounted for by using the profile likelihood analogously to hypothesis testing.

3.2.5 Bayesian statistics

The Bayesian approach to statistics is fundamentally different to the classical (*frequentist*) approach that has been taken so far. In the classical approach the parameter θ is thought to be an unknown, but fixed quantity. In a Bayesian approach, θ is considered to be a quantity whose variation can be described by a probability distribution (called the *prior distribution*), which is subjective based on the experimenter's belief. The Bayesian approach is also different in terms of computation, whereby the classical approach consists of optimisation problems (finding maxima), the Bayesian approach often results in integration problems.

In this approach, when an experiment is performed it updates the prior distribution with new information. The updated prior is called the *posterior distribution* and is computed

through the use of Bayes' Theorem [100]:

$$\pi\left(\boldsymbol{\theta}|\mathbf{x}\right) = \frac{f\left(\mathbf{x}|\boldsymbol{\theta}\right)\pi\left(\boldsymbol{\theta}\right)}{m\left(\mathbf{x}\right)} \tag{3.22}$$

where $\pi\left(\boldsymbol{\theta}|\mathbf{x}\right)$ is the posterior distribution, $f\left(\mathbf{x}|\boldsymbol{\theta}\right) \equiv L\left(\boldsymbol{\theta}|\mathbf{x}\right)$ is the likelihood, $\pi\left(\boldsymbol{\theta}\right)$ is the prior distribution and $m\left(\mathbf{x}\right)$ is the *marginal distribution*,

$$m\left(\mathbf{x}\right) = \int f\left(\mathbf{x}|\boldsymbol{\theta}\right)\pi\left(\boldsymbol{\theta}\right)\mathrm{d}\boldsymbol{\theta} \tag{3.23}$$

The *maximum a posteriori probability* (MAP) estimate of the parameters $\boldsymbol{\theta}$, denoted by $\hat{\boldsymbol{\theta}}_{\mathrm{MAP}}\left(\mathbf{x}\right)$ are attained by maximising $\pi\left(\boldsymbol{\theta}|\mathbf{x}\right)$. This estimator can be interpreted as an analogue of the MLE for Bayesian estimation, where the distribution has become the posterior. An important distinction to make from the classical approach is in the treatment of the nuisance parameters. The priors on θ_ν are naturally included as part of the prior distribution $\pi\left(\boldsymbol{\theta}_\nu\right) = \pi\left(\boldsymbol{\theta}_\nu|\mathbf{y}\right)$ based on a past measurement $\mathbf{y}$. Then the posterior distribution can be obtained for θ_I alone by *marginalising* over the nuisance parameters:

$$\pi\left(\boldsymbol{\theta}_I|\mathbf{x}\right) = \int \pi\left(\boldsymbol{\theta}_I, \boldsymbol{\theta}_\nu|\mathbf{x}\right)\mathrm{d}\boldsymbol{\theta}_\nu \tag{3.24}$$

For this analysis, the Bayesian intervals will also be reported as supplementary material alongside the classical confidence intervals which were described in the previous section. In contrast to the classical approach, where an interval is said to have coverage of the parameter θ, the Bayesian approach allows one to say that θ is inside the interval with a probability $1-\beta$. This distinction is emphasised by referring to Bayesian intervals as *credible intervals* and β is referred to here as the *credible coefficient*. Therefore, both the interpretation and construction is more straightforward than for the classical approach. The credible interval is formed as:

$$\pi\left(\boldsymbol{\theta} \in A|\mathbf{x}\right) = \int_A \pi\left(\boldsymbol{\theta}|\mathbf{x}\right)\mathrm{d}\boldsymbol{\theta} \geq 1-\beta \tag{3.25}$$

This does not uniquely specify the credible interval however. The most useful convention when working in high dimensions is the *Highest Posterior Density* (HPD) credible interval. Here the interval is constructed such that the posterior meets a minimum threshold $A\left(\mathbf{x}\right) = \{\boldsymbol{\theta} : \pi\left(\boldsymbol{\theta}|\mathbf{x}\right) \geq t\left(1-\beta\right)\}$. This can be seen as an interval starting at the MAP, growing to

include an area whose integrated probability is equal to β and where all points inside the interval have a higher posterior value than all points outside the interval.

In the Bayesian approach, hypothesis testing can be generalised further to *model selection* in which possible models (or hypotheses) $\mathcal{M}_0, \mathcal{M}_1, \ldots, \mathcal{M}_k$ of the data $\mathbf{x}$ can be compared. This is again done through Bayes theorem where the posterior probability that $\mathbf{x}$ originates from a model $\mathcal{M}_j$ is

$$\pi\left(\mathcal{M}_j|\mathbf{x}\right) = \frac{f\left(\mathbf{x}|\mathcal{M}_j\right)\pi\left(\mathcal{M}_j\right)}{M\left(\mathbf{x}\right)} \quad \text{where} \quad M\left(\mathbf{x}\right) = \sum_{i=0}^{k} f\left(\mathbf{x}|\mathcal{M}_i\right)\pi\left(\mathcal{M}_i\right) \tag{3.26}$$

the likelihood of the model $f\left(\mathbf{x}|\mathcal{M}_j\right)$ can then be written as the marginal distribution over model parameters $\boldsymbol{\theta}_j$, also referred to as the *evidence* of a particular model:

$$\mathcal{Z}_j\left(\mathbf{x}\right) = f\left(\mathbf{x}|\mathcal{M}_j\right) = \int f_j\left(\mathbf{x}|\boldsymbol{\theta}_j\right)\pi_j\left(\boldsymbol{\theta}_j\right)\mathrm{d}\boldsymbol{\theta}_j \tag{3.27}$$

This was seen before as just a normalisation constant in Equation 3.23; however, this quantity is central in Bayesian model selection, which for two models $\mathcal{M}_0$ and $\mathcal{M}_1$ is realised through the ratio of the posteriors:

$$\frac{\pi\left(\mathcal{M}_0|\mathbf{x}\right)}{\pi\left(\mathcal{M}_1|\mathbf{x}\right)} = B_{0/1}\left(\mathbf{x}\right)\frac{\pi\left(\mathcal{M}_0\right)}{\pi\left(\mathcal{M}_1\right)} \quad \text{where} \quad B_{0/1}\left(\mathbf{x}\right) = \frac{\mathcal{Z}_0\left(\mathbf{x}\right)}{\mathcal{Z}_1\left(\mathbf{x}\right)} \tag{3.28}$$

Bayes factor	Strength of evidence
$B_{0/1} < 10^{-2}$	Evidence against $\mathcal{M}_0$ decisive
$10^{-2} < B_{0/1} < 10^{-3/2}$	Evidence against $\mathcal{M}_0$ very strong
$10^{-3/2} < B_{0/1} < 10^{-1}$	Evidence against $\mathcal{M}_0$ strong
$10^{-1} < B_{0/1} < 10^{-1/2}$	Evidence against $\mathcal{M}_0$ substantial
$10^{-1/2} < B_{0/1} < 1$	Evidence against $\mathcal{M}_0$ barely worth mention
$1 < B_{0/1} < 10^{1/2}$	Evidence for $\mathcal{M}_0$ barely worth mention
$10^{1/2} < B_{0/1} < 10^{1}$	Evidence for $\mathcal{M}_0$ substantial
$10^{1} < B_{0/1} < 10^{3/2}$	Evidence for $\mathcal{M}_0$ strong
$10^{3/2} < B_{0/1} < 10^{2}$	Evidence for $\mathcal{M}_0$ very strong
$10^{2} < B_{0/1}$	Evidence for $\mathcal{M}_0$ decisive

Table 3.2: List of Bayes factors and their inference convention according to Jeffreys' scale [101].

here we denote the quantity $B_{0/1}(\mathbf{x})$ as the *Bayes factor* which measures the relative evidence of each model and can be reported independent of the prior on the model. It can be interpreted as the *strength of evidence* for a particular model and a convention formulated by Jeffreys [101] is one way to interpret this inference, as shown in Table 3.2. In this analysis, the no LV or null hypothesis will represent $\mathcal{M}_0$, and the alternative $\mathcal{M}_1$.

3.2.6 Sampling

The goal of a Bayesian inference is to maintain the full posterior probability distribution. The models in question may contain a large number of parameters and so such a large dimensionality makes analytical evaluations and integrations of the posterior distribution unfeasible. Instead the posterior distribution can be approximated using *Markov Chain Monte Carlo* (MCMC) sampling algorithms. As the name suggests these are based on *Markov chains* which describe a sequence of random variables $\Theta_0, \Theta_1, \ldots$ that can be thought of as evolving over time, with probability of transition depending on the immediate past variable, $P(\Theta_{k+1} \in A|\theta_0, \theta_1, \ldots, \theta_k) = P(\Theta_{k+1} \in A|\theta_k)$ [102]. In an MCMC algorithm, Markov chains are generated by a simulation of *walkers* which randomly walk the parameter space according to an algorithm such that the distribution of the chains asymptotically reaches a *target density* $f(\theta)$ that is unique and stationary (i.e. no longer evolving). This technique is particularly useful as the chains generated for the posterior distribution can automatically provide the chains of any marginalised distribution, e.g. a marginalisation over any or all of the nuisance parameters.

Algorithm 1 Metropolis-Hastings [102, 103]

`Given` $\theta^{(t)}$`,`

1. `Generate` $\theta'_t \sim q\left(\theta'\middle|\theta^{(t)}\right)$.
2. `Take`

$$\theta^{(t+1)} = \begin{cases} \theta'_t & \texttt{with probability} \quad \rho\left(\theta^{(t)}, \theta'_t\right), \\ \theta^{(t)} & \texttt{with probability} \quad 1 - \rho\left(\theta^{(t)}, \theta'_t\right), \end{cases}$$

`where`

$$\rho\left(\theta, \theta'\right) = \min\left\{\frac{f(\theta')}{f(\theta)}\frac{q(\theta|\theta')}{q(\theta'|\theta)}, 1\right\}.$$

The *Metropolis-Hastings* (MH) algorithm [103] is the most well known MCMC algorithm and is shown in Algorithm 1. An initialisation state (seed) is first chosen, $\theta^{(t)}$. The distribution $q\left(\theta'|\theta\right)$, called the *proposal distribution*, is drawn from in order to propose a candidate state θ'_t to transition to. Commonly a Gaussian distribution is used here. Then the MH *acceptance probability*, $\rho\left(\theta, \theta'\right)$ defines the probability of either accepting the candidate state θ'_t, or repeating the state $\theta^{(t)}$ for the next step in the Markov chain. The acceptance probability always accepts the state θ'_t such that the ratio $f\left(\theta'_t\right) / q\left(\theta'_t|\theta^{(t)}\right)$ has increased compared with the previous state $f\left(\theta^{(t)}\right) / q\left(\theta^{(t)}|\theta'_t\right)$, where f is the *target density*. Importantly, in the case that the target density is the posterior distribution, $f\left(\theta\right) = \pi\left(\theta|\mathbf{x}\right)$, the acceptance probability only depends on the ratio of posteriors $\pi\left(\theta'|\mathbf{x}\right) / \pi\left(\theta|\mathbf{x}\right)$, crucially cancelling out the difficult to calculate marginal distribution $m\left(\mathbf{x}\right)$, Equation 3.23. As the chain evolves, the target density relaxes to a stationary state of samples which, in our case, can be used to map out the posterior distribution.

To reduce the impact of any biases arising from the choice of the initialisation state, typically the first few chains after a *burn-in* period are discarded, after which the chains should approximate better the target density f. While the MH algorithm forms the foundation of all MCMC algorithms, its direct application has two disadvantages. First the proposal distribution $q\left(\theta'|\theta\right)$ must be chosen carefully and secondly the chains can get caught in local modes of the target density. More bespoke and sophisticated implementations of the MH algorithm exist, such as *affine invariant* algorithms [104] which use already-drawn samples to define the proposal distribution or *nested sampling* algorithms [105], designed to compute the evidence $\mathcal{Z}$. Both these types will be used in the Bayesian approach of this analysis. A more in depth look into the topic of MCMC algorithms is discussed in detail in Robert and Casella [102] or Collin [106].

3.3 Results

To constrain the LV parameters, two statistical approaches will be used. First a classical likelihood analysis by profiling the likelihood over the nuisance parameters per set of LV parameters as described in Section 3.2.4 is used. From the profile likelihood, the best-fit LV parameters are found (as the MLE) and from that, the 90% and 99% confidence intervals are drawn assuming Wilks' theorem with three degrees of freedom. The second approach taken will be a Bayesian approach as described in Section 3.2.5 where the posterior distribution is sampled by means of an MCMC algorithm as described in Section 3.2.6. The two procedures are found to be complementary and the extracted LV parameters agree with the null hypothesis of no LV.

Conventionally in LV searches using neutrino oscillations, experiments maximise their limits by assuming all but one of the SME elements are zero [68]. The first results shown here in Figure 3.9 follow this convention. This figure shows the *exclusion regions* which are the regions not contained in the 90% or 99% confidence interval. Here, for each dimension of the SME operator, $d = 3, 4, 5, 6, 7, 8$, the diagonal SME element is set to zero and the focus is on setting limits on the real and imaginary parts of the off-diagonal element, $\mathrm{Re}(\mathring{a}^{(d)}_{\mu\tau})$ and $\mathrm{Im}(\mathring{a}^{(d)}_{\mu\tau})$ or $\mathrm{Re}(\mathring{c}^{(d)}_{\mu\tau})$ and $\mathrm{Im}(\mathring{c}^{(d)}_{\mu\tau})$, see Section 3.1.1. There exists a perfect symmetry in the sign of either of these off-diagonal elements, leading to four separated but identically shaped confidence intervals per dimension depending on the signs. Here is shown the case when both real and imaginary elements are positive. Also to note is that in this analysis, a full scan varying over different values of the diagonal element is performed and shown here in the figure is simply a slice of the total three-dimensional parameter space, which can be viewed in full along with points denoting the best-fit values in Appendix A.2.

Although the real and imaginary elements are correlated, they are almost symmetric and so the attainable best exclusion limits are extracted from the intersection of a diagonal $\mathrm{Re}(\mathring{a}^{(d)}_{\mu\tau}) = \mathrm{Im}(\mathring{c}^{(d)}_{\mu\tau})$ line with the exclusion region, i.e. limits for the real and imaginary elements are set to the same value. These limits are limited by the small statistics of high-energy atmospheric neutrinos. Limits shown in Table 3.3 are extracted in this manner and are compared alongside representative best limits from other LV searches across various fields of physics. A comprehensive list of LV test is available in Reference [68].

Unlike previous analyses, this analysis is also done taking into account both the diagonal and non-diagonal terms in the SME operator, $\mathring{c}^{(d)}_{\mu\mu}$, $\mathrm{Re}(\mathring{c}^{(d)}_{\mu\tau})$ and $\mathrm{Im}(\mathring{c}^{(d)}_{\mu\tau})$. A scan in this parameter space is performed (and shown in Appendix A.2), however as motivated in Equation 3.10 and as shall be seen, it is convenient to translate into a spherical representation where:

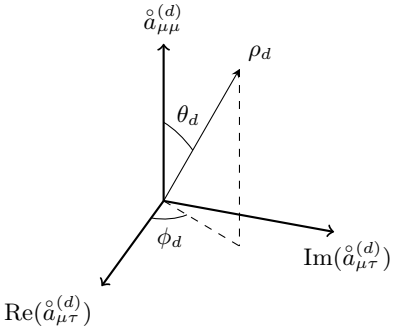

$$\rho_d \equiv \sqrt{(\mathring{a}^{(d)}_{\mu\mu})^2 + \mathrm{Re}(\mathring{a}^{(d)}_{\mu\tau})^2 + \mathrm{Im}(\mathring{a}^{(d)}_{\mu\tau})^2}$$
$$\cos(\theta_d) \equiv \mathring{a}^{(d)}_{\mu\mu}/\rho_d$$
$$\tan(\phi_d) \equiv \mathrm{Im}(\mathring{a}^{(d)}_{\mu\tau})/\mathrm{Re}(\mathring{a}^{(d)}_{\mu\tau})$$

Figure 3.8: Spherical representation of the SME paremeters.

and similar for the $\mathring{c}^{(d)}$ operators. Here, ρ_d represents the strength of LV, $\cos(\theta_d)$ represents the fraction of diagonal terms and $\tan(\phi_d)$ represents the phase of the off-diagonal element.

By probing this three dimensional space, this analysis will probe all parameter correlations, allowing for certain combinations of parameters to be unconstrained. Figure 3.10 shows the exclusion regions obtained for dimensions $d = 3, 4, 5, 6, 7, 8$ in the space of ρ_d, $\cos(\theta_d)$ for a slice in ϕ_d. The three dimensional exclusion regions are shown in Appendix A.2. These exclusion regions exhibit a very weak dependence on the ϕ_d parameter as the complex phase of the off-diagonal is not important at high energies (see Equation 3.10). Here, the conventional limit can be taken as the left most point of the $\cos(\theta_d) = 0$ plane, the point at which this search is maximally sensitive. The rest of the phase space has not been traditionally explored. This can be seen to be important near $\cos\theta_d = \pm 1$, where LV is dominated by the large diagonal element. This diagonal LV field dominates the effective Hamiltonian, surpressing neutrino flavour transitions. Thus, the unshaded regions below and above the exclusion region are very difficult to constrain with terrestrial experiments. At the right most edge, the exclusion region is limited by fast LV-induced oscillations that surpress the flux but lead to no shape distortion, similar to as is seen for standard oscillation with very large oscillation lengths (see Section 1.2). This can be constrained only by the absolute normalisation of the atmospheric neutrino flux. In the case of the dimension-three operator, the right edge can be excluded by other atmospheric neutrino oscillation measurements [107, 108].

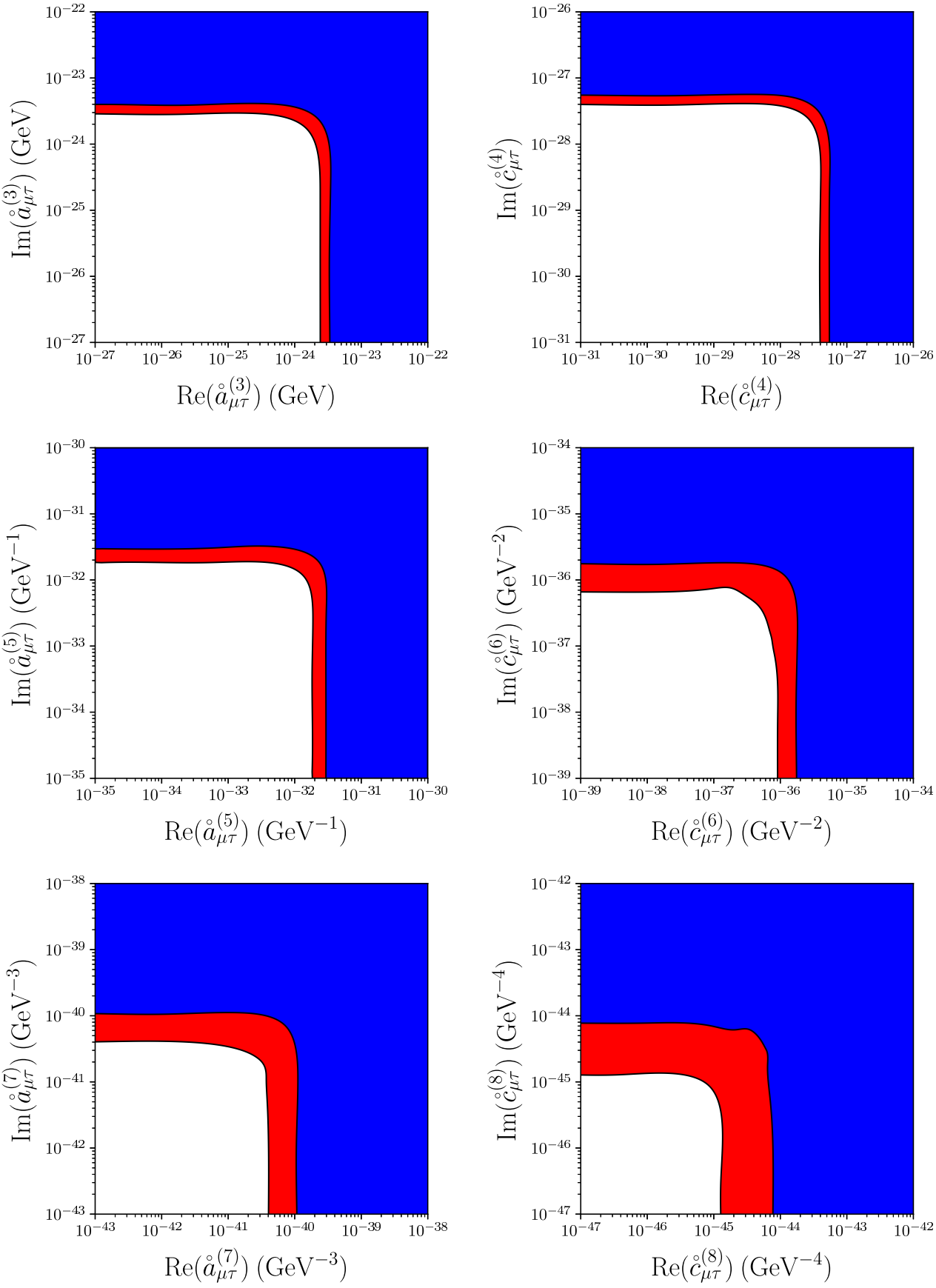

Figure 3.9: Exclusion region assuming only off-diagonal parameters are non-zero. The dimension of the operator d increases from 3 to 8 in these plots, from left to right, and top to bottom. The red (blue) regions are excluded with 90% (99%) confidence.

Dimension	Method	Type	Sector	Limits	Reference
3	CMB polarization	astrophysical	photon	$\sim 10^{-43}$ GeV	[78]
	He-Xe comagnetometer	tabletop	neutron	$\sim 10^{-34}$ GeV	[82]
	torsion pendulum	tabletop	electron	$\sim 10^{-31}$ GeV	[84]
	muon g-2	accelerator	muon	$\sim 10^{-24}$ GeV	[85]
	neutrino oscillation	atmospheric	neutrino	$\lvert\mathrm{Re}(\mathring{a}^{(3)}_{\mu\tau})\rvert, \lvert\mathrm{Im}(\mathring{a}^{(3)}_{\mu\tau})\rvert$ $< 2.9 \times 10^{-24}$ GeV (99% CL) $< 2.0 \times 10^{-24}$ GeV (90% CL)	this work
4	GRB vacuum birefringence	astrophysical	photon	$\sim 10^{-38}$	[79]
	Laser interferometer	LIGO	photon	$\sim 10^{-22}$	[80]
	Sapphire cavity oscillator	tabletop	photon	$\sim 10^{-18}$	[77]
	Ne-Rb-K comagnetometer	tabletop	neutron	$\sim 10^{-29}$	[83]
	trapped Ca^+ ion	tabletop	electron	$\sim 10^{-19}$	[86]
	neutrino oscillation	atmospheric	neutrino	$\lvert\mathrm{Re}(\mathring{c}^{(4)}_{\mu\tau})\rvert, \lvert\mathrm{Im}(\mathring{c}^{(4)}_{\mu\tau})\rvert$ $< 3.9 \times 10^{-28}$ (99% CL) $< 2.7 \times 10^{-28}$ (90% CL)	this work
5	GRB vacuum birefringence	astrophysical	photon	$\sim 10^{-34}$ GeV^{-1}	[79]
	ultra-high-energy cosmic ray	astrophysical	proton	$\sim 10^{-22}$ to 10^{-18} GeV^{-1}	[81]
	neutrino oscillation	atmospheric	neutrino	$\lvert\mathrm{Re}(\mathring{a}^{(5)}_{\mu\tau})\rvert, \lvert\mathrm{Im}(\mathring{a}^{(5)}_{\mu\tau})\rvert$ $< 2.3 \times 10^{-32}$ GeV^{-1} (99% CL) $< 1.5 \times 10^{-32}$ GeV^{-1} (90% CL)	this work
6	GRB vacuum birefringence	astrophysical	photon	$\sim 10^{-31}$ GeV^{-2}	[79]
	ultra-high-energy cosmic ray	astrophysical	proton	$\sim 10^{-42}$ to 10^{-35} GeV^{-2}	[81]
	gravitational Cherenkov radiation	astrophysical	gravity	$\sim 10^{-31}$ GeV^{-2}	[87]
	neutrino oscillation	atmospheric	neutrino	$\lvert\mathrm{Re}(\mathring{c}^{(6)}_{\mu\tau})\rvert, \lvert\mathrm{Im}(\mathring{c}^{(6)}_{\mu\tau})\rvert$ $< 1.5 \times 10^{-36}$ GeV^{-2} (99% CL) $< 9.1 \times 10^{-37}$ GeV^{-2} (90% CL)	this work
7	GRB vacuum birefringence	astrophysical	photon	$\sim 10^{-28}$ GeV^{-3}	[79]
	neutrino oscillation	atmospheric	neutrino	$\lvert\mathrm{Re}(\mathring{a}^{(7)}_{\mu\tau})\rvert, \lvert\mathrm{Im}(\mathring{a}^{(7)}_{\mu\tau})\rvert$ $< 8.3 \times 10^{-41}$ GeV^{-3} (99% CL) $< 3.6 \times 10^{-41}$ GeV^{-3} (90% CL)	this work
8	gravitational Cherenkov radiation	astrophysical	gravity	$\sim 10^{-46}$ GeV^{-4}	[87]
	neutrino oscillation	atmospheric	neutrino	$\lvert\mathrm{Re}(\mathring{c}^{(8)}_{\mu\tau})\rvert, \lvert\mathrm{Im}(\mathring{c}^{(8)}_{\mu\tau})\rvert$ $< 5.2 \times 10^{-45}$ GeV^{-4} (99% CL) $< 1.4 \times 10^{-45}$ GeV^{-4} (90% CL)	this work

Table 3.3: Comparison of attainable best limits of SME operators in various fields shown with limits in this work at 90%/99% confidence level (CL).

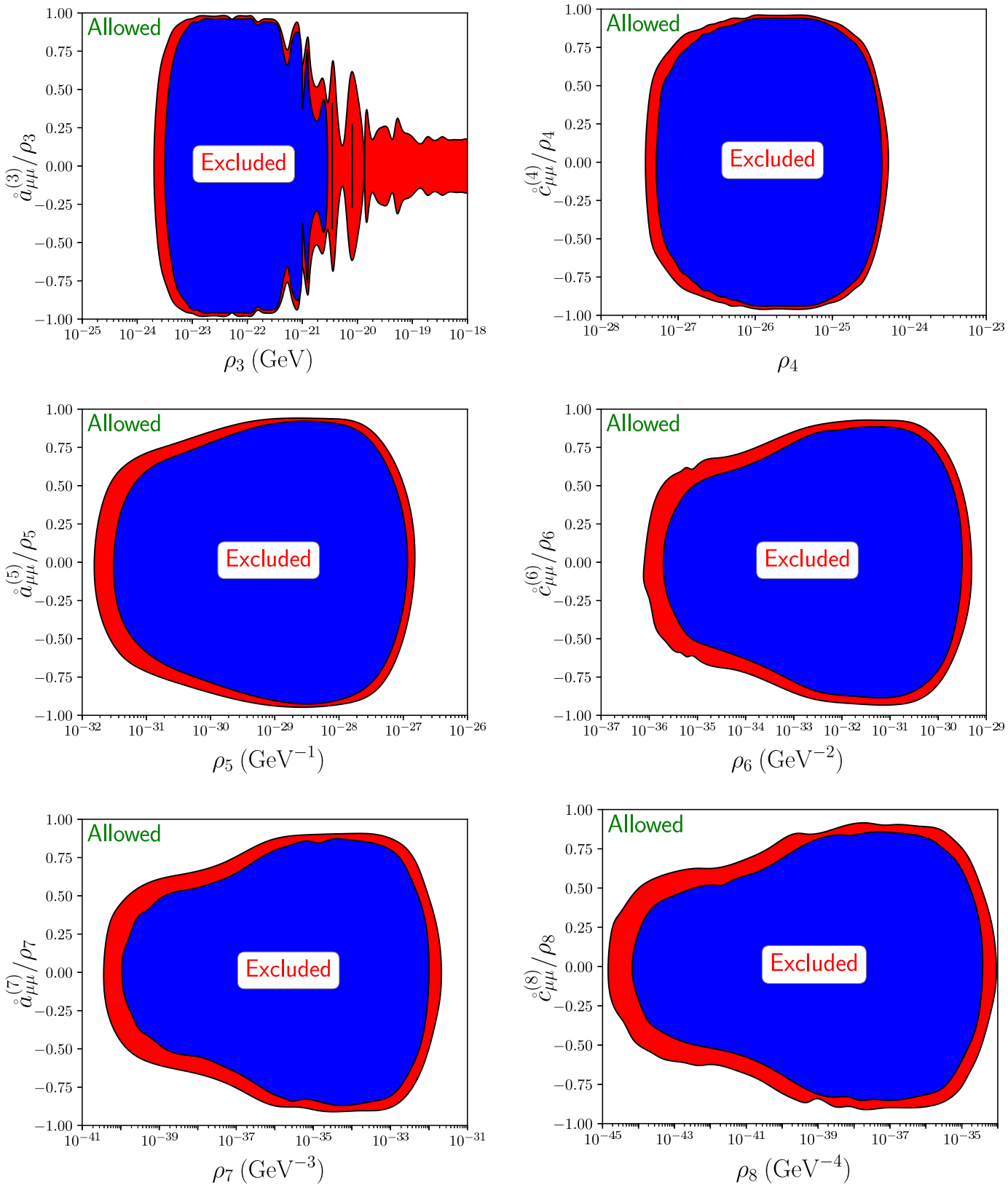

Figure 3.10: Exclusion regions in the space of two parameters: ρ_d and either $\mathring{c}^{(d)}_{\mu\mu}/\rho_d$ (odd d) or $\mathring{a}^{(d)}_{\mu\mu}/\rho_d$ (even d), which are a combination of the three SME operators. The dimension of the operator d increases from 3 to 8 in these plots, from left to right, and top to bottom. The red (blue) regions are excluded with 90% (99%) confidence.

3.3.1 Discussion

The limits obtained in this analysis are highly competitive as shown in Table 3.3. For the dimension-three and -four operators, the searches are conducted using mainly photons [77, 80], nucleons [82, 83] and charged leptons [84–86]. Going beyond terrestrial experiments, limits arising from astrophysical observations provide strong constraints [78, 79]. Among the variety of limits coming from the neutrino sector, the attainable best limits are dominated by atmospheric neutrino oscillation analyses [107, 109, 110], where the longest propagation length and the highest energies enable one to use neutrino oscillations as the biggest interferometer on Earth. The results from this analysis surpass past ones due to higher statistics of high-energy atmospheric neutrinos and the improved control of systematic uncertainties.

Searches of dimension-six and higher SME operators are dominated by astrophysical observations [79, 81, 87]. Among them, ultrahigh-energy cosmic rays (UHECR) have the highest measured energies [111] and are used to set the strongest limits on dimension-six and higher operators [81]. However, these limits are sensitive to the composition of UHECR, which is currently uncertain [69, 112]. These limits assume that the cosmic rays at the highest energies are protons, but if they are in fact iron nuclei, then the UHECR limits are significantly degraded. This analysis sets the most stringent limits in an unambiguous way across all fields for the dimension-six operator. Such high-dimension operators are generic signatures of new physics [113]. For example, the dimension-five operator is an attractive possibility to produce neutrino masses, and dimension-six operators represent new physics interactions that can, for example, mediate proton decay. Although the LV dimension-six operator is well motivated by certain theories [66, 67], it has so far not been probed with elementary particles due to the lack of available high-energy sources. Thus, this work pushes boundaries of new physics beyond the standard model and general relativity.

3.3.2 Bayesian approach

A Bayesian analysis is also performed to show consistency between statistical treatments. The dimension-six results will be compared. Details of this approach are outlined in Section 3.2.5. Exclusion regions will be drawn similar to the above; however, the interpretation here will be as exclusion region with 90%/99% credibility instead of confidence, as discussed in Section 3.2.5. The posterior distribution will be obtained by sampling it using MCMC techniques as described in Section 3.2.6. An important aspect of consideration in this Bayesian approach is the definition of the priors. A flat prior will be used for each of the SME elements in the space of ρ_6, $\cos(\theta_6)$ and ϕ_6 (see Figure 3.8 for definitions). The priors on the nuisance parameters will be set according to Table 3.1, except for N_{prompt} in which a weak Gaussian prior centered at a value of 0 with an error of 0.8 ERS units [92] is introduced, as the marginal distribution for this parameter was seen to have a large tail extending to non-physical values of N_{prompt}. For the LV strength, ρ_6, boundaries are chosen conservatively such that the lower boundary is expected to be equivalent to the null hypothesis of zero LV for each dimensional operator. Priors are summarised in Table 3.4.

The EMCEE MCMC software package [114] will be employed for parameter estimation, from which the credible exclusion regions will be drawn. This particular MCMC uses an affine invariant MCMC algorithm which defines the proposal distribution by using information on already-drawn samples of the posterior, which it does by defining an ensemble

Parameter	Symbol	Prior
LV strength dimension 6	ρ_6	Flat: $10^{-38} \to 10^{-27}\,\text{GeV}^{-2}$
Fraction of diagonal	$\cos(\theta_d)$	Flat: $-1 \to 1$
Non-diagonal phase	ϕ_d	Flat: $-\pi/2 \to \pi/2$
Conventional flux normalisation	N_{conv}	Gaussian: $1 \pm 40\% \in 0.1 \to 5$
Prompt flux normalisation	N_{prompt}	Gaussian: $0 \pm 0.8\,\text{ERS} \in 0 \to 20$
Astrophysical flux normalisation	N_{astro}	Flat: $0 \to 100$
Ratio of pion to kaon production	$R_{\pi/K}$	Gaussian: $1 \pm 10\% \in 0 \to 2$
Cosmic ray spectral index change	$\Delta\gamma_{\text{CR}}$	Gaussian: $0 \pm 0.05 \in -1 \to 1$
Astrophysical spectral index change	$\Delta\gamma_{\text{astro}}$	Flat: $-0.5 \to +0.5$

Table 3.4: Priors used for each parameter in the Bayesian approach for the dimension-six operator.

of chains running in parallel instead of just a single chain. Once the posterior distribution is obtained it can be marginalised (integrated) over to obtain the joint distribution for any parameter(s). The joint distribution over any two parameters can be shown in order to understand correlations between two parameters. Figure 3.12 shows this for the dimension-six operator and Figure 3.13 for the null case. Here, the non-diagonal plots show joint distributions between two parameters, labelled on the x- and y-axis and the diagonal plots show the marginalised distributions for each parameter, as labelled on the x-axis. The blue (light blue) shows the 90% (99%) credibility intervals. The joint posterior over ρ_d and $\cos(\theta_d)$ can then be used to form the exclusion region as shown for the dimension-six operator in Figure 3.11 in light green.

So far, the exclusion regions have been drawn using parameter estimation techniques such that these regions form the credible intervals from the data that the true value of the parameter does not lie within this region with some probability. However, these regions do not say anything with relation to the null hypothesis of no LV. Another type of exclusion region can also be constructed by way of a hypothesis test as described in Section 3.2.5. The evidence, $\mathcal{Z}$, is calculated for many points in ρ_d, $cos(\theta_d)$ space and also in the null case of no LV. By doing the ratio of these evidences with respect to the null evidence, a grid of Bayes factors, $B = \mathcal{Z}_0/\mathcal{Z}_1$, above some threshold can be used to construct another type of exclusion region. This exclusion region has the interpretation of being the region of model (hypothesis) space in which there is large evidence for the null model (hypothesis) $\mathcal{M}_0$ compared to the evidence at that point under $\mathcal{M}_1$. Here, Jeffreys' scale will be used as the convention for the threshold criteria, as shown in Table 3.2. Then, the exclusion region can be formed when the evidence for the null model is above a very strong strength-of-evidence, $B \geq 10^{3/2}$, as is overlaid for the dimension-six operator in Figure 3.11 in dark green. In order to calculate the evidences at each point, the MultiNest software package [115] is used, which is another type of MCMC which uses a nested sampling algorithm, developed specifically for the calculation of the evidence for a particular model.

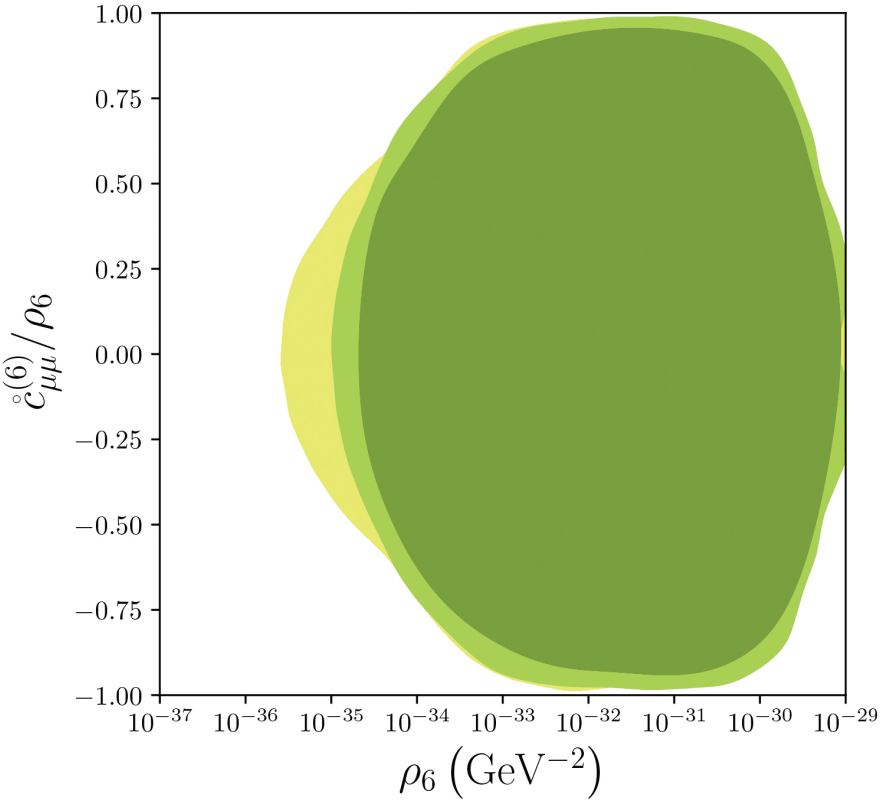

Figure 3.11: Dimension-six operator results from the Bayesian approach for the dimension-six operator elements. The light green area represents the excluded region with a 99% credibility. The yellow area shows the case in which the posterior is profiled over the nuisance parameters instead of marginalised. The dark green area corresponds to a region with a very strong strength-of-evidence for the null hypothesis, Bayes factor $B \geq 10^{3/2}$.

The exclusion region can be seen to be complementary to the ones formed using the classical approach, however it can also be seen there are differences in the left most region of the exclusion zone. This is due to the different interpretation of the exclusion region and different treatment of the systematics as described in Section 3.2.5. This can be seen as the yellow region in Figure 3.11 which shows the exclusion region that would be obtained by instead profiling over the nuisance parameters rather than marginalising.

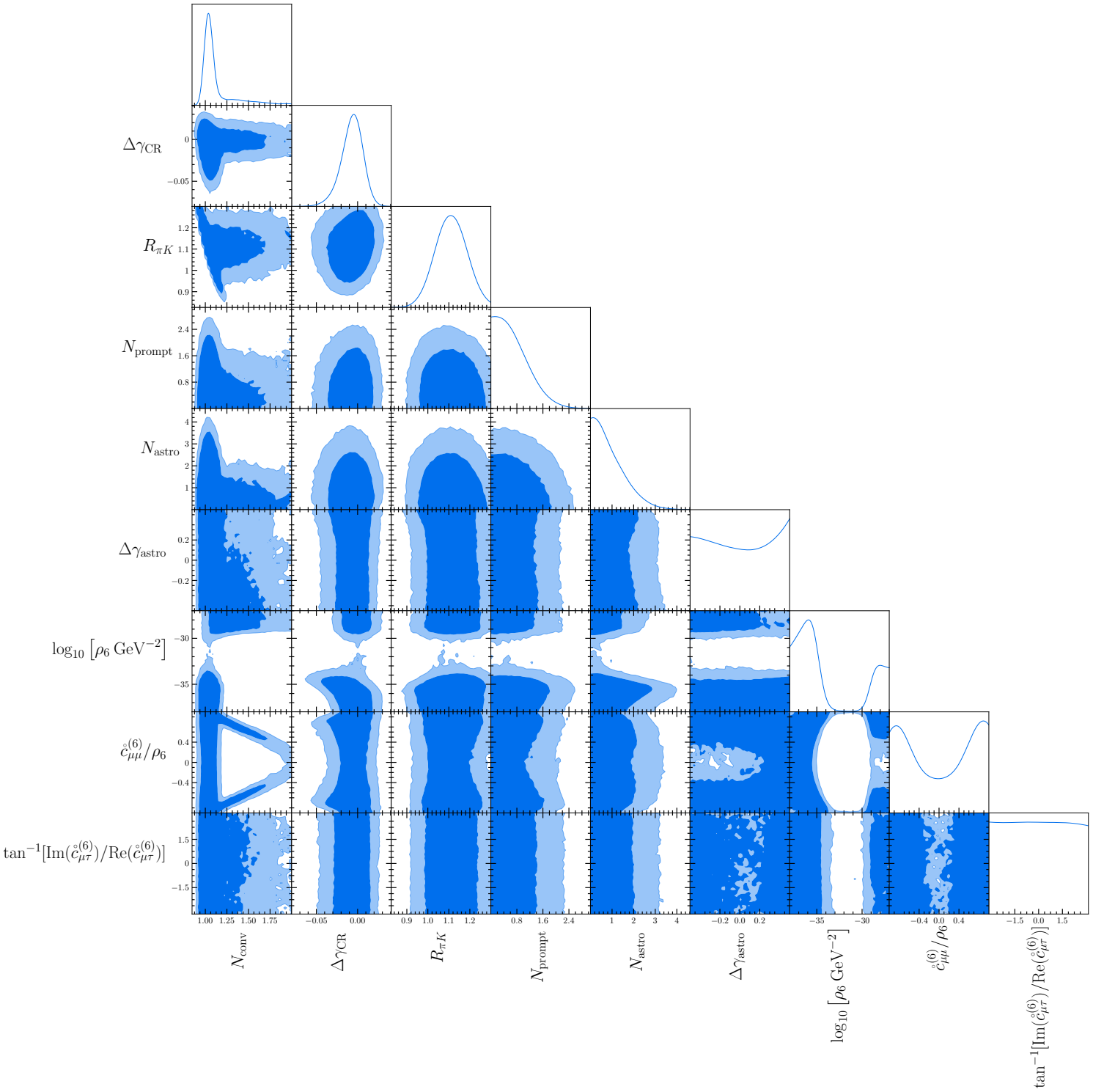

Figure 3.12: Joint posterior distributions for the various nuisance parameters and SME elements for the dimension-six operator. Here, the non-diagonal plots show joint distributions between two parameters, labelled on the x- and y-axis and the diagonal plots show the marginalised distributions for each parameter, as labelled on the x-axis. The blue (light blue) shows the 90% (99%) credibility intervals.

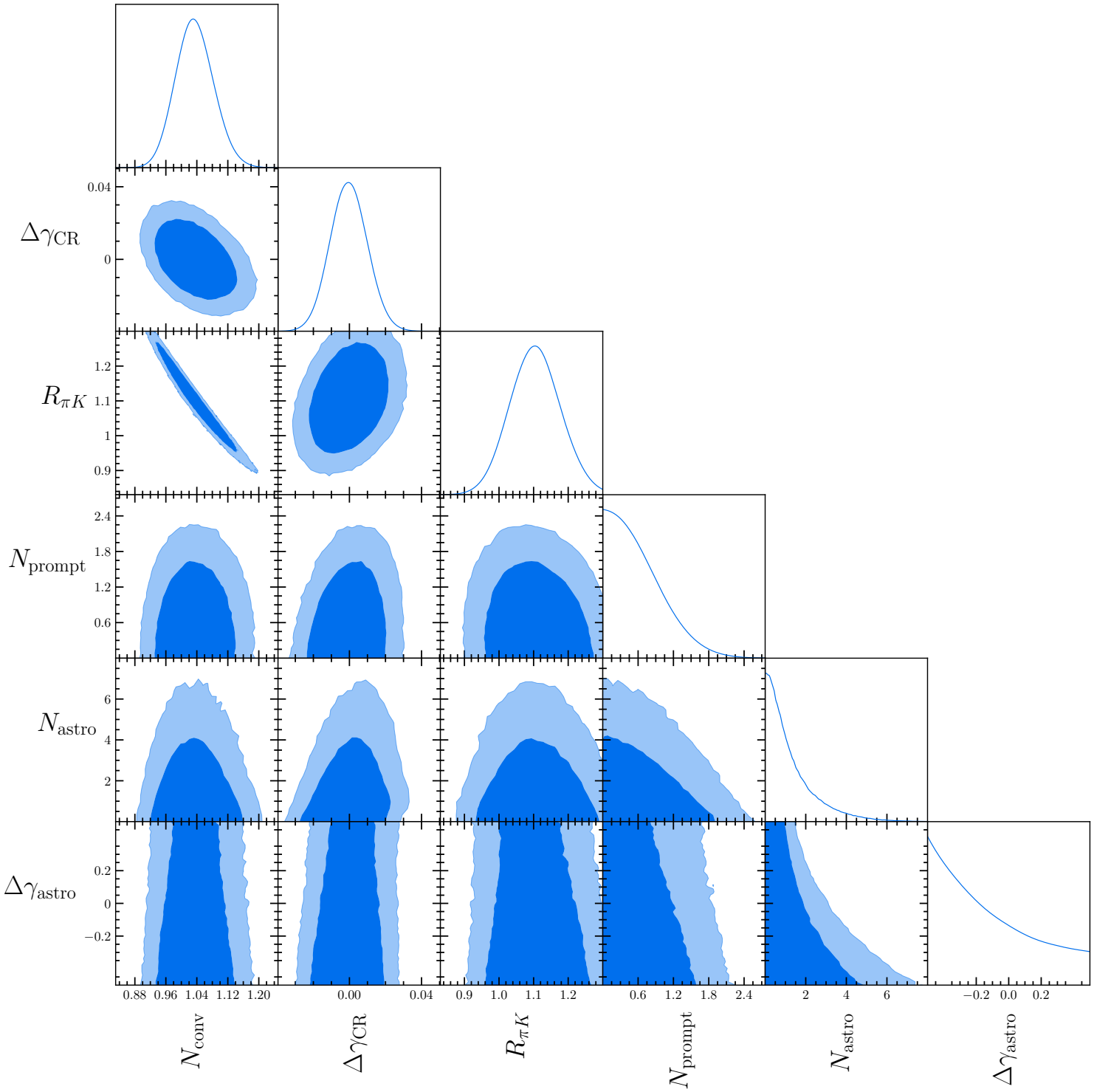

Figure 3.13: Joint posterior distributions for the various nuisance parameters in the case of no LV effects. Here, the non-diagonal plots show joint distributions between two parameters, labelled on the x- and y-axis and the diagonal plots show the marginalised distributions for each parameter, as labelled on the x-axis. The blue (light blue) shows the 90% (99%) credibility intervals.

3.3.3 Other checks

To confirm that this analysis gets its power from the highest energy atmospheric neutrinos, the exclusion region was redrawn implementing a further cut of 2×10^3 on the maximum muon proxy energy (from 18×10^3 see Section 3.2.1). The result for the dimension-six operator is shown in Figure 3.14. As can be seen, the limit which can be obtained suffers when compared to Figure 3.10. Indeed, the highest energy neutrinos provide the best limits in this analysis.

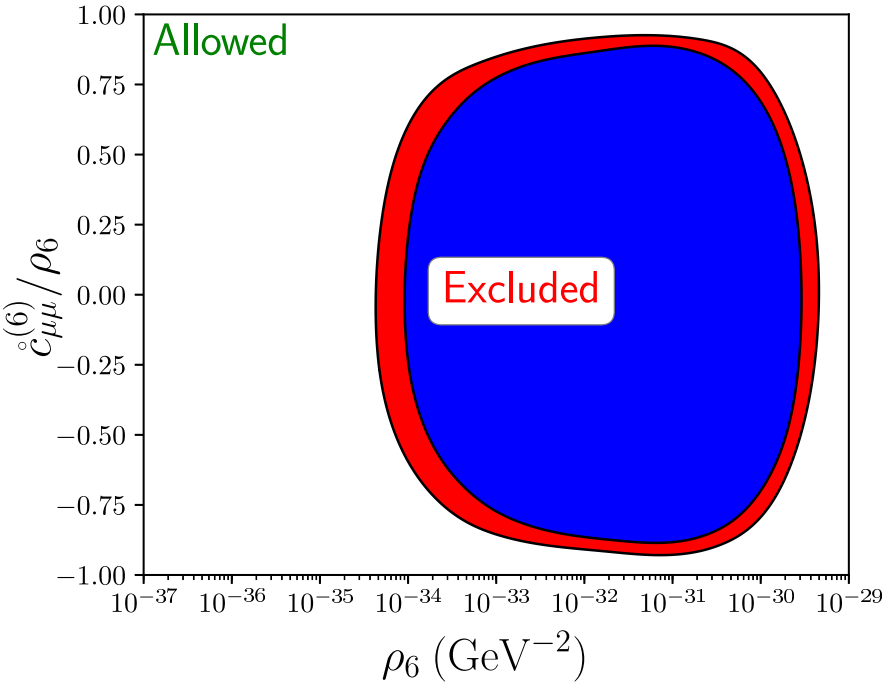

Figure 3.14: Exclusion region for the dimension-six SME operator using a subset of data with a maximum muon proxy energy of 2×10^3.

Another point to note is on the applicability of Wilks' theorem when drawing the confidence intervals in the classical statistical approach (see Section 3.2.4). The test statistic (TS) distribution is approximated as a χ^2 with number of degrees of freedom equal to three, i.e. the three SME elements for each dimensional operator: ρ_d, $\cos(\theta_d)$ and $\tan(\phi_d)$. However, as was motivated in Equation 3.10 and shown in the previous section, there is a very weak dependence on $\tan(\phi_d)$ meaning that the effective number of degrees of freedom is not equal to three. An ensemble of realisations was generated and for each one the TS, λ, was computed. Figure 3.15 shows the distribution of $-2\ln\lambda$, with statistical errors related to the number of generated realisations. Also shown are the χ^2 distributions for two degrees

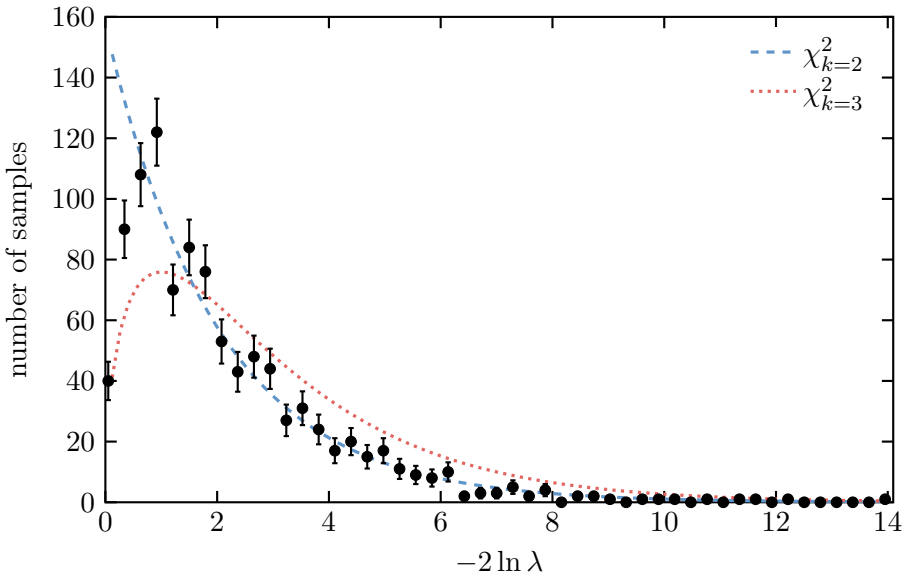

Figure 3.15: Distribution of $-2\ln\lambda$ where λ is the test statistic. Also shown are χ^2 distributions for $k = 2$ degrees of freedom and $k = 3$ degrees of freedom.

of freedom, $\chi^2_{k=2}$, and three degrees of freedom, $\chi^2_{k=3}$. From this, it can be seen that the TS distributions fits somewhere between $k = 2$ and $k = 3$. In this analysis, a conservative approach is taken by using $k = 3$ in order to derive the confidence intervals, and therefore the limits.

3.3.4 Conclusion

The analysis carried out here presents a test of LV with high-energy atmospheric muon neutrinos from IceCube. Correlations of the SME elements are fully taken into account, and systematic errors are controlled by the fit. Although no evidence of LV was found, this analysis provides the best attainable limits on SME elements in the neutrino sector along with limits on higher-order operators. Comparison with limits from other sectors reveals that this work provides the best attainable limits on dimension-six elements across all fields: from tabletop experiments to cosmology. This is a remarkable point that demonstrates how powerful neutrino interferometry can be in the study of fundamental spacetime properties.

Potential improvements on the search for LV in the neutrino sector using IceCube may be possible when the astrophysical neutrino sample is used, as will be discussed in Chapter 4.

4 Search for Quantum Gravity with Astrophysical Neutrinos

The existence of high-energy astrophysical neutrinos has been confirmed by the IceCube Neutrino Observatory [38, 56], revealing a new window into the study of high-energy cosmic ray production mechanisms as well as offering a unique opportunity to study fundamental neutrino properties in an entirely new regime [116, 117]. Figure 4.1 shows the landscape of neutrino physics up to the highest possible energies. So far, terrestrial and sub-TeV neutrinos have failed to find clear evidence of new physics. Astrophysical neutrinos are, however, a fitting yet relatively unexplored probe for new physics as they extend beyond the TeV scale with energies as high as ultra-high-energy cosmic rays. Furthermore, the propagation of astrophysical neutrinos from the source is well understood (see Section 1.3.2); therefore, new physics effects can be spotted more easily than for other charged particles. Neutrino mixing can also be a powerful probe of new physics as seen in Chapter 3. This is enhanced even further here as astrophysical neutrinos come from extragalactic sources located at cosmological distances, therefore even tiny new physics effects can accumulate to produce observable differences in the neutrino flavour composition as measured on Earth [118–141]. Following directly from the analysis and motivations in Chapter 3 which utilised atmospheric neutrino data, this chapter presents a general search for new physics by probing for modifications in the astrophysical neutrino flavour data at IceCube.

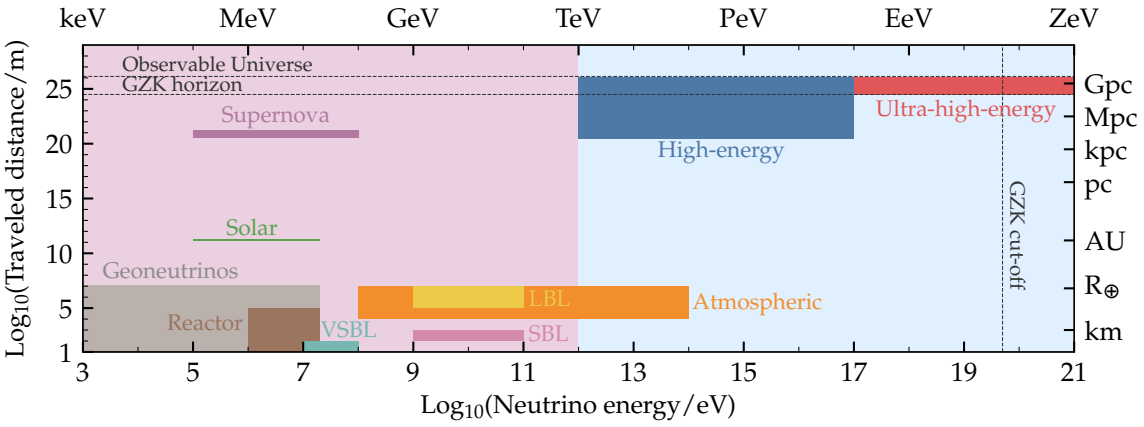

Figure 4.1: The neutrino landscape up to ultra-high-energy scales [116].

4.1 Phenomenology

Even though the production mechanism of astrophysical neutrinos is still unknown, it may still be possible to use them as a tool to find evidence of new physics. The initial composition of the neutrino flavour states are determined by the details of the production process as described in Section 1.3.2. In the standard oscillation scenario, for any given initial flavour composition (also called flavour ratio), the observed flavour composition lies in a well-defined region close to the democratic composition of $f_{\alpha,\oplus} = 1/3$, i.e. $(1:1:1)_\oplus$, shown as the hatched region in Figure 1.10. Therefore, a measured flavoured composition not consistent with this expectation can be interpreted as evidence for new physics.

4.1.1 New physics framework

The new physics framework adopted here is a general approach motivated by the Standard Model Extension (see Section 3.1.1). New effective operators are introduced in the standard three neutrino scenario with unitary evolution following the prescription outlined in Reference [131]. The effective Hamiltonian in the flavour representation can be written as a series expansion of these new effective operators:

$$H_{\text{eff}} = \frac{1}{2E} U M^2 U^\dagger + \sum_{d \geq 3} \frac{E^{d-3}}{\Lambda_d} \tilde{U}_d \, O_d \, \tilde{U}_d^\dagger \tag{4.1}$$

The first term is from the standard three-neutrino Hamiltonian (see Section 1.2) and notably it decreases with energy. Then d is the dimension of the new physics operator, O_d is a diagonal matrix proportional to the "mass" of the operator, $\tilde{U}_d$ is a unitary new physics mixing matrix and Λ_d sets the scale at which new physics enters. In this analysis, O_d is fixed to $\text{diag}\,(0, 1/100, 1)$, similar to the scalings of the standard mass matrix. Also, it is assumed that one of the new physics operators of a given dimension d dominates the effective Hamiltonian at a particular energy scale. Therefore, the effective Hamiltonian takes the following form:

$$H_d = \frac{1}{2E} U M^2 U^\dagger + \frac{E^{d-3}}{\Lambda_d} \tilde{U}_d \, O_d \, \tilde{U}_d^\dagger \tag{4.2}$$

IceCube can detect very-high-energy astrophysical neutrinos with energies ranging from ~ 50 TeV to a few PeV, allowing access to the highest dimensional operators where an enhancement from the terms with dimension greater than four is expected. Typically the sensitivity to new physics is at the order $\Lambda_d \sim E^{d-2}/M^2$ which for higher dimensional operators, gives a sensitivity at the order of the Planck scale, $1/M_P^{d-4}$, where quantum gravity (QG) effects are expected to appear.

4.1.2 New physics in the astrophysical neutrino flavour

Similar to the procedure in Sections 1.2.2, 3.1.2, by diagonalising the effective Hamiltonian, the effective mass matrix Δ_d can be constructed with respect to H_d through the unitary effective mixing matrix $V_d(E)$:

$$H_d = V_d^\dagger(E)\, \Delta_d\, V_d(E) \tag{4.3}$$

This diagonalisation is computed analytically using the Cardano equation [89, 107]. Now the transition probability from flavour state $|\nu_\alpha\rangle$ to $|\nu_\beta\rangle$ can be written as a modification to the standard decoherent mixing as derived in Equation 1.41 by substituting $U \to V_d(E)$:

$$P^{(d)}_{\nu_\alpha \to \nu_\beta}(E) = \sum_i |V_{\alpha i,\, d}(E)|^2\, |V_{\beta i,\, d}(E)|^2 \tag{4.4}$$

where the probability only depends on the effective mixing matrix $V_d(E)$. Using the probability given in this equation and the flux at production $\phi_{\alpha,\mathrm{S}}$, the measured neutrino flux on Earth $\phi_{\beta,\oplus}$ can be calculated. The astrophysical neutrino flux is typically a spectrum over energy, therefore is convenient to define the energy averaged flux composition as:

$$\bar{\phi}^{(d)}_{\beta,\oplus} = \frac{1}{|\Delta E|} \int_{\Delta E} \sum_\alpha P^{(d)}_{\nu_\alpha \to \nu_\beta}(E)\, \phi_{\alpha,\mathrm{S}}(E)\, \mathrm{d}E \tag{4.5}$$

Finally the measured flavour composition can be can be written as $f^{(d)}_{\beta,\oplus} = \bar{\phi}^{(d)}_{\beta,\oplus} / \sum_\gamma \bar{\phi}^{(d)}_{\gamma,\oplus}$. This analysis will fix the source flavour composition to be one from the standard astrophysical source scenarios discussed in Section 1.3.2, namely the set of models with source flavour compositions $(x : 1-x : 0)_\mathrm{S}$. Compositions with a ν_τ source component are not expected in standard astrophysics scenarios. The study of new physics in the production processes at the source can also be done using the astrophysical neutrino flavour [142];

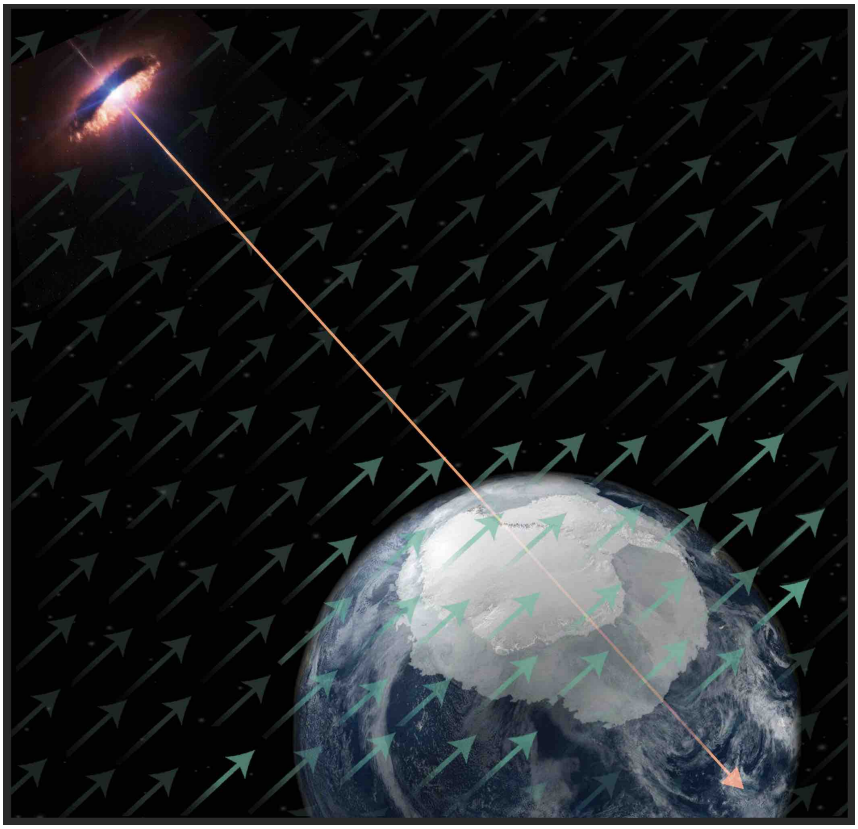

Figure 4.2: Astrophysical neutrinos are emitted from distant high-energy objects. Neutrino propagation may be affected by new spacetime effects, or more specifically any additional interactions which exist in the vacuum modifies neutrino mixings from the standard case.

however, in this analysis new physics is assumed to arise only in the propagation of the neutrinos to Earth. An illustration of the idea of this analysis is shown in Figure 4.2.

This analysis therefore uses a more general framework than that used for the atmospheric neutrino analysis in Chapter 3, which modelled effects of isotropic Lorentz and CPT violation. The framework here remains agnostic about the new physics interpretation and can be used to represent new physics such as Lorentz and CPT violation [72], dark energy [140], non-standard interactions [125] and other exotic models [116, 117]. There are models which this framework does not consider however. First, lepton number is assumed to be conserved and models such as neutrino-antineutrino mixing are not considered. Second, neutrino decay models which violate unitary evolution are not considered as are discussed elsewhere [143]. Similarly, models with sterile neutrino states are not considered [141, 144].

4.1.3 New physics texture

The accessible regions of measured flavour composition with new physics for a dimension d operator, $f^{(d)}_{\beta,\oplus}$, can be displayed on ternary diagram, as described in Section 1.3.2. Here, the new physics mixing matrix $\tilde{U}_d$ is constrained by unitarity, therefore the accessible region in flavour space for any new physics operator is enclosed by the boundaries imposed by only the source flavour composition and this unitarity condition. The coloured shaded regions in Figure 4.3 show these boundaries for the three source flavour compositions of consideration, which are indicated by the filled shapes. These boundaries are calculated numerically following from Reference [145]. The distribution of the coloured points represent the posterior probability distributions in measured flavour space for each respective source composition (see Section 4.2.5 for more). The 68% and 90% credibility intervals (C.I.) are shown as the grey shaded regions for the astrophysical neutrino data set under analysis here (see Section 4.2.1 for more).

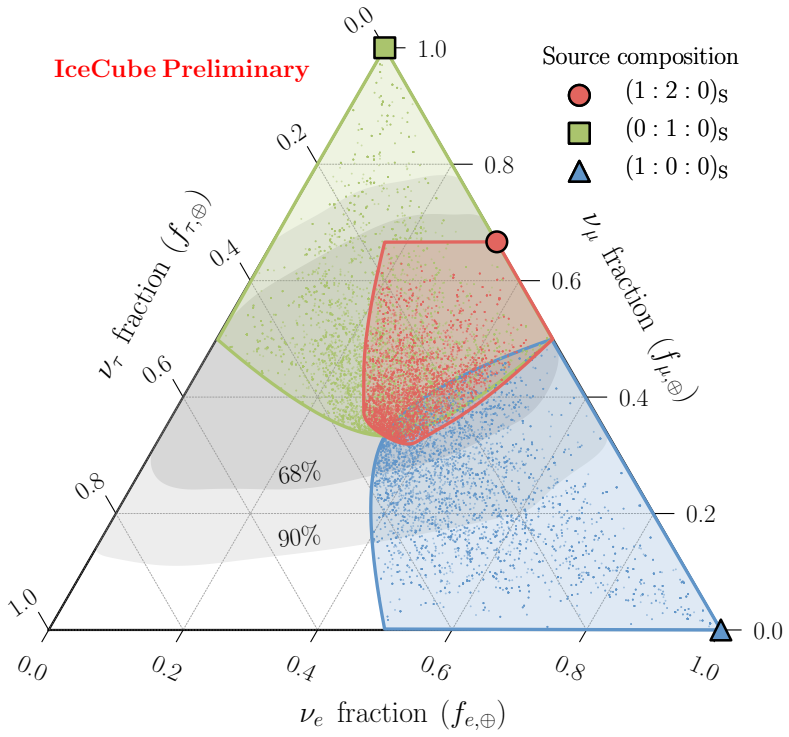

Figure 4.3: Unitary bounds of astrophysical neutrino flavours for three source flavour compositions indicated by the filled shapes [145]. Coloured points represent the posterior probability density for each respective source flavour composition [146]. Flavour composition 68% and 90% credibility intervals from IceCube HESE 7.5yr are shown as the grey-shaded regions.

This analysis will focus on obtaining limits for two *textures* of the new physics mixing matrix $\tilde{U}_d$, chosen such that they result in measured flavour compositions lying in the region that is excluded by the data C.I. This maximises the sensitivity to new physics, as is the spirit in similar new physics searches [68]. The elements of the new physics mixing matrix $\tilde{U}_d$ are parameterised in the standard way as three mixing angles $\tilde{\theta}_{ij,\,d}$ and a phase $\tilde{\delta}_d$ (see Equation 1.15 for full definition). This analysis has no sensitivity to the phase therefore it is fixed to 0. Then, the first texture $\mathcal{O}_{e\tau}$ takes the form such that it maximises mixing between ν_e and ν_τ:

$$\tilde{\theta}_{ij,\,d} = \begin{cases} \pi/4 & \in \tilde{\theta}_{13,\,d} \\ 0 & \text{otherwise} \end{cases} \quad \Longrightarrow \quad \tilde{U}_d = \mathcal{O}_{e\tau} \equiv \begin{pmatrix} \frac{1}{\sqrt{2}} & 0 & \frac{1}{\sqrt{2}} \\ 0 & 1 & 0 \\ -\frac{1}{\sqrt{2}} & 0 & \frac{1}{\sqrt{2}} \end{pmatrix} + \mathbb{0}\, i \tag{4.6}$$

In terms of the measured flavour ratio, this texture has the effect of averaging out the compositions of the ν_e fraction and ν_τ fraction. For example, a source composition of $(1:2:0)_\text{S}$ with mixing described by this texture $\mathcal{O}_{e\tau}$ would result in a measured flavour composition of $(1:2:1)_\oplus$. Another example is $(0:1:0)_\text{S} \xrightarrow{\mathcal{O}_{e\tau}} (0:1:0)_\oplus$, in which no mixing occurs as the flux at the source is entirely composed of ν_μ. Notably, this example demonstrates a measured flavour composition that is not contained within the data C.I. The second texture $\mathcal{O}_{\mu\tau}$, takes the form such it maximises mixing between ν_μ and ν_τ:

$$\tilde{\theta}_{ij,\,d} = \begin{cases} \pi/4 & \in \tilde{\theta}_{23,\,d} \\ 0 & \text{otherwise} \end{cases} \quad \Longrightarrow \quad \tilde{U}_d = \mathcal{O}_{\mu\tau} \equiv \begin{pmatrix} 1 & 0 & 0 \\ 0 & \frac{1}{\sqrt{2}} & \frac{1}{\sqrt{2}} \\ 0 & -\frac{1}{\sqrt{2}} & \frac{1}{\sqrt{2}} \end{pmatrix} + \mathbb{0}\, i \tag{4.7}$$

This averages the measured composition of ν_μ and ν_τ such that, for example, $(1:2:0)_\text{S} \xrightarrow{\mathcal{O}_{\mu\tau}} (1:1:1)_\oplus$ or $(1:0:0)_\text{S} \xrightarrow{\mathcal{O}_{\mu\tau}} (1:0:0)_\oplus$. Notably, the latter example again demonstrates a measured composition not contained inside the data C.I.

The most general approach that could be taken here is to treat the elements in $\tilde{U}_d$ as nuisance parameters, allowing it to take on any form or texture. This would give measured compositions bound only by unitarity as shown in Figure 4.3. However, limits are not able to be obtained in such a case as the accessible phase space overlaps considerably with the data C.I. therefore experimental sensitivity is lost. This will be discussed further in Section 4.3.

4.2 Analysis Method

4.2.1 Data selection

In 2012, the discovery of a diffuse astrophysical neutrino flux was reported by IceCube using the High-Energy Starting Events (HESE) event selection [56]. The HESE event selection provides a high-purity all-flavour astrophysical neutrino data set. This analysis uses the newest iteration of HESE, extracted from 7.5 years of IceCube data taking [147]. 102 events are observed over 2635 days with 60 events above 60 TeV in deposited energy. A short summary will be given here but for more details see References [38, 147–151].

This event selection attempts to isolate astrophysical neutrinos by reducing the atmospheric background. The outer parts of the IceCube array are used as a simple anti-coincidence muon veto, requiring fewer than 3 of the first 250 photo-electrons (PE) to be on the detector boundary within a 3 μs window. This veto mechanism is demonstrated in Figure 4.4. Additionally, to ensure sufficient PE deposition for a reliable veto, only events which deposit at least 6,000 PE in the detector are selected, corresponding to deposited energies of approximately 30 TeV. This technique provides a high-purity sample of very-high-energy astrophysical neutrinos of all flavours, from which a measurement of the flavour composition can be made and will be used in this analysis to search for new physics in the propagation as described in the previous section.

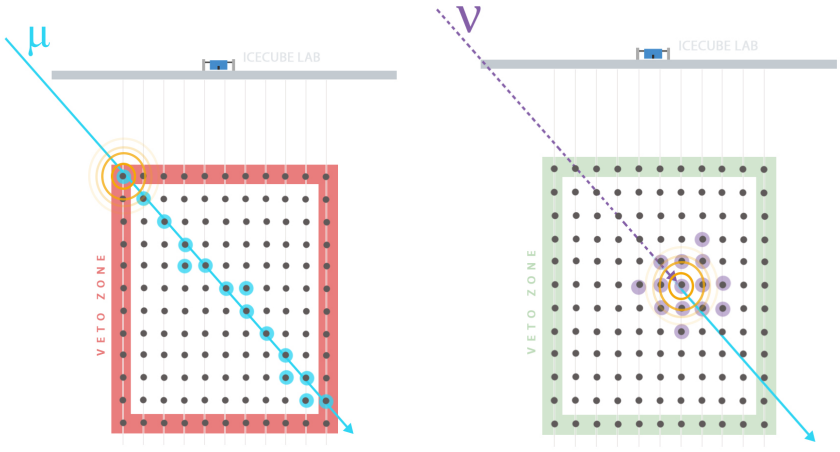

Figure 4.4: Demonstration of the HESE veto. Outer layers of the IceCube array act as an active veto against atmospheric backgrounds as shown on the left. Only events which do not trigger the veto are selected as shown on the right [152].

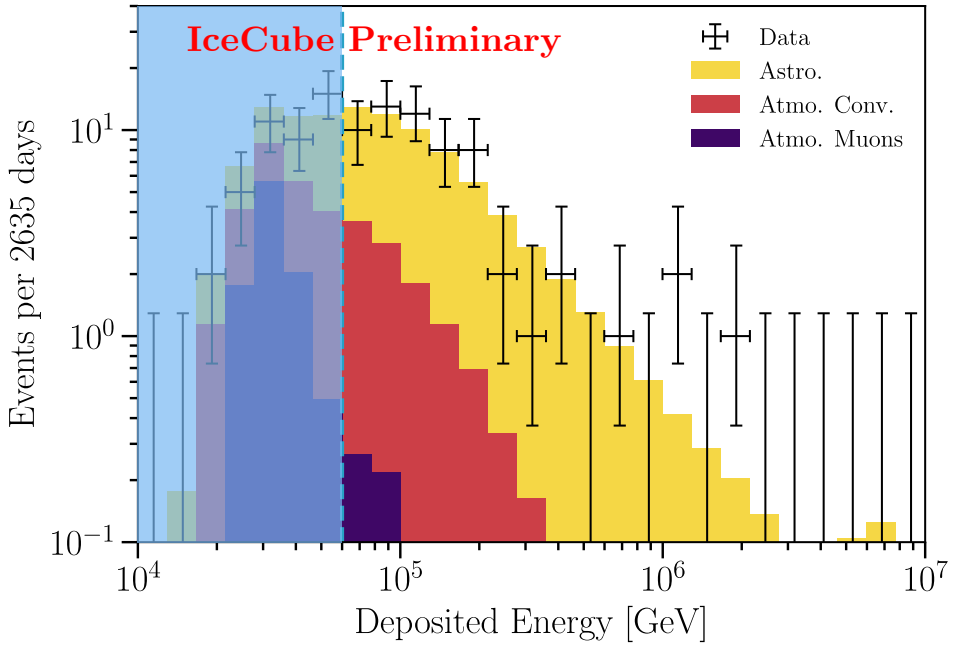

Figure 4.5: The distribution of events in reconstructed deposited energy shown as crosses, compared to the best-fit expectation distributions for a given flux component. The events below 60 TeV (light blue) are ignored in the fit [147].

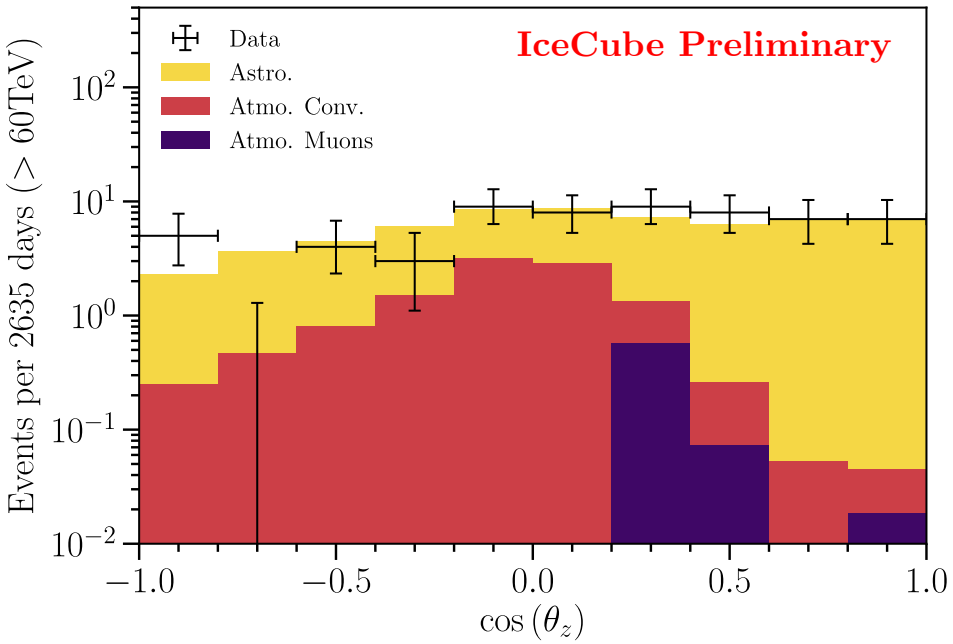

Figure 4.6: The distribution of events above 60 TeV in the cosine of the reconstructed zenith angle $\cos(\theta_z)$ shown as crosses, compared to the best-fit expectation distributions for a given flux component [147].

To reconstruct events, three separate event signature hypotheses are considered: track, cascade, and double-cascade [57, 148]. These signatures along with the energy and angular reconstruction algorithms are described in Sections 2.2 and 3.2.1. Each event is assigned a signature according to the classification algorithm described in Reference [153], which finds the signature that best describes the event. This method produces a high purity selection of tau neutrinos in the double-cascade category, and discriminates well between true cascades and tracks. Then a final cut is placed selecting only events with deposited energies above 60 TeV, resulting in 60 events classified as 42 cascades, 16 tracks and 2 double-cascades. The deposited energy and cosine zenith distributions are shown in Figures 4.5 and 4.6. Here, the astrophysical component is shown in yellow along with the atmospheric backgrounds which are comprised of contributions from conventional atmospheric neutrinos shown in red and cosmic ray induced muons shown in purple. The flavour measurement is performed with binning defined separately for tracks and cascades versus double-cascades. For tracks and cascades, 10 bins in $\cos(\theta_z)$ from -1.0 (upgoing) to 1.0 (downgoing), 20 bins in $\log(E_{\text{deposited}})$ are used from 60 TeV to 10 PeV, and for double-cascades 10 bins in $\log(L_{\text{reco}})$ from 10 m to 100 m and 20 bins in $\log(E_{\text{deposited}})$ are used again from 60 TeV to 10 PeV, where θ_z is the reconstructed zenith angle, $E_{\text{deposited}}$ is the reconstructed deposited energy, and L_{reco} is the reconstructed distance between energy depositions for double cascade signatures.

4.2.2 Simulation

In this analysis, the expected number of events in each bin given some incoming neutrino model $\Phi_{\alpha}^{\text{neutrino}}$ - for the six neutrino species - and cosmic induced muon model Φ^{muon} is computed using a Monte Carlo (MC) simulation of the full detector geometry [154]. Neutrino events and muon events are simulated separately. The HESE event selection is applied to the simulated MC and an expectation in analysis space is produced, which can then be compared to the data. Direct simulation however is impractical as most neutrinos pass through the detector without interacting. The *reweighting* technique resolves this, as well as allowing for the flexibility of changing model parameters without an entire resimulation. MC events are generated assuming a generic flux model $\Phi_{\alpha,0}^{\text{neutrino}}$, Φ_{0}^{muon} and are then forced to interact somewhere in the detector volume. The MC simulation can then be tailored to other flux models $\Phi_{\alpha}^{\text{neutrino}}$, Φ^{muon} by assigning a weight w_i to each MC

event i:

$$w_i = \begin{cases} w_i^{\text{neutrino}} = w_i^{\text{astro}} + w_i^{\text{conv}} + w_i^{\text{prompt}} & \text{for neutrinos} \\ w_i^{\text{muon}} & \text{for muons} \end{cases} \tag{4.8}$$

$$w_i^{\text{neutrino}} = P_{\text{int}} \cdot \left(\frac{\Phi^{\text{astro}}}{\Phi_0^{\text{astro}}} + \frac{\Phi^{\text{conv}}}{\Phi_0^{\text{conv}}} + \frac{\Phi^{\text{prompt}}}{\Phi_0^{\text{prompt}}} \right)_{\alpha} \cdot \frac{t_{\text{data}}}{t_{\nu\,\text{MC}}} \tag{4.9}$$

$$w_i^{\text{muon}} = P_{\text{int}} \cdot \frac{\Phi^{\text{muon}}}{\Phi_0^{\text{muon}}} \cdot \frac{t_{\text{data}}}{t_{\mu\,\text{MC}}} \tag{4.10}$$

where P_{int} is the probability for the event to occur, essentially a convolution of the interaction cross-section and the detector efficiencies. Here, the CSMS calculation [46] for the neutrino cross-section and the PREM model is used to account for Earth absorption (see Sections 1.4.1 and 3.2.2). The second term is the ratio between the flux model of interest and the neutrino flux of MC generation. The final term is the ratio of the livetime of the data with respect to the MC livetime equivalent. The expectation using the flux model of interest can be obtained by simply binning in analysis space with each event carrying a weight w_i. In this way, the effects of new physics can be probed as a modification of the measured flavour composition $\Phi_\alpha^{\text{astro}}(E_\nu) \to f_{\alpha,\oplus}^{(d)} \cdot \Phi_\alpha^{\text{astro}}(E_\nu)$, see Section 4.1.2.

The astrophysical flux $\Phi_\alpha^{\text{astro}}$ is modelled as a power law with normalisation and spectral index $\sim \Phi_\alpha E^{-\gamma}$ for each neutrino species. The atmospheric neutrino background is split into two contributions: conventional and prompt, see Section 1.3.1 for details. For the conventional and prompt neutrino fluxes, the Honda et al. model [155] and the BERSS model [156] are used, respectively. A dedicated simulation is performed for muons [157] and then weighted by the air shower simulation package CORSIKA [158]. Due to uncertainties in the muon yield of cosmic ray air showers, a data-based prior is used to constrain its normalisation and only shape information is used from the simulation.

Figure 4.7 shows the effect of new physics on the astrophysical neutrino flavour for the dimension six operator. Here, points are sampled for two scenarios: $(0:1:0)_{\text{S}}$ with a $\mathcal{O}_{e\tau}$ texture, and $(1:0:0)_{\text{S}}$ with a $\mathcal{O}_{\mu\tau}$ texture. The value of the new physics scale Λ_6^{-1} is represented by the colour of the points, with axes shown below normalised to the Planck mass. Standard mixing values are allowed to float inside the bounds given by global data fits [23] (see Table 1.1). For these two scenarios, the effect of new physics pushes the measured composition outside of the data C.I. giving power to reject such models.

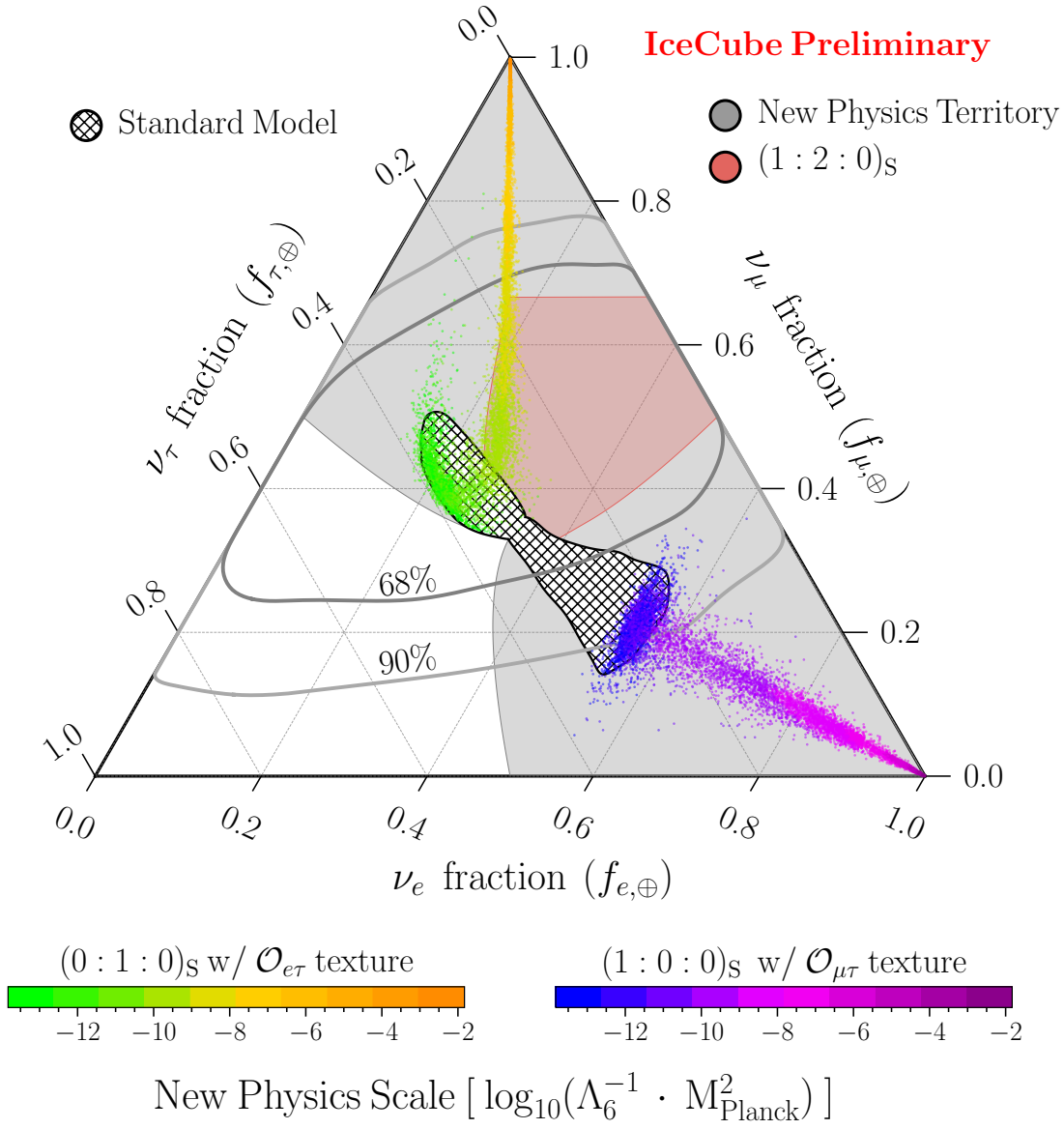

Figure 4.7: Effect of new physics on the astrophysical neutrino flavour for the dimension six operator. For a source composition of $(0:1:0)_S$ with a $\mathcal{O}_{e\tau}$ texture, as the new physics scale Λ_6^{-1} becomes large, the observed flavour composition tends to the ν_μ corner. For a source composition of $(1:0:0)_S$ with a $\mathcal{O}_{\mu\tau}$ texture, as the new physics scale Λ_6^{-1} becomes large, the observed flavour composition tends to the ν_e corner. Credibility intervals at 68% and 90% for the HESE 7.5yr are shown in grey. The hatched area shows the region in which all standard astrophysical models live. The grey shaded area shows the region accessible by new physics phenomena studied here, with the red shaded area restricting only to consider a source composition of $(1:2:0)_S$ [145].

4.2.3 Systematics

The dominant systematic uncertainties in this analysis are related to the astrophysical neutrino flux, however it should be mentioned that the limitation of this analysis is in the low statistics of astrophysical neutrino events[1]. Nevertheless, the uncertainties concerning the neutrino flux predictions must be taken into account. This is done in a very similar manner to that applied for the atmospheric LV search, see Section 3.2.3. A description of the parameters used to quantify this uncertainty will be introduced and discussed here which will then define the nuisance parameters of this analysis.

The systematic uncertainties of this data set have been studied in great detail over the last years for the characterisation of the diffuse astrophysical neutrino flux [38, 147, 148]. A similar approach will be taken here as in these analyses for the estimation of the systematic impact of the neutrino and muon flux models. The atmospheric neutrino flux can be written as:

$$\Phi_{\alpha}^{\mathrm{atm}} = N_{\mathrm{conv}} \cdot \Phi_{\alpha}^{\mathrm{conv}} + N_{\mathrm{prompt}} \cdot \Phi_{\alpha}^{\mathrm{prompt}} \tag{4.11}$$

where $\Phi_{\alpha}^{\mathrm{conv}}$ is the conventional neutrino flux and $\Phi_{\alpha}^{\mathrm{prompt}}$ is the prompt neutrinos flux. These components are discussed in detail in Section 1.3.1. The two systematic parameters introduced are the overall conventional flux normalisation N_{conv} and the overall prompt flux normalisation N_{prompt}. Note in the atmospheric LV search in Section 3.2.3, additional systematic parameters related to the cosmic ray spectral uncertainty and ratio of pions to kaons in the conventional flux were also used; however, the role of the atmospheric neutrino flux in this analysis is sub-leading therefore the normalisations introduced above are sufficient. As motivated in that section, following from Reference [96], a 40% Gaussian prior is imposed for N_{conv} with a lower bound of 0.1. A weak Gaussian prior centered at a value of 0 with an error of 2.4 BERS units [156] is used for N_{prompt} to prevent large tails extending to non-physical values, as was done in the Bayesian approach of the atmospheric LV search, see Section 3.3.1. The cosmic induced muon flux can be written as:

$$\Phi^{\mathrm{muon}} = N_{\mathrm{muon}} \cdot \phi^{\mathrm{muon}} \tag{4.12}$$

[1] The ignorance of the source production mechanism is another significant limitation for a more general new physics search, and for this analysis the source composition will be fixed to certain best case scenarios, see Section 4.1.3.

Here an overall normalisation systematic parameter N_{muon} is introduced. A data based prior is used to constrain N_{muon} [147, 156]. A Gaussian prior with a central value of 1 and a width of 0.5 is used. Figures 4.8a-c demonstrate the effect of the atmospheric neutrino flux and cosmic induced muon systematic parameters in the deposited energy.

The astrophysical neutrino flux model uncertainties have the most impact on this analysis and can be written as:

$$\Phi_{\alpha}^{\text{astro}} = N_{\text{astro}} \cdot \phi_{\alpha}^{\text{astro}} \cdot \left(\frac{E_{\alpha}}{100 \text{ TeV}} \right)^{-\gamma_{\text{astro}}} \tag{4.13}$$

where $\phi_{\alpha}^{\text{astro}}$ is the astrophysical neutrino flux normalisation, N_{astro} is an overall normalisation systematic parameter, and γ_{astro} is the astrophysical neutrino spectral index. As per conventions, the pivot is chosen here to be at 100 TeV. In this analysis, we assume ignorance on both the normalisation and spectral index, and only require that the normalisation never go below 0. Figures 4.8d-e demonstrate the effect of these two systematic parameters in the deposited energy.

Beyond the systematic parameters of the data set, the new physics model used here is also affected by the uncertainties in the standard neutrino mixing matrix U. Therefore the standard mixing angles and phase θ_{12}, θ_{23}, θ_{13}, δ and the two mass differences Δm^2_{21}, Δm^2_{31} are treated as systematic parameters. Global data fits [23] guide the priors chosen for these systematic parameters, as outlined in Table 1.1. The ordering chosen is normal; however, this analysis is not sensitive to this choice. Gaussian priors are used for each of these parameters in a particular representation chosen to ensure unbiased sampling in the elements of the mixing matrix, as will be discussed in Section 4.2.5.

Also to consider are detector and ice related uncertainties; however, they are seen to be small effects at the TeV-PeV energy range of concern here compared to the astrophysical flux and statistical uncertainties. Table 4.1 summarises the eleven systematic parameters used in this analysis, along with the priors for the parameter of interest Λ_d^{-1}.

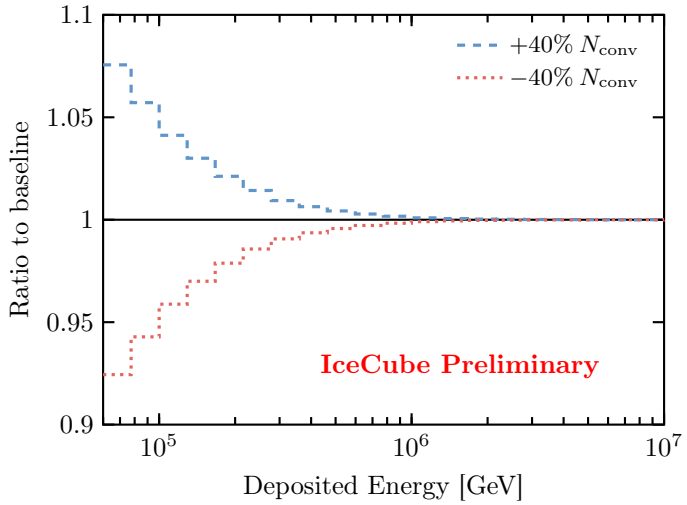

(a) Conventional flux normalisation

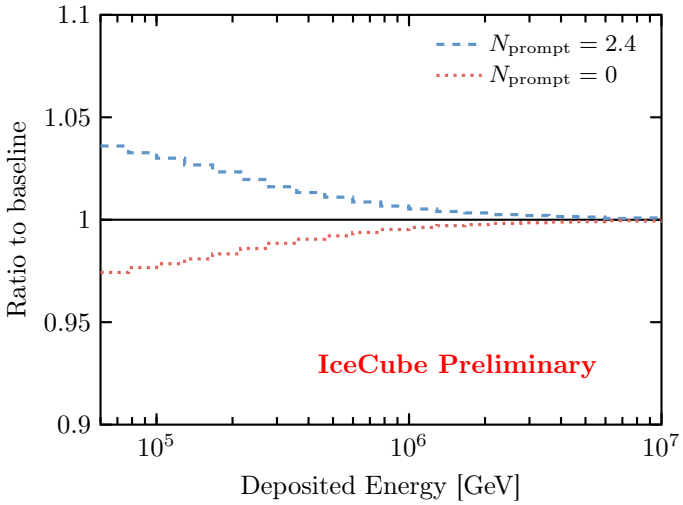

(b) Prompt flux normalisation

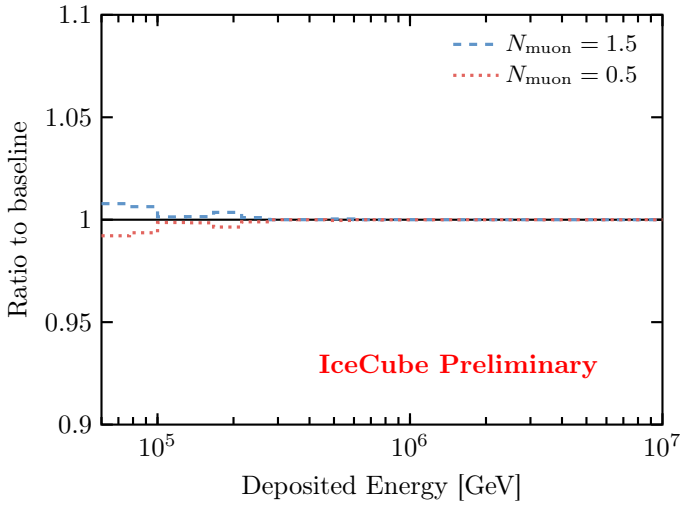

(c) Muon flux normalisation

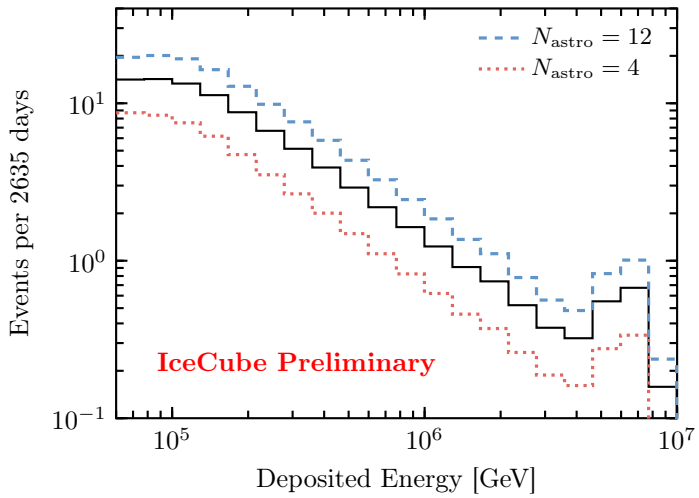

(d) Astrophysical flux normalisation

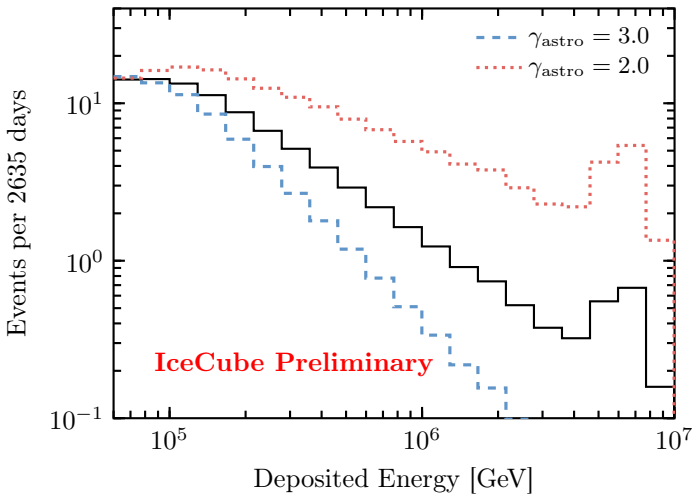

(e) Astrophysical spectral index

Figure 4.8: Effect of the flux related systematic parameters used in this analysis on the event distribution in deposited energy. Black (solid) histogram shows the baseline expectation, blue (dashed) shows an upward fluctuation and red (dotted) shows a downward fluctuation. Note the peak seen at ∼6 PeV is due to the Glashow resonance [159].

Parameter	Symbol	Prior
New physics scale dimension 3	Λ_3^{-1} [GeV]	Flat: $10^{-32} \to 10^{-20}$
New physics scale dimension 4	Λ_4^{-1}	Flat: $10^{-40} \to 10^{-24}$
New physics scale dimension 5	Λ_5^{-1} $\left[\text{GeV}^{-1}\right]$	Flat: $10^{-48} \to 10^{-27}$
New physics scale dimension 6	Λ_6^{-1} $\left[\text{GeV}^{-2}\right]$	Flat: $10^{-56} \to 10^{-30}$
New physics scale dimension 7	Λ_7^{-1} $\left[\text{GeV}^{-3}\right]$	Flat: $10^{-64} \to 10^{-33}$
New physics scale dimension 8	Λ_8^{-1} $\left[\text{GeV}^{-4}\right]$	Flat: $10^{-72} \to 10^{-36}$
Conventional flux normalisation	N_{conv}	Gaussian: $1 \pm 40\% \in 0.1 \to 10$
Prompt flux normalisation	N_{prompt}	Gaussian: 0 ± 2.4 BERS $\in 0 \to 20$
Muon flux normalisation	N_{muon}	Gaussian: $1 \pm 0.5 \in 0 \to 10$
Astrophysical flux normalisation	N_{astro}	Flat: $0 \to 20$
Astrophysical spectral index	γ_{astro}	Flat: $-5.0 \to 5.0$
Mixing angle $\sin^2\theta_{12}$	$\sin^2\theta_{12}$	Gaussian: $0.307 \pm 0.013 \in 0 \to 1$
Mixing angle $\cos^4\theta_{13}$	$\cos^4\theta_{13}$	Gaussian: $0.95637 \pm 0.00147 \in 0 \to 1$
Mixing angle $\sin^2\theta_{23}$	$\sin^2\theta_{23}$	Gaussian: $0.538 \pm 0.069 \in 0 \to 1$
Mixing phase	δ	Flat: $0 \to 2\pi$
Small mass splitting	Δm^2_{21} $\left[10^{-5}\,\text{eV}^2\right]$	Gaussian: $7.40 \pm 0.21 \in 6.80 \to 8.02$
Large mass splitting	Δm^2_{31} $\left[10^{-3}\,\text{eV}^2\right]$	Gaussian: $2.494 \pm 0.033 \in 2.399 \to 2.593$

Table 4.1: Parameters used in this analysis, showing the prior imposed on each parameter.

4.2.4 Statistics

A Bayesian approach will be taken in this analysis for making inferences. Techniques here follow directly from the discussions in Sections 3.2.4-3.2.6. In this analysis, Monte Carlo (MC) techniques have been used in order to simulate the detector response, however it is computationally intensive and in some cases, the stochastic fluctuations in the simulation can bias inferences drawn from the data. Therefore, in order to take into account potential large MC statistical uncertainties that can exist in some bins $\mathbf{n} = (n_i, \ldots, n_N)$, this analysis uses a modified Poisson likelihood function, $L_{\text{eff}}(\boldsymbol{\theta}|\mathbf{n})$, that accounts for MC statistical uncertainties [160]:

$$L_{\text{eff}}(\boldsymbol{\theta}|\mathbf{n}) = \prod_{i=1}^{N} \left(\frac{\mu_i(\boldsymbol{\theta})}{\sigma_i^2(\boldsymbol{\theta})}\right)^{\frac{\mu_i^2(\boldsymbol{\theta})}{\sigma_i^2(\boldsymbol{\theta})}+1} \Gamma\left(n_i + \frac{\mu_i^2(\boldsymbol{\theta})}{\sigma_i^2(\boldsymbol{\theta})} + 1\right) \left[n_i! \left(1 + \frac{\mu_i(\boldsymbol{\theta})}{\sigma_i^2(\boldsymbol{\theta})}\right)^{n_i+\frac{\mu_i^2(\boldsymbol{\theta})}{\sigma_i^2(\boldsymbol{\theta})}+1} \Gamma\left(\frac{\mu_i^2(\boldsymbol{\theta})}{\sigma_i^2(\boldsymbol{\theta})} + 1\right)\right]^{-1} \tag{4.14}$$

where $\mu_i(\boldsymbol{\theta}) \equiv \sum_{j=1}^{M} w_{j,i}(\boldsymbol{\theta})$ and $\sigma_i^2(\boldsymbol{\theta}) \equiv \sum_{j=1}^{M} w_{j,i}^2(\boldsymbol{\theta})$ with M being the number of MC events generated in bin i and $w_{j,i}(\boldsymbol{\theta})$ being the MC weight of the j^{th} generated event in bin i (see Section 4.2.2). For more details on this likelihood prescription see Reference [160].

4.2.5 Anarchic sampling

In order to compute posterior distributions and evidences, MCMC sampling algorithms will be utilised, as discussed in detail in Sections 3.2.6 and 3.3.2. As with any Bayesian based inference, the prior distribution used for a given parameter needs to be chosen carefully. In this analysis, a further technology needs to be introduced in order to ensure the prior distribution is not biasing any drawn inferences. More specifically, the priors on the standard model mixing parameters are of concern. These parameters are defined in Equation 1.15 as a representation of the 3×3 unitary mixing matrix U, in such a way that any valid combination of the mixing angles can be mapped into a unitary matrix. The ideal and most ignorant choice of prior here is one in which there is no distinction among the three neutrino flavours, compatible with the hypothesis of *neutrino mixing anarchy*, which is the hypothesis that U can be described as a result of random draws from an unbiased distribution of unitary 3×3 matrices [146, 161–163]. Simply using a flat prior on the mixing angles however, does not mean that the prior on the elements of U is also flat. Indeed doing

this would introduce a significant bias for the elements of U. Statistical techniques used in the study of neutrino mixing anarchy will be borrowed in order to ensure that U is sampled in an unbiased way. Here, the anarchy hypothesis requires the probability measure of the neutrino mixing matrix to be invariant under changes of basis for the three generations. This is the central assumption of *basis independence* and from this, distributions over the mixing angles are determined by the integration invariant *Haar measure* [162]. For the group $U(3)$ the Haar measure is given by the volume element $\mathrm{d}U$, which can be written using the mixing angles parameterisation as given in Equation 1.15:

$$\mathrm{d}U = \mathrm{d}\left(\sin^2\theta_{12}\right) \wedge \mathrm{d}\left(\cos^4\theta_{13}\right) \wedge \mathrm{d}\left(\sin^2\theta_{23}\right) \wedge \mathrm{d}\delta \tag{4.15}$$

which says that the Haar measure for the group $U(3)$ is flat in $\sin^2\theta_{12}$, $\cos^4\theta_{13}$, $\sin^2\theta_{23}$ and δ. Therefore, in order to ensure the distribution over the mixing matrix U is unbiased, the prior on the mixing angles must be chosen according to this Haar measure, i.e. in $\sin^2\theta_{12}$, $\cos^4\theta_{13}$, $\sin^2\theta_{23}$ and δ. Figure 4.3 shows an example of this in action. The posterior distribution of the measured flavour composition is displayed by the coloured points for a given source composition. Here a flat prior distribution according to the Haar measure variables for the mixing angles is used, therefore it can be seen that under the neutrino mixing anarchy hypothesis, the posterior probability naturally peaks at the democratic composition of $(1:1:1)_\oplus$. In this analysis, global data fits [23] will be used as priors for the mixing angles in the space as defined by the Haar measure (see Table 4.1).

Also to note, but not used directly in this analysis, is the case of a flavour composition measurement using sampling techniques in a Bayesian approach. In this case, the posterior of the measured composition $f_{\alpha,\oplus}$ is sampled over as the parameters of interest. Here, the effective number of parameters can be reduced from three to two due to the requirement $\sum_\alpha f_{\alpha,\oplus} = 1$. Therefore, the prior on these two parameters must be determined by Haar measure of the flavour composition volume element, $\mathrm{d}f_{e,\oplus} \wedge \mathrm{d}f_{\mu,\oplus} \wedge \mathrm{d}f_{\tau,\oplus}$. The following *flavour angles* parameterisation is found to be sufficient:

$$f_{\alpha,\oplus} = \begin{pmatrix} f_{e,\oplus} \\ f_{\mu,\oplus} \\ f_{\tau,\oplus} \end{pmatrix} = \begin{pmatrix} \sin^2\phi_\oplus \cos^2\psi_\oplus \\ \sin^2\phi_\oplus \sin^2\psi_\oplus \\ \cos^2\phi_\oplus \end{pmatrix} \tag{4.16}$$

$$\mathrm{d}f_{e,\oplus} \wedge \mathrm{d}f_{\mu,\oplus} \wedge \mathrm{d}f_{\tau,\oplus} = \mathrm{d}\left(\sin^4\phi_\oplus\right) \wedge \mathrm{d}\left(\cos\left(2\psi_\oplus\right)\right) \tag{4.17}$$

4.3 Results

The search for new physics effects manifesting in the astrophysical neutrino flavour composition is carried out for the first time using an effective Hamiltonian approach motivated by the Standard Model Extension as described in Section 4.1. As with other searches of this type (see Chapter 3) the limits will be maximised, here by assuming a certain source composition as well as a certain new physics texture. For each dimension of new physics, $d = 3, 4, 5, 6, 7, 8$, source compositions in the set $(x : 1 - x : 0)_{\mathrm{S}}$, corresponding to standard astrophysical production mechanisms, are assumed, with new physics textures of the type $\mathcal{O}_{e\tau}$ and $\mathcal{O}_{\mu\tau}$, as described in Section 4.1.3.

A Bayesian statistical approach is used, in which the evidence of the null hypothesis of no new physics is compared to the evidence of a non-zero new physics contribution using the Bayes factor statistic, $B_{0/1}$, as described in Sections 3.2.5 and 3.2.6, with priors as defined in Table 4.1. This is computed using the MultiNest nested sampling algorithm MCMC [115] as a function of the new physics scale Λ_d^{-1} for each scenario discussed above, after which an exclusion region is obtained using Jeffreys' scale (Table 3.2) at a strong strength-of-evidence for the null hypothesis $B_{0/1}\left(\Lambda_d^{-1}\right) > 10$.

The result for the dimension-six operator is shown in Figure 4.9 with a comparison to the atmospheric LV limits as described in Chapter 3. Results for the other dimension operators can be seen in Appendix A.3. Exclusion regions can be drawn for source compositions at both the $(0 : 1 : 0)_{\mathrm{S}}$ and $(1 : 0 : 0)_{\mathrm{S}}$ edges for the new physics textures $\mathcal{O}_{e\tau}$ and $\mathcal{O}_{\mu\tau}$. Note that the new physics texture $\mathcal{O}_{e\mu}$, representing maximum $\nu_e \leftrightarrow \nu_\mu$ mixing, was also tested; however, no limits could be made. With reference to Figure 4.7, these exclusion regions can be seen to correspond to measured flavour compositions which fall outside of the credibility interval from the data. Notably, the standard $(1 : 2 : 0)_{\mathrm{S}}$ pion-decay source composition does not have any attainable limits in this analysis as the measured composition does not fall outside of the credibility interval for any value of the new physics scale, as shown in Figure 4.7 as the red shaded region.

A summary of the obtained limits across all dimensions is shown in Figure 4.10 and Table 4.2 for scenarios with a source composition of $(0 : 1 : 0)_{\mathrm{S}}$ and $(1 : 0 : 0)_{\mathrm{S}}$, and a texture of $\mathcal{O}_{e\tau}$ and $\mathcal{O}_{\mu\tau}$, respectively, representing the best-case limits that can be obtained.

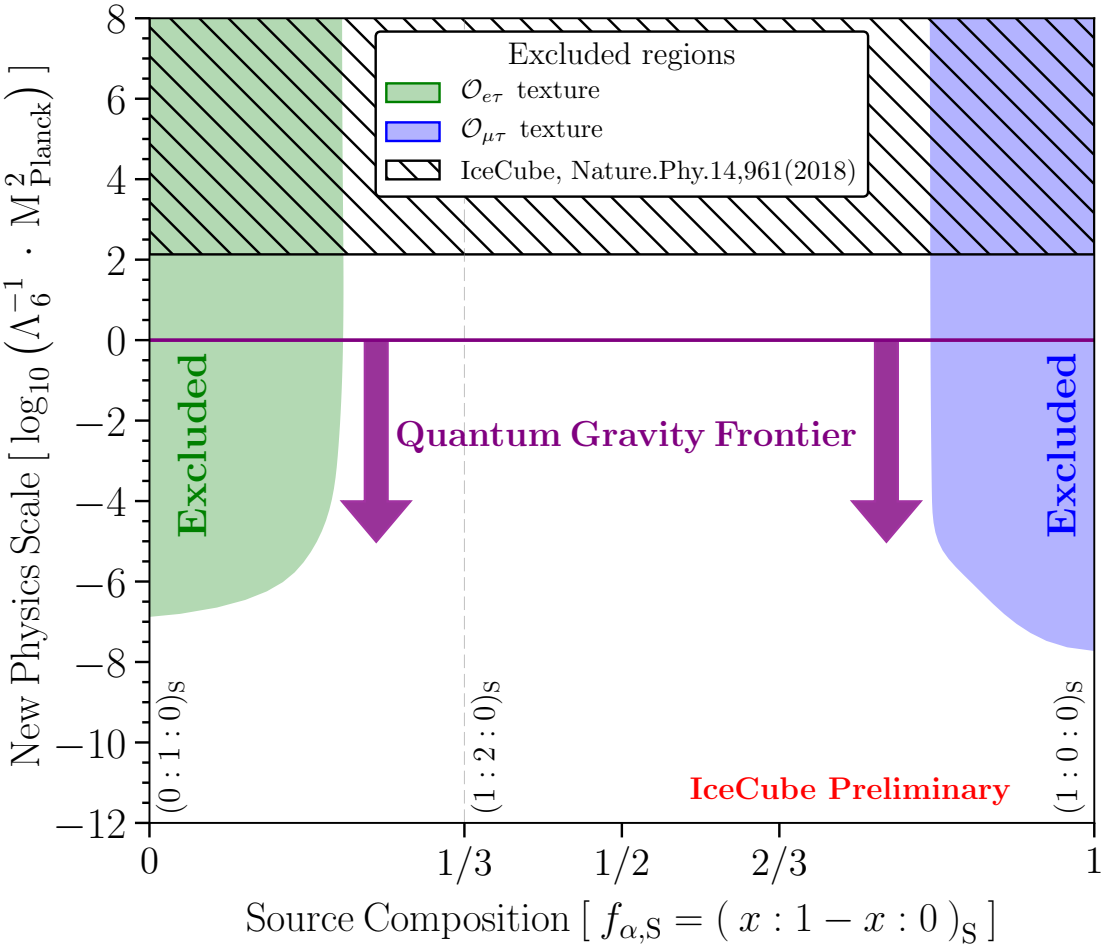

Figure 4.9: Exclusion regions for the dimension-six new physics operator. Limits are obtained for the new physics scale (vertical axis) as a function of the source flavour composition (horizontal axis) for certain new physics flavour textures. Green and blue shaded regions are excluded with a strong strength-of-evidence for the null hypothesis (Bayes factor, $B_{0/1} > 10$) according to Jeffreys' scale [101]. New physics scale is shown normalised to the Planck scale expectation, with the purple line indicating the point below which Planck scale physics is being probed. The hashed region shows the previous IceCube limit [72].

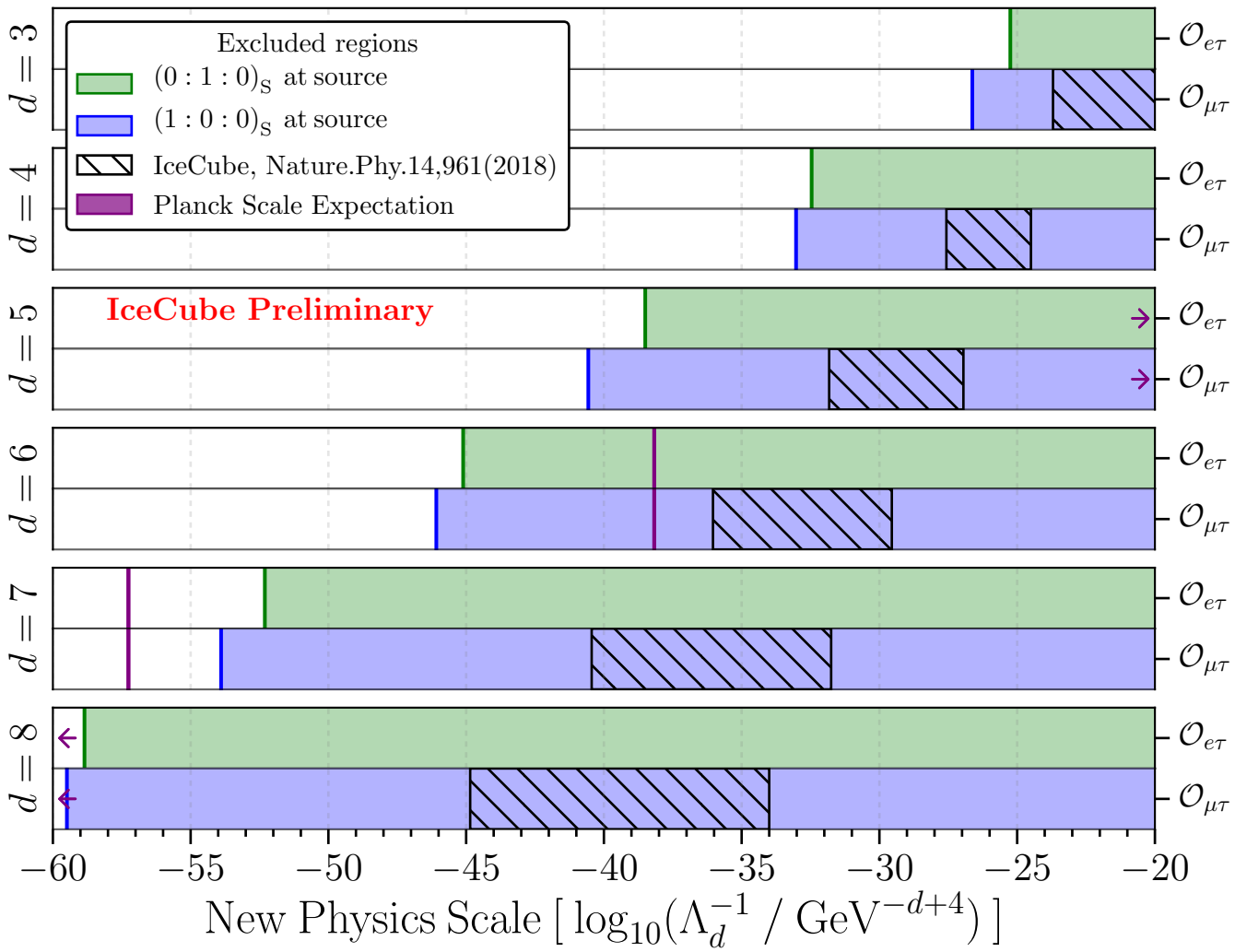

Figure 4.10: Exclusion limits obtained for the new physics scale (horizontal axis) for dimension-three to dimension-eight new physics operators. Limits are obtained for each dimension (left vertical axis) corresponding to certain assumptions on the source flavour composition and also on the new physics flavour texture (right vertical axis). Green and blue shaded regions are excluded with a strong strength-of-evidence for the null hypothesis (Bayes factor, $B_{0/1} > 10$) according to Jeffreys' scale [101]. The purple line indicates the point at which Planck scale physics is being probed. The hashed region shows the previous IceCube limit [72].

Dimension	Method	Type	Sector	Limits	Reference
3	CMB polarization	astrophysical	photon	$\sim 10^{-43}$ GeV	[78]
	He-Xe comagnetometer	tabletop	neutron	$\sim 10^{-34}$ GeV	[82]
	torsion pendulum	tabletop	electron	$\sim 10^{-31}$ GeV	[84]
	muon g-2	accelerator	muon	$\sim 10^{-24}$ GeV	[85]
	neutrino oscillation	atmospheric	neutrino	$\lvert\mathrm{Re}(\mathring{a}^{(3)}_{\mu\tau})\rvert, \lvert\mathrm{Im}(\mathring{a}^{(3)}_{\mu\tau})\rvert$ $< 2.9 \times 10^{-24}$ GeV (99% CL) $< 2.0 \times 10^{-24}$ GeV (90% CL)	[72]
	neutrino mixing	astrophysical	neutrino	$\sim 10^{-26}$ GeV	this work
4	GRB vacuum birefringence	astrophysical	photon	$\sim 10^{-38}$	[79]
	Laser interferometer	LIGO	photon	$\sim 10^{-22}$	[80]
	Sapphire cavity oscillator	tabletop	photon	$\sim 10^{-18}$	[77]
	Ne-Rb-K comagnetometer	tabletop	neutron	$\sim 10^{-29}$	[83]
	trapped Ca^+ ion	tabletop	electron	$\sim 10^{-19}$	[86]
	neutrino oscillation	atmospheric	neutrino	$\lvert\mathrm{Re}(\mathring{c}^{(4)}_{\mu\tau})\rvert, \lvert\mathrm{Im}(\mathring{c}^{(4)}_{\mu\tau})\rvert$ $< 3.9 \times 10^{-28}$ (99% CL) $< 2.7 \times 10^{-28}$ (90% CL)	[72]
	neutrino mixing	astrophysical	neutrino	$\sim 10^{-33}$	this work
5	GRB vacuum birefringence	astrophysical	photon	$\sim 10^{-34}$ GeV^{-1}	[79]
	ultra-high-energy cosmic ray	astrophysical	proton	$\sim 10^{-22}$ to 10^{-18} GeV^{-1}	[81]
	neutrino oscillation	atmospheric	neutrino	$\lvert\mathrm{Re}(\mathring{a}^{(5)}_{\mu\tau})\rvert, \lvert\mathrm{Im}(\mathring{a}^{(5)}_{\mu\tau})\rvert$ $< 2.3 \times 10^{-32}$ GeV^{-1} (99% CL) $< 1.5 \times 10^{-32}$ GeV^{-1} (90% CL)	[72]
	neutrino mixing	astrophysical	neutrino	$\sim 10^{-40}$ GeV^{-1}	this work
6	GRB vacuum birefringence	astrophysical	photon	$\sim 10^{-31}$ GeV^{-2}	[79]
	ultra-high-energy cosmic ray	astrophysical	proton	$\sim 10^{-42}$ to 10^{-35} GeV^{-2}	[81]
	gravitational Cherenkov radiation	astrophysical	gravity	$\sim 10^{-31}$ GeV^{-2}	[87]
	neutrino oscillation	atmospheric	neutrino	$\lvert\mathrm{Re}(\mathring{c}^{(6)}_{\mu\tau})\rvert, \lvert\mathrm{Im}(\mathring{c}^{(6)}_{\mu\tau})\rvert$ $< 1.5 \times 10^{-36}$ GeV^{-2} (99% CL) $< 9.1 \times 10^{-37}$ GeV^{-2} (90% CL)	[72]
	neutrino mixing	astrophysical	neutrino	$\sim 10^{-46}$ GeV^{-2}	this work
7	GRB vacuum birefringence	astrophysical	photon	$\sim 10^{-28}$ GeV^{-3}	[79]
	neutrino oscillation	atmospheric	neutrino	$\lvert\mathrm{Re}(\mathring{a}^{(7)}_{\mu\tau})\rvert, \lvert\mathrm{Im}(\mathring{a}^{(7)}_{\mu\tau})\rvert$ $< 8.3 \times 10^{-41}$ GeV^{-3} (99% CL) $< 3.6 \times 10^{-41}$ GeV^{-3} (90% CL)	[72]
	neutrino mixing	astrophysical	neutrino	$\sim 10^{-53}$ GeV^{-3}	this work
8	gravitational Cherenkov radiation	astrophysical	gravity	$\sim 10^{-46}$ GeV^{-4}	[87]
	neutrino oscillation	atmospheric	neutrino	$\lvert\mathrm{Re}(\mathring{c}^{(8)}_{\mu\tau})\rvert, \lvert\mathrm{Im}(\mathring{c}^{(8)}_{\mu\tau})\rvert$ $< 5.2 \times 10^{-45}$ GeV^{-4} (99% CL) $< 1.4 \times 10^{-45}$ GeV^{-4} (90% CL)	[72]
	neutrino mixing	astrophysical	neutrino	$\sim 10^{-59}$ GeV^{-4}	this work

Table 4.2: Comparison of attainable best limits of SME operators in various fields. Note, astrophysical neutrino limits are applied under the assumption of a produced neutrino flavour composition of either $(0:1:0)_S$ or $(1:0:0)_S$ at the source.

4.3.1 Discussion

The limits obtained in this analysis demonstrate the capability of using very-high-energy astrophysical neutrinos to probe for new effects. For the dimension-three and -four operators, the searches are conducted using mainly photons [77, 80], nucleons [82, 83] and charged leptons [84–86]. Going beyond terrestrial experiments, limits arising from astrophysical observations provide strong constraints [78, 79]. The result from this analysis uses neutrinos from the astrophysical sector for the first time. By using very-high-energy neutrinos of up to PeV energies, the limits obtained have the potential to surpass all limits coming from the neutrino sector [72, 107, 109, 110], see Chapter 3.

Searches of dimension-five and higher SME operators are dominated by astrophysical observations [79, 81, 87]. Among these, this analysis has the potential to probe new regions across all fields for all operators and notably, is able to explore the Planck scale regime for the dimension-six operator. Such high-dimension operators are generic signatures of new physics [113]. For example, the dimension-five operator is an attractive possibility to produce neutrino masses, and dimension-six operators represent new physics interactions that can, for example, mediate proton decay.

However, in contrast to other searches such as the atmospheric LV search in Chapter 3 in which limits could be attained in an unambiguous way, the limits here represent certain restricted scenarios of the source composition and new physics texture. This limitation is a consequence of the relatively unconstrained flavour measurement as shown by the credibility intervals in Figure 4.7, which notably envelop the accessible region for the standard astrophysical source composition of $(1:2:0)_{\mathrm{S}}$. In time and with the IceCube-Upgrade, improvements to this measurement through more data and better calibration which improves the reconstruction algorithms, particularly with respect to particle identification between the ν_e and ν_τ initiated events, this analysis shows promise in being able to maintain the strong limits obtained in a more unambiguous way across all standard astrophysical source compositions. With that said, this analysis shows for the first time, the potential of astrophysical neutrinos in the search for new physics beyond the standard model and general relativity.

4.3.2 Other checks

The landscape of the Bayes factor test statistic as used to define the exclusion region can be looked at more closely as is done in Figure 4.11. This is shown for two scenarios $(0:1:0)_{\mathrm{S}}$ with an $\mathcal{O}_{e\tau}$ texture and $(1:0:0)_{\mathrm{S}}$ with an $\mathcal{O}_{\mu\tau}$ texture in green and in blue, respectively. A value of one for the Bayes factor corresponds to perfect agreement with the null hypothesis, where the evidence of the hypothesis is equal to the evidence of the null. This is true for values of the new physics scale which are small $\Lambda_6^{-1} \sim 10^{-55}\ \mathrm{GeV}^{-2}$. As the new physics scale increases so too does the Bayes factor, indicating that the null hypothesis is more favoured than this hypothesis. As the values of the new physics scale become large in comparison to the standard mass matrix $\Lambda_d \gg E^{d-2}/M^2$, the standard mixings have little effect and mixing is instead dominated by the new physics mixing matrix. For the two scenarios shown on the plot this correspond to measured flavour compositions of $(0:1:0)_{\mathrm{S}} \xrightarrow{\mathcal{O}_{e\tau}} (0:1:0)_{\oplus}$ and $(1:0:0)_{\mathrm{S}} \xrightarrow{\mathcal{O}_{\mu\tau}} (0:1:0)_{\oplus}$, respectively. Finally to note, the scenario $(0:1:0)_{\mathrm{S}}$ with an $\mathcal{O}_{e\tau}$ texture, while setting a similar limit as $(1:0:0)_{\mathrm{S}}$ with an $\mathcal{O}_{\mu\tau}$ texture, the Bayes factor for large values of the new physics scale is much larger. This is due to the much better particle identification of ν_μ events, as they are the only neutrino flavour that can initiate muon tracks in the detector (see Section 2.2).

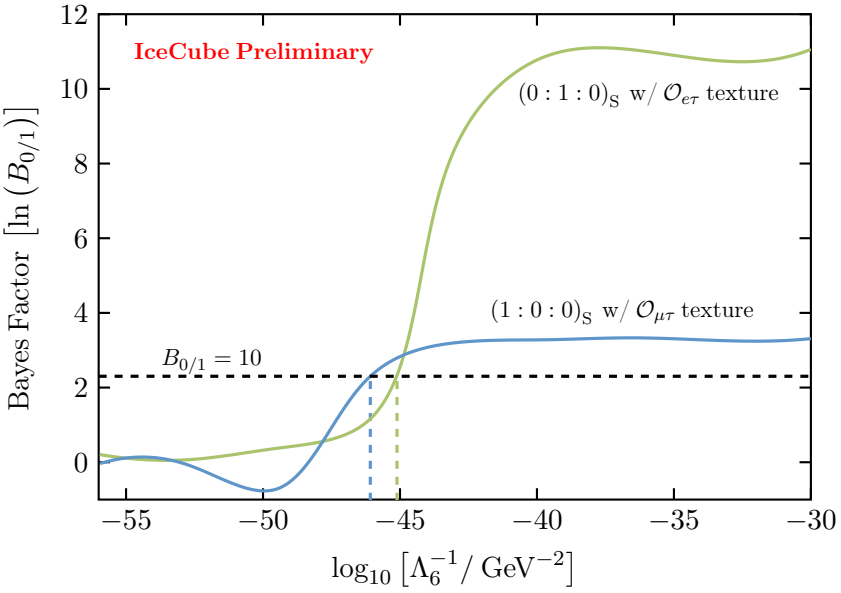

Figure 4.11: Bayes factor $B_{0/1}$ for two scenarios, shown as a function of the new physics scale for the dimension-six operator. Excluded region is defined with a strong strength-of-evidence for the null hypothesis according to Jeffreys' scale [101], $B_{0/1} > 10$, as indicated by the dashed horizontal line.

In order to visualise the correlations between the various nuisance parameters (see Table 4.1), the posterior can be computed in full using the affine invariant MCMC algorithm package EMCEE [114], as is described in Section 3.2.6 and also employed in Section 3.3.2. The joint distribution over any two parameters can then be shown in order to understand correlations between any two parameters. Figures 4.12 and 4.13 show this for the dimension-six operator. The two scenarios shown here are for a source composition of $(0:1:0)_{\mathrm{S}}$ with texture $\mathcal{O}_{e\tau}$ and source composition of $(1:0:0)_{\mathrm{S}}$ with texture $\mathcal{O}_{\mu\tau}$. Here, the non-diagonal plots show joint distributions between two parameters, labelled on the x- and y-axis and the diagonal plots show the marginalised distributions for each parameter, as labelled on the x-axis. The blue (light blue) shows the 90% (99%) credibility intervals.

In addition to this, the posterior distribution of a standard flavour composition measurement with no new physics effects can be viewed. The flavour composition is written in terms of the two flavour angles $\sin^4\phi_\oplus$, $\cos(2\psi_\oplus)$ as in Equation 4.17, derived from the Haar measure of the flavour composition volume element $\mathrm{d}f_{e,\oplus} \wedge \mathrm{d}f_{\mu,\oplus} \wedge \mathrm{d}f_{\tau,\oplus}$. This ensures that the prior on the flavour composition makes no distinction between any neutrino flavour, which will be flat in $\sin^4\phi_\oplus$, $\cos(2\psi_\oplus)$ with ranges $0 \to 1$ and $-1 \to 1$, respectively. Nuisance parameter priors are kept the same as shown in Table 4.1. Figure 4.14 shows the joint posterior distributions between any two parameters, either nuisance or measured flavour angle, in which the blue (light blue) shows the 90% (99%) credibility intervals. It is by marginalising over the nuisance parameters and translating back into flavour fractions that the data credibility interval contours as shown in Figures 4.3 and 4.7 are computed.

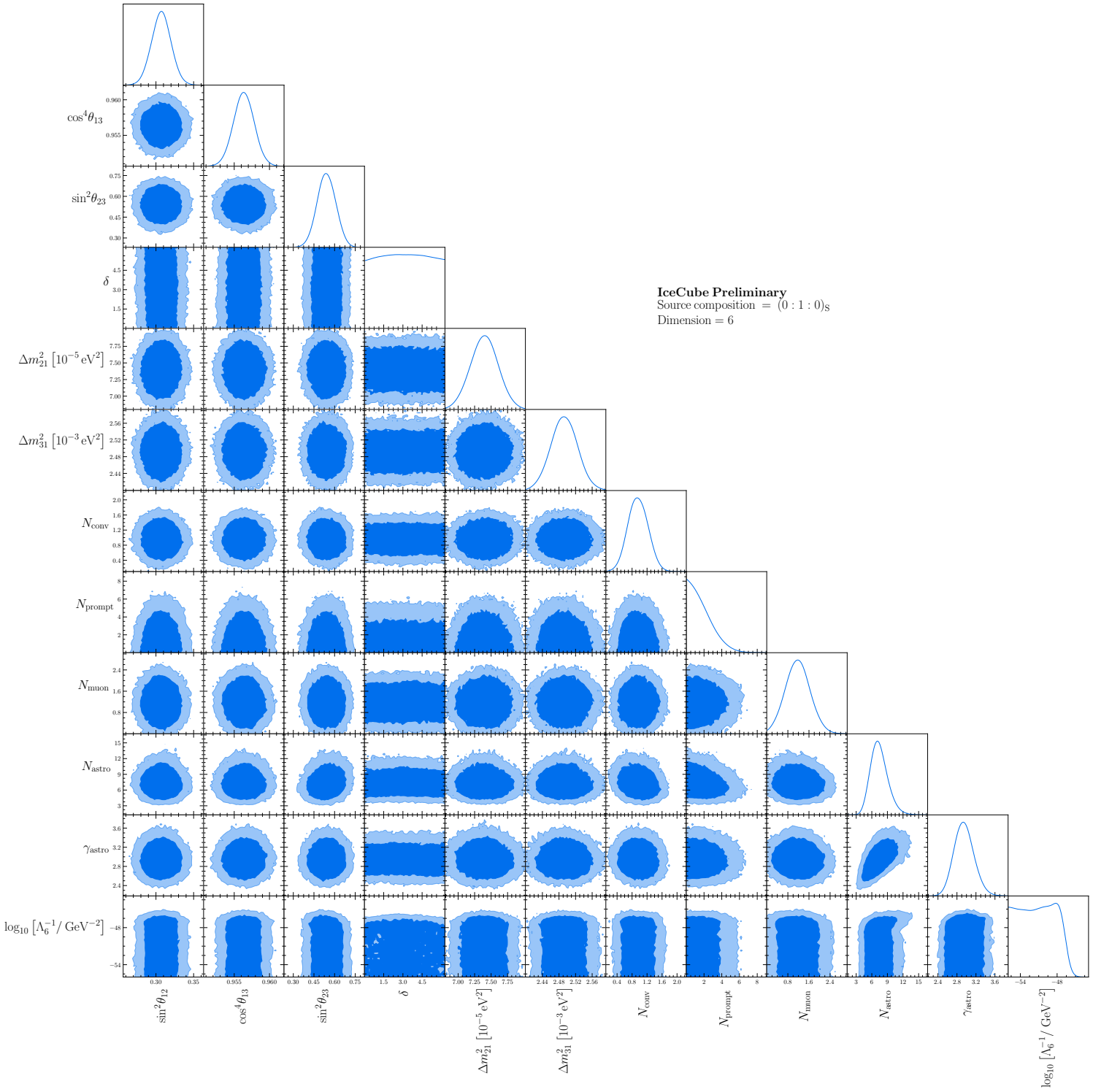

Figure 4.12: Joint posterior distributions for the various nuisance parameters and the new physics scale for the dimension-six operator here with a source composition $(0:1:0)_S$ and texture $\mathcal{O}_{e\tau}$.

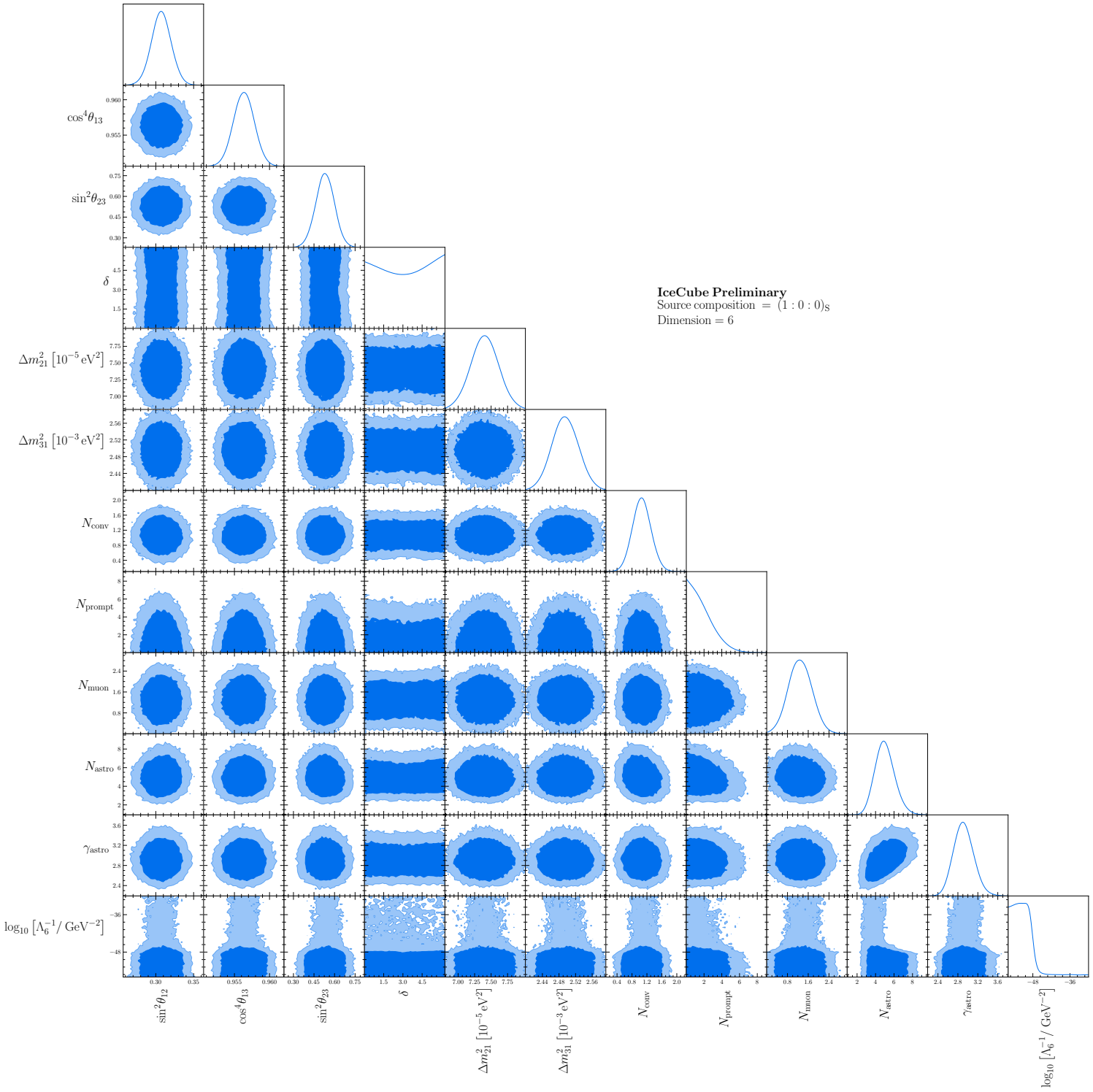

Figure 4.13: Joint posterior distributions for the various nuisance parameters and the new physics scale for the dimension-six operator here with a source composition $(1:0:0)_S$ and texture $\mathcal{O}_{\mu\tau}$.

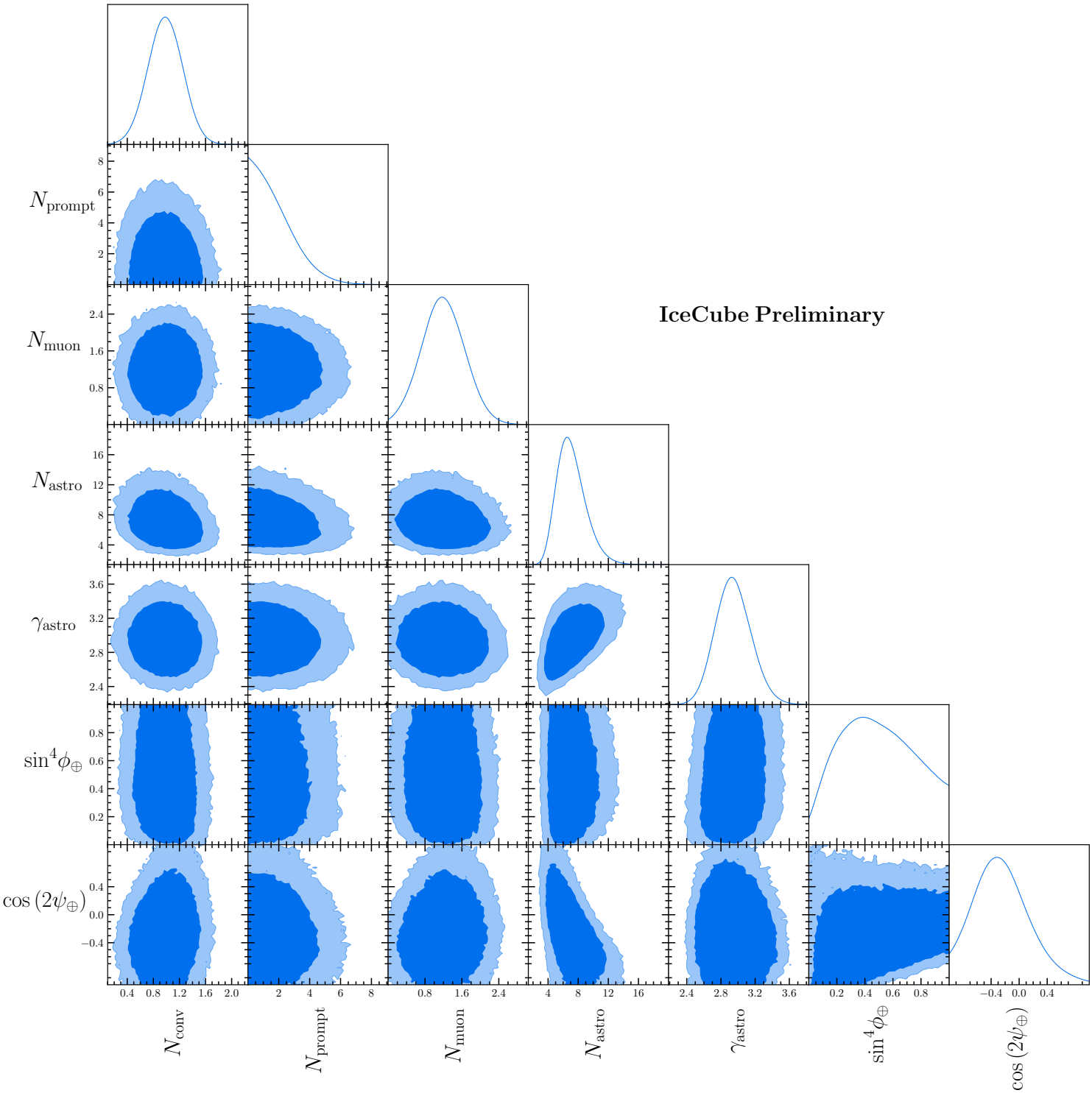

Figure 4.14: Joint posterior distributions for the various nuisance parameters and the measured flavour composition in terms of the flavour angles $\sin^4\phi_\oplus$, $\cos(2\psi_\oplus)$ (see text).

4.3.3 Conclusion

The analysis carried out here presents for the first time a test of new physics with very-high-energy astrophysical neutrino flavour data taken at IceCube. The new physics mechanism is modelled under the effective Hamiltonian formalism motivated by the SME. No evidence of new physics was found; however, this analysis demonstrates the potential in searching for new physics using the astrophysical neutrino flavour measurements. Although the current statistics and detector sensitivity allows for searches for only rather special new physics effects, it is demonstrated that the sensitivity of this new approach goes far beyond any known technologies, and reaches for the first time the necessary precision to look for new physics within the Planck scale expectation.

Future extensions of IceCube such as the IceCube-Upgrade and IceCube-Gen2 [59, 164] have the ability to greatly improve the measurement of the astrophysical neutrino flavour. With more statistics and better calibration, this analysis shows promise in being able to investigate Planck scale physics at an unprecedented level, providing IceCube with a real discovery potential in the search for new physics beyond the standard model and general relativity.

Part III

IceCube DOM Beam Test at the Fermilab Test Beam Facility

5 IceCube DOM Beam Test at the Fermilab Test Beam Facility

The next generation IceCube-Upgrade (see Section 2.3) will enhance the physics potential of IceCube at both the high and low energy regimes. At the high energies, enhanced calibration equipment will provide the tools to greatly improve reconstruction algorithms and at lower energies, the denser array and improved optical modules will allow for a more precise measurement of the neutrino mixing parameters using atmopsherically produced neutrinos.

Although the energy threshold of DeepCore and the IceCube-Upgrade is much lower than the full IceCube array, the nearest DOMs are still spaced $\sim$7m apart which, when compared to other water Cherenkov detectors such as Super-Kamiokande [13], is still very sparse. As a consequence, the number of PMTs which detect photo-electrons (PMT hits) in each event is relatively low, which is a problem since it is very difficult to perform any *particle identification* (PID) with just a few PMT hits. This has prompted the development of the multi-PMT DOM (mDOM) [63] and the Dual optical sensors in an Ellipsoid Glass for Gen2 (DEgg) [62] for the IceCube-Upgrade, so that more PMT hits can be collected per interaction [164]. Currently at these energies, high level parameters such as the reconstructed track length are used as a discriminator to do some basic PID [165], where the charge distributions get fed into the reconstruction algorithms.

Alternatively, here, the *pulse shape* information is used to perform PID. Such low level PMT information is currently unused; however, given a sufficient deposited PE yield, the pulse shape shares characteristics of the parent particle. More specifically, minimally ionizing particles (MIPs, see Section 1.4.2) tend to deposit photons in a short amount of time, whereas electromagnetic showers (EM showers) produce a photon spectrum with a wider distribution. At the energy range of interest here at a few GeV, the particle content of MIPs corresponds to muons and pions, and EM showers comprise of electrons and high-energy photons.

For this IceCube DOM beam test at the Fermilab Test Beam Facility, a tank filled with distilled water is utilised, upon which a PMT in a glass housing is floating, observing Cherenkov light inside the tank. Pulse shape information is studied as a discriminator that can be used for PID between MIPs and EM showers in the context of future water or ice Cherenkov neutrino telescope experiments.

5.1 The Fermilab Test Beam Facility

5.1.1 FTBF MTest beam line

The Fermilab Test Beam Facility (FTBF) at the Fermi National Accelerator Laboratory (FNAL) [166] provides researchers with open access to high-energy and high intensity beam lines. Two beam lines are available for use: the MTest beam line and the MCenter beam line. For the beam test discussed in this chapter the MTest beam line was used, as this is the beam line that is appropriate for short term experiments. At the end of this beam line, there is a wide area to place experiment-specific instrumentation. For this beam test, the beam time allocated was from 14th June to 27th June 2017 [167].

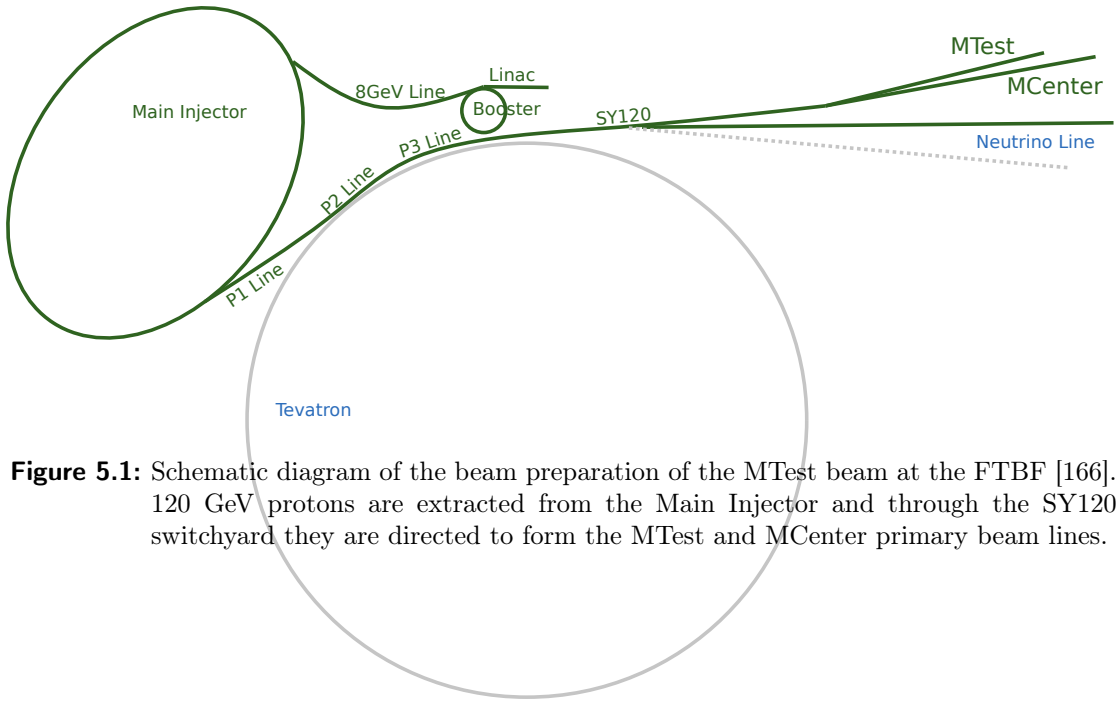

Figure 5.1: Schematic diagram of the beam preparation of the MTest beam at the FTBF [166]. 120 GeV protons are extracted from the Main Injector and through the SY120 switchyard they are directed to form the MTest and MCenter primary beam lines.

5.1.2 FTBF beam structure

The primary beam which is supplied to the FTBF comprises of protons which are extracted from the Main Injector (120 GeV proton synchrotron). This beam is structured into radio frequency (RF) buckets at a frequency of 53 MHz, with a spill duration of 4.2 seconds every minute. The intensity of the beam is tunable with a maximum intensity of 5×10^5 protons per spill. A schematic diagram of the primary beam preparation is shown in Figure 5.1. The primary beam can be collided into two movable aluminium block targets (MT1 and MT4) to create secondary beams with energies as low as ~ 2 GeV, consisting of pions, muons and/or electrons. More precise tuning of the beam is available in the form of three sets of focusing magnets, two dipole magnets for selecting momenta, five trim/vernier magnets for small corrections to the beam trajectory and four collimators. In general, the uncertainty on the upstream energy of the beam is between 2-3%, however energy loss can occur as a particle propagates through the various instrumentation [166, 168].

5.1.3 FTBF instrumentation

The FTBF provides multiple types of beam detector instrumentation for tracking, particle identification and triggering. A schematic of the MTest beam line is shown in Figure 5.2. For this beam test, the scintillation counters, Cherenkov detectors and wire chambers were used. The scintillation counters consist of a square plastic scintillator paddle connected to a PMT. There are a total of four such scintillation counters, three of them having a scintillator surface area of $4'' \times 4''$ (labelled SC1, SC2 and SC3) and one having an area of $1'' \times 1''$ (labelled SC4). There are two Cherenkov counters at MTest, one being upstream (labelled CC1) and another downstream (labelled CC2). These counters consist of $80''$ and $50''$ pressure tanks respectively, each filled with nitrogen gas as the radiative medium. These can each be utilised to enable PID based on the particle mass, by altering the gas pressure in the tanks. There are also four Multi-Wire Proportional Chamber (MWPC) tracking systems, located in the MTest area. Note, that the second most upstream one (MWPC2) was malfunctioning and thus was not used. Each system consists of a two-plane (X,Y) $5.2'' \times 5.2''$ wire chamber filled with argon/isobutane gas. With this, the spatial distribution and fluctuations of the MTest beam line can be profiled. Figure 5.3 shows a picture for each instrumentation discussed.

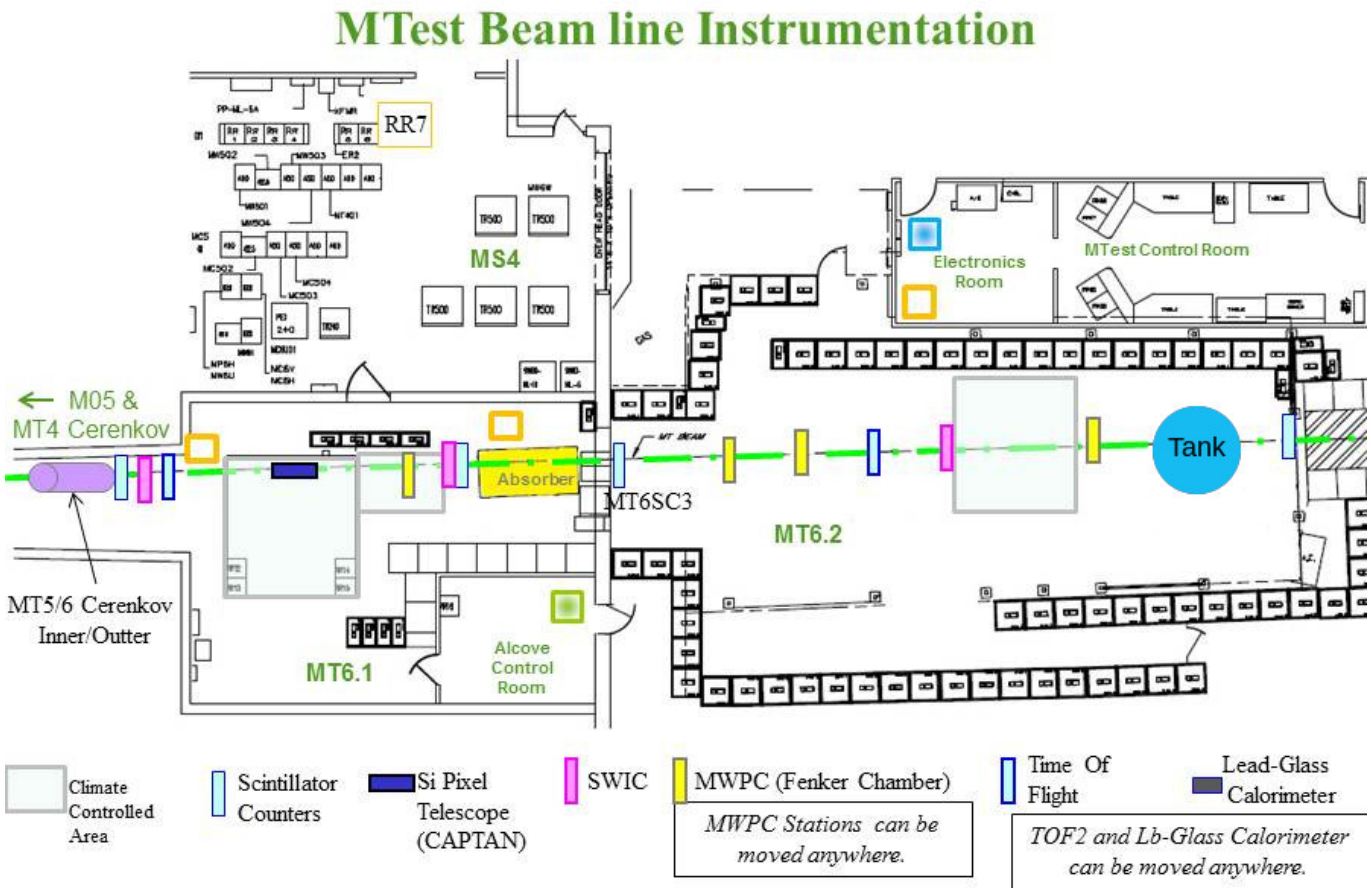

Figure 5.2: Plan view of the MTest area highlighting the various instrumentation available [166]. The beam enters from the left. Upstream and highlighted in purple, are the two Cherenkov counters which are used for PID. four scintillators, SC1, SC2, SC3 and SC4 are placed throughout the beam line as can be seen in light blue, with SC4 being the most downstream. MWPCs, shown in yellow are also distributed throughout the beam line for monitoring of the beam. The tank used in this beam test was placed in the location shown in the diagram.

5.1.4 Beam trigger

For this beam test, only the negatively charged particles are selected for the beam, in order to avoid backgrounds from protons. Figure 5.4 shows the beam composition as a function of the beam energy. One of the aluminium targets (MT4) was lowered to produce the secondary beam and the collimators were set to 10 mm. The focusing/dipole magnets were set to select low energy pions and electrons. For this beam test, data is taken at energies of 4, 6 and 8 GeV with triggering set to select either pions or electrons (see Section 5.1.4). Data is also taken at an energy of 2 GeV with triggering set to select electrons (note that a 2 GeV pion run was attempted, but the event rate dropped too low for any significant measurements). The intensity of the beam was kept relatively low at $\sim$20,000 counts on SC1 per spill. After including the coincidence condition described in the next paragraph, the maximum trigger rate seen was $\sim$8 triggers per spill. By taking into account the frequency of the beam, one can estimate that there is on average a $\sim$200 μs separation between particles incident on SC1 during a spill, leaving sufficient time between triggers. This minimises any pileup while also keeping the trigger rate below the *data acquisition* (DAQ) threshold which is around 10 Hz (see Section 5.2.3).

Here, the interest is in selecting particles which are either MIPs (muons, pions) or not MIPs, which in this beam corresponds to particles which undergo EM showering (electrons, photons). This is done using the FTBF instrumentation described in Section 5.1.3. The coincidence of the four scintillator counters can be used to select beam particles which follow a direct trajectory into the tank. This also significantly reduces the possibility of backgrounds from cosmic rays causing contamination of signal. Note, it was found that scintillator SC3 was misbehaving and as such it was unused, meaning that only three of the scintillation counters were used for triggering. From here, a further constraint can be made to select MIPs, by utilising the two Cherenkov counters. The upstream counter CC1 is set to a pressure of 2.9 psia and the downstream counter CC2 is set to 3.5 psia. This configuration is chosen as at the energy ranges of interest (below 10 GeV), only electrons traversing the chambers will produce Cherenkov radiation, and so by using this as a trigger, electrons can be selected. Therefore, by using this in coincidence with the three scintillation counters, electrons from the beam which penetrate the tank are selected. The majority of the beam particles that are not electrons are pions (see Figure 5.4) therefore the Cherenkov counters can be used in anti-coincidence with the three scintillation counters to select all

Figure 5.3: Pictures of the FTBF instrumentation used for this beam test. Left two images show the scintillation counters, SC1 and SC4 respectively. Upper right image shows one of the Multi Wire Proportional Chambers (MWPC) and bottom right image shows a Cherenkov counter.

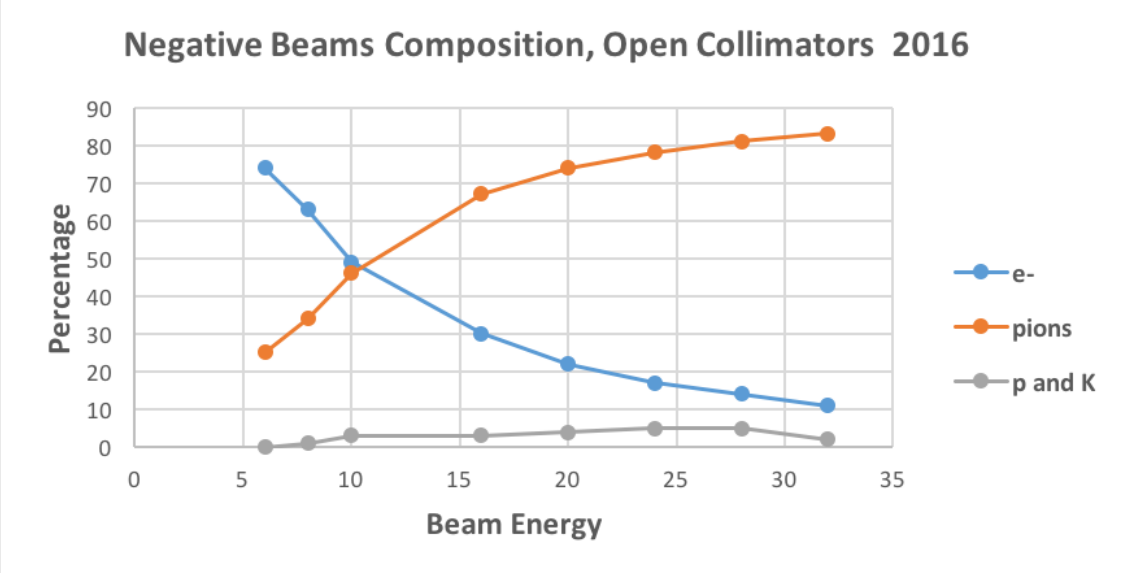

Figure 5.4: Beam composition of the MTest beam line using a negative beam as a function of the beam energy in GeV [166].

pions or MIPs from the beam which penetrate the tank. This explains how triggering on MIPs versus EM showering particles from the beam line is performed.

5.1.5 Beam performance

Besides the intrinsic nature of MIPs and EM showers, the beam profile can influence the shape of PMT waveforms. The PMT is susceptible to pileup which occurs when photons are recorded from more than just the triggered particle within the 316 ns trigger window. This distorts the charge distributions and pulse shape by introducing an addition signal.

One potential source of pileup is cosmic rays. By estimating the flux of atmospheric muons as 1 per square centimetre per minute, the expected rate is of order 1×10^{-5} muons incident on the tank per RF bucket. Therefore, the likelihood of pileup occurring due to cosmic rays is extremely small.

Another source of pileup is from the "halo" of the particle beam. This is caused by beam

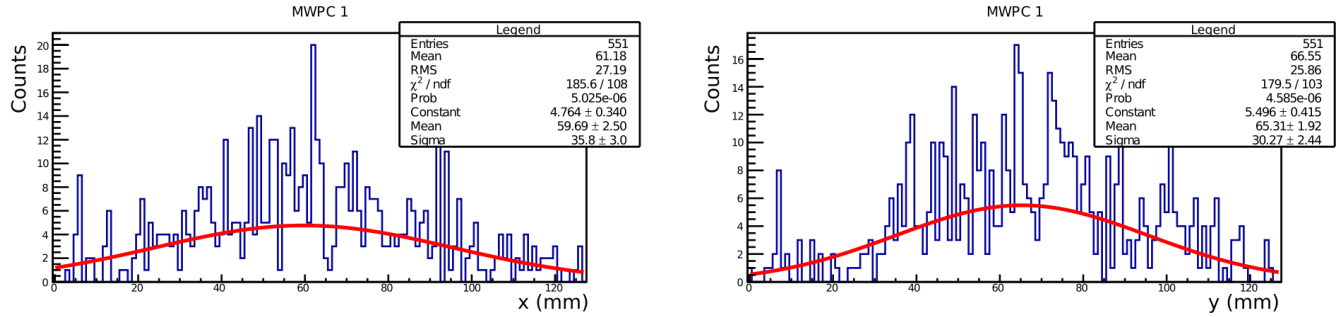

(a) 2 GeV beam data (blue) triggering on electrons shows broad distribution. A gaussian is then fitted to the distribution (red).

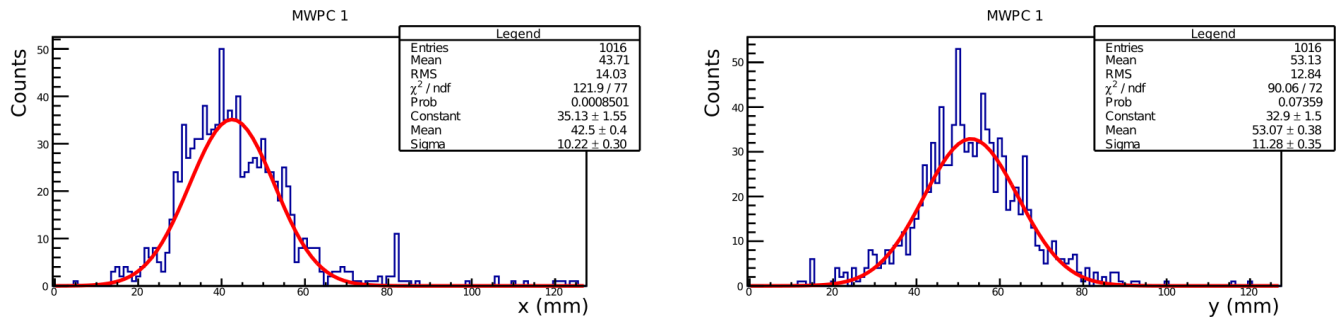

(b) 8 GeV beam data (blue) triggering on pions shows a more focused beam with less fluctuations. It is slightly offset from the centre of the detector. A gaussian is then fitted to the distribution (red).

Figure 5.5: Spatial variation of particles detected in the X-Y plane of the MWPCs. Left plots show the variation in the X-plane and right plots show variation in the Y-plane.

particles whose trajectories are outside of the three triggered scintillator detectors but still enter into the tank volume, while coincidentally, a particle penetrates all three scintillators and activates the trigger. If this is the case, photons from halo particles are also recorded along with the triggered particle signal. If the surface area of the scintillators sufficiently covered the surface area of the tank volume, then the halo particles are vetoed. However, in this beam test, the area covered by the scintillators is much smaller than the area of the tank volume and they are only used to define a beam trajectory. Therefore, there is a need to evaluate whether or not halo particles are causing pileup. Since this is a property of the beam, the beam profile data taken with the MWPCs can be inspected.

Figure 5.5 shows an example of data from the MWPC. Figure 5.5a shows the spatial spread in X and Y for a 2 GeV beam when electrons are triggered. Figure 5.5b is X and Y spatial spread for an 8 GeV beam when pions are triggered. If halo particles (which are mostly electrons) are present, they contribute to the spread of the beam. As can be seen from Figure 5.5b, an 8 GeV pion beam with a pion trigger has a narrow MWPC distribution, and it was found to be roughly constant between 4 to 8 GeV. This indicates halo particles are not present in these energy ranges and an 8 GeV beam with a pion trigger are pion dominant.

As will be discussed in more detail later (Section 5.3.5), the 2 GeV data with an electron trigger has a wider MWPC distribution. The distribution becomes narrower at higher energies, but the 8 GeV electron beam still shows a $\sim$10 mm wider distribution than the 8 GeV pion beam (Figure 5.17, left). This behavior is consistent with our understanding of the beam line. Thus, whilst a wide beam is expected at 2 GeV, the possibility that halo particles are present in the 2 GeV electron data cannot be eliminated. On the other hand, the beam was run with very low rate (see Section 5.1.4) and the fact that there is no indication of halo particles emerging in the 4 GeV pion beam suggests that halo particle contamination for 2 GeV data is not significant.

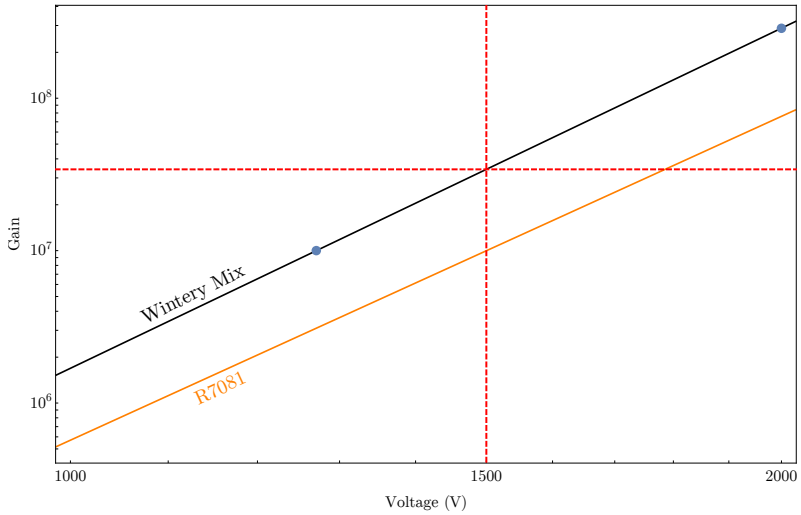

Figure 5.6: Gain extrapolation using two lab measurements of the PMT used in this beam test [169]. Measurements are shown as the blue dots. Gain is specified to have a power law relationship to the input voltage [170], which is used to fit to these data points as is shown as the black line. For reference the R7081 Hamamatsu PMT profile is shown in orange [171].

5.2 Experimental Setup

5.2.1 PMT unit specification

The sole photon detection and digitisation unit in IceCube is the DOM [50], as discussed in Section 2.1. Each module contains a Hamamatsu R7081-02 10″ PMT, which has a spectral response between 300 nm to 650 nm with a peak quantum efficiency around 25% near 390 nm. It features a box-and-line dynode chain with 10 stages, operated at a gain of 10^7. The DOM houses a high voltage generator, various circuit boards for digitisation and calibration all inside a 35 cm pressurised borosilicate glass sphere. Analog and digital signal processing and calibration electronics are integrated onto the mainboard and the LED flasher board. The PMT and surrounding electronics are secured in a high-strength silicon gel that optically couples components to the glass sphere. This particular glass material is chosen as it has a wide transparency window, down to 350 nm.

The IceCube PMT used in this beam test (named "*Wintery Mix*") was a DOM that had the main board removed, giving direct access to the signal and high voltage (HV) cables, so that a custom Data Acquisition (DAQ) system could be used, instead of the traditional but bulky DOMHub DAQ [50]. A hole at the top of the PMT for passing the two cables through ("penetrator") was sealed with RTV glue to prevent any water from damaging

internal electronics. From a previous lab calibration, the gain of this PMT was measured at 2000 V and the voltage needed for a gain of 10^7 was also measured [169]. The gain is specified by the manufacturer as having a power law relationship with the input voltage, $g \propto V^{\alpha n}$, where n is the number of dynode stages [170]. Therefore, the gain of this PMT at the operational voltage of 1500 V may be extracted from these two lab measurements as is shown in Figure 5.6. This PMT was seen to have a gain of 3.4×10^7 at the operation voltage of 1500 V.

Before moving to the full scale tank, a smaller scale setup was constructed using a standard 55 gallon drum. The PMT was placed through a foam ring for stability and buoyancy, ensuring that the underside active PMT region was not masked by the foam. The drum was filled with distilled water and the PMT was floated on top. The drum was closed and wrapped in black plastic bags to prevent too many photons from leaking in. The PMT was then switched on with a voltage of 1500 V, with the signal cable connected to an oscilloscope. The trigger used here was on the leaked photon signal. This small scale setup served to verify that the PMT is functioning as expected.

5.2.2 Tank specification

The detector volume consists of a cylindrical 70″(w) × 77″(h)[1] food-grade polyethylene tank filled with ∼720 gallons of distilled water [172]. A diagram of the experimental setup of the tank in this beam test is shown in Figure 5.7. The inner and outer layers were coated with black Tedlar film (polyvinyl fluoride) to suppress the reflection of photons from within the tank and reduce photon contamination from outside the tank. The PMT is placed on the surface of the water with the photocathode faced down. A foam ring is fit to the PMT unit to stabilise the location as seen in Figure 5.8, right. The opening in this ring defines the photo-sensitive area exposed to the Cherenkov radiation in the water. The beam penetrates the tank along the beam axis, creating Cherenkov photons when it enters the tank which are detected by the PMT, similar to the way in which the IceCube detector operates. The PMT is also placed at an angle of 42° to the beam axis, which corresponds to the Cherenkov angle in water. A commercial green LED, located outside the tank, is coupled to an optical fibre that threads into the tank, so that it points toward

[1] 70″(w) × 77″(h) = 177.8 cm(w) × 195.58 cm(h)

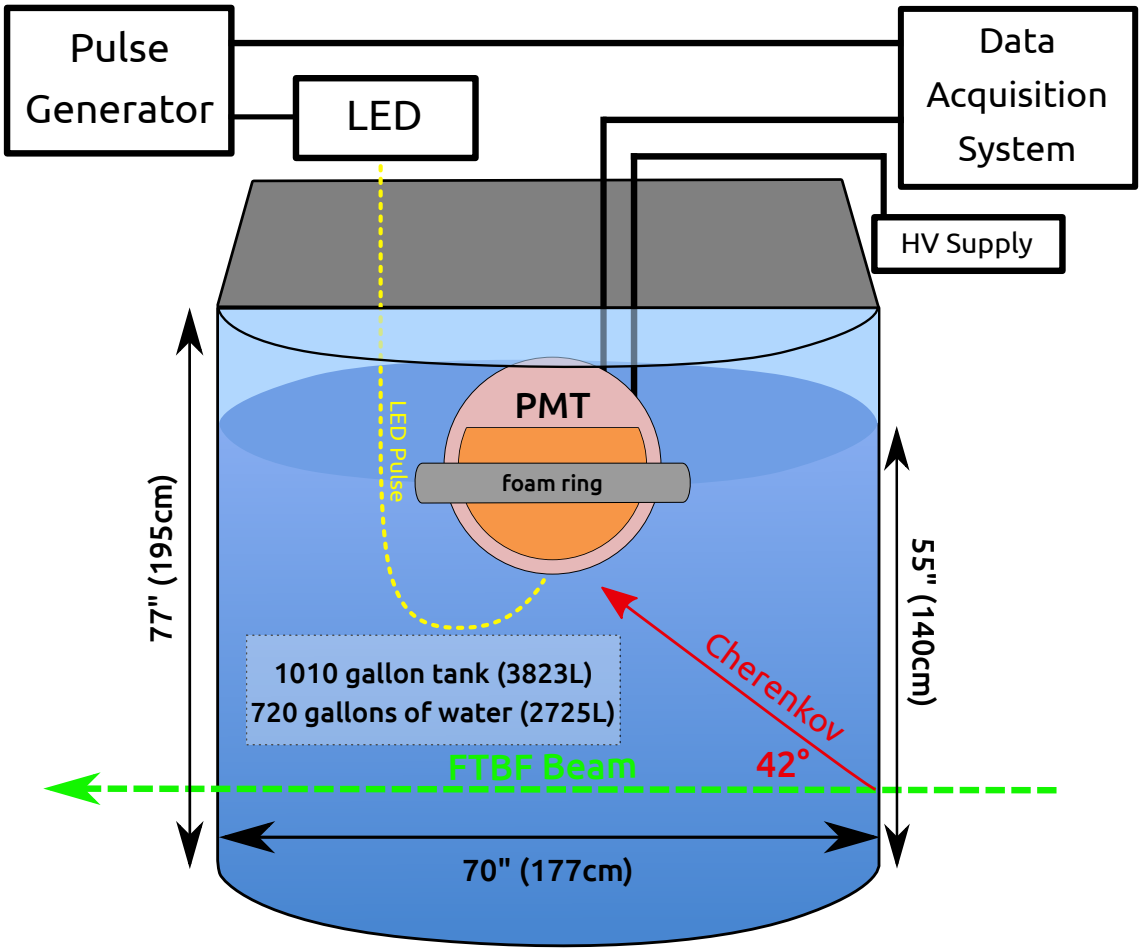

Figure 5.7: Diagram showing the layout of the tank with the PMT placed inside. DAQ and calibration components are labelled. The LED is connected to an optical fibre thread passed into the tank to the underside of the PMT. The beam is shown by the green arrow and the propagation of the Cherenkov photons is represented by the red arrow.

the PMT's photocathode. This is used to calibrate the PMT (Section 5.2.4). The tank is placed in the MT6.2 enclosure as shown in Figure 5.2 and Figure 5.8.

5.2.3 DAQ specification

As mentioned in Section 5.2.1, the PMT has the mainboard removed, so the PMT signal is accessed directly. The raw PMT signal is not digitised, therefore a prototype Digital Acquisition (DAQ) system is used which is being developed for IceCube-Upgrade. The central element to this DAQ is the waveform digitiser DDC2 (Digitizer Daughter Card, revision 2) [173, 174]. A photograph of this card is shown in Figure 5.9. The PMT signal is sent to the DDC2 and processed by a continuously sampling Analog-to-Digital Converter (ADC) [175]. This converts an analog input voltage into a 14-bit digital value (an ADC count) at a rate of 4 ns/sample. At signal frequencies above 10 MHz, the DDC2 has an AC drop-off, meaning that the ADC counts to voltage conversion (see Section 5.2.4) becomes non-linear and so difficult to describe. This is due to a low pass filter installed in the DDC2 which filters the higher frequency signal component to make the waveform signal smoother. Since the interest here is in doing a pulse shape analysis, to preserve the shape of the waveform, the low pass filter in the DDC2 was removed, extending the AC drop-off to above 10 MHz (see Figure 5.9). During data taking, a TTL (Transistor-Transistor Logic) signal generated from the beam monitor coincidence (Section 5.1.4) is sent as an external trigger to the DDC2. Note, IceCube is a neutrino telescope and so the ability to accept an external trigger is designed only for test purposes.

Another element of the DAQ system is the FPGA (field programmable gate array), which is used to programme the DDC2 functions and also to interface it with a computer so that the data can be saved. The FPGA used in this beam test is the Intel (formerly Altera) Cyclone V SX FPGA, which is consumer available [176]. By connecting the DDC2 to a computer via this FPGA, the configuration settings on the DDC2 such as the triggering can be managed. During operation, when a PMT signal is produced, the digitised PMT signal from the DDC2 is handled by the FPGA and then forwarded to the computer through a USB cable as an ASCII (text) table, with an entry for the timing and also the ADC count for each sample. Transfer of data using ASCII is slow, and for this beam test it was found that a triggering frequency of above $\sim$10 Hz starts to cause loss of data in the FPGA

Figure 5.8: Picture of tank placed inside the MT6.2 enclosure (left) and picture of the PMT floating inside the tank which is filled with distilled water (right).

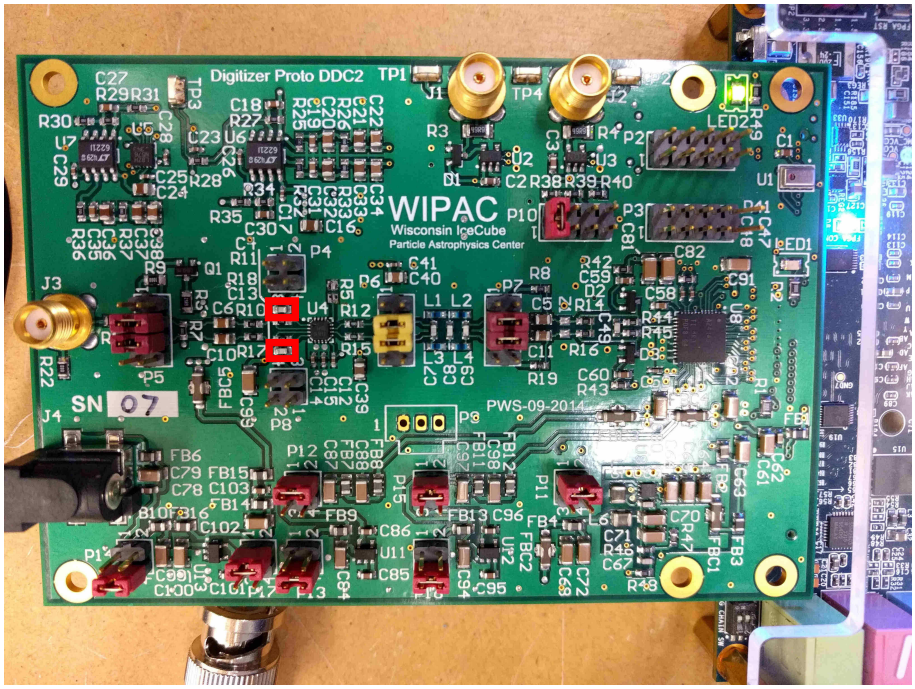

Figure 5.9: Photograph of the DDC2 (Digitizer Daughter Card, revision 2) which is the waveform digitiser used in this beam test. Highlighted in red are 2 capacitors, C4 and C13, which form the low pass filter with resistors R11 and R18. These two capacitors were removed to disable the low pass filter.

output. The data rate is at maximum 2 Hz because of the requested low intensity beam and low coincidence rate so this does not cause any issues. It would be more efficient to use a binary format data transfer and this is currently in development.

5.2.4 Calibration

The DAQ needs to be calibrated so that conversion can be made between ADC counts, which is the raw output from the DDC2, to a value of the voltage. This conversion factor is called the least significant bit (LSB) and is obtained by triggering the digitiser to record a known voltage, which is done using a pulse generator. A 1 MHz sine wave of amplitude 1 V is used as the signal. From this, the LSB was found to be 0.220 mV/ADC count. After subtracting the baseline, the dynamic range of the DDC2 was found to be 2 V.

The gain variation of the PMT is monitored daily by the LED system which is shown in Figure 5.7. This LED is a standard commercially available green LED. A 4 V square pulse with a width of 40 ns was used to flash the LED and also used as an external trigger on the DDC2, to record waveforms detected from the LED photons. Each of the recorded waveforms is integrated over to get the total charge deposited on the PMT. A charge histogram is produced, such as the one shown in Figure 5.10. A Gaussian distribution with a normalization A, mean μ and standard deviation σ is fitted to the distribution. As outlined in Appendix A.1, the average number of PE liberated from the photocathode per waveform (PE) and the PMT gain (g) can be estimated using the following equations:

$$PE = \left(\frac{\mu}{\sigma}\right)^2 \tag{5.1}$$

$$g = \frac{\mu}{PE \cdot C \cdot R} \tag{5.2}$$

where g is the gain, C is the charge of a single electron i.e. 1.6×10^{-19} C and R is the impedance, which for the DDC2 is 150 Ω.

Figure 5.11 shows the stability of the gain and PE as a function of the day. It was later found that the LED intensity saturates the PMT which breaks the relation shown in Equation 5.1, therefore the extracted PE and gain are only effective. In this analysis, we rely on the known gain of this PMT. Effective PE and gain can still, however, demonstrate the stability of the PMT and water condition. The LED was seen to be malfunctioning in

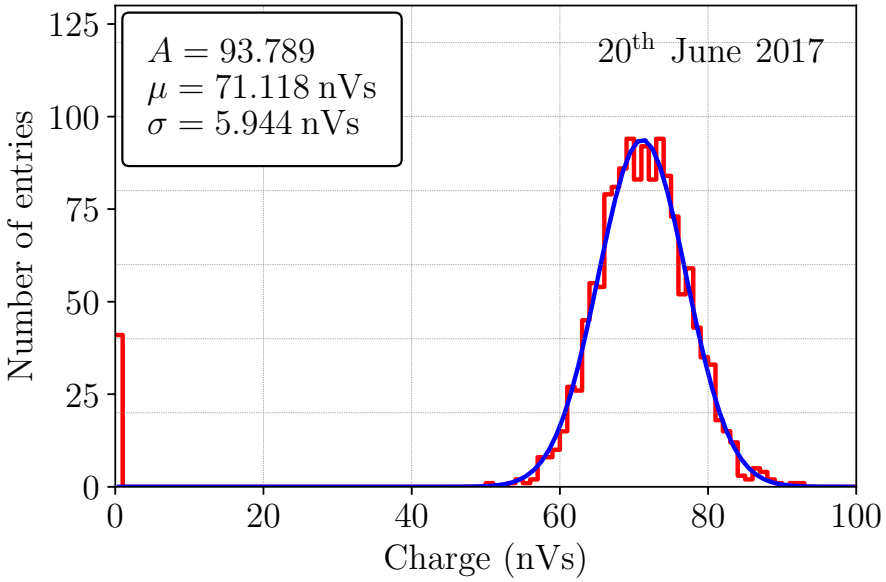

Figure 5.10: Charge distribution of data in nanovolt-seconds collected with the PMT on 20^{th} June 2017 of a flashing LED pulse. Fitted to this distribution is a Gaussian distribution with normalization A, mean μ and standard deviation σ.

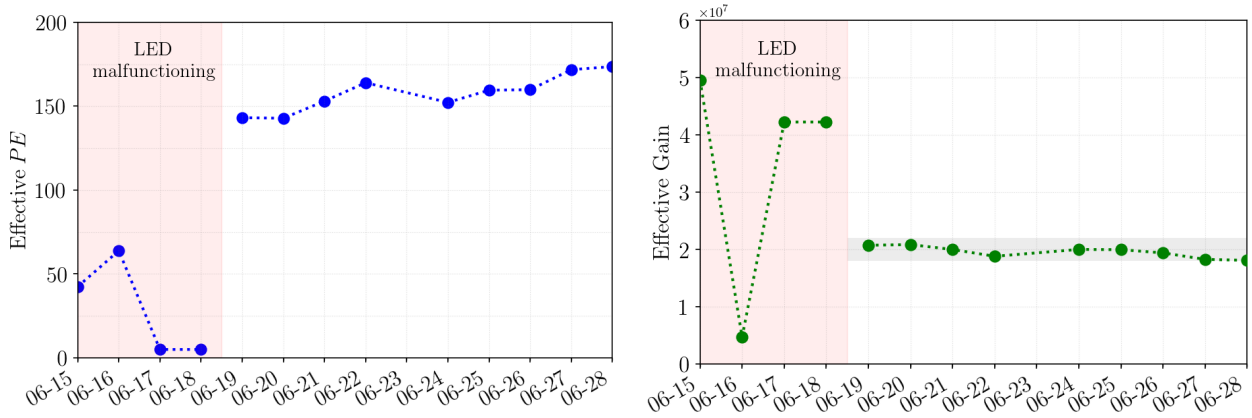

Figure 5.11: On the left, a plot showing the variability of the average number of effective PE liberated from the photocathode per waveform as a function of the date and on the right a plot showing the variability of the effective gain as a function of the date, with a 10% error shaded in grey. For the dates June 15–June 18, the LED was found to be malfunctioning.

the first 4 days of data taking, and on June 19, a visual inspection found the LED to be very wet. The LED was then moved further from the tank to prevent water condensation. After this, the effective gain and PE can be seen to be stable with time, the effective gain being at a value of 2×10^7 and the effective PE at ~ 150. This means that the experimental setup was stable over the period of data taking. From this measurement a 10% error is assigned on the PMT gain (as shown on the figure). By assuming the stability of the LED system, it was concluded that water transparency degradation is not a problem for any of the measurements taken in this beam test.

5.3 Results

5.3.1 PMT waveforms

Figures 5.12 and 5.13 show the digitised waveforms for 2 GeV electron and 8 GeV pion data. These data sets are used to do the pulse shape comparison, where an EM shower and a MIP like particle deposit similar charges. Each digitised waveform represents a triggered event that produced Cherenkov radiation in the detector volume. Waveforms are plotted into 16 charge bins.

Each charge bin contains a collection of waveforms. From an initial observation, both electron and pion produced waveforms appear to have a marginal difference in width and share a reasonably similar shape. Each waveform consists of a primary and secondary pulse located between 100-200 ns for each waveform. The amplitude of the first pulse in each bin grows with charge until ~ 1500 mV, which may be an indication of saturation (see Section 5.3.4). Similarly, the second pulse demonstrates a linear growth with increasing charge.

At this stage, it is difficult to distinguish between the electron and pion produced waveforms. Further pulse shape analysis is explored by:

- Characterising the primary pulse.
- Characterising the secondary pulse.
- Understanding saturation of the pulse amplitude despite the sufficient dynamic range.
- Determining whether the spread of the beam influences the width of the pulses.

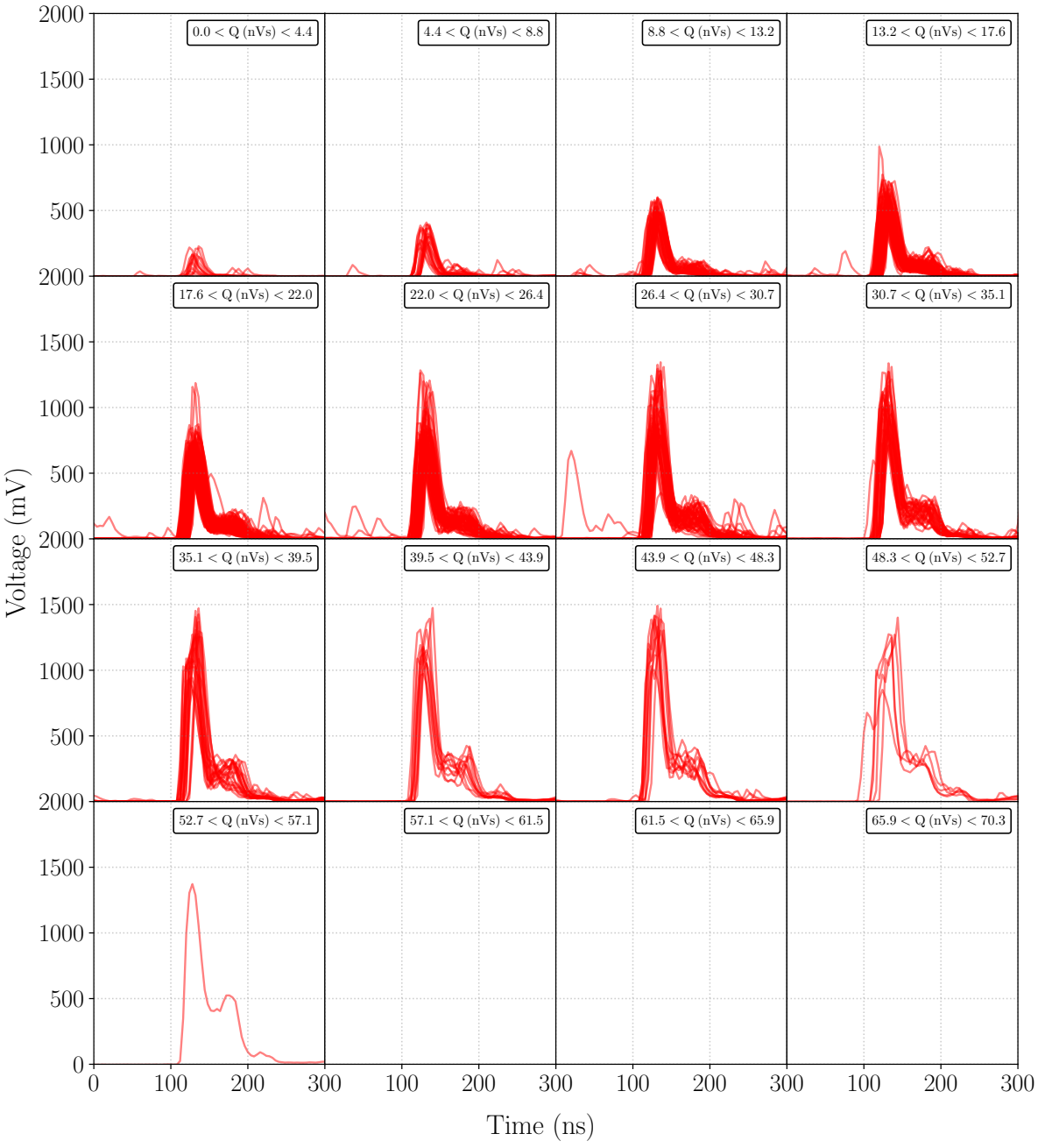

Figure 5.12: PMT waveforms for a 2 GeV electron triggered beam, split up into respective charge bins labelled on the top right of each plot.

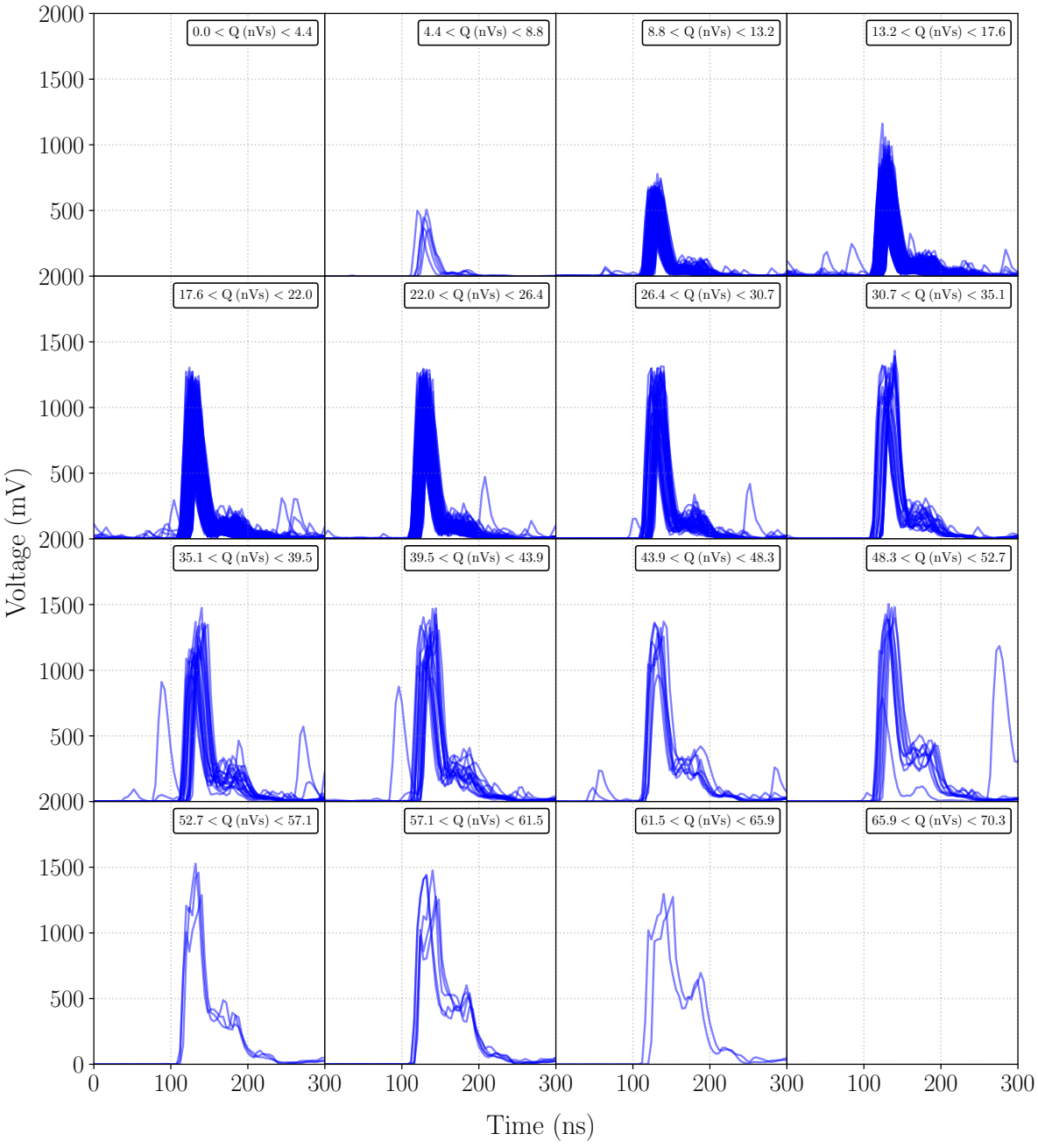

Figure 5.13: PMT waveforms for an 8 GeV pion triggered beam, split up into respective charge bins labelled on the top right of each plot.

5.3.2 Primary pulse

In order to identify the features of the waveform, it is split into two regions: primary pulse and secondary pulse. The primary pulse occurs in the timing region of $\sim$100-150 ns and it reflects the pulse generated by the PMT from standard photo multiplication. To isolate the primary pulse, a Gaussian distribution with normalization A_p, mean μ_p and standard deviation σ_p is fitted, ignoring the waveform contributions above 150 ns so as to approximate only the primary pulse. The produced pulses can be seen in Figure 5.14 for a 2 GeV electron beam and Figure 5.15 for an 8 GeV pion beam. For the majority of waveforms, this procedure can be seen to be a reasonable estimate of the primary pulse. However, there are outliers which either did not fit well to the waveform or simply did not fit all, either because the fit failed or because the waveform was anomalous. These can be identified and removed simply by requiring 100 ns $< \mu_p <$ 150 ns and 2.5 ns $< \sigma_p <$ 15 ns, thus only selecting the higher quality waveforms. In total, this cut removed $\sim$2% of waveforms. All primary pulse results shown from now will have this selection imposed. Pulse shape analysis can now be done to compare the two datasets, but first the three other points discussed above are looked into to understand the impact they might have on the pulse shape analysis.

5.3.3 Secondary pulse

The waveforms in Figures 5.12 and 5.13 can be seen to exhibit a non-Gaussian secondary peak that grows with increasing charge at timings of above $\sim$150 ns. Such behaviour is a common feature of PMTs and can be described as:

- Afterpulse: Electrons accelerated between dynodes induce ionization of residual gas molecules. Afterpulsing is described to grow linearly with charge; however, the timing range they are expected to be seen in is from 300 ns to 11 μs and so the secondary pulse seen in the waveforms here are not likely due to afterpulsing [52].
- Late pulse: The primary PE which impact the first dynode elastically or inelastically backscatter. It briefly decelerates and accelerates again towards the dynode chain, due to the electric field. The delay between the first and second peak should equal twice the PE transit time between the photocathode and amplification chain. The resultant peak is completely separate from the main pulse with a broadened response

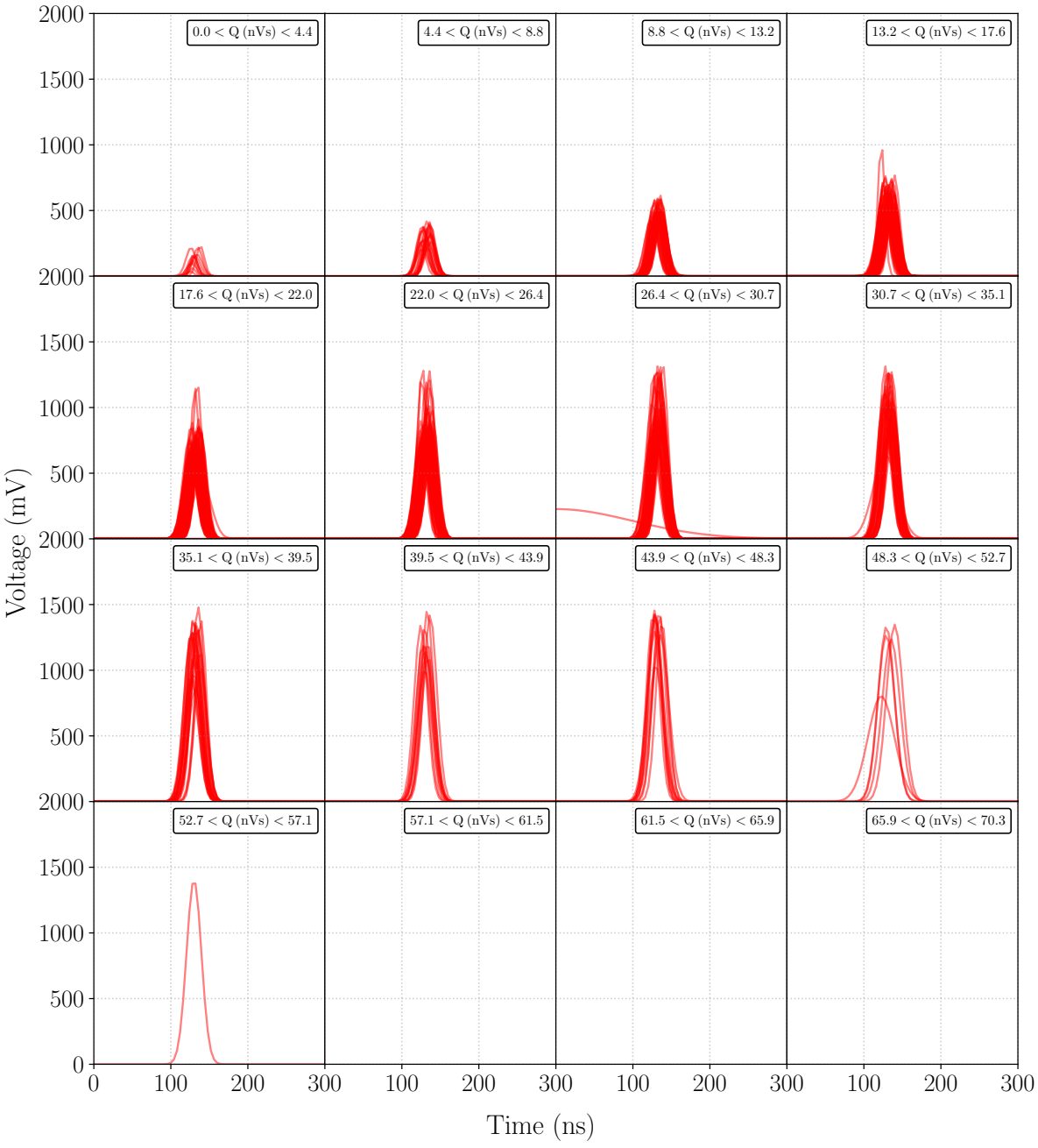

Figure 5.14: Primary pulse extracted with a Gaussian fit for a 2 GeV electron beam, split up into respective charge bins labelled on the top right of each plots.

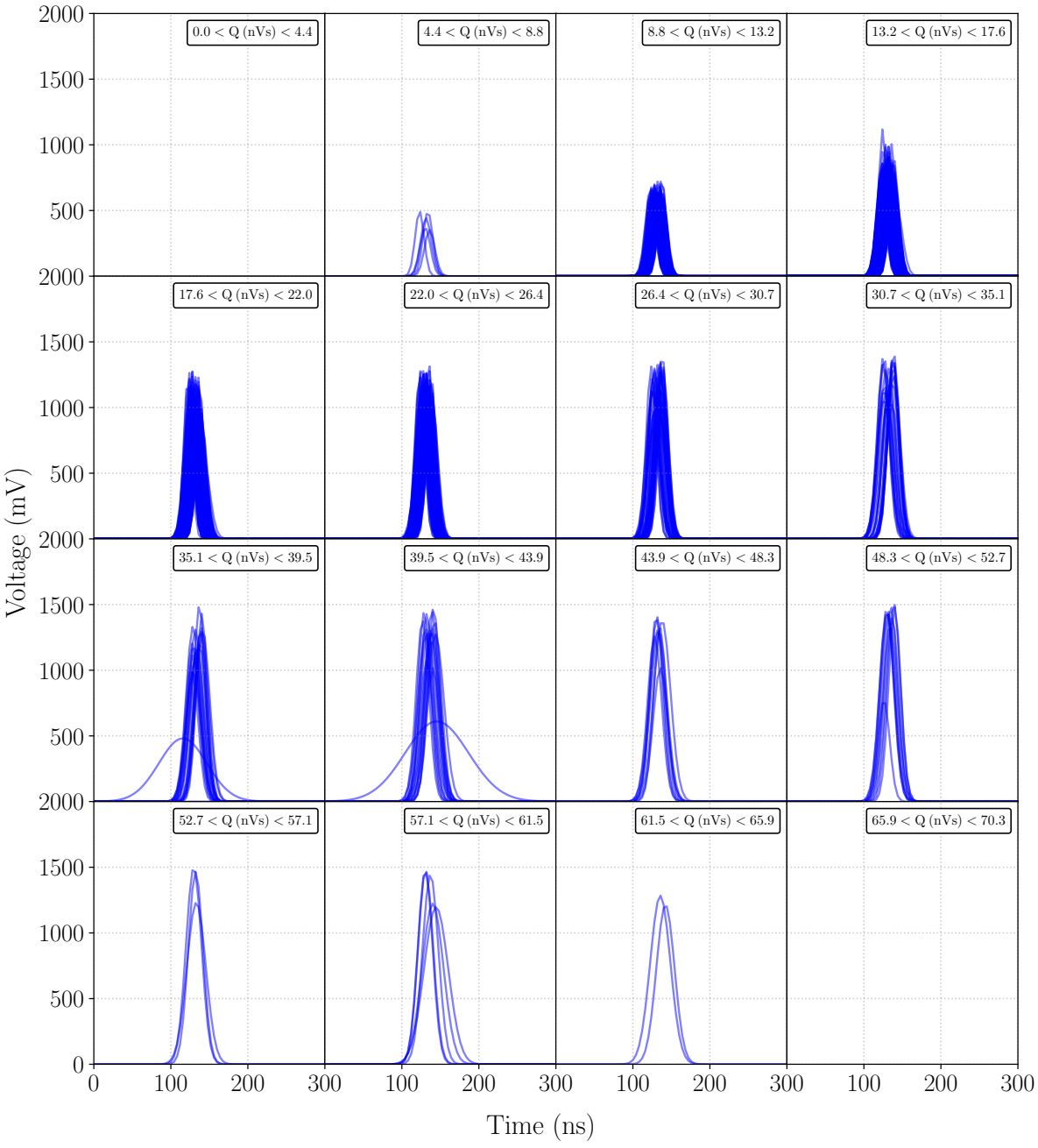

Figure 5.15: Primary pulse extracted with a Gaussian fit for an 8 GeV pion beam, split up into respective charge bins labelled on the top right of each plots.

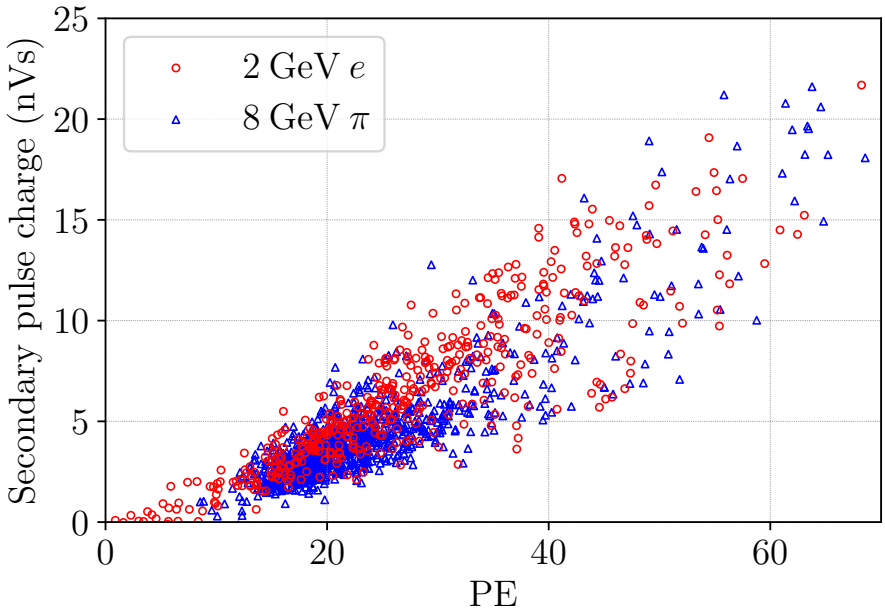

Figure 5.16: Charge of the secondary pulse plotted as a function of the charge of the waveform. In red circles show data points for a 2 GeV electron beam and in blue triangles show data points for an 8 GeV pion beam. For both configurations, it can be seen that the second pulse grows linearly with the total waveform.

time. Generally, this occurs on a timescale of up to 70 ns after the primary pulse and is expected to grow linearly with increasing charge [177].

From the timing, the secondary peak is likely to be due to late pulses and to confirm this one can check whether there is a linear relationship between the total charge and the secondary peak charge. To calculate the secondary peak charge, the charge of the Gaussian primary peak is subtracted from the total charge of the waveform (see Section 5.3.2). Figure 5.16 shows the secondary pulse charge as a function of the total charge of the waveform for both the 2 GeV electron beam and an 8 GeV pion beam. This plot demonstrates the linearity between the two, and so confirms that the secondary pulse is due to late pulses. The linear behaviour continues even for high values of charge, suggesting that it is not limited by saturation effects of the primary pulse.

5.3.4 Saturation

PMT saturation arises when the number of PE impacting the dynode chain exceeds its amplification capability. That is, the dynode is not able to emit enough electrons in response to primaries and so fails to amplify the PE with the proper gain multiplication.

Although each dynode is connected to a ground that replenishes the electrons, there is a threshold to the rate at which the electrons can be ejected from a dynode. The onset of saturation causes the voltage read out from the PMT to become non linear with respect to the number of incident PE until, with increasing PE, it eventually plateaus.

Figures 5.12 and 5.13 show the effect of PMT saturation. The waveform voltage stops increasing around $\sim$1500 mV suggesting the PMT is saturated. For a given energy, waveforms for the electron data experience more saturation compared to waveforms from pion data because of the larger charge deposition by EM showers vs MIP tracks. Saturation becomes an issue for data using an electron beam at the high energies, motivating the use of the lower energy electron data for this analysis.

5.3.5 Beam spread

As mentioned in Section 5.1.5, the beam features may also have an impact on the waveform features. This was studied by looking at the beam profile data taken using the MWPCs as shown in Figure 5.5. Figure 5.17, left, shows the spread of the beam as a function of the beam energy. Here, the average spread over the X-Y plane and the 3 MWPC data is computed and plotted as a function of the beam energy for an electron trigger in red and a pion trigger in blue. This plot shows that the beam is more focused at the higher energies

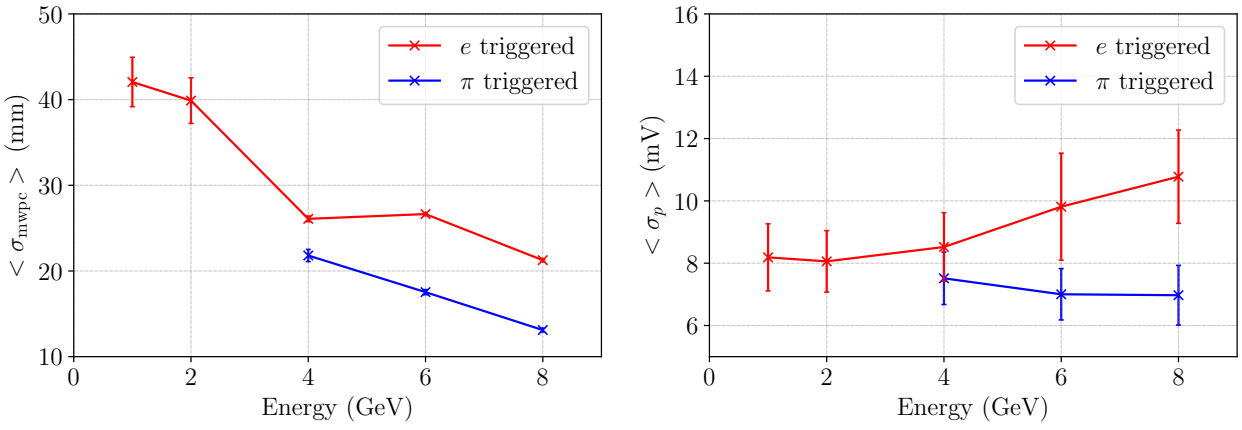

Figure 5.17: Left figure shows the average spread of the beam as a function of the beam energy for an electron trigger and pion trigger. Spread was computed from beam profile data which was taken using 3 multi-wire proportional chambers (see Figure 5.5). The right figure shows the average of the primary peak width as a function of the beam energy. In both figures electron and pion triggered data are shown in red and blue, respectively.

for both electron and pion triggering. This is to be expected as it takes more secondary collisions to produce the lower energy beams from the initial 120 GeV primary beam. The beam will spread and the overall flux will also reduce as particles of a lower energy are selected. Indeed, when triggering on pions for energies less than 4 GeV, the flux drops so low that a significant amount of waveforms could not be recorded.

MWPC data shows the spatial spread of the beam entry location. At energies below 4 GeV for electrons, this becomes $\sim$20 mm greater (a factor $\sim$1.75) than at 4 GeV and above. However, Cherenkov photons from an electron, displaced a distance of $\sim$20 mm from the beam entry location would correspond to a timing difference of only $\sim$100 ps as detected on the PMT inside the tank. Therefore, the spatial spread of the beam at the lower energies is not expcted to impact the pulse shape. The effect of beam halo increases as the energy is decreased but, as mentioned in Section 5.1.5, this should not be significant due to the requested low flux of the beam.

Figure 5.17, right, shows the spread of the primary PMT pulse (σ_p). The electron beam is shown in red and the pion beam is shown in blue. Unlike the beam monitor data, measured σ_p increases for electron data but not pion data. This trend is different from the beam monitor data therefore, the beam spread is not seen to have an influence in the waveform data.

5.3.6 Pulse shape analysis

In the previous sections it is demonstrated that the higher energy beam configurations have problems caused by the growth in the secondary peak and additionally for the electron beam, the saturation of the primary peak. Alternatively, at the lower beam energies the flux becomes small and the beam more spread to the point where beam halo effects may be significant or large enough statistics cannot be collected. On top of this, the pulse shape analysis must occur for similar charge waveforms as this is what IceCube detects, therefore the datasets to compare must be chosen such that they have similar charge. With these points in mind, the 2 GeV electron data has been chosen to compare to the 8 GeV pion data (waveforms shown in Figures 5.12 and 5.13). With these datasets, the effects from the secondary pulse, saturation and beam spread are kept to a minimum, while still allowing the comparison of similar charge waveforms. Note, although the *in situ* calibration has a

problem, the observed charge deposition corresponds to ∼20 PE assuming a known gain of this PMT.

The discriminator that will be used to do the pulse shape analysis here will be the spread of the primary pulse σ_p. This is shown in Figure 5.18, where σ_p is plotted against the charge, where the red circles represent a waveform from the 2 GeV electron data and the blue triangle a waveform from the 8 GeV pion data. The red band shows the one sigma containment region for the 2 GeV electron data and the blue band shows the one sigma containment region for the 8 GeV pion data. By comparing the two, it can be seen that at the low charge, a statistical discrimination can be made. Here, the EM shower events tend to produce primary pulses which are more spread than for MIP events. The significance to which the discrimination can be made is not however to a degree at which the majority waveforms can individually be identified as being from either a MIP or EM shower event. At the higher charges, the power to discriminate is completely lost which can be understood as the result of saturation and secondary pulse effects as previously discussed.

5.4 Simulation

5.4.1 Geant4

A simulation of this beam test is performed using Geant4 [178], a comprehensive software toolkit designed to simulate physics processes related to particle propagation within matter. Here C++ object-orientated code is utilised to generate a geometrical layout of the experiment and simulate charged particle interactions in the constructed detector. The geometry is setup as follows. The "world" is defined as a $4 \times 4 \times 4$ m box which will contain all objects. The tank is placed inside this world and its material, dimensions and water content reflect the description given in Section 5.2.2. A PMT is constructed consisting of a sphere with radius 7″. The PMT is placed inside the tank such that the bottom half of the PMT is immersed in the water. The submerged surface of the PMT is then defined to be the sensitive detector. The simulation does not include the foam ring which has the potential to block some photons, or the response of the Tedlar lining which may lead to reflections. Figure 5.19 shows a schematic of the geometry of this simulation. The beam particles are generated upstream and the simulated events are recorded if the beam

particle hits the SC4 scintillator (described in Section 5.1.4). Note that a full simulation of the MTest beam line is not performed, instead mono-energetic particles are generated in front of the detector assuming that energy loss and spread due to known materials are small. Physics processes are then chosen. For this beam test, the GEANT4 libraries for EM physics and muon physics are added, which incorporate processes such as Cherenkov radiation, multiple scattering, Bremsstrahlung radiation and ionization for the electrons and muons, and then pair production, Compton scattering and the photoelectric effect for photons (see Section 1.4.2).

The efficiency and spectral response of the PMT must also be considered. The PMT is specified by Hamamatsu for the wavelength range 300–650 nm [50]. However, the optical transmission of the glass falls at wavelengths below 350 nm and at the larger wavelengths the efficiency of the PMT decreases. Therefore, in the simulation, only the Cherenkov

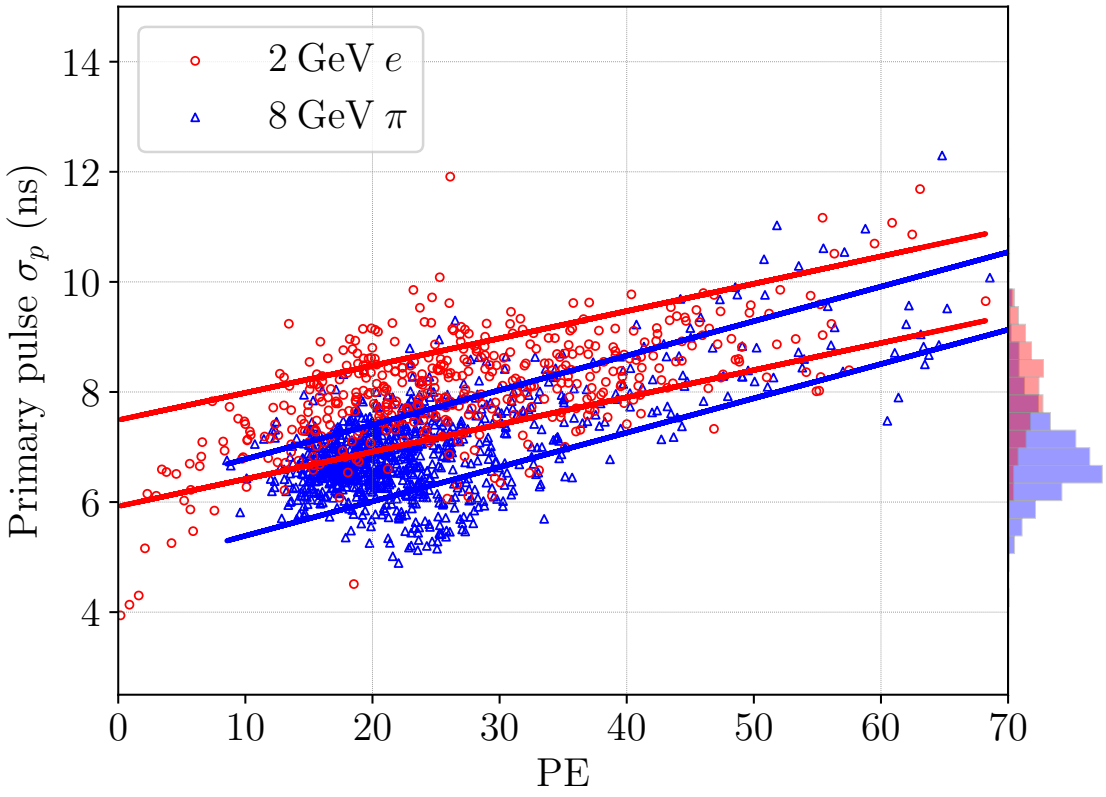

Figure 5.18: Scatter plot showing the spread of the primary pulse σ_p vs the deposited charge. Each red circle corresponds to a waveform from the 2 GeV electron beam and each blue triangle corresponds to a waveform from the 8 GeV pion beam. The red and blue bands show the one sigma containment region for the 2 GeV electron and 8 GeV pion beams, respectively. On the right is shown a histogram of the primary pulse σ_p for the respective waveform data.

photons produced with wavelengths between 350–550 nm are registered as hits on the PMT. The efficiency of the PMT takes into account the quantum efficiency of the PMT, optical absorption in the PMT, glass shell absorption, discriminator threshold effects, and photocathode non-uniformity. Here a flat 10% [50] efficiency is used for the photons inside the spectral range specified. The simulation is still idealised, in that it does not take into account the SPE spread and the angular dependence of the efficiency of incident photons. Such effects would smear the hit distribution, which is accounted for in an ad hoc way using a Gaussian kernel.

5.4.2 Hit distribution

In this section, the hit distribution from data and simulation will be compared to infer how saturation affects the high charge waveform data. Although the efficiencies are estimated, there is a disagreement between data and simulation for the overall hit distribution. Here, the horizontal axis is scaled such that the simulated hit distribution peak of the 8 GeV pion data agrees with the simulation. A smearing is also applied on the simulation to again match the pion distribution. The same Gaussian kernel is applied for both pion and electron simulations by assuming the unknown smearing is due to photon propagation physics.

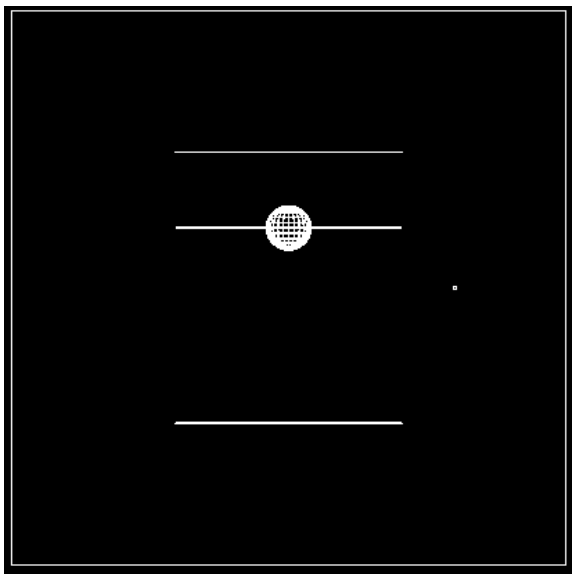

Figure 5.19: GEANT4 simulation [178] geometry of the beam test. The underside of the halfway immersed PMT is defined to be the sensitive detector. PMT hits are logged when the electron/pion penetrates the tank and hits the downstream SC4 scintillator.

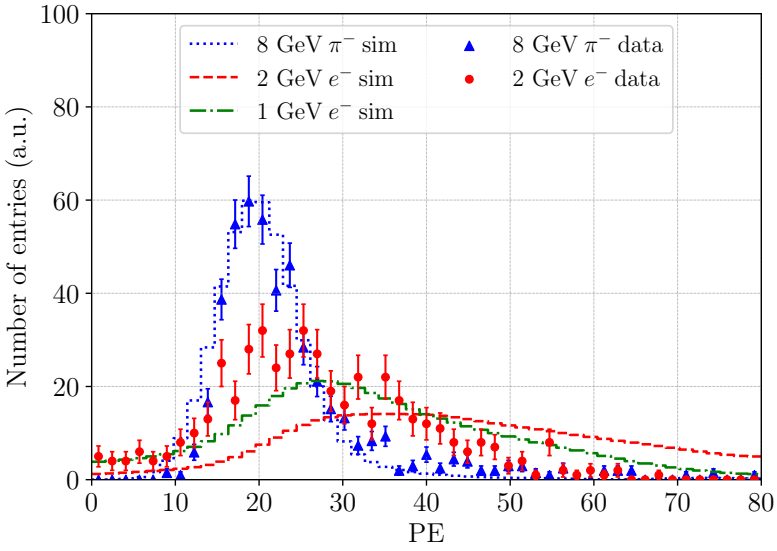

Figure 5.20: Hit distribution of the number of photons hitting the PMT for both electron and pion events. Data points taken from this beam test are compared to GEANT4 simulations. The presence of saturation can be seen to have a large affect for very high charge data, such as for the 2 GeV data with electron triggering.

The results are shown in Figure 5.20. Data is shown for 8 GeV pions as blue triangular points and for 2 GeV electron as circular red points, where both are shown with statistical error bars. The dashed blue line shows the simulation for 8 GeV pions, the dashed red line shows the simulation for 2 GeV electrons and the dashed green line shows the simulation for 1 GeV electrons. The 8 GeV pion simulation is fitted to the data as described above. The same correction is applied to the 1 GeV and 2 GeV electron simulations. Under these conditions, long tails are observed in the electron simulations. This implies that the 2 GeV electron data is saturated at high charge with the PMT entering the non-linear regime discussed in Section 5.3.4, causing the voltage read out to plateau. Events with high charge are expected to migrate to lower charge as the data suggest. It is also observed that the 1 GeV electron simulation has a better agreement with the electron data. This suggests electrons experience energy losses in the beam line through the instrumentation such as the Cherenkov counters, MWPCs, and scintillators (Section 5.1.2). Significant energy loss is not expected for MIP particles such as pions.

5.5 Conclusion

Current water Cherenkov telescopes such as IceCube have difficulties identifying particles at low energies (few GeV) due to the relatively sparse instrumentation. The low level PMT waveform features are not currently utilised; however, the pulse shape shares characteristics of the parent particle. It is demonstrated in this beam test the possibility of performing particle identification using pulse shape analysis of waveforms from a single PMT between MIP-like particles, such as pions, and electromagnetic showering particles, such as electrons. A PMT was floated inside a tank filled with distilled water and using the beam provided by the Fermilab Test Beam Facility, electrons and pions were shot into the tank at different energies. 2 GeV electron and 8 GeV pion waveforms are compared as they deposit similar amounts of charge. The primary pulse spread was used as a discriminator and it is shown that at low charge, there is a discrimination that can be made between 2 GeV electron and 8 GeV pions. Such techniques can be applied to future neutrino telescopes focusing on low energy physics, such as the IceCube-Upgrade.

Part IV

Hadronization processes in neutrino interactions

6 Hadronization processes in neutrino interactions

Current and future long-baseline oscillation experiments, such as the IceCube-Upgrade [59], T2K [179], NOvA [180], ORCA [181], INO [182], Hyper-Kamiokande [183], and DUNE [184] utilise neutrinos with energies in the 1 to 10 GeV range. In the past, lepton kinematics were sufficient to extract oscillation parameters, however, higher precision measurements can be possible by exploiting information from hadronic system. The hadronic system was often neglected or poorly modeled in the past, but can have significant effects on high precision neutrino oscillation and cross-section measurements. Among the physics of hadronic systems in neutrino interactions, the hadronization model controls multiplicities and kinematics of final state hadrons from the primary interaction vertex. For relatively high invariant mass events, many neutrino experiments rely on the PYTHIA program [185]. Current neutrino interaction generators such as GENIE [43] and NEUT [186] rely on the outdated and no longer supported PYTHIA, version 6 (PYTHIA 6). In this chapter, the PYTHIA 6 hadronization model is updated in the GENIE neutrino interaction generator to the contemporary PYTHIA 8 model, which is the successor to PYTHIA 6 [187].

6.1 Hadronization Modelling

6.1.1 GENIE neutrino interaction generator

GENIE is a ROOT-based neutrino Monte-Carlo event generator [43, 188]. It stands for "Generates Events for Neutrino Interaction Experiments". It was developed over a period of three years, from 2004 to 2007, entirely in C++ using object-oriented methodologies and has been continously improved ever since. Previous generations of neutrino interaction simulations were developed and maintained for the particular experiment at hand. Well known examples are the Soudan-2 experiment, which developed the event generator

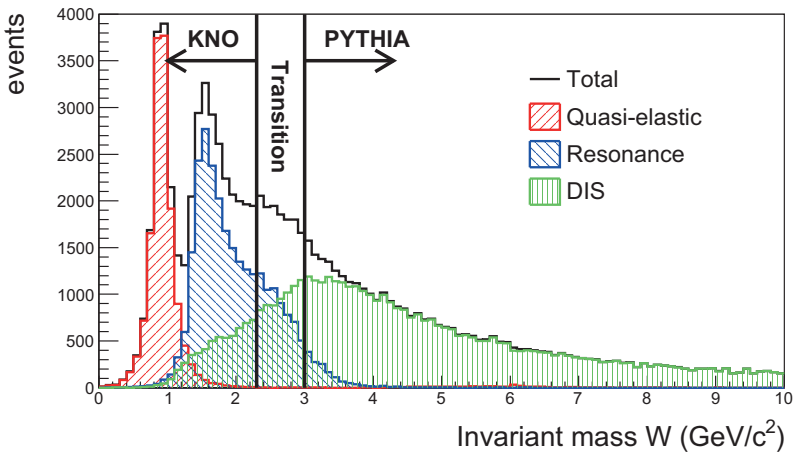

Figure 6.1: W distribution of ν_μ-water target interaction in GENIE. Left red hatched region is quasi-elastic scattering, middle hatched region is resonance interaction, and right green hatched region is from DIS. The W distribution can be split into three regions, KNO scaling-based model only region, PYTHIA 6 only region, and the transition region [190]

NEUGEN [189], and Super-Kamiokande and K2K experiments which use the event generator NEUT [186]. These event generators were developed with the needs of the specific experiments in mind and so were heavily tuned in order to have good agreements with the experimental data. GENIE strives to provide a more general framework that is valid over a range of energies, nuclear targets and neutrino flavours. Its long term goal is to become a "canonical" neutrino event generator, allowing future experiments to adopt GENIE as a complete neutrino event generator.

The few-GeV energy range is particularly important for neutrino oscillation experiments, where an accurate reconstruction of the final state particles is crucial in order to keep cross-section uncertainties to a minimum, which in turn would translate to measurements of the oscillation parameters of a higher precision. The mixing of QE, resonance and DIS interactions (see Figure 1.12) at this energy range make accurate simulations of the transition region challenging as each interaction has its own model. In GENIE, the type of neutrino interaction is determined by the value of the invariant hadronic mass W (see Figure 1.13 for definition). Figure 6.1 shows the contributions from the interaction types as a function of W. At low $W \sim 1$ GeV, there is a sharp peak for the contribution from QE scattering which fades quickly as W is increased to 2 GeV, where resonance and DIS interactions become dominant. The transition from resonance to DIS takes place gradually over a wide W range, $\sim$2–3 GeV after which the only interaction mechanism is via DIS.

GENIE employs its own hadronization model for DIS events called the AGKY (Andreopoulos-Gallagher-Kehayias-Yang) model [191]. It was created in order to improve MC simulations for the MINOS experiment and is now the default hadronization model in GENIE. The AGKY model is split into two parts: a phenomenological description based on the Koba-Nielson-Olesen (KNO) scaling law [192] which is used at low W and the well known PYTHIA 6 [185] hadronization model which is used at high W. The transition takes place gradually over a transition window $\left[W^{\text{tr}}_{\text{min}} = 2.3\,\text{GeV}\,,\, W^{\text{tr}}_{\text{max}} = 3.0\,\text{GeV}\right]$ over which the fraction of events hadronized using the PYTHIA 6 (KNO) model increases (decreases) linearly, as highlighted in Figure 6.1.

6.1.2 KNO hadronization model

The KNO scaling model is a phenomenological model that is tuned with data from the Fermilab deuterium-filled 15-foot bubble chamber [193] and the Big European Bubble Chamber (BEBC) at CERN [194]. The generation of the hadron shower particle content and 4-momenta in the AGKY model for low W, begins with the empirical expression:

$$\langle n_{ch} \rangle = a_{ch} + b_{ch}\, \ln W^2 \tag{6.1}$$

in which n_{ch} is the charged hadron multiplicity, so $\langle n_{ch} \rangle$ represents the average of the charged hadron multiplicity and the coefficients a and b are tuned for the particular collision using relevant data from bubble-chamber experiments. Once $\langle n_{ch} \rangle$ has been determined, the average hadron multiplicity $\langle n \rangle$ is calculated using $\langle n \rangle = 1.5\,\langle n_{ch} \rangle$ [195]. Now that $\langle n_{ch} \rangle$ is known, n_{ch} can be calculated by using the KNO scaling law [192]

$$\langle n \rangle \times P(n) = f(n/\langle n \rangle) \tag{6.2}$$

which asserts that the scaled multiplicity distribution is parameterised by a universal scaling function f, which is given by the Levy function [192]:

$$f(z;c) = 2e^{-c}c^{cz+1}/\,\Gamma\,(cz+1) \tag{6.3}$$

where $z = n/\langle n \rangle$ and c is an input parameter which depends on the initial state and Γ is the gamma function.

Now the hadrons are selected up to the calculated n, taking into account conservation laws and kinematic constraints. Once a particle is generated, the hadronization model then performs the hadron decay. This is done by generating the baryon four-momentum P_N^* using nucleon parton distribution functions (PDFs), which represent the number density to find a parton (quark or gluon) carrying a momentum fraction, x_F (see Section 1.4.1). This process is then iterated over once P_N^* has been generated in order to calculate the four-momentum of the remaining hadrons.

6.1.3 PYTHIA hadronization model

At high W hadronization is performed using the PYTHIA MC generator [185]. PYTHIA is regarded as one of the standard tools for the generation of high-energy collisions. Fragmentation in PYTHIA is described by the Lund string fragmentation model, which was originally developed in the late seventies by the Lund group [197]. Formerly this model was packaged in a separate program called JETSET, which has now been merged with PYTHIA.

The Lund fragmentation model is based on the dynamics of one-dimensional relativistic strings that are stretched between coloured partons. These strings represent the colour flux and in particular, are subject to a linear confinement potential. The hadronization process is described by break-ups in the strings through the production of new quark-antiquark pairs (Figure 6.2). An iterative approach is used to perform the fragmentation as each break up is causally disconnected, until the individual systems reach a cut-off energy threshold.

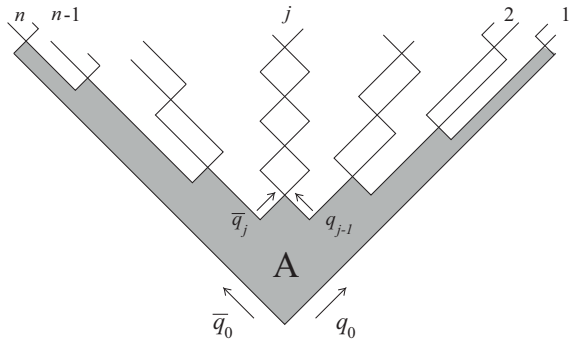

Figure 6.2: Illustrative depiction of the massless relativistic string in the Lund string fragmentation model. New $q\bar{q}$ pairs are created by breakups in the string from an intiaited quark-antiquark pair $q_0\bar{q}_0$ [196].

After the creation of a $q\bar{q}$ pair, the transverse momentum, $p_\perp$, of the created $q\bar{q}$ pair is determined using the tunnelling mechanism, which leads to a Gaussian spectrum of the $p_\perp$ for the produced hadron. This is done in order to account for the energy contained in the transverse mass, $m_\perp = \sqrt{m^2 + p_\perp^2}$. The variable z gives the fraction of energy transferred to the produced hadron out of the total energy available (see Section 1.4.1). An associated fragmentation function $f(z)$ gives the probability that a given z is chosen. The simplified Lund symmetric fragmentation is given by [197]

$$f(z) \propto z^{-1} (1-z)^a \exp\left(\frac{-bm_\perp^2}{z}\right) \tag{6.4}$$

where a and b are left as tunable variables so as to have a means of regulating the distribution of energy across the final states.

Pythia typically caters to high-energy accelerator experiments such as those at the LHC and so its default tuning is not quite suitable for neutrino oscillation experiments which are lower in energy. It is shown in Reference [198] that by borrowing tuning expertise from accelerator experiments at lower energies, specifically the HERMES experiment [199], an improvement in the charged hadron multiplicity bubble chamber data can be obtained.

This describes the underlying model of both pythia 6 and pythia 8, which fundamentally means they are the same model. However, in terms of the implementation, there exists notable differences. Pythia 6 is written entirely in Fortran which introduces the need for wrapper classes to interact with the C++ code in genie. Pythia 8 does away with this as it is has been rewritten from scratch in modern C++, meaning genie can have direct access to its libraries. Pythia 8 is also the officially supported release of pythia, therefore more advanced event generation features (such as beam remnant structure) which do not currently exist in genie can be implemented here with the support and guidance of the pythia authors.

6.2 Approaches

6.2.1 Direct translation

The most direct and straightforward approach to take is to directly translate the PYTHIA 6 routines in GENIE into the PYTHIA 8 equivalents. Two immediate issues arise, however they can be easily circumvented. The first is the dependence on ROOT classes which exist only when PYTHIA 6 is built. GENIE interfaces with PYTHIA 6 through the ROOT singleton class `TPythia6`, which contains the PYTHIA 6 instance along with necessary wrapper classes to port the generated PYTHIA 6 event list into C++. Each particle in the PYTHIA 6 event list is translated into a C++ container class called `TMCParticle`, which is able to store information such as the particle type, energy and other event generation details. This manipulation is no longer needed when interfacing with PYTHIA 8. All that is needed is a new singleton class in GENIE (`Pythia8Singleton`) holding the instance of PYTHIA 8, from which the hadronization routines can be called and the event list can be accessed directly. Note that PYTHIA is also available in GENIE for its decay routines, therefore when translating routines to PYTHIA 8 equivalents, both the hadronization and decay in GENIE is affected. Essentially, there is no dependency on ROOT classes when using PYTHIA 8. With that said, there is, however, a complication in GENIE due to the misunderstanding of the scope of the `TMCParticle` class which has been used in GENIE in places unrelated to PYTHIA 6. There does already exist a similar particle container class in GENIE therefore the `TMCParticle` class must be replaced in order to completely excise the dependence on the ROOT PYTHIA 6 routines. Once this is done, PYTHIA 8 can be used in GENIE with ROOT no longer needing to be built with any version of PYTHIA.

The second issue is a minor issue to do with the status code conventions for particles that have been updated in PYTHIA 8 and are no longer compatible with PYTHIA 6. These status codes are integers which signify how the particle was produced. GENIE convention is based on PYTHIA 6 status codes, therefore a simple solution is to covert the status codes of PYTHIA 8 generated particles into the older PYTHIA 6 status codes to maintain compatibility with GENIE. Once this is done, the PYTHIA 8 can be run successfully in GENIE as shown in Reference [190].

The complication encountered relating to the `TMCParticle` class is, however, one symptom

of outdated code inside GENIE. The first implementation described above, while being able to run PYTHIA 8 inside GENIE is not substantial for the future maintainability of GENIE and so this work prompted the refactorisation of the hadronization and decay routines inside GENIE. This basically entails rewriting the hadronization and decay base classes to use more modular classes, as had already been done in other areas of GENIE [200]. Another point of concern in the above implementation was that PYTHIA 6 support was completely lost which may not be desirable for some GENIE users. Therefore, support of PYTHIA 6 must be maintained and further to this, the option of running PYTHIA 6 alongside PYTHIA 8 is also desirable (for example, in the situation when one wants to run with PYTHIA 8 hadronization routines, but also PYTHIA 6 decay routines). This is possible to implement though appropriate pre-processor flags.

The principal observable of interest here is the averaged charged hadron multiplicity $\langle n_{ch} \rangle$. This is one of the basic variables used to study hadronization processes and $\langle n_{ch} \rangle$ data is an essential input for hadronic shower modelling. Events were generated in GENIE using an arbitrary E^{-1} flux spectrum ranging from 0.5–80 GeV for ν_μ interactions with proton and neutrons. The `HadronizationTest` event generator list was used for generation, which restricts GENIE to simulate only CC DIS and CC resonance interactions (see Section 1.4.1). Figure 6.3 shows the $\langle n_{ch} \rangle$ distribution as a function of W^2 compared to data from the Fermilab deuterium-filled 15-foot bubble chamber [193] and the Big European Bubble

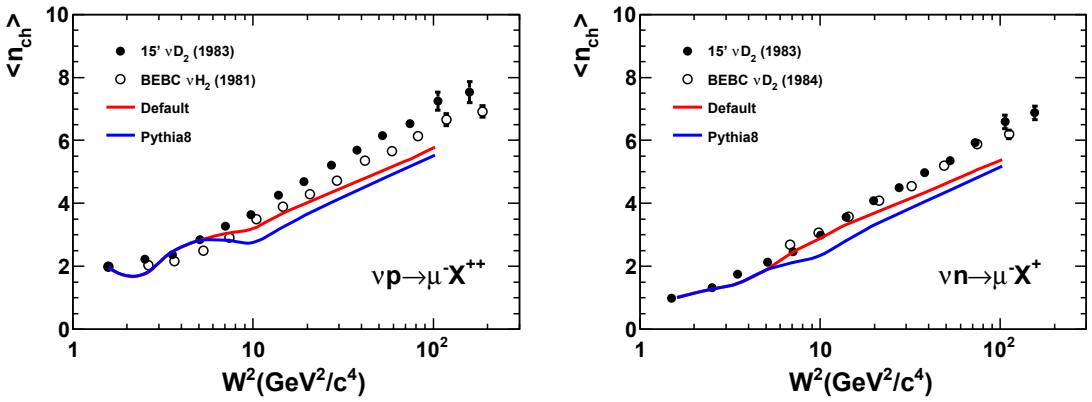

Figure 6.3: Averaged charged hadron multiplicity as a function of W^2. Here, two predictions from GENIE are compared with bubble chamber neutrino hadron production data from ν_μ-proton (left) and ν_μ-neutron (right) interactions [193, 194]. The upper red line represents default GENIE which uses PYTHIA 6 and the blue line represents GENIE with PYTHIA 8.

Chamber (BEBC) at CERN [194]. The left plot is for ν_μ-proton interactions and on the right is for ν_μ-neutron interactions. Shown in red is the distribution obtained for the current default GENIE, i.e. GENIE using PYTHIA 6. For details on the performance of PYTHIA 6 in GENIE see Reference [198]. In blue is shown the distribution obtained after translating to PYTHIA 8 as described above. Here, the latest version of GENIE is used from the GitHub code repository [43], commit number `951b40d` and for PYTHIA 8, version `8.243` is used.

At low W, the predicted curves follow the data points as the hadronization process is dominated by the KNO scaling-based model. As W increases, the predicted curves show deviations with bubble chamber data. This is because the default PYTHIA parameter tunings are tailored to higher energy LHC experiments, and so better agreement can be achieved by customised tuning of the Lund hadronization model parameters as demonstrated in Reference [198]. These parameters have been updated in PYTHIA 8 which is the cause of the discrepancy between it and the PYTHIA 6 distribution. In the future, once this PYTHIA 8 implementation is merged into the next version of GENIE, the tuning technology described in Reference [198] can be used once again to provide PYTHIA 8 parameter sets more tailored for neutrino experiments in the 1 to 10 GeV energy region. Distributions of other hadronization observables such as x_F are also examined and no major discrepancies are found between the PYTHIA 6 and PYTHIA 8 implementations.

6.2.2 Further features

With recommendations from the PYTHIA authors (S. Prestel in particular), improvements to the way hadronization is handled in GENIE is possible. More specifically, in GENIE the particles which are fed into PYTHIA are quark+diquark pairs conditional on the initial state and hit quark. This is shown in Table 6.1, taken from C. Andreopoulos [201]. The beam remnants are particles left behind from the incoming beam particle, which do not take an active part in the hard-scattering process. These still need to be accounted for as they are colour connected to the rest of the event. These can be quite complicated and PYTHIA has dedicated functionality to account for such effects [187]. However, GENIE in its current form does not take advantage of this, and so an improvement would be to handle this within PYTHIA. Instead of feeding PYTHIA with a quark+diquark to hadronize, the full

Init state	Hit quark	Leading quark	Remnant system	PYTHIA 6 assignment	Weirdness level
ν + p CC	d valence	(d $\rightarrow$) u	uu	u + uu	
ν + p CC	d sea	(d $\rightarrow$) u	$\bar{\text{d}}$ + uud	u + uu	$*$
ν + p CC	s sea	(s $\rightarrow$) u	$\bar{\text{s}}$ + uud	u + uu	$**$
ν + p CC	$\bar{\text{u}}$ sea	($\bar{\text{u}}$ $\rightarrow$) $\bar{\text{d}}$	u + uud	u + uu	$***$
ν + n CC	d valence	(d $\rightarrow$) u	ud	u + ud	
ν + n CC	d sea	(d $\rightarrow$) u	$\bar{\text{d}}$ + udd	u + ud	$*$
ν + n CC	s sea	(s $\rightarrow$) u	$\bar{\text{s}}$ + udd	u + ud	$**$
ν + n CC	$\bar{\text{u}}$ sea	($\bar{\text{u}}$ $\rightarrow$) $\bar{\text{d}}$	u + udd	u + ud	$***$
...	...	...	...	...	...
...	...	...	...	...	...

Table 6.1: Driving PYTHIA 6 from GENIE. "Some amount of monkey business in making quark+diquark assignments most certainly due to our own unfamiliarity with PYTHIA. Luckily, overall generation outcomes not sensitive to choices made" [201].

event kinematics can be supplied and in this way more complicated behaviour such as the beam remnant structure can be managed within PYTHIA.

The event kinematics are then fed to PYTHIA 8 using the `LHAup` class provided in PYTHIA 8. A few technical challenges arise when attempting to implement this, mostly centered around the initialisation of the PYTHIA 8 instance. The kinematics of the probe and hit nucleon is unique for each individual PYTHIA 8 instance and cannot be modified with re-initialisation. A simple fix is to do this re-initialisation event by event however the computation time increases by an order of magnitude as the initialisation call is expensive. Instead, the singleton class `Pythia8Singleton` is modified such that it only creates a new PYTHIA 8 instance if the probe and hit nucleon composition changes, therefore minimising the number of PYTHIA 8 instances needed. A re-initialisation was also required when the energy of the probe changed; however, the PYTHIA team (S. Mrenna in particular) was able to implement in PYTHIA 8, through the `GBeamShape` PYTHIA 8 class, a way to circumvent this. Therefore, in the recent releases of PYTHIA 8, only the maximum energy needs to be supplied during initialisation after which the PYTHIA 8 instance can be used for any energies. The results are shown in Figure 6.4, again in terms of $\langle n_{ch} \rangle$ vs W^2 distribution compared to bubble chamber data [193, 194]. Once again, PYTHIA 8 tends to underestimate the $\langle n_{ch} \rangle$ compared to the data. Once the above features are implemented into GENIE, a

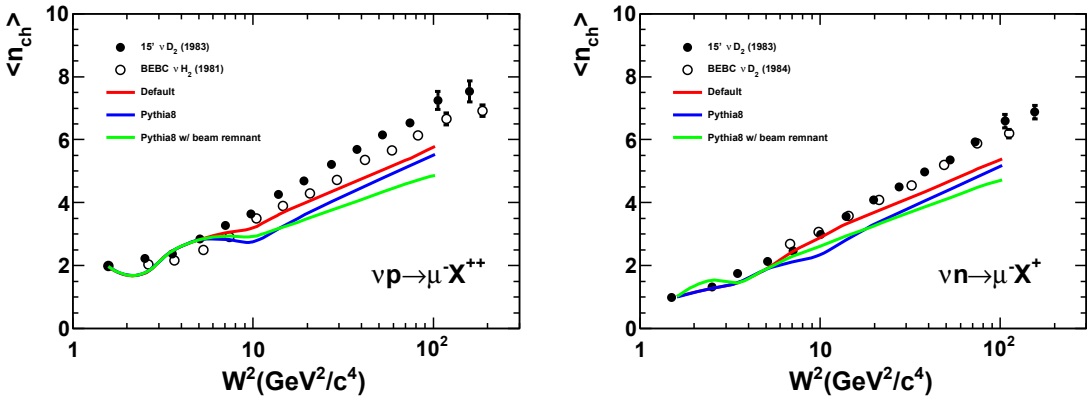

Figure 6.4: Averaged charged hadron multiplicity as a function of W^2. Here, two predictions from GENIE are compared with bubble chamber neutrino hadron production data from ν_μ-proton (left) and ν_μ-neutron (right) interactions [193, 194]. The red line represents default GENIE which uses PYTHIA 6, the blue line represents GENIE with a direct translation of the PYTHIA 6 routines into PYTHIA 8 and the green line represents an implementation of PYTHIA 8 in GENIE in which the beam remnant structure is also handled by PYTHIA 8 (see text for details).

hadronization process tuning, very similar to the one described in Reference [198], can be performed to tailor PYTHIA 8 for use in neutrino interaction processes.

6.3 Conclusion

Hadronization in the GENIE neutrino interaction generator is examined and the possibility of upgrading the hadronization model from the outdated and no longer supported PYTHIA 6 to the contemporary and rewritten C++ based model of PYTHIA 8 is attempted. First a direct translation of the PYTHIA 6 routines to the PYTHIA 8 is successfully carried out, along with a refactorisation of the GENIE hadronization routines. Comparison are made of the hadron multiplicites between the models and it is found that PYTHIA 8 agrees with PYTHIA 6, both however underestimating bubble chamber data. Further improvements to the GENIE hadronization implementation are attempted by allowing PYTHIA 8 to handle the beam remnant structure, rather than relying on its own ad-hoc model. PYTHIA 8 is by default tuned for higher energy LHC experiments, therefore, in the future, a tuning of the PYTHIA 8 parameters for neutrino experiments is needed.

Part V

Conclusion

7 Conclusion

The IceCube neutrino observatory has revealed a new frontier in the study of neutrino physics. Using a relatively simple detection mechanism combined with an immense fiducial volume, it has facilitated the study of neutrinos and particle physics in general, across magnitudes of order $\sim$GeV all the way up to $\sim$10 PeV. The work in this thesis makes this apparent, containing studies of fundamental spacetime symmetries using both atmospheric and astrophysically produced neutrinos, studies on the pulse shape characteristics of secondary particles produced in neutrino interactions and finally a study of the hadronization model used in these interactions.

Chapter 3 presents an analysis using atmospheric neutrino data of order $\sim$10 TeV to search for violations of Lorentz symmetry by using $\nu_\mu \to \nu_\tau$ oscillations as a natural interferometer with a size equal to the diameter of Earth. The Standard Model Extension (SME) framework is introduced, where each SME operator represents a type of Lorentz violation (LV). Contrary to previous searches of LV, the analysis presented here explores correlations between the SME elements for each operator. Although no LV was found, this analysis had provided the best attainable limits in the neutrino sector on higher-order operators. Comparison with limits from other sectors revealed that this work provided the best attainable limits on dimension-six elements across all fields: from tabletop experiments to cosmology. This is a remarkable point that demonstrates how powerful neutrino interferometry can be in the study of fundamental spacetime properties.

Chapter 4 builds upon the foundation laid down in the previous chapter, now utilising very-high-energy astrophysical neutrino data of up to $\sim$10 PeV to search for new physics signals. With a baseline of cosmological distances, even tiny new physics effects can accumulate to produce observable differences in the neutrino flavour composition as measured on Earth. No evidence of new physics was found, however this analysis demonstrates the potential in searching for new physics using astrophysical neutrino flavour measurements. Although the current statistics and detector sensitivity allow for searches for only rather special new physics effects, it is demonstrated that the sensitivity of this new approach goes far

beyond any known technologies, and reaches for the first time the necessary precision to look for new physics within the Planck scale expectation. Future extensions of IceCube such as the IceCube-Upgrade and IceCube-Gen2 [59, 164] have the ability to greatly improve the measurement of the astrophysical neutrino flavour. With more statistics and better calibration, this analysis shows promise in being able to investigate Planck scale physics at an unprecedented level, providing IceCube with a real discovery potential in the search for new physics beyond the standard model and general relativity.

Chapter 5 focuses on the lower energy aspects of IceCube – IceCube-DeepCore and the upcoming IceCube-Upgrade. Particle identification (PID) is difficult at these energies, and so in this chapter an R&D project with the goal of using the pulse shape from a single photomultiplier tube (PMT) to do PID between electromagnetic (EM) showering particles and minimum ionizing particles (MIPs) is described. A PMT was floated inside a tank filled with distilled water and using the beam provided by the Fermilab Test Beam Facility, electrons and pions were shot into the tank at different energies. 2 GeV electron and 8 GeV pion waveforms are compared as they deposit similar amounts of charge. The primary pulse spread was used as a discriminator and it is shown that at low charge, there is a discrimination that can be made between 2 GeV electrons and 8 GeV pions. Such techniques can be applied to future neutrino telescopes focusing on low energy physics, such as the IceCube-Upgrade.

Chapter 6 deals with the modelling of hadronization in the neutrino interaction generator GENIE [43], again at the few GeV regime of IceCube-DeepCore and the IceCube-Upgrade. The possibility of upgrading the hadronization model from the outdated and no longer supported PYTHIA 6 [187] to the contemporary and rewritten C++ based model of PYTHIA 8 is presented. Both a direct translation of PYTHIA 6 routines is carried out and further improvements to the GENIE hadronization implementation are attempted by allowing PYTHIA 8 to handle the beam remnant structure, rather than relying on its own ad-hoc model.

A Appendix

A.1 Gain calculation from LED charge distribution

By looking at the charge distribution produced from the PMT using light from a flashing LED, the gain can be estimated as will be shown in this section. This method is not considered to be accurate however it does yield a quick result which for the purposes of this thesis, is sufficient to be able to verify the stability of the beam test over time.

First, an estimate of the average number of PE liberated from the photocathode per LED pulse is obtained. The distribution measured is the charge distribution, so firstly the relationship between the charge and the number of PE can be written as:

$$Q = PE \cdot g \cdot C \tag{A.1}$$

$$PE = \frac{Q}{g \cdot C} = N \cdot Q \tag{A.2}$$

where Q is the charge, PE is the number of PE, g is the gain, C is the charge on a single electron, i.e. 1.6×10^{-19} C and N represents a normalisation factor. From this, it is seen that the number of PE is proportional to the charge.

The number of PE is distributed as a Poisson distribution, and the charge distribution is related to the PE through a normalisation N. Therefore, by looking at the ratio between the mean μ and variance σ^2 of the charge distribution, the average number of PE can be estimated.

$$\mu = N \cdot m \qquad \sigma = N \cdot s \tag{A.3}$$

$$\left(\frac{\mu}{\sigma}\right)^2 = \frac{m^2}{s^2} \tag{A.4}$$

where m is the mean and s^2 is the variance of the PE distribution. Then from Poisson

statistics,

$$m = s^2 \implies \left(\frac{\mu}{\sigma}\right)^2 = \frac{m^2}{s^2} \tag{A.5}$$

$$\therefore \; < PE > = m = \left(\frac{\mu}{\sigma}\right)^2 \tag{A.6}$$

Note, throughout these calculations it is assumed there is no other source contributing to the width of the charge distribution. Since the average number of PE is large, the charge distribution can be approximated as a Gaussian, so μ and σ can be obtained from the charge distribution by fitting it to a Gaussian, as demonstrated in Figure 5.10.

$$Q = \frac{V \cdot t}{R} \qquad V \cdot t = PE \cdot g \cdot C \cdot R \tag{A.7}$$

$$\implies g = \frac{V \cdot t}{PE \cdot C \cdot R} \tag{A.8}$$

where R is the impedance, which for the DDC2 is 150 Ω and t is the time. The product $V \cdot t$ is the mean of the charge distribution.

$$V \cdot t = \mu \tag{A.9}$$

Therefore, the gain can be estimated as being:

$$g = \frac{V \cdot t}{PE \cdot C \cdot R} \implies g = \frac{\mu}{\left(\frac{\mu}{\sigma}\right)^2 \cdot C \cdot R} \tag{A.10}$$

A.2 Atmospheric neutrino LV exclusion regions

Following from Section 3.3, the Figures A.1-A.6 show the exclusion regions in terms of the three SME elements $\mathring{c}^{(d)}_{\mu\mu}$, $\mathrm{Re}(\mathring{c}^{(d)}_{\mu\tau})$ and $\mathrm{Im}(\mathring{c}^{(d)}_{\mu\tau})$. While 40 slices in $\mathring{c}^{(d)}_{\mu\mu}$ are shown for each dimension, $d = 3, 4, 5, 6, 7, 8$, the full likelihood scan used 200 points in each dimension. The closest visible value of the true best-fit point is displayed as the yellow star for each dimension. Note that for dimension 3, the most extreme values for $\mathring{c}^{(d)}_{\mu\mu}$ show plotting artefacts due to very fast LV oscillations as described in Section 3.3.1 and the structure here is more visible in the spherical representation of the SME elements.

Figures A.7-A.12 show the exclusion regions in terms of the spherical SME elements ρ_d, $\cos(\theta)$ and $\tan(\phi)$ as defined in Figure 3.8. 20 slides in $\tan(\phi)$ are shown for each dimension, $d = 3, 4, 5, 6, 7, 8$, where the full likelihood scan used 100 points in each dimension. Once again, the closest visible value of the true best-fit point is displayed as the yellow star for each dimension.

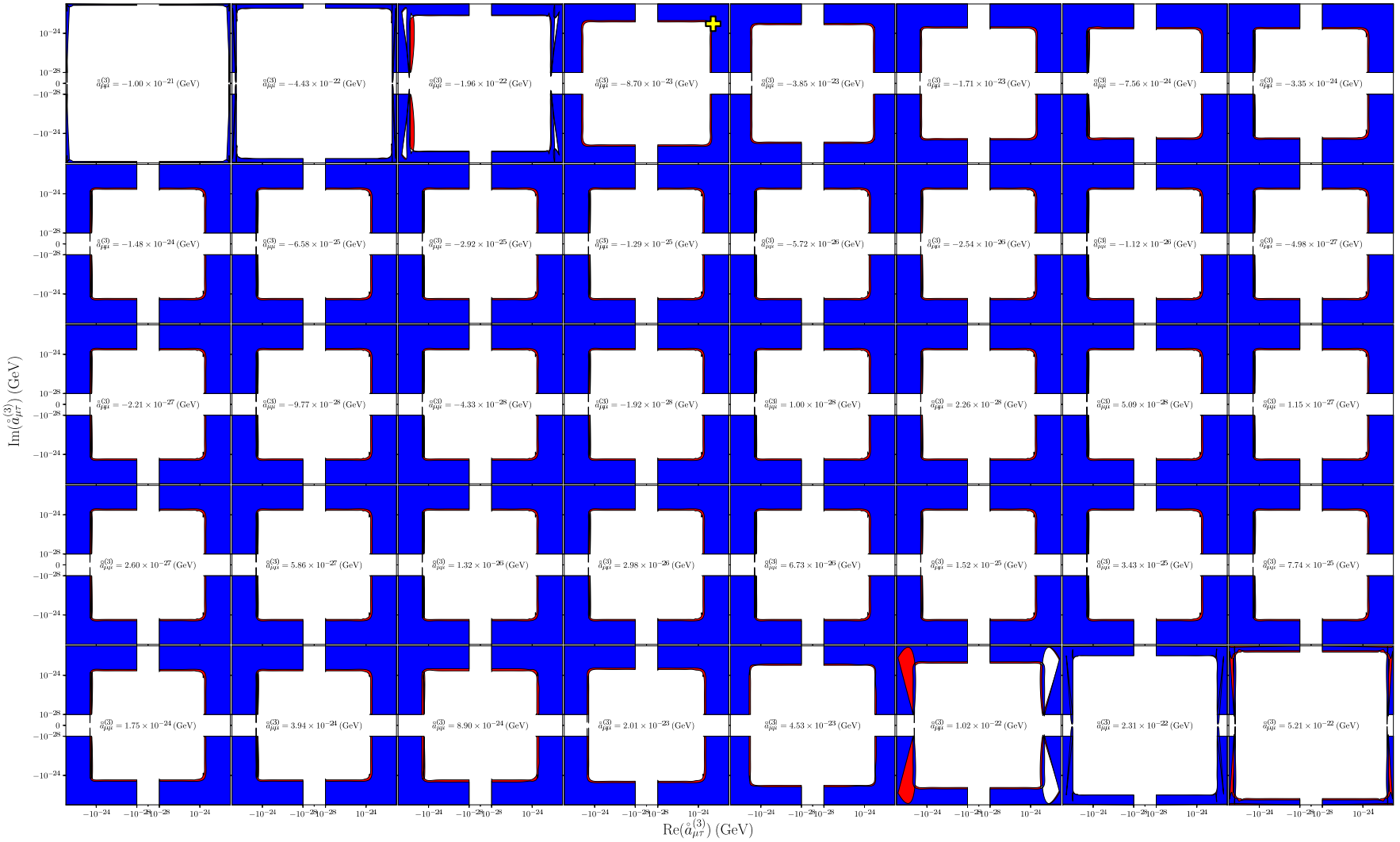

Figure A.1: SME exclusion regions at 90% (99%) confidence in red (blue) for dimension $d = 3$.

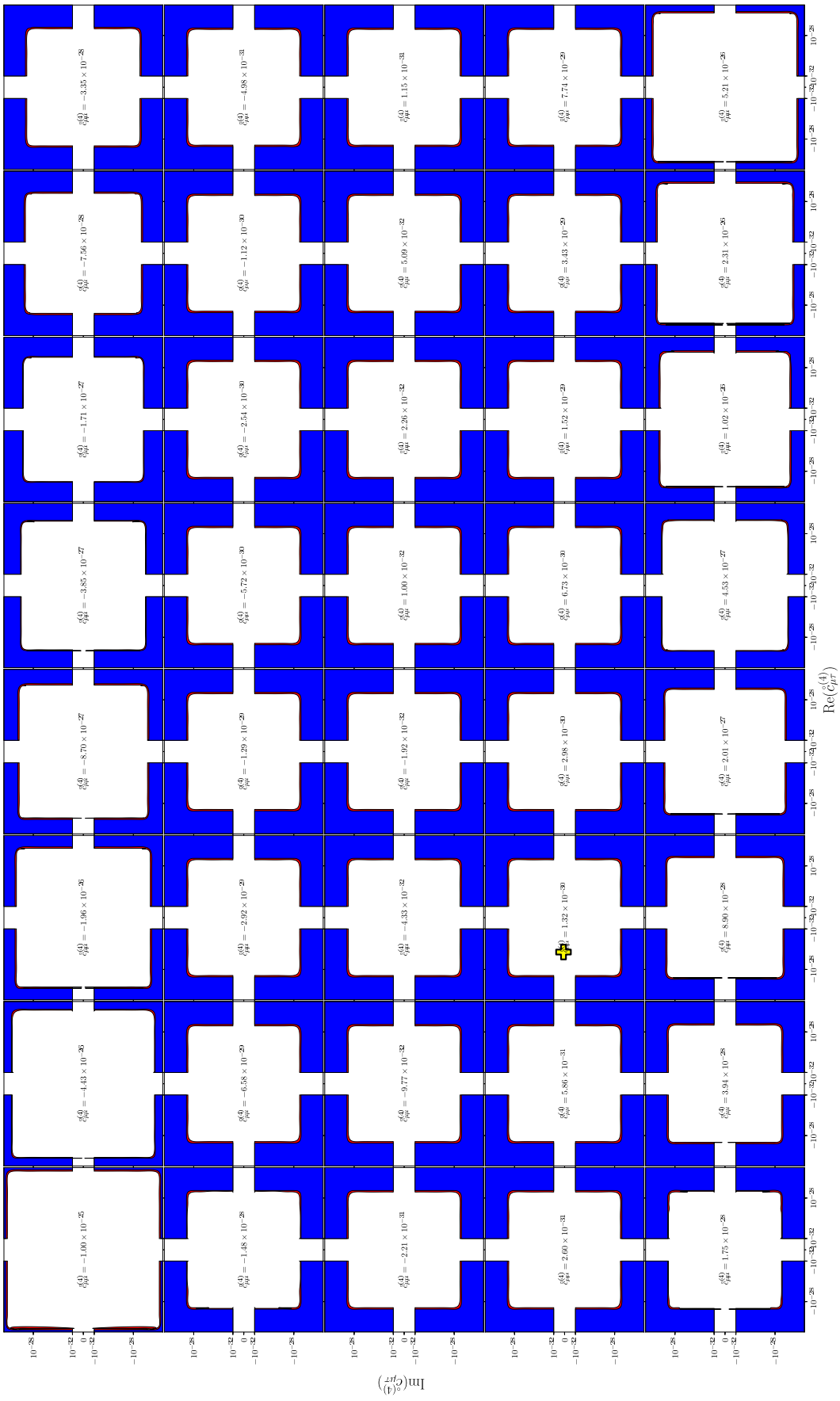

Figure A.2: SME exclusion regions at 90% (99%) confidence in red (blue) for dimension $d = 4$.

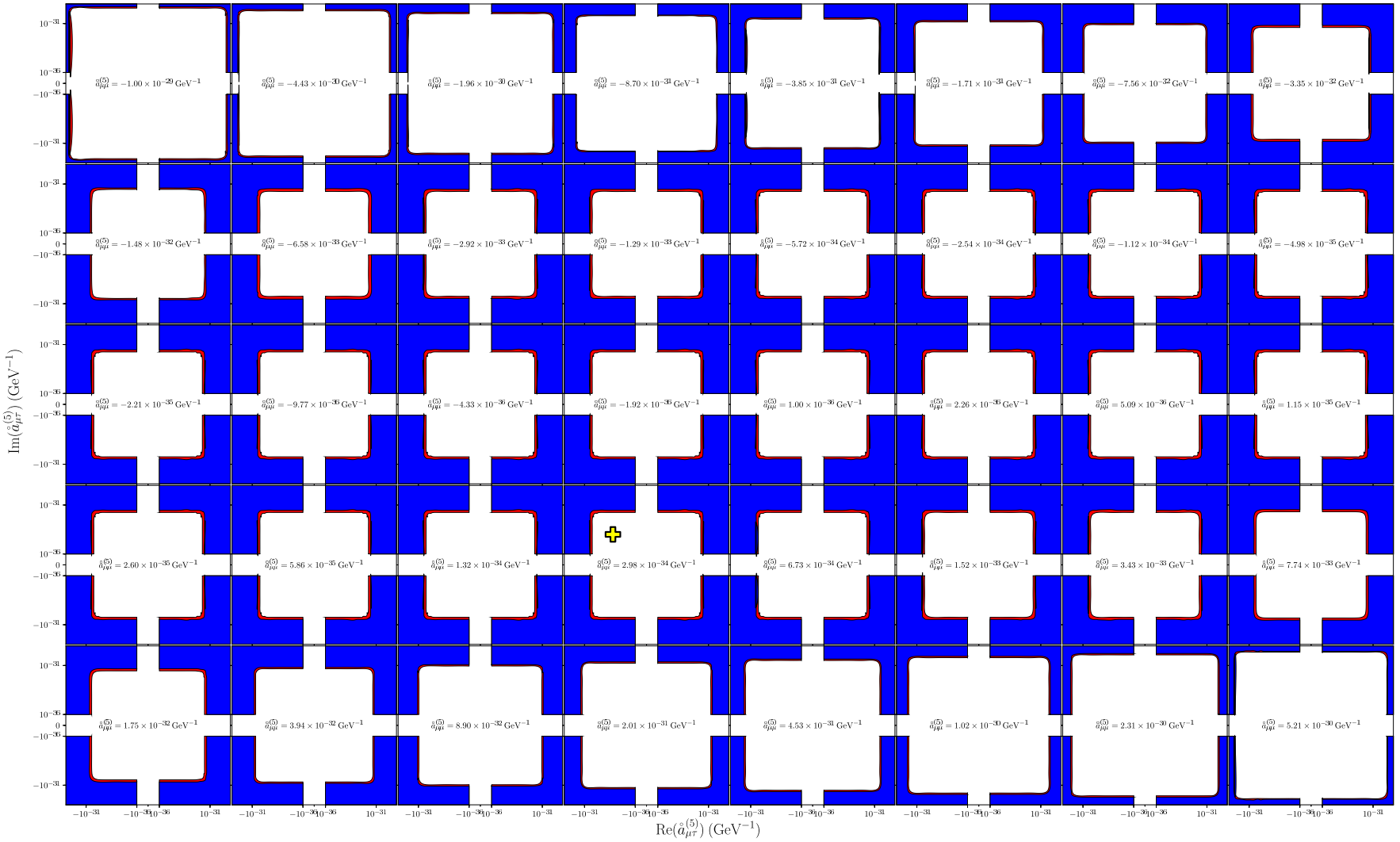

Figure A.3: SME exclusion regions at 90% (99%) confidence in red (blue) for dimension $d = 5$.

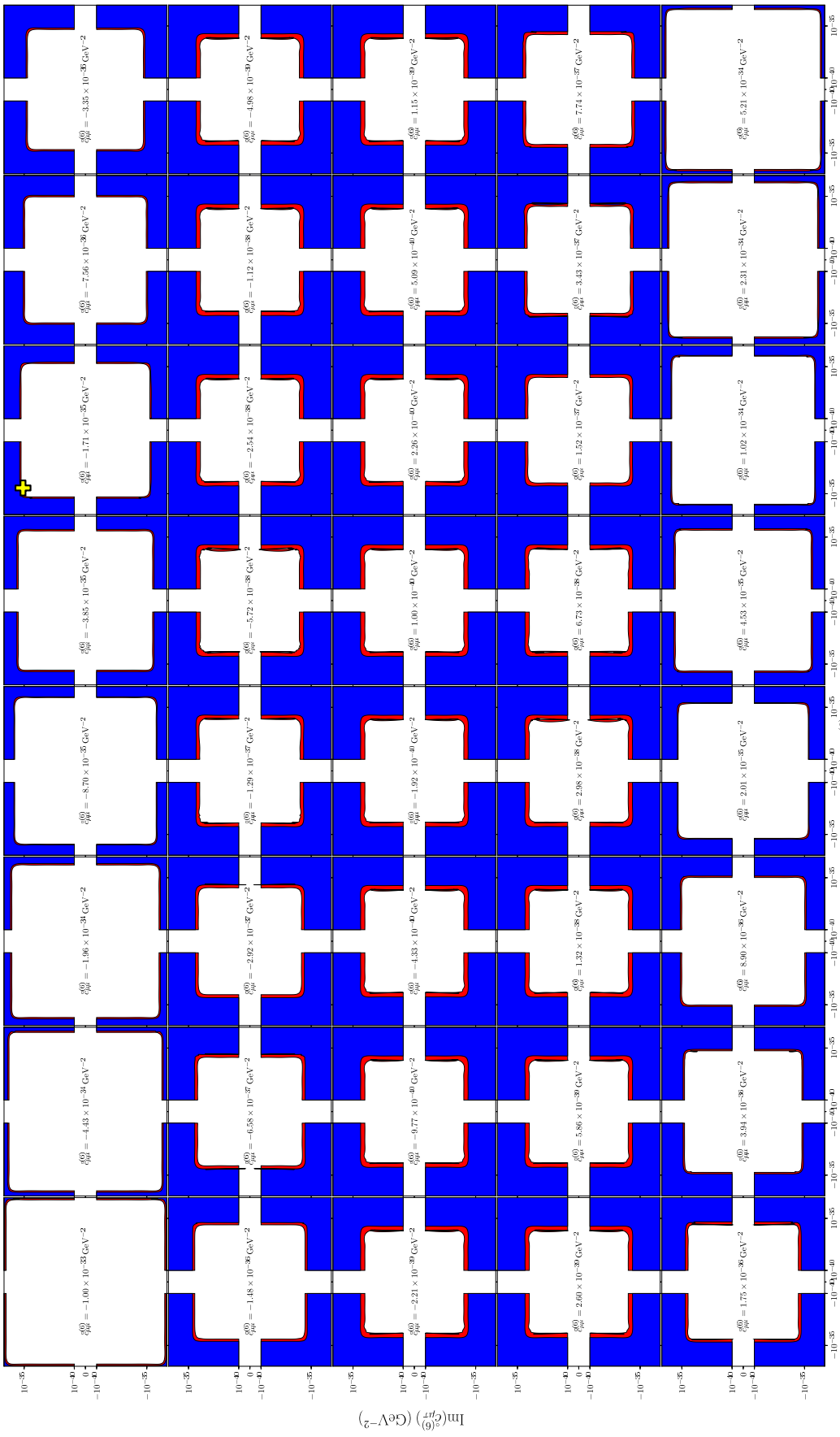

Figure A.4: SME exclusion regions at 90% (99%) confidence in red (blue) for dimension $d = 6$.

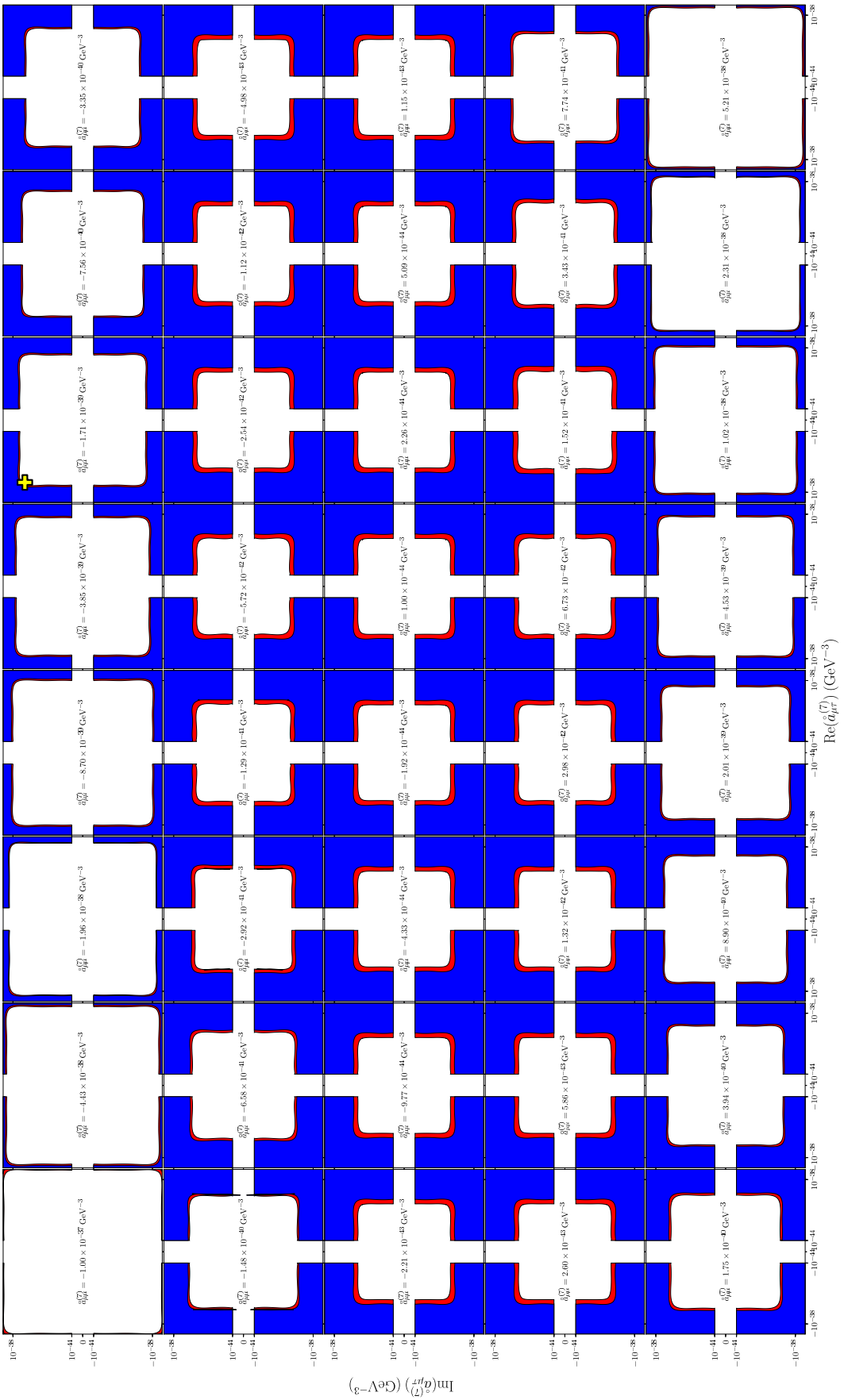

Figure A.5: SME exclusion regions at 90% (99%) confidence in red (blue) for dimension $d = 7$.

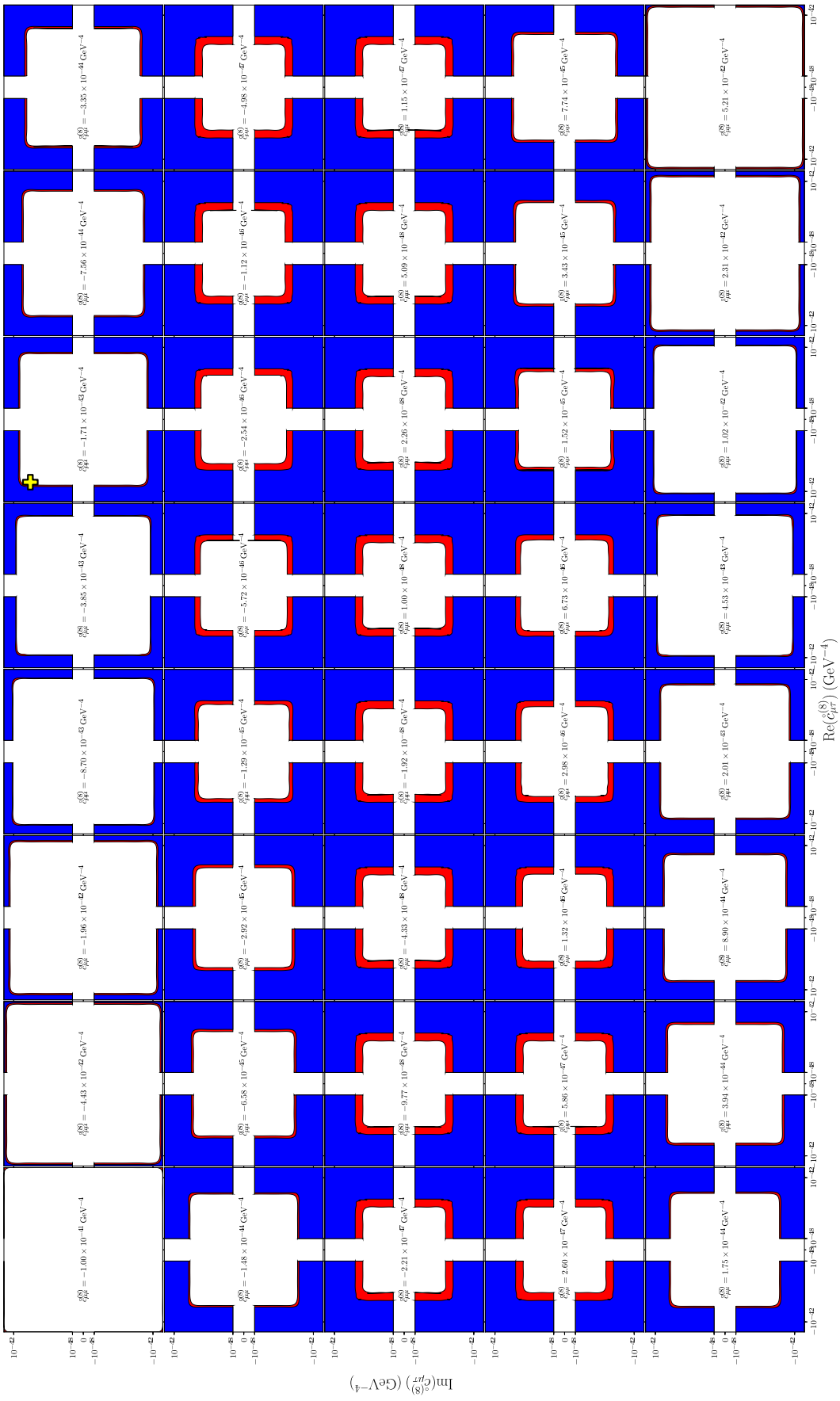

Figure A.6: SME exclusion regions at 90% (99%) confidence in red (blue) for dimension $d = 8$.

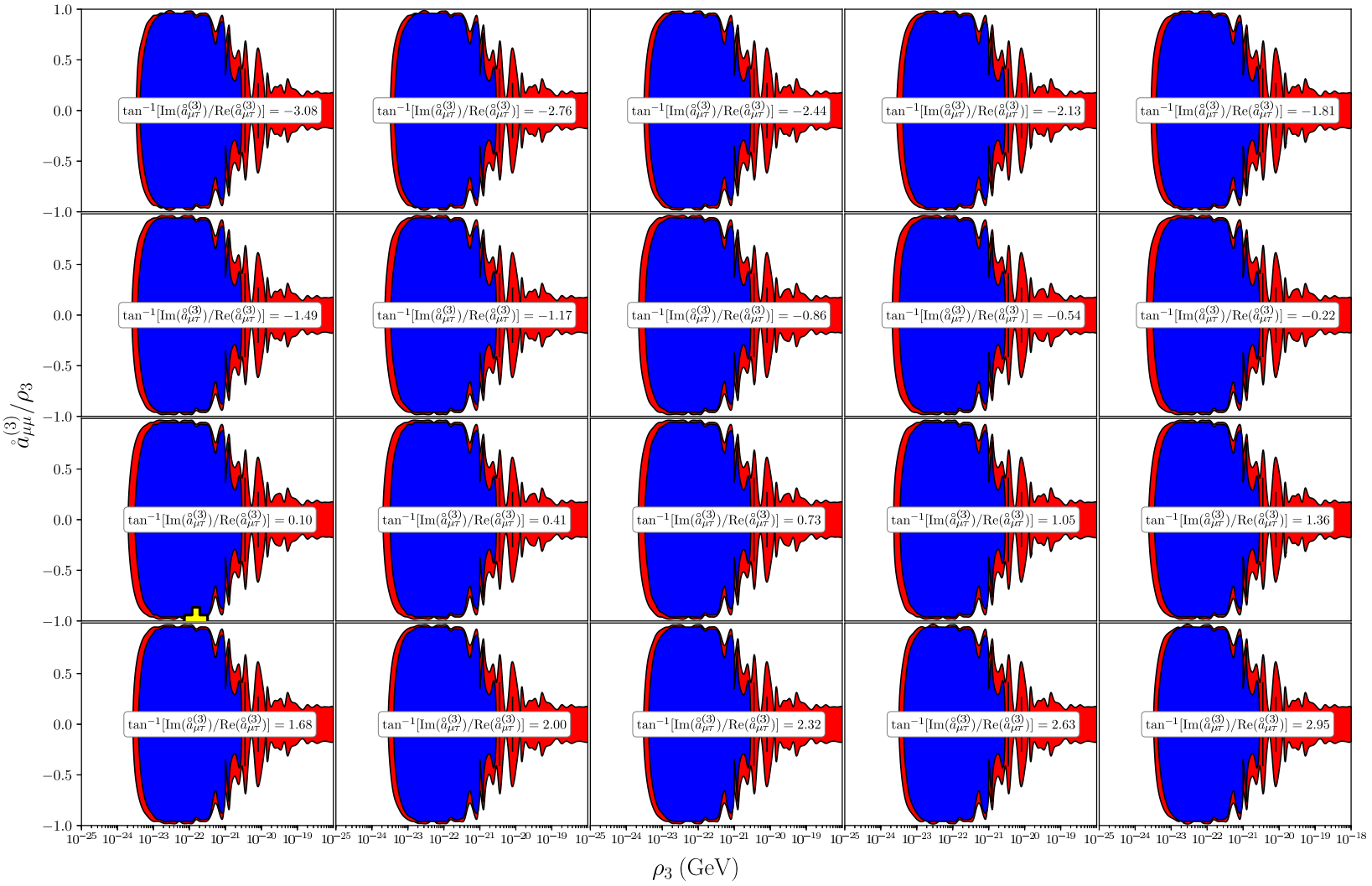

Figure A.7: SME exclusion regions at 90% (99%) confidence in red (blue) for dimension $d = 3$.

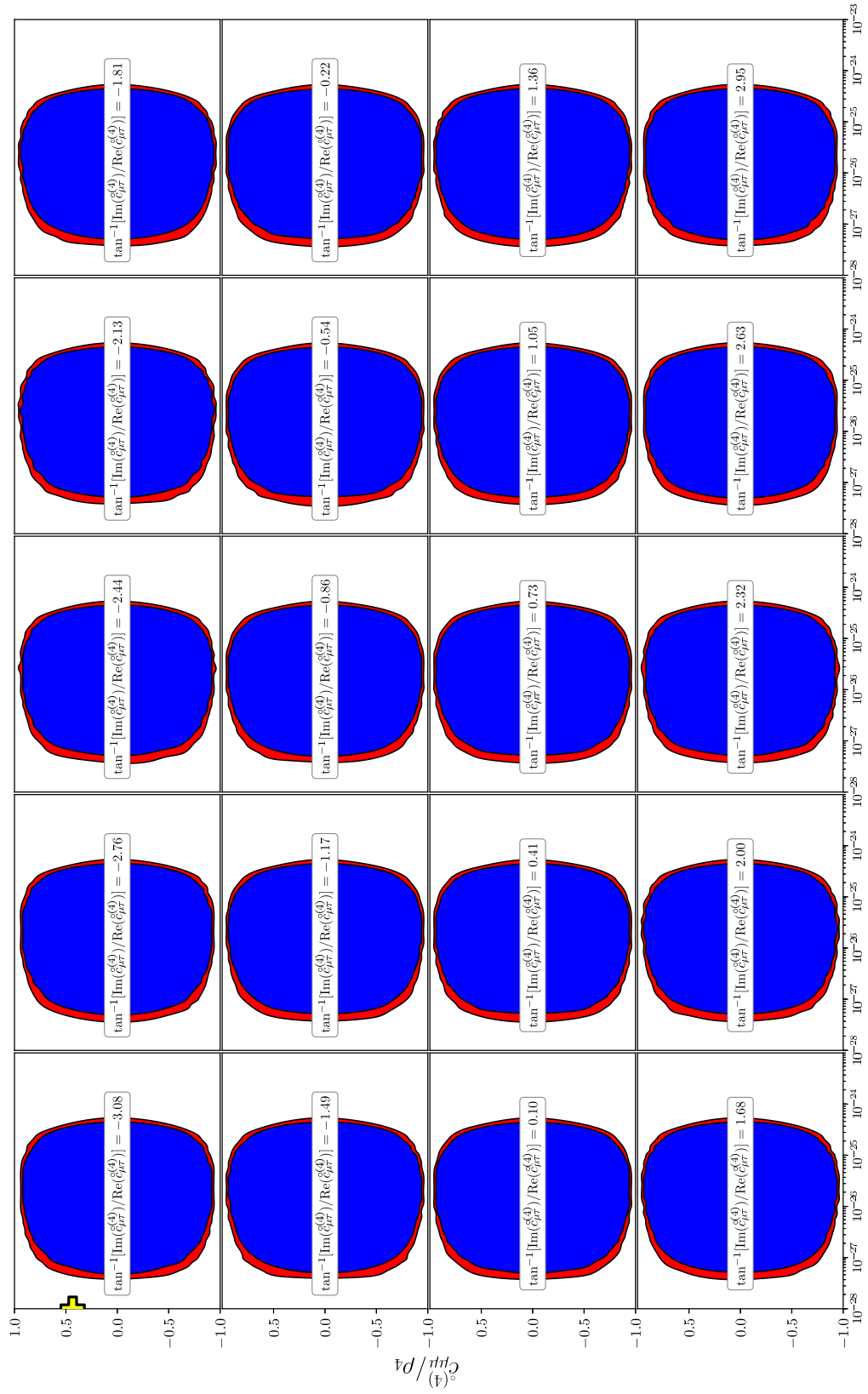

Figure A.8: SME exclusion regions at 90% (99%) confidence in red (blue) for dimension $d = 4$.

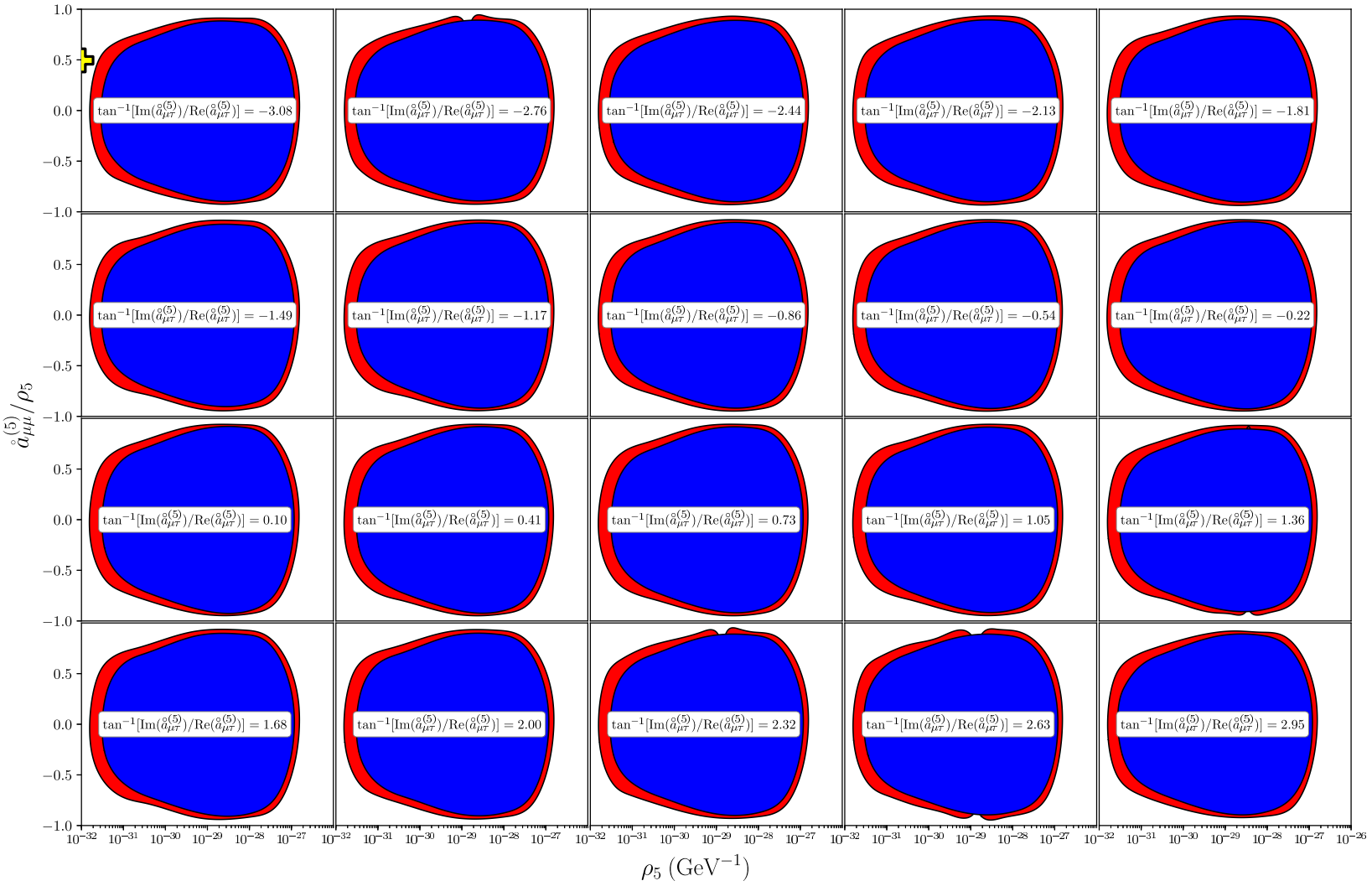

Figure A.9: SME exclusion regions at 90% (99%) confidence in red (blue) for dimension $d = 5$.

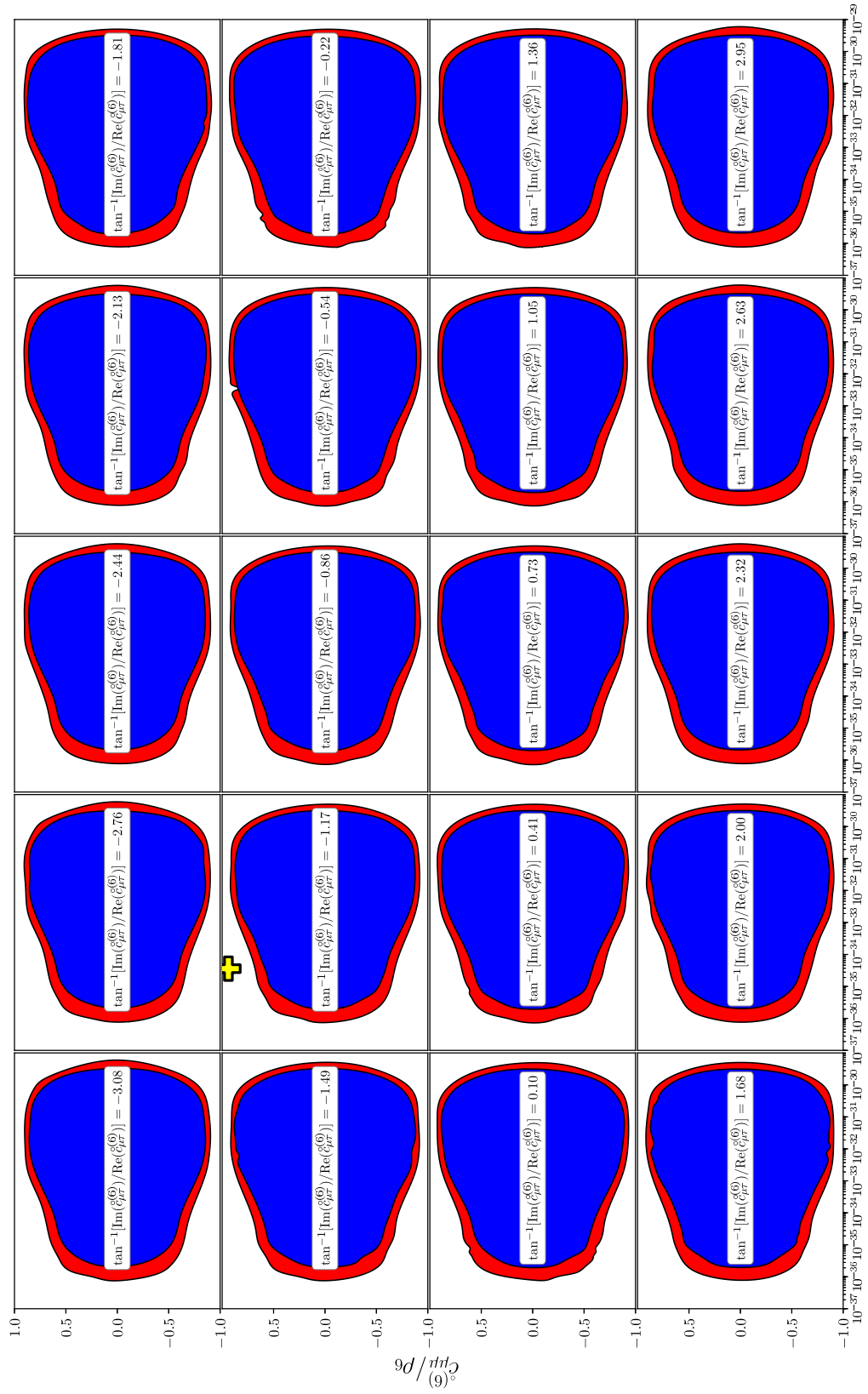

Figure A.10: SME exclusion regions at 90% (99%) confidence in red (blue) for dimension $d = 6$.

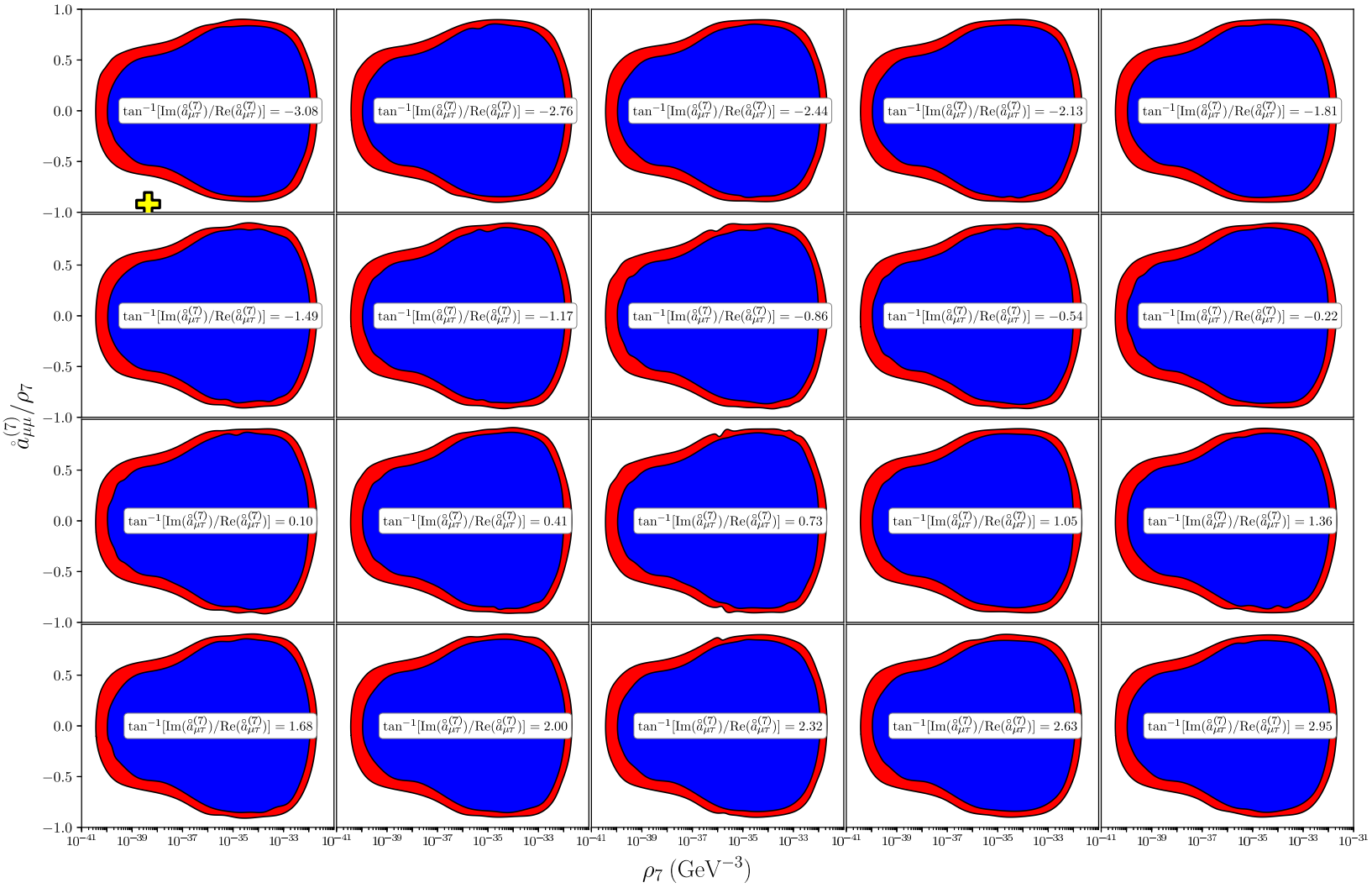

Figure A.11: SME exclusion regions at 90% (99%) confidence in red (blue) for dimension $d = 7$.

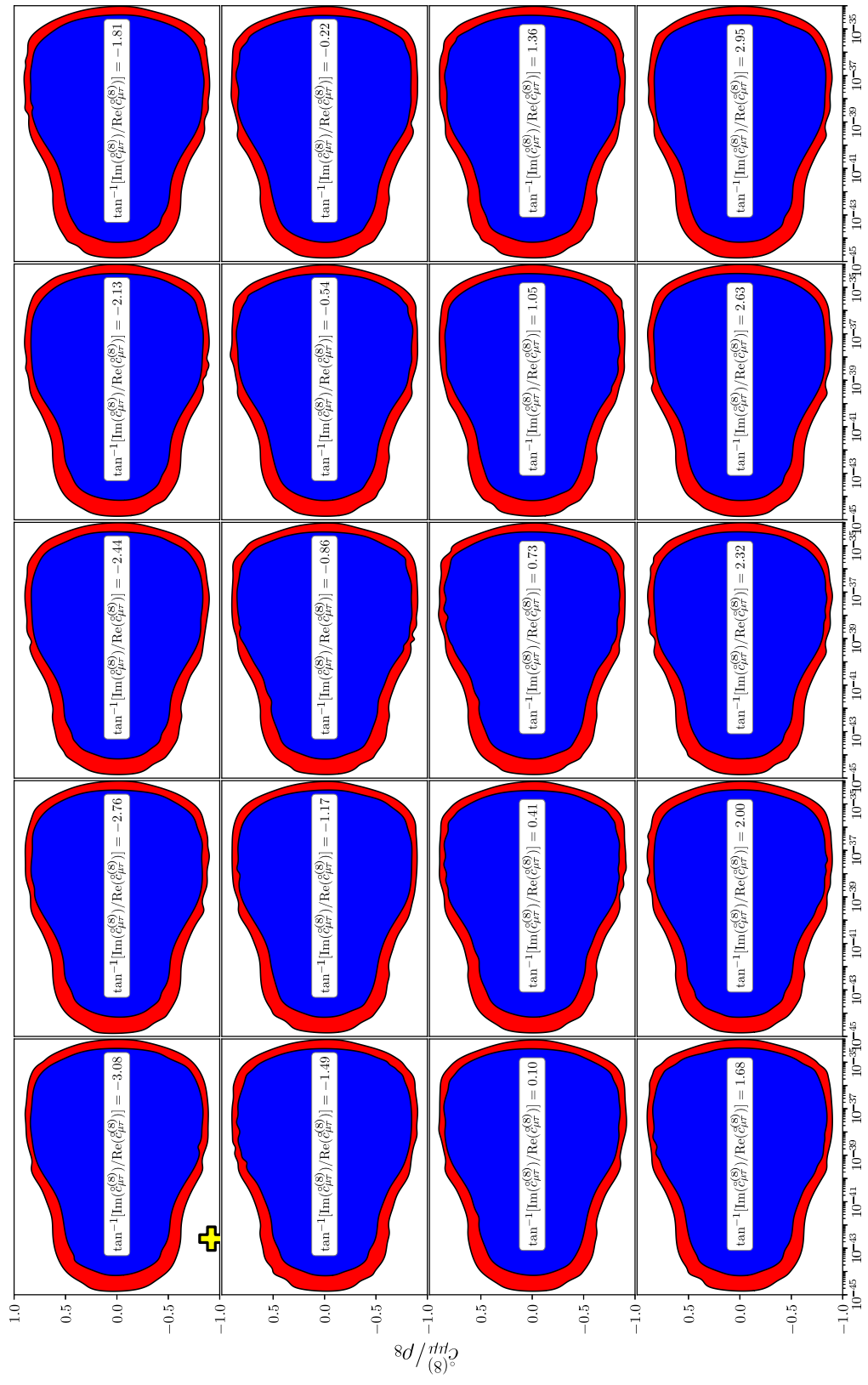

Figure A.12: SME exclusion regions at 90% (99%) confidence in red (blue) for dimension $d = 8$.

A.3 Astrophysical flavour exclusion regions

Following from Section 4.3, the Figures A.13-A.17 show the exclusion regions for the scale of new physics (vertical axis) as a function of the source flavour composition (horizontal axis) for certain new physics flavour textures. Green and blue shaded regions are excluded with a strong strength-of-evidence (Bayes factor, $B_{0/1} > 10$) according to Jeffreys' scale [101]. New physics scale is shown normalised to the Planck scale expectation, with the purple line indicating the point below which Planck scale physics is being probed. The hashed region shows the previous IceCube limit [72].

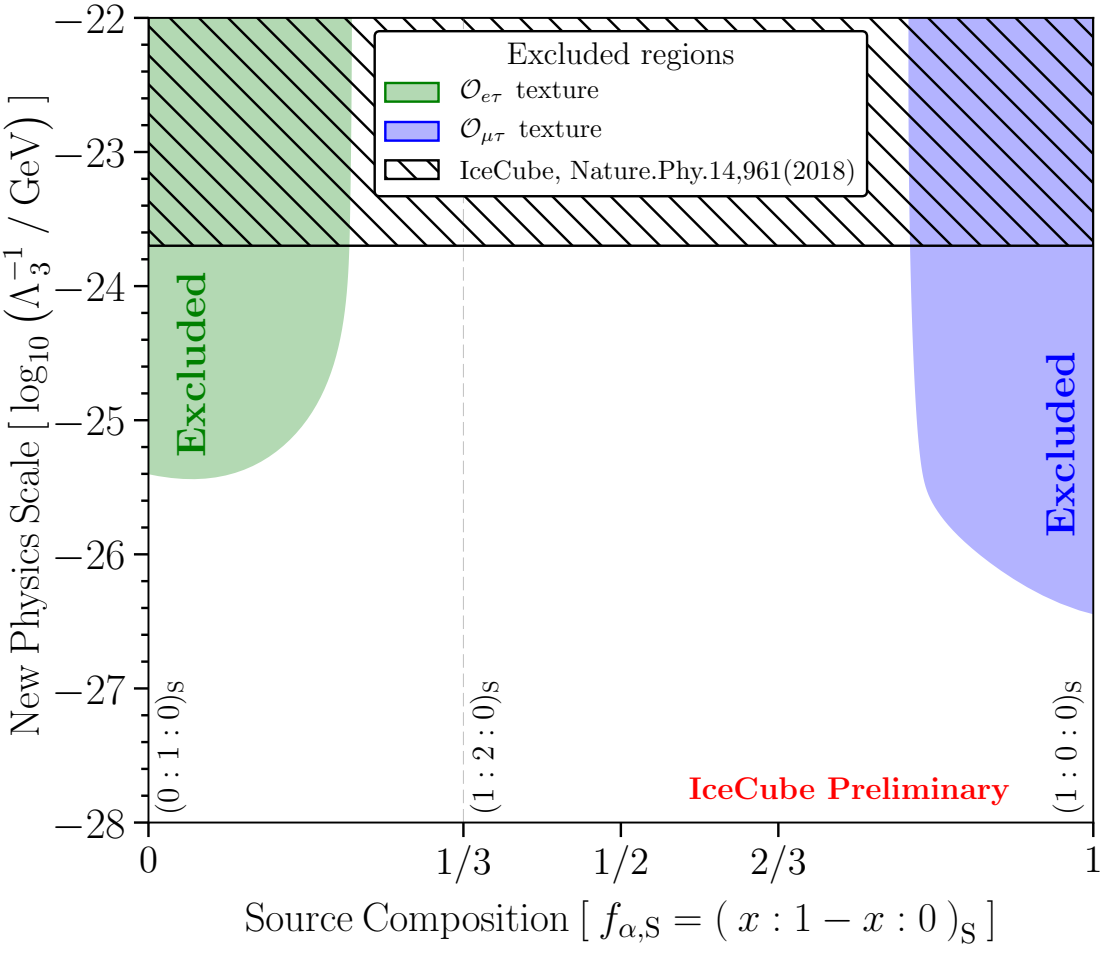

Figure A.13: Exclusion regions for the dimension-three new physics operator.

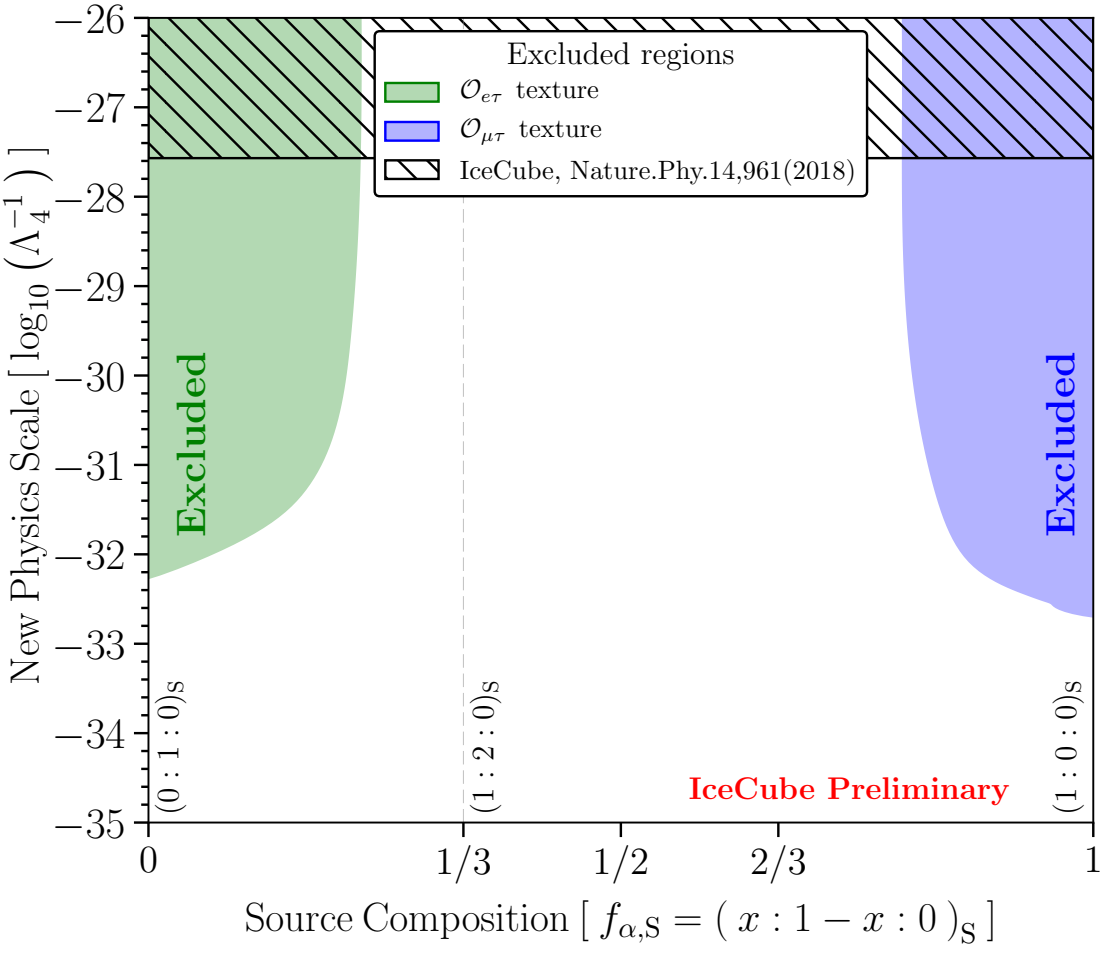

Figure A.14: Exclusion regions for the dimension-four new physics operator.

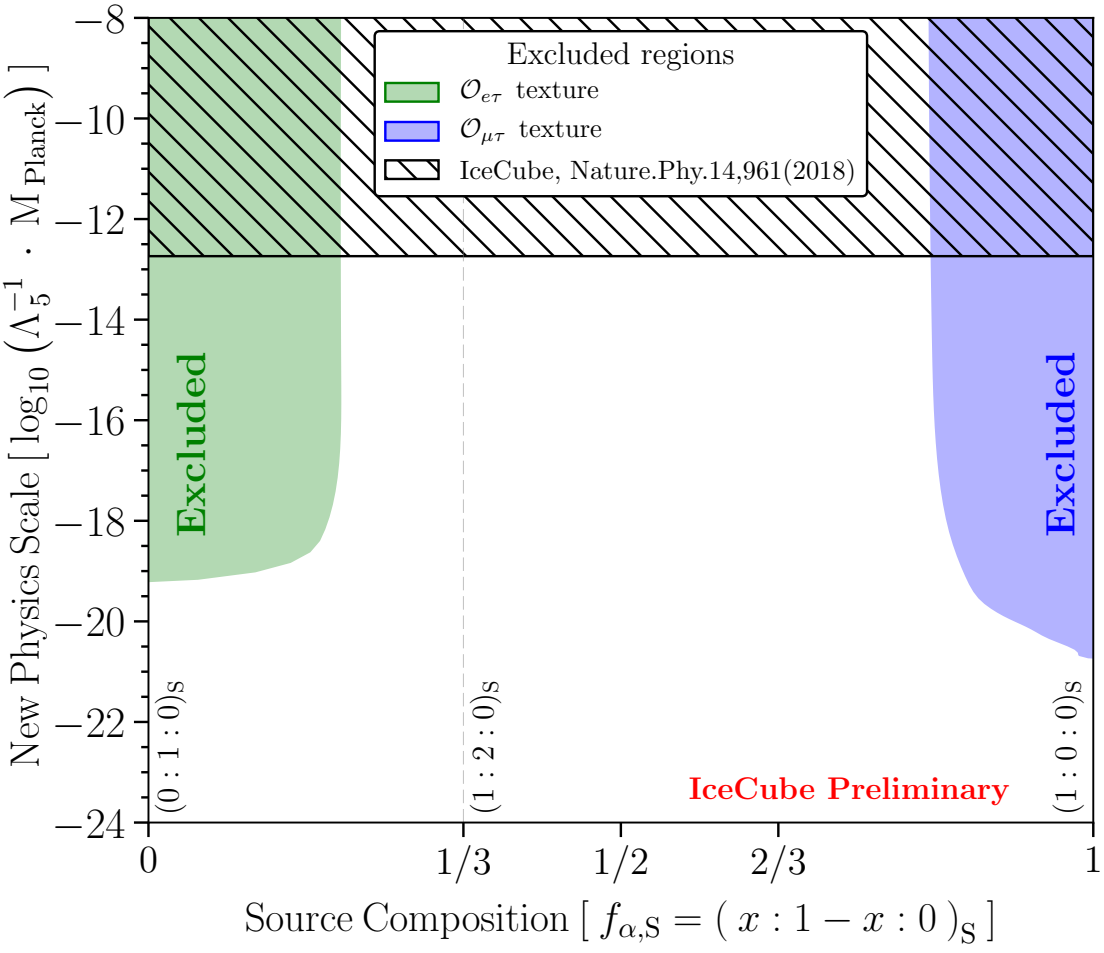

Figure A.15: Exclusion regions for the dimension-five new physics operator.

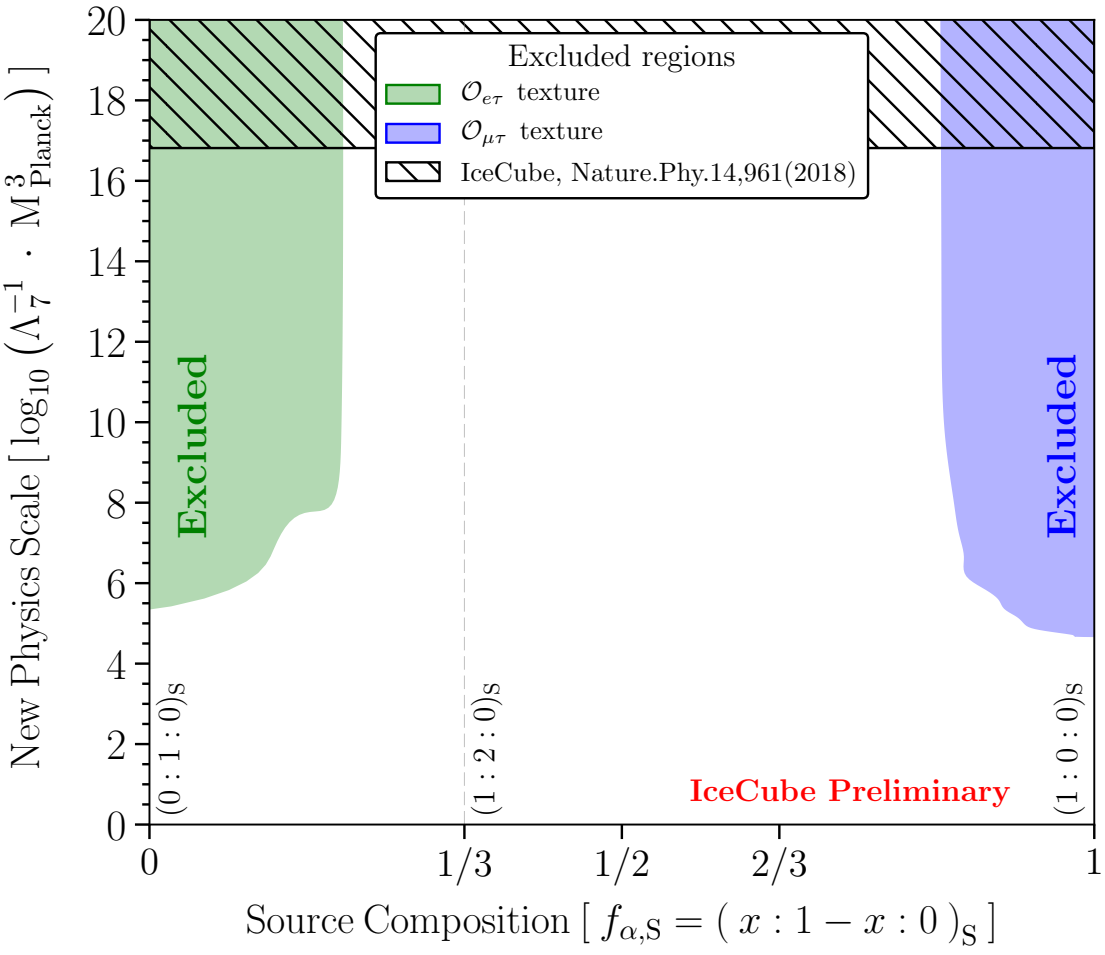

Figure A.16: Exclusion regions for the dimension-seven new physics operator.

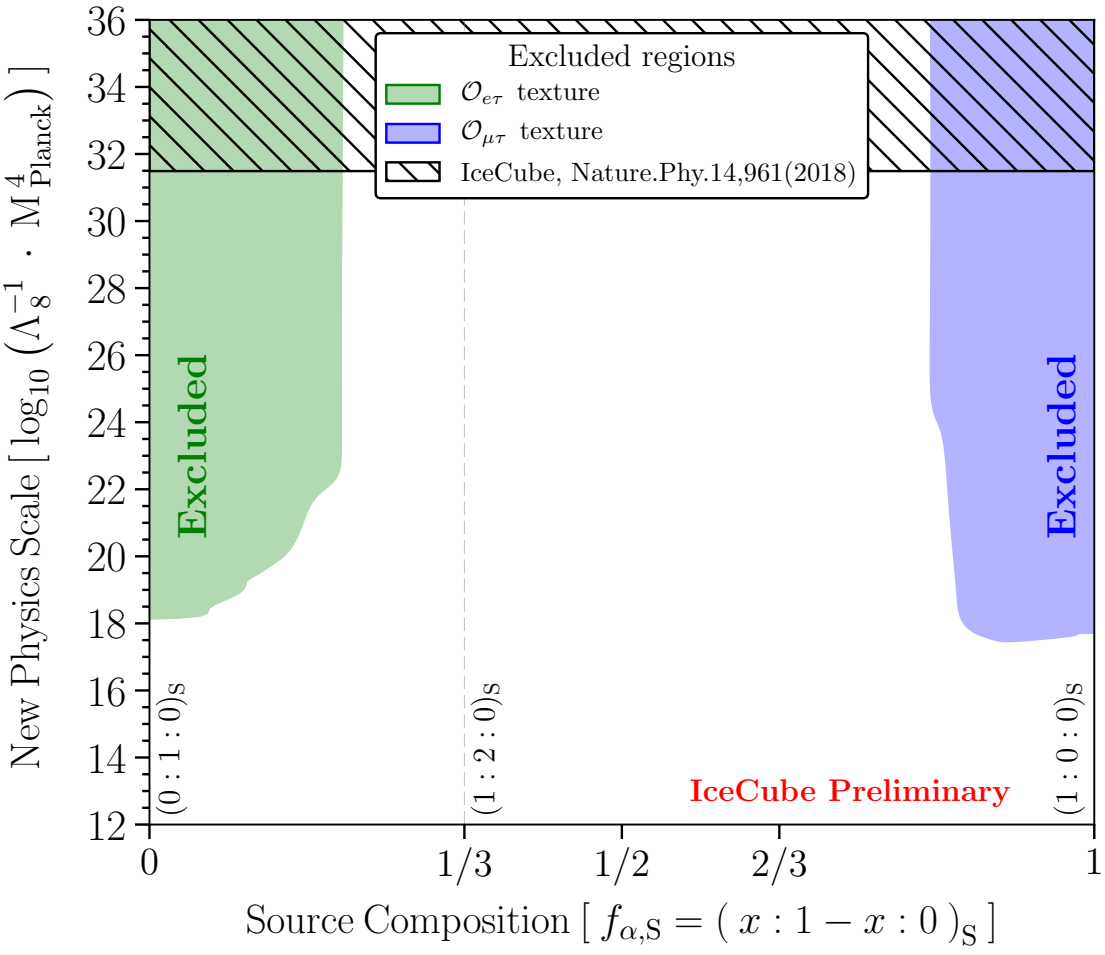

Figure A.17: Exclusion regions for the dimension-eight new physics operator.

nature physics

ARTICLES

https://doi.org/10.1038/s41567-018-0172-2

Neutrino interferometry for high-precision tests of Lorentz symmetry with IceCube

The IceCube Collaboration*

Lorentz symmetry is a fundamental spacetime symmetry underlying both the standard model of particle physics and general relativity. This symmetry guarantees that physical phenomena are observed to be the same by all inertial observers. However, unified theories, such as string theory, allow for violation of this symmetry by inducing new spacetime structure at the quantum gravity scale. Thus, the discovery of Lorentz symmetry violation could be the first hint of these theories in nature. Here we report the results of the most precise test of spacetime symmetry in the neutrino sector to date. We use high-energy atmospheric neutrinos observed at the IceCube Neutrino Observatory to search for anomalous neutrino oscillations as signals of Lorentz violation. We find no evidence for such phenomena. This allows us to constrain the size of the dimension-four operator in the standard-model extension for Lorentz violation to the 10^{-28} level and to set limits on higher-dimensional operators in this framework. These are among the most stringent limits on Lorentz violation set by any physical experiment.

Very small violations of Lorentz symmetry, or Lorentz violation (LV), are allowed in many ultrahigh-energy theories, including string theory[1], non-commutative field theory[2] and supersymmetry[3]. The discovery of LV could be the first indication of such new physics. Worldwide efforts are therefore underway to search for evidence of LV. The standard-model extension (SME) is an effective-field-theory framework to systematically study LV[4]. The SME includes all possible types of LV that respect other symmetries of the standard model such as energy–momentum conservation and coordinate independence. Thus, the SME can provide a framework to compare results of LV searches from many different fields such as photons[5–8], nucleons[9–11], charged leptons[12–14] and gravity[15]. Recently, neutrino experiments have performed searches for LV[16–18]. So far, all searches have obtained null results. The full list of existing limits from all sectors and a brief overview of the field are available elsewhere[19,20]. Our focus here is to present the most precise test of LV in the neutrino sector.

The fact that neutrinos have mass has been established by a series of experiments[21–26]. The field has incorporated these results into the neutrino standard model (νSM)—the standard model with three massive neutrinos. Although the νSM parameters are not yet fully determined[27], the model is rigorous enough to be brought to bear on the question of LV. In the Methods, we briefly review the history of neutrino oscillation physics and tests of LV with neutrinos.

To date, neutrino masses have proved to be too small to be measured kinematically, but the mass differences are known via neutrino oscillations. This phenomenon arises from the fact that production and detection of neutrinos involves the flavour states, while the propagation is given by the Hamiltonian eigenstates. Thus, a neutrino with flavour $|\nu_\alpha\rangle$ can be written as a superposition of Hamiltonian eigenstates $|\nu_i\rangle$; that is, $|\nu_\alpha\rangle = \sum_{i=1}^{3} V_{\alpha i}(E)|\nu_i\rangle$, where V is the unitary matrix that diagonalizes the Hamiltonian and, in general, is a function of neutrino energy E. When the neutrino travels in vacuum without new physics, the Hamiltonian depends only on the neutrino masses, and the Hamiltonian eigenstates coincide with the mass eigenstates. That is, $H = \frac{1}{2E}U^\dagger \mathrm{diag}(m_1^2, m_2^2, m_3^2)U = \frac{m^2}{2E}$, where m_i are the neutrino masses and U is the Pontecorvo–Maki–Nakagawa–Sakata matrix that diagonalizes the mass matrix m (ref. [27]).

A consequence of the flavour misalignment is that a neutrino beam that is produced purely of one flavour will evolve to produce other flavours. Experiments measure the number of neutrinos of different flavours, observed as a function of the reconstructed energy of the neutrino, E, and the distance the beam has travelled, L. The microscopic neutrino masses are directly tied to the macroscopic neutrino oscillation length. In this sense, neutrino oscillations are similar to photon interference experiments in their ability to probe very small scales in nature.

Lorentz-violating neutrino oscillations

Here, we use neutrino oscillations as a natural interferometer with a size equal to the diameter of Earth. We look for anomalous flavour-changing effects caused by LV that would modify the observed energy and zenith angle distributions of atmospheric muon neutrinos observed in the IceCube Neutrino Observatory[28] (see Fig. 1). Beyond flavour change due to small neutrino masses, any hypothetical LV fields could contribute to muon neutrino flavour conversion. We therefore look for distortion of the expected muon neutrino distribution. As this analysis does not distinguish between a muon neutrino (ν_μ) and its antineutrino ($\overline{\nu_\mu}$), when the word 'neutrino' is used, we are referring to both.

Past searches for LV have mainly focused on the directional effect in the Sun-centred celestial-equatorial frame[19] by looking only at the time dependence of physics observables as direction-dependent physics appears as a function of Earth's rotation. However, in our case, we assume no time dependence, and instead look at the energy distribution distortions caused by direction- and time-independent isotropic LV. Isotropic LV may be a factor ~10^3 larger than direction-dependent LV in the Sun-centred celestial-equatorial frame if we assume that the new physics is isotropic in the cosmic microwave background frame[20]. It would be most optimal to simultaneously look for both effects, but our limited statistics do not allow for this.

*A full list of authors and affiliations appears in the online version of this paper.

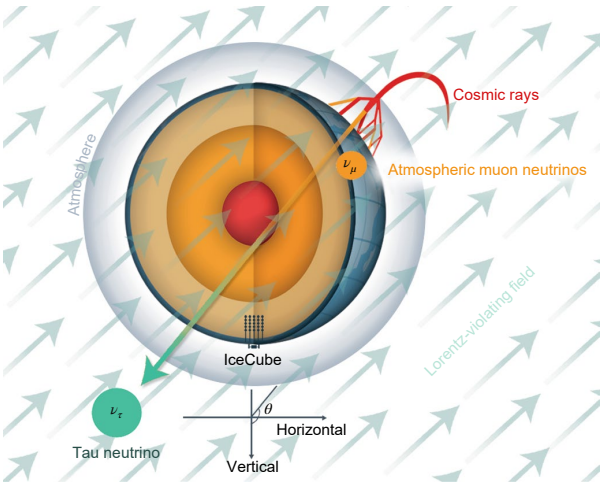

Fig. 1 | Test of LV with atmospheric neutrinos. Muon neutrinos are produced in the upper atmosphere by the collisions of cosmic rays with air molecules. These atmospheric muon neutrinos pass through the entire Earth and are then detected by IceCube in Antarctica. The LV, indicated by arrows, permeates space and could induce an anomalous neutrino oscillation to tau neutrinos. Therefore, a potential signal of LV is the anomalous disappearance of muon neutrinos. Note, here we test only the isotropic component.

To calculate the effect, we start from an effective Hamiltonian derived from the SME[4], which can be written as

$$H \approx \frac{m^2}{2E} + \mathring{a}^{(3)} - E\mathring{c}^{(4)} + E^2\mathring{a}^{(5)} - E^3\mathring{c}^{(6)} \cdots \quad (1)$$

The first term of equation (1) is from the νSM; however, its impact decreases at high energy. The remaining terms ($\mathring{a}^{(3)}$, $\mathring{c}^{(4)}$, $\mathring{a}^{(5)}$ and so on) arise from the SME and describe isotropic Lorentz-violating effects. The circle symbol on the top indicates isotropic coefficients, and the number in the bracket is the dimension of the operator. These terms are typically classified by charge, parity and time reversal (CPT) symmetry; CPT-odd ($\mathring{a}^{(d)}$) and CPT-even ($\mathring{c}^{(d)}$). Focusing on muon neutrino to tau neutrino ($\nu_\mu \rightarrow \nu_\tau$) oscillations, all SME terms in equation (1) can be expressed as 2×2 matrices, such as

$$\mathring{c}^{(6)} = \begin{pmatrix} \mathring{c}^{(6)}_{\mu\mu} & \mathring{c}^{(6)}_{\mu\tau} \\ \mathring{c}^{(6)\star}_{\mu\tau} & -\mathring{c}^{(6)}_{\mu\mu} \end{pmatrix} \quad (2)$$

Without loss of generality, we can define the matrices so that they are traceless, leaving three independent parameters, in this case: $\mathring{c}^{(6)}_{\mu\mu}$, $\mathrm{Re}(\mathring{c}^{(6)}_{\mu\tau})$ and $\mathrm{Im}(\mathring{c}^{(6)}_{\mu\tau})$. The off-diagonal Lorentz-violating term $\mathring{c}^{(6)}_{\mu\tau}$ dominates neutrino oscillations at high energy, which is the main interest of this paper. In this formalism, LV can be described by an infinite series, but higher-order terms are expected to be suppressed. Therefore, most terrestrial experiments focus on searching for effects of dimension-three and -four operators; $\mathring{a}^{(3)}$ and $E\,\mathring{c}^{(4)}$ respectively. However, our analysis extends to dimension-eight; that is, $E^2\,\mathring{a}^{(5)}$, $E^3\,\mathring{c}^{(6)}$, $E^4\,\mathring{a}^{(7)}$ and $E^5\,\mathring{c}^{(8)}$. Such higher orders are accessible by IceCube, which observes high-energy neutrinos where we expect an enhancement from the terms with dimension greater than four. In fact, some theories, such as non-commutative field theory[2] and supersymmetry[3], allow for LV to appear in higher-order operators. As an example, we expect dimension-six new physics operators of order $\frac{1}{M_P^2} \approx 10^{-38}\,\mathrm{GeV}^{-2}$, where M_P is the Planck mass, which is the natural energy scale of the unification of all matter and forces including gravity. We assume that only one dimension is important at any given energy scale, because the strength of LV is expected to be different at different orders.

We use the $\nu_\mu \rightarrow \nu_\tau$ two-flavour oscillation scheme following ref. [29]. This is appropriate because we assume there is no significant interference with ν_e. Details of the model used in this analysis are given in the Methods. The oscillation probability is given by

$$P(\nu_\mu \rightarrow \nu_\tau) = -4V_{\mu1}V_{\mu2}V_{\tau1}V_{\tau2}\sin^2\left(\frac{\lambda_2-\lambda_1}{2}L\right) \quad (3)$$

where $V_{\alpha i}$ are the mixing matrix elements of the effective Hamiltonian (equation (1)), and λ_i are its eigenvalues. Both mixing matrix elements and eigenvalues are a function of energy, νSM oscillation parameters and SME coefficients.

The IceCube neutrino observatory

The IceCube Neutrino Observatory is located at the geographic South Pole[30,31]. The detector volume is one cubic kilometre of clear Antarctic ice. Atmospheric muon neutrinos interacting on surrounding ice or bedrock may produce high-energy muons, which emit photons that are subsequently detected by digital optical modules (DOMs) embedded in the ice. The DOMs consist of a 25-cm-diameter Hamamatsu photomultiplier tube, with readout electronics, contained within a 36.5 cm glass pressure housing. These are installed in holes in the ice with roughly 125 m separation. There are 86 holes in the ice with a total of 5,160 DOMs, which are distributed at depths of 1,450 m to 2,450 m below the surface, instrumenting 1 Gt of ice. The full detector description can be found in an earlier study[31].

This detector observes Cherenkov light from muons produced in charged-current ν_μ interactions. Photons detected by the DOMs allow for the reconstruction of the muon energy and direction, which is related to the energy of the primary ν_μ. As the muons are above critical energy, their energy can be determined by measuring the stochastic losses that produce Cherenkov light. See earlier work[28] for details on the muon energy proxy used in this analysis. In the teraelectronvolt (TeV) energy range, these muons traverse distances of the order of kilometres, and have a small scattering angle due to the large Lorentz boost, resulting in 0.75° resolution on the reconstructed direction at 1 TeV (ref. [32]). We use up-going muon data of TeV-scale energy from two years of detector operation[28] representing 34,975 events with a 0.1% atmospheric muon contamination.

Analysis set-up

To obtain the prediction for LV effects, we multiply the oscillation probability, given in equation (3), with the predicted atmospheric neutrino flux calculated using the matrix cascade equation (MCEq)[33]. These 'atmospheric neutrinos' originate from the decay of muons and various mesons produced by collisions of primary cosmic rays and air molecules, and consist of both neutrinos and antineutrinos. The atmospheric neutrinos have two main components: 'conventional', from pion and kaon decay, and 'prompt', from charmed meson decay. The conventional flux dominates at energies less than 18 TeV because of the larger production cross-section, whereas the harder prompt spectrum becomes relevant at higher energy. In the energy range of interest, the astrophysical neutrino contribution is small. We include it modelled as a power law with normalization and spectral index, $\sim\Phi E^{-\gamma}$. The absorption of each flux component propagating through Earth to IceCube is properly modelled[34,35]. Muon production from ν_μ charged-current events at IceCube proceeds through deep inelastic neutrino interactions as calculated in ref. [36].

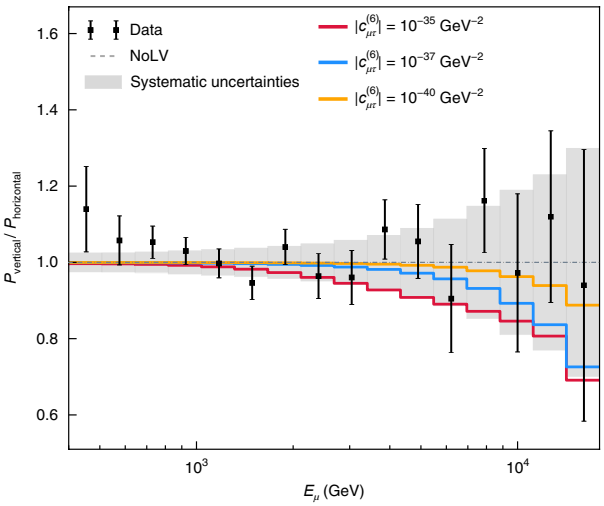

Fig. 2 | The ratio of vertical to horizontal neutrino transition probabilities at IceCube. Here, vertical events are defined by $\cos\theta \leq -0.6$ and the horizontal events are defined by $\cos\theta > -0.6$. The transition probability ratio with 1 s.d. statistical errors (error bars), extracted from the data, is compared to the prediction for various dimension-six operator values. The range of uncorrelated systematic uncertainties is shown as a light grey band. This is constructed from ensembles of many simulations where the nuisance parameters are varied within their uncertainties.

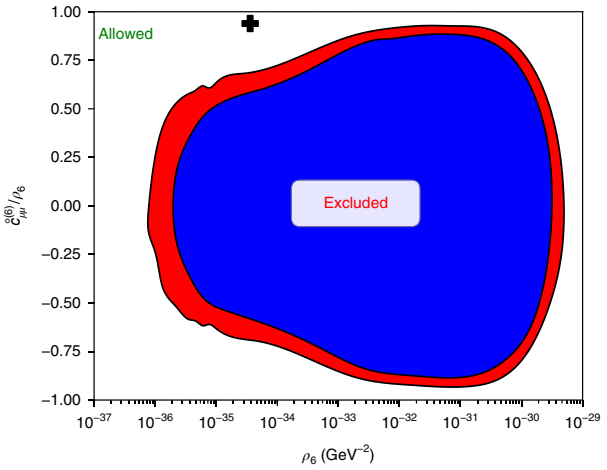

Fig. 3 | The excluded parameter space region for the dimension-six SME coefficients. The figure shows the exclusion region of the dimension-six SME coefficients in the space of two parameters: ρ_6 and $\mathring{c}^{(6)}_{\mu\mu}/\rho_6$. Here, $\rho_6 \equiv \sqrt{(\mathring{c}^{(6)}_{\mu\mu})^2 + \mathrm{Re}(\mathring{c}^{(6)}_{\mu\tau})^2 + \mathrm{Im}(\mathring{c}^{(6)}_{\mu\tau})^2}$ (horizontal axis) and $\mathring{c}^{(6)}_{\mu\mu}/\rho_6$ (vertical axis) are a combination of the three SME coefficients: ρ represents LV strength, and $\mathring{c}^{(6)}_{\mu\mu}/\rho_6$ represents a fraction of the diagonal element, while the subscript 6 indicates the dimension. In the white region, LV is allowed. The best-fit point of this sample for this operator is shown by the black cross. The blue and red regions are excluded at 99% CL and 90% CL, respectively.

The short distance of travel for horizontal neutrinos leads to negligible spectral distortion due to LV, whereas the long path length for vertical neutrinos leads to modifications. Therefore, if we compare the zenith angle distribution (θ) of the expectation from simulations and ν_μ data from $\cos\theta = -1.0$ (vertical) to $\cos\theta = 0.0$ (horizontal) (see Fig. 1), then one can determine the allowed LV parameters. Figure 2 shows the ratio of transition probabilities of vertical events to horizontal events. The data transition probability is defined by the ratio of observed events to expected events, and the simulation transition probability is defined by the expected events in the presence of LV to the number of events in the absence of LV. In the absence of LV, this ratio equals 1. Here, as an example, we show several predictions from simulations with different dimension-six LV parameters $\left|\mathring{c}^{(6)}_{\mu\tau}\right|$. In general, higher-order terms are more important at higher energies. To assess the existence of LV, we perform a binned Poisson likelihood analysis by binning the data in zenith angle and energy. We use 10 linearly spaced bins in cosine of zenith angle from −1.0 to 0.0 and 17 logarithmically spaced bins in reconstructed muon energy ranging from 400 GeV to 18 TeV. Systematic uncertainties are incorporated as nuisance parameters in our likelihood. We introduce six systematic parameters related to the neutrino flux prediction: normalizations of conventional (40% error), prompt (no constraint) and astrophysical (no constraint) neutrino flux components; ratio of pion and kaon contributions for conventional flux (10% error); spectral index of primary cosmic rays (2% error); and astrophysical neutrino spectral index (25% error). The absolute photon detection efficiency has been shown to have negligible impact on the exclusion contours in a search for sterile neutrinos that uses an equivalent analysis technique for a subset of the IceCube data considered here[34,37]. The impact of light propagation model uncertainties on the horizontal to vertical ratio is less than 5% at a few TeV, where this analysis is most sensitive[35]. Thus, the impact of these uncertainties on the exclusion contours is negligible.

To constrain the LV parameters, we use two statistical techniques. First, we performed a likelihood analysis by profiling the likelihood over the nuisance parameters per set of LV parameters. From the profiled likelihood, we find the best-fit LV parameters and derive the 90% and 99% confidence levels (CLs) assuming Wilks's theorem with three degrees of freedom[37]. Second, we set the priors to the nuisance parameter uncertainties and scan the posterior space of the likelihood by means of a Markov chain Monte Carlo (MCMC) method[38]. These two procedures are found to be complementary, and the extracted LV parameters agree with the null hypothesis. For simplicity, we present the likelihood results in this paper and show the MCMC results in the Methods.

Results

Figure 3 shows the excluded region of dimension-six SME coefficients. The results for all operators are available in the Supplementary Information. The fit was performed in a three-dimensional phase space; however, the complex phase of the off-diagonal terms is not important at high energy, and we choose the following representation methods. The horizontal axis shows the strength of LV, $\rho_6 \equiv \sqrt{(\mathring{c}^{(6)}_{\mu\mu})^2 + \mathrm{Re}(\mathring{c}^{(6)}_{\mu\tau})^2 + \mathrm{Im}(\mathring{c}^{(6)}_{\mu\tau})^2}$, and the vertical axis represents a fraction of the diagonal element, $\mathring{c}^{(6)}_{\mu\mu}/\rho_6$. The best-fit point shown by the marker is compatible with the absence of LV; therefore, we present 90% CL (red) and 99% CL (blue) exclusion regions. The contour extends to small values, beyond the phase space explored by previous analyses[16–18]. The leftmost edge of our exclusion region is limited by the small statistics of high-energy atmospheric neutrinos. The rightmost edge of the exclusion region is limited by fast LV-induced oscillations that suppress the flux but lead to no shape distortion. This can be constrained only by the absolute normalization of the flux. In the case of the dimension-three operator, the right edge can be excluded by other atmospheric neutrino oscillation measurements[18,39]. We have studied the applicability of Wilks's theorem via simulations.

Table 1 | Comparison of attainable best limits of SME coefficients in various fields

Dimension	Method	Type	Sector	Limits	Reference
Three	Cosmic microwave background polarization	Astrophysical	Photon	~10^{-43} GeV	5
	He–Xe co-magnetometer	Tabletop	Neutron	~10^{-34} GeV	10
	Torsion pendulum	Tabletop	Electron	~10^{-31} GeV	12
	Muon g−2	Accelerator	Muon	~10^{-24} GeV	13
	Neutrino oscillation	Atmospheric	Neutrino	$\lvert\mathrm{Re}(\mathring{a}^{(3)}_{\mu\tau})\rvert$, $\lvert\mathrm{Im}(\mathring{a}^{(3)}_{\mu\tau})\rvert$	This work
				$<2.9\times10^{-24}$ GeV(99% CL)	
				$<2.0\times10^{-24}$ GeV(90% CL)	
Four	Gamma-ray-burst (GRB) vacuum birefringence	Astrophysical	Photon	~10^{-38}	6
	Laser interferometer	Gravitational-wave observatory	Photon	~10^{-22}	7
	Sapphire cavity oscillator	Tabletop	Photon	~10^{-18}	8
	Ne–Rb–K co-magnetometer	Tabletop	Neutron	~10^{-29}	11
	Trapped Ca^+ ion	Tabletop	Electron	~10^{-19}	14
	Neutrino oscillation	Atmospheric	Neutrino	$\mathrm{Re}(\mathring{c}^{(4)}_{\mu\tau})$, $\lvert\mathrm{Im}(\mathring{c}^{(4)}_{\mu\tau})\rvert$	This work
				$<3.9\times10^{-28}$(99% CL)	
				$<2.7\times10^{-28}$(90% CL)	
Five	GRB vacuum birefringence	Astrophysical	Photon	~10^{-34} GeV^{-1}	6
	Ultrahigh-energy cosmic ray	Astrophysical	Proton	~10^{-22} to 10^{-18} GeV^{-1}	9
	Neutrino oscillation	Atmospheric	Neutrino	$\lvert\mathrm{Re}(\mathring{a}^{(5)}_{\mu\tau})\rvert$, $\lvert\mathrm{Im}(\mathring{a}^{(5)}_{\mu\tau})\rvert$	This work
				$<2.3\times10^{-32}$ GeV^{-1}(99% CL)	
				$<1.5\times10^{-32}$ GeV^{-1}(90% CL)	
Six	GRB vacuum birefringence	Astrophysical	Photon	~10^{-31} GeV^{-2}	6
	Ultrahigh-energy cosmic ray	Astrophysical	Proton	~10^{-42} to 10^{-35} GeV^{-2}	9
	Gravitational Cherenkov radiation	Astrophysical	Gravity	~10^{-31} GeV^{-2}	15
	Neutrino oscillation	Atmospheric	Neutrino	$\lvert\mathrm{Re}(\mathring{c}^{(6)}_{\mu\tau})\rvert$, $\lvert\mathrm{Im}(\mathring{c}^{(6)}_{\mu\tau})\rvert$	This work
				$<1.5\times10^{-36}$ GeV^{-2}(99% CL)	
				$<9.1\times10^{-37}$ GeV^{-2}(90% CL)	
Seven	GRB vacuum birefringence	Astrophysical	Photon	~10^{-28} GeV^{-3}	6
	Neutrino oscillation	Atmospheric	Neutrino	$\lvert\mathrm{Re}(\mathring{a}^{(7)}_{\mu\tau})\rvert$, $\lvert\mathrm{Im}(\mathring{a}^{(7)}_{\mu\tau})\rvert$	This work
				$<8.3\times10^{-41}$$GeV^{-3}$(99% CL)	
				$<3.6\times10^{-41}$ GeV^{-3}(90% CL)	
Eight	Gravitational Cherenkov radiation	Astrophysical	Gravity	~10^{-46} GeV^{-4}	15
	Neutrino oscillation	Atmospheric	Neutrino	$\lvert\mathrm{Re}(\mathring{c}^{(8)}_{\mu\tau})\rvert$, $\lvert\mathrm{Im}(\mathring{c}^{(8)}_{\mu\tau})\rvert$	This work
				$<5.2\times10^{-45}$ GeV^{-4}(99% CL)	
				$<1.4\times10^{-45}$ GeV^{-4}(90% CL)	

Near-degenerate real and imaginary parameters reduce the expected degrees of freedom from three and the results here are interpreted as conservative confidence intervals.

Unlike previous results[16–18], this analysis includes all parameter correlations, allowing for certain combinations of parameters to be unconstrained. This can be seen near $\mathring{c}^{(6)}_{\mu\mu}/\rho_6 = -1$ and 1, where LV is dominated by the large diagonal component. This induces the quantum Zeno effect[40], where a neutrino flavour state is 'arrested' in one state by a continuous interaction with a LV field suppressing flavour transitions. Thus, the unshaded regions below and above our exclusion zone are very difficult to constrain with terrestrial experiments.

Table 1 summarizes the results of this work along with representative best limits. A comprehensive list of LV tests is available in ref. [19]. To date, there is no experimental indication of LV, and all of these experiments have maximized their limits by assuming that all but one of the SME parameters are zero[19]. Therefore, to make our results comparable with previous limits, we adopt the same convention. For this, we set the diagonal SME parameters to zero and focus on setting limits on the off-diagonal elements.

The details of the procedure used to set limits are given in the Supplementary Information.

Let us consider the limits from the lowest to highest order. Dimension-three and -four operators are included in the renormalizable sector of SME. These are the main focus of experiments using photons[7,8], nucleons[10,11] and charged leptons[12–14]. Going beyond terrestrial experiments, limits arising from astrophysical observations provide strong constraints[5,6]. Among the variety of limits coming from the neutrino sector, the attainable best limits are dominated by atmospheric neutrino oscillation analyses[16–18], where the longest propagation length and the highest energies enable us to use neutrino oscillations as the biggest interferometer on Earth. The results from our analysis surpass past ones due to the higher statistics of high-energy atmospheric neutrinos and our improved control of systematic uncertainties. Using a traditional metric, which assumes neutrinos to be massless, we can recast our result as an upper limit on any deviation of the speed of massless neutrinos from the speed of light due to LV. That is less than 10^{-28} at 99% CL. This is about an order-of-magnitude improvement over past analyses[16–18], and is of the same order as the deviation in speed that is expected due to the known neutrino mass at the energies relevant for this analysis.

Searches of dimension-five and higher LV operators are dominated by astrophysical observations[6,9,15]. Among them, ultrahigh-energy cosmic rays have the highest measured energy[41] and are used to set the strongest limits on dimension-six and higher operators[9]. However, these limits are sensitive to the composition of ultrahigh-energy cosmic rays, which is currently uncertain[20,42]. These limits assume that the cosmic rays at the highest energies are protons, but if they are in fact iron nuclei, then the ultrahigh-energy cosmic ray limits are significantly reduced. Our analysis sets the most stringent limits in an unambiguous way across all fields for the dimension-six operator. Such high-dimension operators are generic signatures of new physics[43]. For example, the dimension-five operator is an attractive possibility to produce neutrino masses, and dimension-six operators represent new physics interactions that can, for example, mediate proton decay. Although LV dimension-six operators, such as $\mathring{c}^{(6)}_{\mu\tau}$, are well motivated by certain theories including non-commutative field theory[2] and supersymmetry[3], they have so far not been probed with elementary particles due to the lack of available high-energy sources. Thus, our work pushes boundaries on new physics beyond the standard model and general relativity.

Conclusion

We have presented a test of LV with high-energy atmospheric muon neutrinos from IceCube. Correlations of the SME coefficients are fully taken into account, and systematic errors are controlled by the fit. Although we did not find evidence for LV, this analysis provides the best attainable limits on SME coefficients in the neutrino sector along with limits on the higher-order operators. Comparison with limits from other sectors reveals that this work provides among the best attainable limits on dimension-six coefficients across all fields: from tabletop experiments to cosmology. This is a remarkable point that demonstrates how powerful neutrino interferometry can be in the study of fundamental spacetime properties.

Further improvements on the search for LV in the neutrino sector using IceCube will be possible when the astrophysical neutrino sample is included[44]. Such analyses[45,46] will require a substantial improvement of detector and flux systematic uncertainty evaluations[47,48]. In the near future, water-based neutrino telescopes such as KM3NeT[49] and the ten-times-larger IceCube-Gen2[50] will be in a position to observe more astrophysical neutrinos. With the higher statistics and improved sensitivity, these experiments will have an enhanced potential for discovery of LV.

Methods

Methods, including statements of data availability and any associated accession codes and references, are available at https://doi.org/10.1038/s41567-018-0172-2.

Received: 13 September 2017; Accepted: 15 May 2018;
Published online: 16 July 2018

References

1. Kostelecký, V. A. & Samuel, S. Spontaneous breaking of Lorentz symmetry in string theory. *Phys. Rev. D* **39**, 683–685 (1989).
2. Carroll, S. M., Harvey, J. A., Kostelecký, V. A., Lane, C. D. & Okamoto, T. Noncommutative Field Theory and Lorentz Violation. *Phys. Rev. Lett.* **87**, 141601 (2001).
3. Groot Nibbelink, S. & Pospelov, M. Lorentz violation in supersymmetric field theories. *Phys. Rev. Lett.* **94**, 081601 (2005).
4. Kostelecký, A. & Mewes, M. Neutrinos with Lorentz-violating operators of arbitrary dimension. *Phys. Rev. D* **85**, 096005 (2012).
5. Komatsu, E. et al. Five-year Wilkinson microwave anisotropy probe (WMAP) observations: cosmological interpretation. *Astrophys. J. Suppl.* **180**, 330–376 (2009).
6. Kostelecký, V. A. & Mewes, M. Constraints on relativity violations from gamma-ray bursts. *Phys. Rev. Lett.* **110**, 201601 (2013).
7. Kostelecký, V. A., Melissinos, A. C. & Mewes, M. Searching for photon-sector Lorentz violation using gravitational-wave detectors. *Phys. Lett. B* **761**, 1–7 (2016).
8. Nagel, M. et al. Direct terrestrial test of Lorentz symmetry in electrodynamics to 10^{-18}. *Nat. Commun.* **6**, 8174 (2015).
9. Maccione, L., Taylor, A. M., Mattingly, D. M. & Liberati, S. Planck-scale Lorentz violation constrained by ultra-high-energy cosmic rays. *J. Cosmol. Astropart. Phys.* **0904**, 022 (2009).
10. Allmendinger, F. et al. New limit on Lorentz-invariance- and CPT-violating neutron spin interactions using a free-spin-precession ^{3}He-^{129}Xe comagnetometer. *Phys. Rev. Lett.* **112**, 110801 (2014).
11. Smiciklas, M., Brown, J. M., Cheuk, L. W. & Romalis, M. V. A new test of local Lorentz invariance using ^{21}Ne-Rb-K comagnetometer. *Phys. Rev. Lett.* **107**, 171604 (2011).
12. Heckel, B. R. et al. New CP-violation and preferred-frame tests with polarized electrons. *Phys. Rev. Lett.* **97**, 021603 (2006).
13. Bennett, G. W. et al. Search for Lorentz and CPT violation effects in muon spin precession. *Phys. Rev. Lett.* **100**, 091602 (2008).
14. Pruttivarasin, T. et al. A Michelson–Morley test of Lorentz symmetry for electrons. *Nature* **517**, 592–595 (2015).
15. Kostelecký, V. A. & Tasson, J. D. Constraints on Lorentz violation from gravitational Čerenkov radiation. *Phys. Lett. B* **749**, 551–559 (2015).
16. Abbasi, R. et al. Determination of the atmospheric neutrino flux and searches for new physics with AMANDA-II. *Phys. Rev. D* **79**, 102005 (2009).
17. Abbasi, R. et al. Search for a Lorentz-violating sidereal signal with atmospheric neutrinos in IceCube. *Phys. Rev. D* **82**, 112003 (2010).
18. Abe, K. et al. Test of Lorentz invariance with atmospheric neutrinos. *Phys. Rev. D* **91**, 052003 (2015).
19. Kostelecký, V. A. & Russell, N. Data tables for Lorentz and CPT violation. *Rev. Mod. Phys.* **83**, 11–31 (2011).
20. Liberati, S. Tests of Lorentz invariance: a 2013 update. *Class. Quant. Grav.* **30**, 133001 (2013).
21. Fukuda, Y. et al. Evidence for oscillation of atmospheric neutrinos. *Phys. Rev. Lett.* **81**, 1562–1567 (1998).
22. Ahmad, Q. R. et al. Measurement of the rate of $\nu_e + d \rightarrow p + p + e-$ interactions produced by ^{8}B solar neutrinos at the Sudbury Neutrino Observatory. *Phys. Rev. Lett.* **87**, 071301 (2001).
23. Ahn, M. H. et al. Indications of neutrino oscillation in a 250 km long baseline experiment. *Phys. Rev. Lett.* **90**, 041801 (2003).
24. Eguchi, K. et al. First results from KamLAND: Evidence for reactor anti-neutrino disappearance. *Phys. Rev. Lett.* **90**, 021802 (2003).
25. Abe, K. et al. Indication of electron neutrino appearance from an accelerator-produced off-axis muon neutrino beam. *Phys. Rev. Lett.* **107**, 041801 (2011).
26. An, F. P. et al. Observation of electron-antineutrino disappearance at Daya Bay. *Phys. Rev. Lett.* **108**, 171803 (2012).
27. Esteban, I., Gonzalez-Garcia, M. C., Maltoni, M., Martinez-Soler, I. & Schwetz, T. Updated fit to three neutrino mixing: exploring the accelerator-reactor complementarity. *J. High Energy Phys.* **1701**, 087 (2017).
28. Aartsen, M. G. et al. Evidence for astrophysical muon neutrinos from the northern sky with IceCube. *Phys. Rev. Lett.* **115**, 081102 (2015).
29. Gonzalez-Garcia, M. C., Halzen, F. & Maltoni, M. Physics reach of high-energy and high-statistics IceCube atmospheric neutrino data. *Phys. Rev. D* **71**, 093010 (2005).
30. Abbasi, R. et al. The IceCube data acquisition system: signal capture, digitization, and timestamping. *Nucl. Instrum. Meth. A* **601**, 294–316 (2009).
31. Aartsen, M. G. et al. The IceCube Neutrino Observatory: instrumentation and online systems. *J. Instrum.* **12**, P03012 (2017).
32. Weaver, C. N. *Evidence for Astrophysical Muon Neutrinos from the Northern Sky*. PhD thesis, Univ. Wisconsin–Madison (2015).
33. Fedynitch, A., Engel, R., Gaisser, T. K., Riehn, F. & Stanev, T. Calculation of conventional and prompt lepton fluxes at very high energy. *Eur. Phys. J. Web Conf.* **99**, 08001 (2015).

34. Jones, B. J. P. *Sterile Neutrinos in Cold Climates*. PhD thesis, MIT (2015).
35. Argüelles Delgado, C. A. *New Physics with Atmospheric Neutrinos*. PhD thesis, Univ. Wisconsin–Madison (2015).
36. Cooper-Sarkar, A. & Sarkar, S. Predictions for high energy neutrino cross-sections from the ZEUS global PDF fits. *J. High Energy Phys.* **0801**, 075 (2008).
37. Aartsen, M. G. et al. Searches for sterile neutrinos with the IceCube detector. *Phys. Rev. Lett.* **117**, 071801 (2016).
38. Foreman-Mackey, D., Hogg, D. W., Lang, D. & Goodman, J. emcee: the MCMC hammer. *Publ. Astron. Soc. Pac.* **125**, 306–312 (2013).
39. Aartsen, M. G. et al. Determining neutrino oscillation parameters from atmospheric muon neutrino disappearance with three years of IceCube DeepCore data. *Phys. Rev. D* **91**, 072004 (2015).
40. Harris, R. A. & Stodolsky, L. Two state systems in media and "Turing's paradox". *Phys. Lett. B* **116**, 464–468 (1982).
41. Abraham, J. et al. Observation of the suppression of the flux of cosmic rays above 4 x 10^{19}eV. *Phys. Rev. Lett.* **101**, 061101 (2008).
42. Aab, A. et al. Evidence for a mixed mass composition at the 'ankle' in the cosmic-ray spectrum. *Phys. Lett. B* **762**, 288–295 (2016).
43. Chalmers, M. Interview: Steven Weinberg. *CERN Courier* **57**, 31–35 (2017).
44. Aartsen, M. G. et al. Evidence for high-energy extraterrestrial neutrinos at the IceCube detector. *Science* **342**, 1242856 (2013).
45. Stecker, F. W., Scully, S. T., Liberati, S. & Mattingly, D. Searching for traces of Planck-scale physics with high energy neutrinos. *Phys. Rev. D* **91**, 045009 (2015).
46. Argüelles, C. A., Katori, T. & Salvado, J. New physics in astrophysical neutrino flavor. *Phys. Rev. Lett.* **115**, 161303 (2015).
47. Aartsen, M. G. et al. Measurement of South Pole ice transparency with the IceCube LED calibration system. *Nucl. Instrum. Meth. A* **711**, 73–89 (2013).
48. Aartsen, M. G. et al. Measurement of the atmospheric ν_e spectrum with IceCube. *Phys. Rev. D* **91**, 122004 (2015).
49. Adrian-Martinez, S. et al. Letter of intent for KM3NeT 2.0. *J. Phys. G* **43**, 084001 (2016).
50. Aartsen, M. G. et al. IceCube-Gen2: a vision for the future of neutrino astronomy in Antarctica. Preprint at https://arxiv.org/abs/1412.5106 (2014).

Acknowledgements

We acknowledge the support from the following agencies: USA—US National Science Foundation–Office of Polar Programs, US National Science Foundation–Physics Division, Wisconsin Alumni Research Foundation, Center for High Throughput Computing (CHTC) at the University of Wisconsin–Madison, Open Science Grid (OSG), Extreme Science and Engineering Discovery Environment (XSEDE), US Department of Energy–National Energy Research Scientific Computing Center, Particle astrophysics research computing centre at the University of Maryland, Institute for Cyber-Enabled Research at Michigan State University and Astroparticle physics computational facility at Marquette University; Belgium—Funds for Scientific Research (FRS-FNRS and FWO), FWO Odysseus and Big Science programmes, and Belgian Federal Science Policy Office (Belspo); Germany—Bundesministerium für Bildung und Forschung (BMBF), Deutsche Forschungsgemeinschaft (DFG), Helmholtz Alliance for Astroparticle Physics (HAP), Initiative and Networking Fund of the Helmholtz Association, Deutsches Elektronen Synchrotron (DESY), and High Performance Computing cluster of the RWTH Aachen; Sweden—Swedish Research Council, Swedish Polar Research Secretariat, Swedish National Infrastructure for Computing (SNIC), and Knut and Alice Wallenberg Foundation; Australia—Australian Research Council; Canada—Natural Sciences and Engineering Research Council of Canada, Calcul Québec, Compute Ontario, Canada Foundation for Innovation, WestGrid and Compute Canada; Denmark—Villum Fonden, Danish National Research Foundation (DNRF); New Zealand—Marsden Fund; Japan—Japan Society for Promotion of Science (JSPS) and Institute for Global Prominent Research (IGPR) of Chiba University; Korea—National Research Foundation of Korea (NRF); Switzerland—Swiss National Science Foundation (SNSF); UK—Science and Technology Facilities Council (STFC) and The Royal Society.

Author contributions

The IceCube Collaboration designed, constructed and now operates the IceCube Neutrino Observatory. Data processing and calibration, Monte Carlo simulations of the detector and of theoretical models, and data analyses were performed by a large number of collaboration members, who also discussed and approved the scientific results presented here. The main authors of this manuscript were C. Argüelles, A. Kheirandish, G. Collin, S. Mandalia, J. Conrad and T. Katori. It was reviewed by the entire collaboration before publication, and all authors approved the final version of the manuscript.

Competing interests

The authors declare no competing interests.

Additional information

Supplementary information is available for this paper at https://doi.org/10.1038/s41567-018-0172-2.

Reprints and permissions information is available at www.nature.com/reprints.

Correspondence and requests for materials should be addressed to C.A. or G.H.C. or J.M.C. or A.K. or T.K. or S.M.

Publisher's note: Springer Nature remains neutral with regard to jurisdictional claims in published maps and institutional affiliations.

Methods

Neutrino oscillations and tests of LV. The field of neutrino oscillations has been developed through a series of measurements of solar[51–55], atmospheric[56–58], reactor[59–62] and accelerator neutrinos[57,63,64]. In the early days, the cause of neutrino oscillations was not precisely known, and LV was suggested as a possible source of neutrino flavour anomalies[65] and so tests of LV with high-energy astrophysical sources started to generate a lot of interest[66]. Subsequently, the L/E dependence of standard neutrino oscillations was measured[56]. As the neutrino mass term in the effective Hamiltonian has a $1/E$ energy dependence, it was a strong indication that a non-zero neutrino mass is in fact the cause of neutrino oscillations, not LV. Then, the focus of the community shifted to consider LV to be a second-order effect in neutrino oscillations, and so neutrino oscillation data have been used to look for small deviations due to LV from the standard neutrino mass oscillations.

One approach to look for LV is to use a model-independent effective field theory, such as the SME[67–69]. The SME is widely used in communities from low-energy tabletop experiments to high-energy particle physics and cosmology, to search for LV. This formalism incorporates various fundamental features of quantum field theories, such as energy–momentum conservation, observer Lorentz transformations and spin statistics; however, it includes violations of particle Lorentz transformations. A number of neutrino oscillation data sets have been analysed using this formalism, including LSND[70], MiniBooNE[71], MINOS[72–75], Double Chooz[76,77], SNO[78] and T2K[79], as well as the aforementioned IceCube-40 and Super-Kamiokande. These experiments can be classified into two groups. First, the presence of a direction-dependent field induces direction-dependent physics. In particular, neutrino beam lines are fixed and so such direction-dependent physics would show up as a time-dependence of neutrino oscillation data[70–76,78,79]. Second, a search of LV is possible even without assuming the presence of a spatial component (that is, no time-dependent physics), by utilizing distortions of the spectrum[77]. The results presented here are based on this second approach.

Neutrino oscillation formula. Here, we illustrate how to calculate the oscillation probability for the case with non-zero isotropic LVs, such as $\mathring{a}^{(d)}$ and $\mathring{c}^{(d)}$. The effective Hamiltonian relevant for oscillation is given by

$$H \approx \frac{m^2}{2E} + \sum_{d\geq 3} E^{d-3}(\mathring{a}^{(d)} - \mathring{c}^{(d)})$$

Note that $\mathring{a}^{(d)}$ are non-zero for $d=$ odd, and $\mathring{c}^{(d)}$ are non-zero for $d=$ even. We assume that either one of them is non-zero. We use the $\nu_\mu \to \nu_\tau$ two-flavour approximation that allows us to solve the time-dependent Schrödinger equation analytically to derive the neutrino oscillation formula with neutrino masses and LV. This choice is allowed because a large matter potential 'arrests' ν_e (quantum Zeno effect[40]) and prevent transitions from ν_μ. As the matter potential of ν_e is much bigger than that due to LV effects, the size of LV that we consider here hardly induces any $\nu_\mu \to \nu_e$ transition. Our choice of the two-flavour oscillation model does not diminish the strength of our constraints on parameters in the $\nu_\mu - \nu_\tau$ block matrix with respect to a full three-flavour calculation. Hence, the mass matrix m^2 can be diagonalized to $M^2 = \mathrm{diag}(m_2^2, m_3^2)$ by a mixing matrix U with mixing angle ϕ,

$$\begin{aligned} m^2 &= UM^2U^\dagger \\ &= \begin{pmatrix} \cos\phi & \sin\phi \\ -\sin\phi & \cos\phi \end{pmatrix} \begin{pmatrix} m_2^2 & 0 \\ 0 & m_3^2 \end{pmatrix} \begin{pmatrix} \cos\phi & -\sin\phi \\ \sin\phi & \cos\phi \end{pmatrix} \end{aligned}$$

By adding $E^{d-3}(\mathring{a}^{(d)} - \mathring{c}^{(d)})$, this 2×2 Hamiltonian can be diagonalized with two eigenvalues, λ_1 and λ_2. Here, we define $\lambda_2 > \lambda_1$. Then the oscillation formula is

$$P(\nu_\mu \to \nu_\tau) = \frac{|2A_2|^2}{(\lambda_2 - \lambda_1)^2} \sin^2\left(\frac{\lambda_2 - \lambda_1}{2} L\right)$$

where

$$\begin{aligned} \lambda_1 &= \frac{1}{2}[(A_1 + A_3) - \sqrt{|A_1 - A_3|^2 + |2A_2|^2}] \\ \lambda_2 &= \frac{1}{2}[(A_1 + A_3) + \sqrt{|A_1 - A_3|^2 + |2A_2|^2}] \\ A_1 &= \frac{1}{2E}(m_2^2 \cos^2\phi + m_3^2 \sin^2\phi) + E^{d-3}(\mathring{a}_{\mu\mu}^{(d)} - \mathring{c}_{\mu\mu}^{(d)}) \\ A_2 &= \frac{1}{2E}\cos\phi \sin\phi (m_2^2 - m_3^2) + E^{d-3}(\mathring{a}_{\mu\tau}^{(d)} - \mathring{c}_{\mu\tau}^{(d)}) \\ A_3 &= \frac{1}{2E}(m_2^2 \sin^2\phi + m_3^2 \cos\phi) - E^{d-3}(\mathring{a}_{\mu\mu}^{(d)} - \mathring{c}_{\mu\mu}^{(d)}) \end{aligned}$$

In the high-energy limit, the neutrino mass effect is negligible in comparison to Lorentz-violating effects,

$$\begin{aligned} P(\nu_\mu \to \nu_\tau) &\sim \left(1 - \frac{\left|\mathring{a}_{\mu\mu}^{(d)} - \mathring{c}_{\mu\mu}^{(d)}\right|^2}{\rho_d^2}\right) \sin^2(L\rho_d E^{d-3}) \\ &= \frac{|\mathring{a}_{\mu\tau}^{(d)} - \mathring{c}_{\mu\tau}^{(d)}|^2}{\rho_d^2} \sin^2(L\rho_d E^{d-3}) \end{aligned}$$

Here we use $\rho_d \equiv \sqrt{(\mathring{a}_{\mu\mu}^{(d)})^2 + \mathrm{Re}(\mathring{a}_{\mu\tau}^{(d)})^2 + \mathrm{Im}(\mathring{a}_{\mu\tau}^{(d)})^2}$ or $\sqrt{(\mathring{c}_{\mu\mu}^{(d)})^2 + \mathrm{Re}(\mathring{c}_{\mu\tau}^{(d)})^2 + \mathrm{Im}(\mathring{c}_{\mu\tau}^{(d)})^2}$, which represents the strength of LV. Then, $\mathring{a}_{\mu\mu}^{(d)}/\rho_d$ and $\mathring{c}_{\mu\mu}^{(d)}/\rho_d$ become fractions of diagonal terms that are bounded between -1 and $+1$. The result suggests that there are no LV neutrino oscillations without off-diagonal terms and that the LV oscillations are symmetric between the real and imaginary parts of the off-diagonal SME parameters.

Bayesian framework. The main results of this paper are extracted using Wilks's theorem so as to be directly comparable with frequentist results reported by other neutrino experiments. For completeness, we have also performed a Bayesian analysis that uses a joint distribution over the nine systematic and LV parameters. This joint distribution is constructed from the same likelihood and prior distributions used in the frequentist analysis, except that we also added conservative constraints on all flux normalizations to avoid a strong prior range dependence. The Bayesian study is presented in two results (see Supplementary Fig. 1), which were both generated by the EMCEE MCMC software package[38]. First, we constructed the 99% exclusion credibility region from a sampling of the joint distribution, with two different treatments on nuisance parameters. Second, we extracted the result based on the Bayes factor of marginalizing the likelihood over nuisance parameters using the MultiNest algorithm[80]. These studies highlight the differences in results obtained using different treatments of nuisance parameters.

Data availability. The data that were used in this study are available in the IceCube Public Data Access 'Astrophysical muon neutrino flux in the northern sky with 2 years of IceCube data'[28] (http://icecube.wisc.edu/science/data/).

References

51. Altmann, M. et al. GNO solar neutrino observations: Results for GNO I. *Phys. Lett. B* **490**, 16–26 (2000).
52. Abdurashitov, J. N. et al. Solar neutrino flux measurements by the Soviet–American Gallium Experiment(SAGE) for half the 22 year solar cycle. *J. Exp. Theor. Phys.* **95**, 181 (2002).
53. Hosaka, J. et al. Solar neutrino measurements in super-Kamiokande-I. *Phys. Rev. D.* **73**, 112001 (2006).
54. Aharmim, B. et al. Electron energy spectra, fluxes, and day–night asymmetries of B-8 solar neutrinos from measurements with NaCl dissolved in the heavy-water detector at the Sudbury Neutrino Observatory. *Phys. Rev. C* **72**, 055502 (2005).
55. Arpesella, C. et al. Direct measurement of the Be-7 solar neutrino flux with 192 days of Borexino data. *Phys. Rev. Lett.* **101**, 091302 (2008).
56. Ashie, Y. et al. Evidence for an oscillatory signature in atmospheric neutrino oscillation. *Phys. Rev. Lett.* **93**, 101801 (2004).
57. Adamson, P. et al. Combined analysis of ν_μ disappearance and $\nu_\mu \to \nu_e$ appearance in MINOS using accelerator and atmospheric neutrinos. *Phys. Rev. Lett.* **112**, 191801 (2014).
58. Aartsen, M. G. et al. Measurement of atmospheric neutrino oscillations at 6–56 GeV with IceCube DeepCore. *Phys. Rev. Lett.* **120**, 071801 (2018).
59. Abe, S. et al. Precision measurement of neutrino oscillation parameters with KamLAND. *Phys. Rev. Lett.* **100**, 221803 (2008).
60. Abe, Y. et al. Indication of reactor disappearance in the Double Chooz experiment. *Phys. Rev. Lett.* **108**, 131801 (2012).
61. Ahn, J. K. et al. Observation of reactor electron antineutrino disappearance in the RENO experiment. *Phys. Rev. Lett.* **108**, 191802 (2012).
62. An, F. P. et al. Spectral measurement of electron antineutrino oscillation amplitude and frequency at Daya Bay. *Phys. Rev. Lett.* **112**, 061801 (2014).
63. Abe, K. et al. Combined analysis of neutrino and antineutrino oscillations at T2K. *Phys. Rev. Lett.* **118**, 151801 (2017).
64. Adamson, P. et al. Constraints on oscillation parameters from ν_e appearance and ν_μ disappearance in NOvA. *Phys. Rev. Lett.* **118**, 231801 (2017).
65. Coleman, S. R. & Glashow, S. L. High-energy tests of Lorentz invariance. *Phys. Rev. D* **59**, 116008 (1999).
66. Amelino-Camelia, G., Ellis, J. R., Mavromatos, N. E., Nanopoulos, D. V. & Sarkar, S. Tests of quantum gravity from observations of gamma-ray bursts. *Nature* **393**, 763–765 (1998).

67. Colladay, D. & Kostelecký, V. A. CPT violation and the standard model. *Phys. Rev. D.* **55**, 6760–6774 (1997).
68. Colladay, D. & Kostelecký, V. A. Lorentz violating extension of the standard model. *Phys. Rev. D.* **58**, 116002 (1998).
69. Kostelecký, V. A. Gravity, Lorentz violation, and the standard model. *Phys. Rev. D.* **69**, 105009 (2004).
70. Auerbach, L. B. et al. Tests of Lorentz violation in $\overline{\nu_\mu} \rightarrow \overline{\nu_e}$ oscillations. *Phys. Rev. D* **72**, 076004 (2005).
71. Aguilar-Arevalo, A. A. et al. Test of Lorentz and CPT violation with short baseline neutrino oscillation excesses. *Phys. Lett. B* **718**, 1303–1308 (2013).
72. Adamson, P. et al. Testing Lorentz invariance and CPT conservation with NuMI neutrinos in the MINOS near detector. *Phys. Rev. Lett.* **101**, 151601 (2008).
73. Adamson, P. et al. A search for Lorentz invariance and CPT violation with the MINOS far detector. *Phys. Rev. Lett.* **105**, 151601 (2010).
74. Adamson, P. et al. Search for Lorentz invariance and CPT violation with muon antineutrinos in the MINOS near detector. *Phys. Rev. D* **85**, 031101 (2012).
75. Rebel, B. & Mufson, S. The search for neutrino-antineutrino mixing resulting from Lorentz invariance violation using neutrino interactions in MINOS. *Astropart. Phys.* **48**, 78–81 (2013).
76. Abe, Y. et al. First test of Lorentz violation with a reactor-based antineutrino experiment. *Phys. Rev. D* **86**, 112009 (2012).
77. Díaz, J. S., Katori, T., Spitz, J. & Conrad, J. M. Search for neutrino-antineutrino oscillations with a reactor experiment. *Phys. Lett. B* **727**, 412 (2013).
78. Diaz, J. S. & Schwetz, T. Limits on CPT violation from solar neutrinos. *Phys. Rev. D* **93**, 093004 (2016).
79. Abe, K. et al. Search for Lorentz and CPT violation using sidereal time dependence of neutrino flavor transitions over a short baseline. *Phys. Rev. D* **95**, 111101 (2017).
80. Feroz, F., Hobson, M. P. & Bridges, M. MultiNest: an efficient and robust Bayesian inference tool for cosmology and particle physics. *Mon. Not. R. Astron. Soc.* **398**, 1601–1614 (2009).

The IceCube Collaboration

M. G. Aartsen[1], G. C. Hill[1], A. Kyriacou[1], S. Robertson[1], A. Wallace[1], B. J. Whelan[1], M. Ackermann[2], E. Bernardini[2], S. Blot[2], F. Bradascio[2], H.-P. Bretz[2], J. Brostean-Kaiser[2], A. Franckowiak[2], E. Jacobi[2], T. Karg[2], T. Kintscher[2], S. Kunwar[2], R. Nahnhauer[2], K. Satalecka[2], C. Spiering[2], J. Stachurska[2], A. Stasik[2], N. L. Strotjohann[2], A. Terliuk[2], M. Usner[2], J. van Santen[2], J. Adams[3], H. Bagherpour[3], J. A. Aguilar[4], I. Ansseau[4], D. Heereman[4], K. Meagher[4], T. Meures[4], A. O'Murchadha[4], E. Pinat[4], C. Raab[4], M. Ahlers[5], E. Bourbeau[5], D. J. Koskinen[5], M. J. Larson[5], M. Medici[5], M. Rameez[5], T. Stuttard[5], M. Ahrens[6], C. Bohm[6], J. P. Dumm[6], C. Finley[6], S. Flis[6], K. Hultqvist[6], C. Walck[6], M. Zoll[6], I. Al Samarai[7], S. Bron[7], T. Carver[7], A. Christov[7], T. Montaruli[7], D. Altmann[8], G. Anton[8], T. Glüsenkamp[8], U. Katz[8], T. Kittler[8], M. Tselengidou[8], K. Andeen[9], M. Plum[9], T. Anderson[10], J. J. DeLaunay[10], M. Dunkman[10], P. Eller[10], F. Huang[10], A. Keivani[10], J. L. Lanfranchi[10], D. V. Pankova[10], G. Tešić[10], C. F. Turley[10], M. J. Weiss[10], C. Argüelles[11]*, S. Axani[11], G. H. Collin[11]*, J. M. Conrad[11]*, M. Moulai[11], J. Auffenberg[12], M. Brenzke[12], T. Glauch[12], C. Haack[12], P. Kalaczynski[12], J. P. Koschinsky[12], M. Leuermann[12], L. Rädel[12], R. Reimann[12], M. Rongen[12], T. Sälzer[12], S. Schoenen[12], L. Schumacher[12], J. Stettner[12], M. Vehring[12], E. Vogel[12], M. Wallraff[12], A. Waza[12], C. H. Wiebusch[12], X. Bai[13], E. Dvorak[13], J. P. Barron[14], W. Giang[14], D. Grant[14], C. Kopper[14], R. W. Moore[14], S. C. Nowicki[14], S. E. Sanchez Herrera[14], S. Sarkar[14], F. D. Wandler[14], C. Weaver[14], T. R. Wood[14], E. Woolsey[14], J. P. Yanez[14], S. W. Barwick[15], G. Yodh[15], V. Baum[16], S. Böser[16], V. di Lorenzo[16], B. Eberhardt[16], T. Ehrhardt[16], L. Köpke[16], G. Krückl[16], G. Momenté[16], P. Peiffer[16], J. Sandroos[16], A. Steuer[16], K. Wiebe[16], R. Bay[17], K. Filimonov[17], P. B. Price[17], K. Woschnagg[17], J. J. Beatty[18,19], J. Becker Tjus[20], F. Bos[20], B. Eichmann[20], M. Kroll[20], S. Schöneberg[20], F. Tenholt[20], K.-H. Becker[21], D. Bindig[21], K. Helbing[21], S. Hickford[21], R. Hoffmann[21], F. Lauber[21], U. Naumann[21], A. Obertacke Pollmann[21], D. Soldin[21], S. BenZvi[22], R. Cross[22], D. Berley[23], E. Blaufuss[23], E. Cheung[23], J. Felde[23], E. Friedman[23], R. Hellauer[23], K. D. Hoffman[23], R. Maunu[23], A. Olivas[23], T. Schmidt[23], M. Song[23], G. W. Sullivan[23], D. Z. Besson[24], G. Binder[17,25], S. R. Klein[17,25], S. Miarecki[17,25], T. Palczewski[17,25], J. Tatar[17,25], M. Börner[26], T. Fuchs[26], M. Hünnefeld[26], M. Meier[26], T. Menne[26], D. Pieloth[26], W. Rhode[26], T. Ruhe[26], A. Sandrock[26], P. Schlunder[26], J. Soedingrekso[26], J. Werthebach[26], D. Bose[27], H. Dujmovic[27], S. In[27], M. Jeong[27], W. Kang[27], J. Kim[27], C. Rott[27], O. Botner[28], A. Burgman[28], A. Hallgren[28], C. Pérez de los Heros[28], E. Unger[28], J. Bourbeau[29], J. Braun[29], J. Casey[29], D. Chirkin[29], M. Day[29], P. Desiati[29], J. C. Díaz-Vélez[29], S. Fahey[29], K. Ghorbani[29], Z. Griffith[29], F. Halzen[29], K. Hanson[29], B. Hokanson-Fasig[29], K. Jero[29], A. Karle[29], M. Kauer[29], J. L. Kelley[29], A. Kheirandish[29]*, Q. R. Liu[29], W. Luszczak[29], S. Mancina[29], F. McNally[29], G. Merino[29], A. Schneider[29], M. N. Tobin[29], D. Tosi[29], B. Ty[29], J. Vandenbroucke[29], N. Wandkowsky[29], C. Wendt[29], S. Westerhoff[29], L. Wille[29], M. Wolf[29], J. Wood[29],

D. L. Xu[29], T. Yuan[29], L. Brayeur[30], M. Casier[30], C. De Clercq[30], K. D. de Vries[30], G. de Wasseige[30], J. Kunnen[30], J. Lünemann[30], G. Maggi[30], S. Toscano[30], N. van Eijndhoven[30], K. Clark[31], L. Classen[32], A. Kappes[32], S. Coenders[33], M. Huber[33], K. Krings[33], I. C. Rea[33], E. Resconi[33], A. Turcati[33], D. F. Cowen[10,34], J. P. A. M. de André[35], T. DeYoung[35], J. Hignight[35], K. B. M. Mahn[35], J. Micallef[35], G. Neer[35], D. Rysewyk[35], H. Dembinski[36], P. A. Evenson[36], T. K. Gaisser[36], J. G. Gonzalez[36], R. Koirala[36], H. Pandya[36], D. Seckel[36], T. Stanev[36], S. Tilav[36], S. De Ridder[37], M. Labare[37], D. Ryckbosch[37], W. Van Driessche[37], S. Vanheule[37], M. Vraeghe[37], M. de With[38], D. Hebecker[38], H. Kolanoski[38], A. R. Fazely[39], S. Ter-Antonyan[39], X. W. Xu[39], J. Gallagher[40], L. Gerhardt[25], A. Goldschmidt[25], D. R. Nygren[25], G. T. Przybylski[25], T. Stezelberger[25], R. G. Stokstad[25], K. Hoshina[29,41], A. Ishihara[42], M. Kim[42], T. Kuwabara[42], L. Lu[42], K. Mase[42], M. Relich[42], A. Stößl[42], S. Yoshida[42], G. S. Japaridze[43], B. J. P. Jones[44], T. Katori[45*], S. Mandalia[45*], J. Kiryluk[46], M. Lesiak-Bzdak[46], H. Niederhausen[46], Y. Xu[46], G. Kohnen[47], S. Kopper[48], P. Nakarmi[48], J. A. Pepper[48], M. Santander[48], P. A. Toale[48], D. R. Williams[48], M. Kowalski[2,38], N. Kurahashi[49], B. Relethford[49], M. Richman[49], L. Wills[49], J. Madsen[50], S. Seunarine[50], G. M. Spiczak[50], R. Maruyama[51], K. Rawlins[52], S. Sarkar[5,53], M. Stamatikos[18], M. Sutherland[18], I. Taboada[54] and C. F. Tung[54]

[1]Department of Physics, University of Adelaide, Adelaide, Australia. [2]DESY, Zeuthen, Germany. [3]Department of Physics and Astronomy, University of Canterbury, Christchurch, New Zealand. [4]Science Faculty, Université Libre de Bruxelles, Brussels, Belgium. [5]Niels Bohr Institute, University of Copenhagen, Copenhagen, Denmark. [6]Oskar Klein Centre and Department of Physics, Stockholm University, Stockholm, Sweden. [7]Département de physique nucléaire et corpusculaire, Université de Genève, Geneva, Switzerland. [8]Erlangen Centre for Astroparticle Physics, Friedrich-Alexander-Universität Erlangen-Nürnberg, Erlangen, Germany. [9]Department of Physics, Marquette University, Milwaukee, WI, USA. [10]Department of Physics, Pennsylvania State University, University Park, PA, USA. [11]Department of Physics, Massachusetts Institute of Technology, Cambridge, MA, USA. [12]III. Physikalisches Institut, RWTH Aachen University, Aachen, Germany. [13]Physics Department, South Dakota School of Mines and Technology, Rapid City, SD, USA. [14]Department of Physics, University of Alberta, Edmonton, Alberta, Canada. [15]Department of Physics and Astronomy, University of California, Irvine, CA, USA. [16]Institute of Physics, University of Mainz, Mainz, Germany. [17]Department of Physics, University of California, Berkeley, CA, USA. [18]Department of Physics and Center for Cosmology and Astro-Particle Physics, Ohio State University, Columbus, OH, USA. [19]Department of Astronomy, Ohio State University, Columbus, OH, USA. [20]Fakultät für Physik & Astronomie, Ruhr-Universität Bochum, Bochum, Germany. [21]Department of Physics, University of Wuppertal, Wuppertal, Germany. [22]Department of Physics and Astronomy, University of Rochester, Rochester, NY, USA. [23]Department of Physics, University of Maryland, College Park, MD, USA. [24]Department of Physics and Astronomy, University of Kansas, Lawrence, KS, USA. [25]Lawrence Berkeley National Laboratory, Berkeley, CA, USA. [26]Department of Physics, TU Dortmund University, Dortmund, Germany. [27]Department of Physics, Sungkyunkwan University, Suwon, Korea. [28]Department of Physics and Astronomy, Uppsala University, Uppsala, Sweden. [29]Department of Physics and Wisconsin IceCube Particle Astrophysics Center, University of Wisconsin, Madison, WI, USA. [30]Dienst ELEM, Vrije Universiteit Brussel (VUB), Brussels, Belgium. [31]SNOLAB, Lively, ON, Canada. [32]Institut für Kernphysik, Westfälische Wilhelms-Universität Münster, Münster, Germany. [33]Physik-department, Technische Universität München, Garching, Germany. [34]Department of Astronomy and Astrophysics, Pennsylvania State University, University Park, PA, USA. [35]Department of Physics and Astronomy, Michigan State University, East Lansing, MI, USA. [36]Bartol Research Institute and Department of Physics and Astronomy, University of Delaware, Newark, DE, USA. [37]Department of Physics and Astronomy, University of Gent, Gent, Belgium. [38]Institut für Physik, Humboldt-Universität zu Berlin, Berlin, Germany. [39]Department of Physics, Southern University, Baton Rouge, LA, USA. [40]Department of Astronomy, University of Wisconsin, Madison, WI, USA. [41]Earthquake Research Institute, University of Tokyo, Bunkyo, Tokyo, Japan. [42]Department of Physics and Institute for Global Prominent Research, Chiba University, Chiba, Japan. [43]CTSPS, Clark-Atlanta University, Atlanta, GA, USA. [44]Department of Physics, University of Texas at Arlington, Arlington, TX, USA. [45]School of Physics and Astronomy, Queen Mary University of London, London, UK. [46]Department of Physics and Astronomy, Stony Brook University, Stony Brook, NY, USA. [47]Universitee de Mons, Mons, Belgium. [48]Department of Physics and Astronomy, University of Alabama, Tuscaloosa, AL, USA. [49]Department of Physics, Drexel University, Philadelphia, PA, USA. [50]Department of Physics, University of Wisconsin, River Falls, WI, USA. [51]Department of Physics, Yale University, New Haven, CT, USA. [52]Department of Physics and Astronomy, University of Alaska Anchorage, Anchorage, AK, USA. [53]Department of Physics, University of Oxford, Oxford, UK. [54]School of Physics and Center for Relativistic Astrophysics, Georgia Institute of Technology, Atlanta, GA, USA. *e-mail: caad@mit.edu; gabrielc@mit.edu; conrad@mit.edu; akheirandish@icecube.wisc.edu; katori@fnal.gov; s.p.mandalia@qmul.ac.uk

Journal of Physics G: Nuclear and Particle Physics

PAPER

PYTHIA hadronization process tuning in the GENIE neutrino interaction generator

To cite this article: Teppei Katori and Shivesh Mandalia 2015 *J. Phys. G: Nucl. Part. Phys.* **42** 115004

IOP Publishing Journal of Physics G: Nuclear and Particle Physics
J. Phys. G: Nucl. Part. Phys. **42** (2015) 115004 (13pp) doi:10.1088/0954-3899/42/11/115004

PYTHIA hadronization process tuning in the GENIE neutrino interaction generator

Teppei Katori and Shivesh Mandalia

School of Physics and Astronomy, Queen Mary University of London, London E1 4NS, UK

E-mail: t.katori@qmul.ac.uk

Received 7 July 2015, revised 26 August 2015
Accepted for publication 15 September 2015
Published 16 October 2015

Abstract

Next-generation neutrino oscillation experiments utilize details of hadronic final states to improve the precision of neutrino interaction measurements. The hadronic system was often neglected or poorly modeled in the past, but they have significant effects on high precision neutrino oscillation and cross-section measurements. Among the physics of hadronic systems in neutrino interactions, the hadronization model controls multiplicities and kinematics of final state hadrons from the primary interaction vertex. For relatively high invariant mass events, many neutrino experiments rely on the PYTHIA program. Here, we show a possible improvement of this process in neutrino event generators, by utilizing expertise from the HERMES experiment. Finally, we estimate the impact on the systematics of hadronization models for neutrino mass hierarchy analysis using atmospheric neutrinos such as the PINGU experiment.

Keywords: neutrino cross section, hadronization, PYTHIA, GENIE

(Some figures may appear in colour only in the online journal)

1. Introduction, future long baseline neutrino oscillation experiments

Neutrino oscillations are functions of the neutrino baseline L, and neutrino energy E_ν. By optimizing factors such as cost, neutrino production, and detection processes, typical oscillation experiments often choose $L \sim$ 100–1000 km and $E_\nu \sim$ 1–10 GeV. Some examples include T2K [1], which uses a 600 MeV off-axis J-PARC neutrino beam [2], and NOvA [3], which uses a 2 GeV off-axis NuMI beam [4]. Their flux peaks are tuned to quasielastic and resonance dominant regions in order to perform neutrino oscillation measurements. Therefore, in the past few years, the neutrino interaction community has spent a significant amount of time trying to understand the physics at these energy regions [5–8], especially after the discovery of the importance of two-body current in neutrino physics [9–11].

0954-3899/15/115004+13$33.00

Although off-axis beams from J-PARC and NuMI are tuned to narrow 600 MeV and 2 GeV peaks, off-axis neutrino beams made from wide-band decay-in-flight mesons have long high-energy tails, and the contribution from large W interactions is always present. For example, multi-pion production processes contribute significant amounts in single pion production measurements at T2K [12], and NOvA [3] uses hadronic shower information to reconstruct the neutrino energy. On top of that, future long baseline oscillation experiments, such as PINGU [13], ORCA [14], Hyper-Kamiokande [15], and DUNE [16] are trying to use hadronic information from the atmospheric neutrino interactions around 2–20 GeV. Therefore correct modeling of hadronization processes is an important subject for current and future neutrino oscillation experiments.

In this paper, we study how the hadronization model based on PYTHIA can be improved by utilizing HERMES expertise for current and future neutrino oscillation experiments. In sections 2 and 3, we introduce the PYTHIA hadronization simulator and the GENIE neutrino interaction generator, two of the most important tools in our studies. Then we briefly discuss the HERMES experiment in section 4. Our main results are described in sections 5–8. Finally, in section 9, we demonstrate the impact of hadronization models for the PINGU experiment.

2. PYTHIA, the standard hadronization model

The PYTHIA Monte Carlo (MC) generator [17, 18] is regarded as one of the standard hadronization tools for high energy physics experiments. Fragmentation in PYTHIA is described by the Lund string fragmentation model, which is a model based on the dynamics of one-dimensional relativistic strings that are stretched between colored partons. These strings represent the color flux and, in particular, subject to a linear confinement potential. The hadronization process is described by break-ups in the strings through the production of new quark–antiquark pairs. An iterative approach is used to perform the fragmentation as each break up is causally disconnected. The production rate of the created $q\bar{q}$ pair is determined using the tunneling mechanism, which leads to a Gaussian spectrum of the transverse momentum, $p_\perp^2 (= p_x^2 + p_y^2)$, for the produced hadron. The fraction of $E + p_z$ taken by the produced hadron is given by the variable z, defined by the hadron energy E and energy transfer ν ($z = E/\nu$). An associated fragmentation function $f(z)$ gives the probability that a given z is chosen. The simplified Lund symmetric fragmentation function is given by

$$f(z) \propto z^{-1}(1 - z)^a \cdot \exp\left(\frac{-bm_\perp^2}{z}\right). \quad (1)$$

Here, $m_\perp^2$ is the transverse mass of the hadron ($m_\perp^2 \equiv m^2 + p_\perp^2$). The Gaussian term describes quantum tunneling in the transverse direction, and tunable 'Lund a' and 'Lund b' parameters decide the longitudinal distribution of energy. Thus, these two parameters mainly decide how to distribute available energy to the produced hadrons. Figure 1 shows the Lund symmetric function. Larger Lund a and smaller Lund b parameters shift the fragmentation function to a lower z region. The values of these parameters are obtained from the shapes of the measured fragmentation functions, and the default values of Lund a and Lund b in PYTHIA6.3 are 0.3 and 0.58 GeV c^{-2}, respectively.

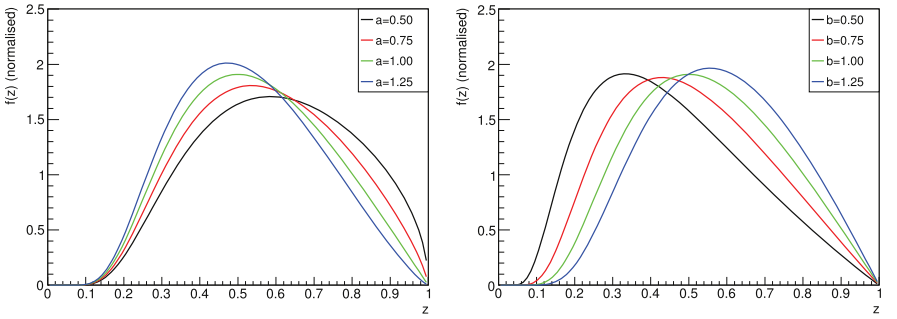

Figure 1. The Lund symmetric fragmentation function (equation (1)) for different values of Lund a and Lund b. The parameter is altered while keeping all other variables fixed.

3. GENIE AGKY model

GENIE is a ROOT-based neutrino interaction MC generator [19]. In the few-GeV energy regions which are particularly important in oscillation experiments, GENIE employs a new hadronization model called the AGKY model [20, 21].

The AGKY model is split into two parts. At lower energy regions where PYTHIA hadronization models deteriorate, a phenomenological description based on the Koba–Nielson–Olesen (KNO) scaling law is used [22]. First, averaged charged hadron multiplicity data are fitted to a function of invariant mass squared, W^2, in order to extract the parameters $a_{\rm ch}$ and $b_{\rm ch}$,

$$\langle n_{\rm ch}\rangle = a_{\rm ch} + b_{\rm ch}\cdot\log W^2, \tag{2}$$

then, the total averaged hadron multiplicity is deduced to be $\langle n_{\rm tot}\rangle = 1.5\langle n_{\rm ch}\rangle$. In this way, averaged hadron multiplicity is assigned for any interaction. To simulate the actual hadron multiplicity for each interaction, the KNO scaling law is used. The KNO scaling law relates the dispersion of hadron multiplicity at different invariant masses with a universal scaling function $f\,(n/\langle n\rangle)$,

$$\langle n\rangle \times P(n) = f\left(\frac{n}{\langle n\rangle}\right), \tag{3}$$

where $\langle n\rangle$ is the averaged hadron multiplicity and $P(n)$ is the probability of generating n hadrons. The scaling function is parameterized by the Levy function

$$L(z,\,c) = \frac{2\mathrm{e}^{-c}c^{cz+1}}{\Gamma(cz+1)}, \tag{4}$$

$z = n/\langle n\rangle$ and an input parameter c. The input parameter is used to tune the function to agree with data, which is mainly taken from the Fermilab 15-foot Bubble Chamber experiment [23]. Although more recent hadron multiplicity data are available from CHORUS [24], the heavy target data require more sophisticated final state interaction models to access to the primary hadron multiplicity information, and we do not take these into account in this article.

At higher energy regions the AGKY model gradually transitions from the KNO scaling-based model to PYTHIA, as discussed previously. A transition window based on the value of the invariant hadronic mass W is used, over which the fraction of events hadronized using the

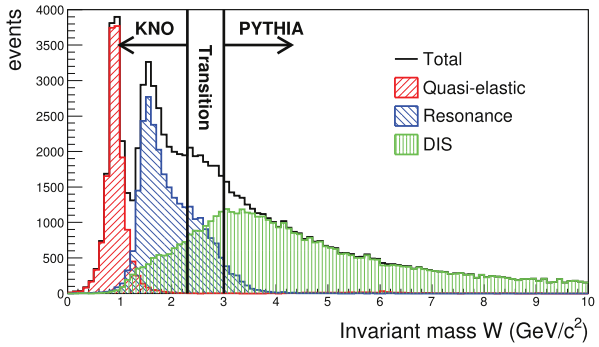

Figure 2. W distribution of ν_μ-water target interaction in GENIE. For the flux, we use an atmospheric ν_μ neutrino spectrum. Left red hatched region is quasi-elastic scattering, middle hatched region is resonance interactions, and right green hatched region is from DIS. The W distribution can be split to three regions, KNO scaling-based model only region, PYTHIA only region, and the transition region.

PYTHIA (KNO) model increases (decreases) linearly. The default values used in the AGKY model are

- $W < 2.3$ GeV c^{-2}, KNO scaling-based model only region,
- 2.3 GeV c^{-2} $< W <$ 3.0 GeV c^{-2}, transition region, and
- 3.0 GeV c^{-2} $< W$, PYTHIA only region.

Figure 2 shows this situation graphically. This is the W distribution for ν_μ-water interactions simulated with GENIE. Here, we used a simple formula to model the atmospheric ν_μ neutrino spectrum [25, 26], described later. As you can see, the W-distribution in this energy region can be split into three main interaction modes, quasi-elastic (red hatched, left peak), resonance (blue hatched, middle), and DIS (green hatched, right). The AGKY model is applied to DIS interactions. Also note DIS is extended to the low W region to describe non-resonance interactions in the resonance region. Although charm production processes are possible at the high energies, contributions are minor and throughout this article we ignore charm production processes.

All studies in this paper use GENIE version 2.8.0, also figures 3–7 are generated by the hadronization validation tool in GENIE.

4. HERMES experiment

HERMES is a fixed target experiment at DESY [27]. The ring stores 27.6 GeV electrons or positrons, and collisions take place in the HERMES gas-jet target.

The HERMES experiment has a long history of tuning PYTHIA for their purposes. The main motivation of this is because the default PYTHIA parameters are tuned to higher energy $e^+ - e^-$experiments ($\sqrt{s} \sim 35$ GeV) and are not quite suitable for HERMES. Since modern neutrino oscillation experiments are also lower energy (1–10 GeV) compared with collider experiments, it is interesting to test the PYTHIA developed for the HERMES experiment within GENIE. Various alterations have been applied to PYTHIA by HERMES collaborators

A Appendix

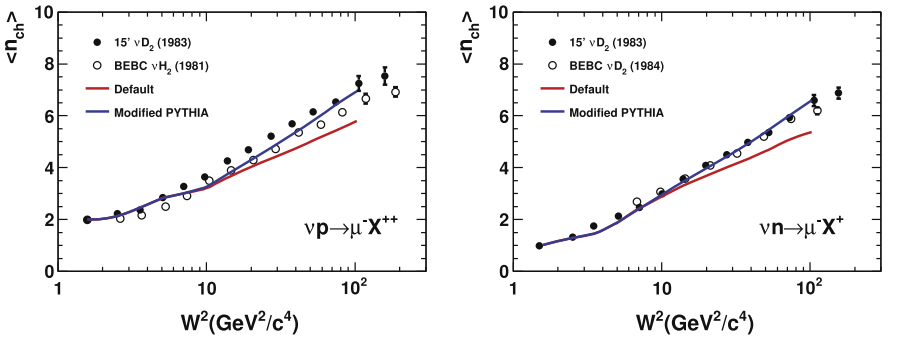

Figure 3. Averaged charged hadron multiplicity plot. Here, two predictions from GENIE are compared with bubble chamber $\nu_\mu - p$ and $\nu_\mu - n$ hadron production data [23, 32].

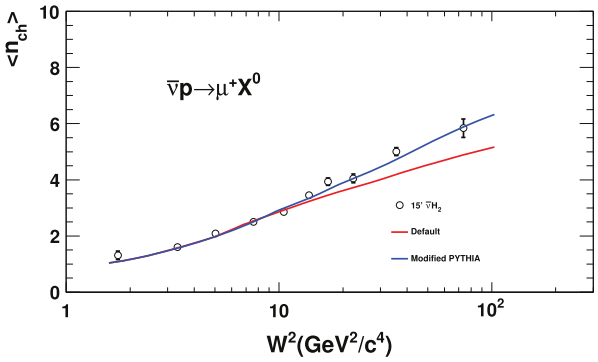

Figure 4. Averaged charged hadron multiplicity plot. Here, two predictions from GENIE are compared with bubble chamber $\bar{\nu}_\mu - p$ hadron production data [39].

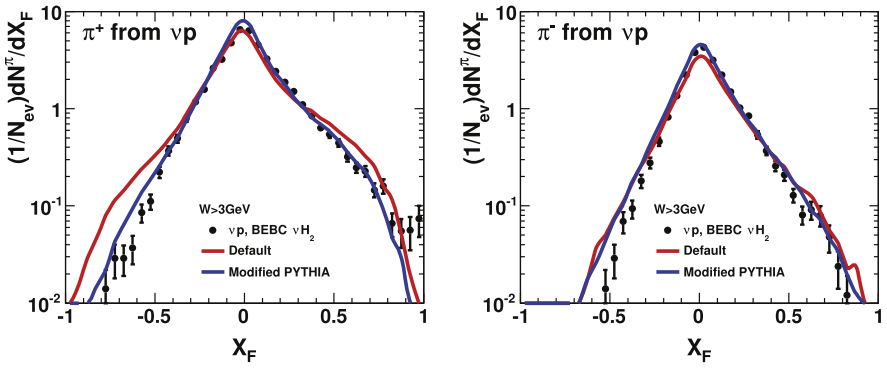

Figure 5. x_F distribution for π^+ and π^- from $\nu_\mu - p$ interactions [40]. Again, modified PYTHIA has a better agreement with data.

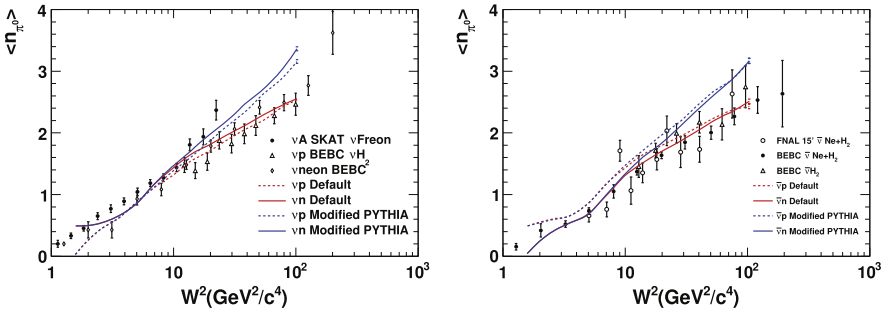

Figure 6. Averaged neutral pion multiplicity plot. Here, two predictions from GENIE are compared with bubble chamber $\nu_\mu - p$, $\nu_\mu - n$, $\bar{\nu}_\mu - p$, and $\bar{\nu}_\mu - n$ π° production data [41–44].

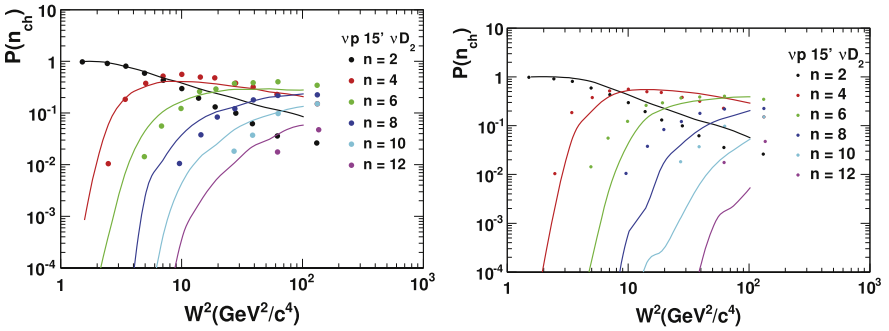

Figure 7. Topological cross sections of charged hadrons for $\nu_\mu - p$ interaction. In both plots, data points are from deuteron target bubble chamber experiments [23]. In the left plot, PYTHIA is turned off and data are compared with GENIE with only the KNO scaling-based hadronization model. On the other hand, in the right plot, hadronization is solely handled by PYTHIA.

and, among them, we are most interested in the adjustment to the fragmentation model made by tuning PYTHIA parameters without modifying the source code.

Parameter sets developed by HERMES collaborators are available elsewhere (for example, [28–31]). Table 1 summarizes the parameter sets we studied (Lund-scan, $\Delta q(x)$, 2004c), as well as their default values in PYTHIA and GENIE. In the second column, the default PYTHIA parameters are shown fully while the second to the sixth columns are shown only if the parameters have been changed from the default PYTHIA values. In this article, we focus on the parameter set called 'Lund-scan' [29], which we found had the best agreement with neutrino hadron production data.

Note we only tested PYTHIA parameters which are publicly available; however, HERMES also made modifications to the source code of PYTHIA itself. Therefore, in this paper we are not testing with the exact hadronization model used in the HERMES experiment. Also 'default GENIE' quoted in this paper is not GENIE with default PYTHIA 6.3 parameters, since by default, GENIE modified the three parameters listed in table 1: however,

A Appendix

Table 1. Parameter values for data sets $\Delta q(x)$ [28], `Lund-scan` [29] and `2004c` [30] along with the default PYTHIA and GENIE values. Blank cells represent that the parameter takes on the default PYTHIA value.

Parameter	PYTHIA	GENIE	`Lund-scan`	$\Delta q(x)$	`2004c`	Descriptions
`PARJ1`	0.10		0.02		0.029	di-quark suppression
`PARJ2`	0.30	0.21	0.25	0.20	0.283	strange quark suppression
`PARJ11`	0.50		0.51			light vector meson suppression
`PARJ12`	0.60		0.57			strange vector meson suppression
`PARJ21`	0.36	0.44	0.42	0.37	0.38	width of Gaussian $p_\perp$ distribution
`PARJ23`	0.01			0.03		non-Gaussian tail of $p_\perp$ distribution
`PARJ33`	0.80	0.20	0.47			string breaking mass cutoff
`PARJ41`	0.30		0.68	1.74	1.94	Lund a parameter
`PARJ42`	0.58		0.35	0.23	0.544	Lund b parameter
`PARJ45`	0.50		0.74		1.05	adjustment of Lund a for di-quark

we confirm the difference in predictions between the default GENIE and the GENIE with the default PYTHIA parameters is very small within our studies.

5. Averaged charged hadron multiplicity

Averaged charged hadron multiplicity data is fundamental in the development of hadronization models. It describes the average number of charged hadrons, mainly π^+ and π^-, measured as a function of invariant hadron mass W. Neutrino hadronization models are largely guided by such data from bubble chamber experiments. Recently, Kuzmin and Naumov performed detailed surveys of neutrino bubble chamber data, and chose the best sets of data to tune their model [33]. It is shown that all modern neutrino interaction generators, such as GENIE [19], NuWro [34], and GiBUU [35], all appear to underestimate averaged charged hadron multiplicity. Note, it is also shown that the NEUT neutrino interaction generator [36], which is used by T2K and Super-Kamiokande, also underestimates averaged charged hadron multiplicity [12].

This problem largely originates from the PYTHIA fragmentation model, because, as mentioned in the previous section, the default PYTHIA parameters are tuned to higher energy experiments. Both GENIE and NuWro [37] tuned these PYTHIA parameters to improve the agreement with data but the effect is marginal. Note NuWro and GiBUU use their own models for fragmentation, and only later processes are based on PYTHIA.

Figure 3 shows the data-MC comparison of the averaged charged hadron multiplicity in $\nu_\mu - p$ and $\nu_\mu - n$ interactions. Here, the two curves represent predictions from default GENIE and GENIE with a PYTHIA modified using the Lund-scan parameter set [29]. Note, because the $W < 2.3$ GeV c^{-2} range of the AGKY model is hadronized using the KNO scaling-based model, these two curves should be identical at $W < 2.3$ GeV c^{-2}. As you can see, the HERMES tune describes the data better. Here, two data sets from the Fermilab Bubble Chamber and BEBC agree in $\nu_\mu - n$ interactions (both deuterium targets) but not in $\nu_\mu - p$ data (hydrogen and deuterium target), suggesting the conflict of data we see in figure 3 is due to nuclear effects in deuterium [20, 21, 33, 38]. Despite the conflict of data, the HERMES parameterization in general increases the averaged charged hadron multiplicity, which improves the agreement with averaged charged hadron multiplicity data from neutrino bubble chamber experiments.

Figure 4 is the same plot for $\bar{\nu}_\mu - p$ interactions. Again, the agreement with the data is better for GENIE with the modified PYTHIA parameter set. Therefore, this new parameter set works better for both neutrino and antineutrino interactions.

The main effect of this new parameterization originates from the increase of the Lund a parameter and the decrease of the Lund b parameter (equation (1)). As shown in figure 1, these changes make the fragmentation function softer. This enhances emissions of soft hadrons, i.e., this increases averaged charged hadron multiplicity and thus it agrees better with data. In the higher energy experiments that PYTHIA is designed for, high order QCD effects cause additional low energy parton emissions. This causes hadrons to be produced with a broader spectrum in z. Because these effects are negligible for the neutrino experiments we are concerned with, we shift the peak of the fragmentation function to a lower z value by increasing (decreasing) the Lund a (b) parameter [30].

In fact, all parameterization schemes from HERMES we checked (table 1) have a high (low) Lund a (b) parameter, and many have more extreme values than the ones we use here. However, these higher (lower) Lund a (b) parameter models tend to overestimate hadron multiplicities compared to neutrino hadron production data from bubble chamber experiments

and as a result the data-MC agreement becomes worse. The neutrino hadronization data prefer a relatively smaller Lund a parameter than most HERMES parameter sets, yet bigger than the default PYTHIA choice, and this is the main reason why we chose this specific parameterization scheme in this paper.

6. x_F distribution

Feynman x, x_F, is the fraction of longitudinal momentum available for a hadron, defined in the hadronic center mass system, i.e., $x_F = \frac{P_L^*}{P_{L\,\max}^*} \sim \frac{2P_L^*}{W}$, here asterisks stand for the hadron c.m.s. Figure 5 shows the data-MC comparison. The agreement of modified PYTHIA with bubble chamber data is excellent for both π^+ and π^- data. Therefore the tuning we applied is valid not only for averaged charged hadrons, but also valid for positive and negative hadrons separately.

7. Averaged neutral pion multiplicity

In figure 6, predictions are compared with the averaged π° multiplicity. Here the data from ν_μ and $\bar{\nu}_\mu$ interactions are from various targets [41–44]. Although the data here have larger errors, now the default GENIE has a better agreement with the data. The ratio of the number of produced charged pions and neutral pions is strongly tied due to isospin symmetry, i.e. $N(\pi^+) + N(\pi^-) : N(\pi^\circ) = 2 : 1$. Thus, if we increase the charged hadron multiplicity, the model will also have higher multiplicities of neutral pions. The charged pion and neutral pion multiplicity ratio is 2:1 in BEBC neon target bubble chamber data [41], however, this relationship is not obvious in other bubble chamber data. As we see from figures 3 and 6, it is not easy to achieve good agreements with both charged hadron and neutral pion multiplicities by tuning PYTHIA parameters. On the other hand, PYTHIA shows excellent agreements in both charged and neutral pion fragmentation functions with HERMES data [27, 45].

8. Topological cross sections

In the low W region, PYTHIA does not predict the multiplicity properly. In GENIE, the AGKY model uses a phenomenological approach based on KNO scaling [22], where dispersion is assumed to follow a scaling law as data suggest. Thus, by definition, the AGKY model has a better data-MC agreement for the dispersion of the multiplicity in the low W region. This is not the case in PYTHIA, where physics is simulated from a more first principles approach, which is based on quark–diquark fragmentation. By tuning PYTHIA parameters, the data-MC agreement of the averaged charged hadron multiplicity can be improved, but it is not easy to fully correct the dispersion.

Figure 7 shows the data-MC comparisons of the topological cross sections of charged hadrons, that is, the fraction of final particle topologies of a given interaction as function of invariant mass. In both plots, the GENIE predictions are compared with deuteron target $\nu_\mu - p$ data from the Fermilab 15-foot Bubble Chamber experiment [23]. In the left plot, the hadronization model in GENIE is solely carried out by the KNO scaling-based model. Since the KNO scaling-based approach is designed to reproduce the dispersion data, GENIE can make the large multiplicities, such as $n = 6$, $n = 8$, etc, as data suggested. On the other hand, in the right plot, the GENIE hadronization model solely depends on PYTHIA. In this case, we

see PYTHIA has problems reproducing large hadron multiplicity events. Therefore, the combination of KNO scaling-based model and PYTHIA cannot make smooth topological cross sections. This indicates the dispersion of hadron multiplicity reproduced by PYTHIA is smaller than the data.

High resolution liquid argon time projection chamber (LArTPC) experiments, such as MicroBooNE [46], are in a good position to identify high multiplicity hadron events. These data may offer the opportunity to test neutrino hadronization processes. However, to test hadronization models with hadron data from heavy nuclear targets such as argon, it is also necessary to have a good model for primary interactions [6–8] and nuclear effects [47]. In inelastic interaction processes, both primary interactions and nuclear effects play significant roles and currently disagreements between data and predictions are not well understood [48]. Therefore, it is challenging to develop a hadronization model solely from neutrino experimental data, and input from other fields, especially electron scattering experiments, is very important.

9. Impact on hadronization models for PINGU

In previous sections, we discussed how PYTHIA can be improved inside GENIE in order to reproduce neutrino bubble chamber data. However, it is not obvious how such improvements affect current and future neutrino experiments, unless a realistic neutrino flux is integrated in the interaction simulations. In this section, we use an atmospheric neutrino flux prediction to simulate neutrino interactions in order to study how different hadronization models affect analysis in PINGU [13], which will try to use hadronic information to improve their sensitivity on oscillation physics.

PINGU is a low energy extension of the IceCube detector [49]. By placing optical sensors closer together compared to the original IceCube detector, PINGU is able to measure atmospheric neutrinos below 20 GeV where matter oscillations are important. Although PINGU has a significantly smaller volume coverage compared with the $1\,\mathrm{km}^3$ IceCube detector, the estimated PINGU volume coverage is still $\sim$6 Mton and high statistics is expected. The capability of atmospheric neutrino oscillation measurements has also been demonstrated recently [50].

The goal of PINGU is to determine the neutrino mass hierarchy (NMH) through matter oscillations. In the two-neutrino oscillation approximation, the muon neutrino disappearance oscillation probability in the normal hierarchy ($P^{\mathrm{NH}}_{\alpha\beta}$) and the muon anti-neutrino disappearance oscillation probability in the inverted hierarchy ($\bar{P}^{\mathrm{IH}}_{\alpha\beta}$) are the same ($P^{\mathrm{NH}}_{\alpha\beta} = \bar{P}^{\mathrm{IH}}_{\alpha\beta},\ \bar{P}^{\mathrm{NH}}_{\alpha\beta} = P^{\mathrm{IH}}_{\alpha\beta}$) [51]. Thus, it is also desirable to separate muon neutrinos and muon anti-neutrinos where final state leptons are indistinguishable by Cherenkov detectors such as PINGU.

Recently, Ribordy and Smirnov pointed out that the charge separation, through the precise measurement of inelasticity distributions, improves the PINGU and ORCA NMH sensitivity [51]. The same arguments may be applied to Hyper-Kamiokande [15] and DUNE [16]. Since inelasticity measurements rely on the energy deposits of hadronic showers, it is interesting to check the impact of different hadronization models in this situation.

For this purpose, we estimated the impact of hadronization models on the effective inelasticity. We define the effective inelasticity from the visible hadron shower energy

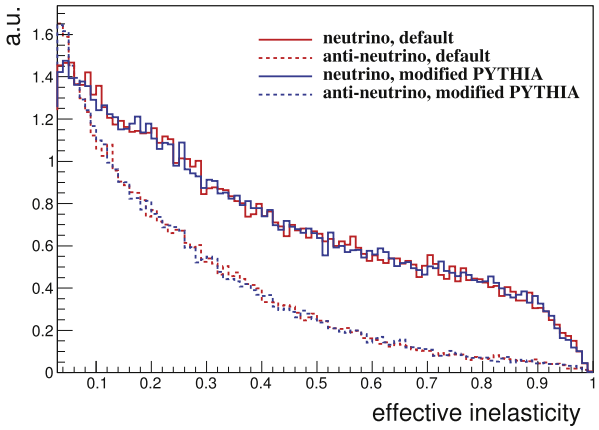

Figure 8. Effective inelasticity distribution with atmospheric neutrino spectrum. Here, all histograms are arbitrarily normalized. Solid histograms are muon neutrino distributions, and dashed histograms are muon anti-neutrino distributions. Red histograms are from GENIE with the default hadronization model, and blue histograms are from GENIE with the modified hadronization model discussed in this paper.

$$E_{\rm h}^{\rm vis} = \sum_{E_{\rm h}^i > E_{\rm th}^i} T_{\rm h}^i + \sum E_\gamma^i. \tag{5}$$

The first term is the sum of kinetic energies of charged hadrons above the Cherenkov threshold. Here we assume that the charged hadrons above the Cherenkov threshold are visible and we take into account their kinetic energies. The second term is the sum of all the final state photons, including the decays of neutral mesons. Thus, the visible hadron energy corresponds to the energy deposit from the hadronic system to the perfect photon detector, where inefficiency is only from neutrons or hadrons below the Cherenkov threshold. Then, the effective inelasticity, $y^{\rm eff}$, is defined by

$$y^{\rm eff} = \frac{E_{\rm h}^{\rm vis}}{E_{\rm h}^{\rm vis} + E_\mu}. \tag{6}$$

Here E_μ is the muon (anti-muon) energy.

To simulate effective inelasticity on a water target, we modeled the atmospheric neutrino flux with a simple formula ($\sim a + b \cdot E^{-c}$, where $c \sim 2.8$) which reproduces the typical energy spectrum of atmospheric neutrinos [25, 26]. Then we simulate neutrino interactions from 2 to 30 GeV, which is the energy region of interest for NMH analysis.

Figure 8 shows the simulated $y^{\rm eff}$ distributions with arbitrary normalization. The $y^{\rm eff}$ distributions for neutrino and anti-neutrino interactions are well separated, however, $y^{\rm eff}$ distributions based on different hadronization models are very similar. This study does not include the detector simulation, and the quantitative evaluation of the impact of hadronization models in PINGU is difficult. However, the inclusion of a detector simulation in general smears structures and it will make the results of two different hadronization models nearly identical. This result can be understood from a simulated W distribution of PINGU. PINGU is dominated by few GeV low W interactions (<5 GeV) where PYTHIA hadronization processes have a minor role (figure 2). This indicates alternations of the hadronization model

only provide minor changes to the systematics of the PINGU inelasticity measurement, however, details have yet to be tested with a full PINGU detector simulation.

Conclusion

In this article, we studied neutrino hadronization processes in GENIE. Our main focus is to improve the averaged charged hadron multiplicity, and it is shown that suitable parameterization developed by the HERMES collaboration dramatically improves the data-MC agreement with neutrino bubble chamber data. However, this tuning may make the π° multiplicity agreement slightly worse. Also dispersion of hadron multiplicity is still not under control. All studies in the paper are qualitative in nature, and quantitative studies are beyond the scope of this paper. At the present moment, PYTHIA parameter tunings based on fits to neutrino experimental data are not being performed. An example of the difficulty of PYTHIA tunings is the correlations between different PYTHIA parameters, as HERMES collaborators noted [29]. In this article, we find that controlling the shape of the Lund string fragmentation function using the Lund a and Lund b parameters is the key to control the averaged hadron multiplicity, and a more precise tuning is left as a direction for future work. Near future LArTPC experiments, such as MicroBooNE, could test the hadronization models by measuring high hadron multiplicity events.

Finally, we tested different hadronization models with a modeled atmospheric neutrino flux. It is seen that the difference in the inelasticity distributions is small, suggesting that hadronization processes only play a minor role in the systematics for NMH analysis at atmospheric neutrino oscillation experiments. Careful analysis including the detector simulation will find more accurate systematics of hadronization interactions for future atmospheric neutrino experiments, such as PINGU, ORCA, Hyper-Kamiokande and DUNE.

Acknowledgments

TK thanks Ulrich Mosel for introducing this subject to us. We thank Elke Aschenauer and Josh Rubin for useful information about the HERMES experiment. We also appreciate the various help given to us by Gabe Perdue and Julia Yarba on the GENIE simulations. Finally, TK would like to thank the organizer of CETUP* (Center for Theoretical Underground Physics and Related Areas) for the hospitality during my stay at Deadwood, SD, to engage on this work.

References

[1] Abe K *et al* (T2K Collaboration) 2014 *Phys. Rev. Lett.* **112** 061802
[2] Abe K *et al* (T2K Collaboration) 2013 *Phys. Rev.* D **87** 012001
[3] Childress S and Strait J 2013 *J. Phys.: Conf. Ser.* **408** 012007
[4] Adamson P *et al* 2015 (arXiv:1507.06690)
[5] Gallagher H, Garvey G and Zeller G 2011 *Ann. Rev. Nucl. Part. Sci.* **61** 355
[6] Morfin J G, Nieves J and Sobczyk J T 2012 *Adv. High Energy Phys.* **2012** 934597
[7] Alvarez-Ruso L, Hayato Y and Nieves J 2014 *New J. Phys.* **16** 075015
[8] Garvey G, Harris D, Tanaka H, Tayloe R and Zeller G 2015 *Phys. Rep.* **580** 1
[9] Grange J and Katori T 2014 *Mod. Phys. Lett.* A **29** 1430011
[10] Martini M, Ericson M, Chanfray G and Marteau J 2009 *Phys. Rev.* C **80** 065501
[11] Nieves J, Ruiz Simo I and Vacas M Vicente 2011 *Phys. Rev.* C **83** 045501
[12] Connolly K T 2014 *PhD Thesis* University of Washington, Seattle

A Appendix

[13] Aartsen M *et al* (IceCube-PINGU Collaboration) 2014 (arXiv:1401.2046)
[14] Kouchner A 2014 *Phys. Dark Univ.* **4** 60
[15] Kearns E *et al* (Hyper-Kamiokande Working Group) 2013 (arXiv:1309.0184)
[16] Adams C *et al* (LBNE Collaboration) 2013 (arXiv:1307.7335)
[17] Sjöstrand T, Mrenna S and Skands P Z 2006 *J. High Energy Phys.* JHEP05(2006)026
[18] Sjöstrand T, Mrenna S and Skands P Z 2008 *Comput. Phys. Commun.* **178** 852
[19] Andreopoulos C *et al* 2010 *Nucl. Instrum. Meth.* A **614** 87
[20] Yang T, Andreopoulos C, Gallagher H, Hoffmann K and Kehayias P 2009 *Eur. Phys. J.* C **63** 1
[21] Yang T 2009 *PhD Thesis* Stanford University
[22] Koba Z, Nielsen H B and Olesen P 1972 *Nucl. Phys.* B **40** 317
[23] Zieminska D *et al* 1983 *Phys. Rev.* D **27** 47
[24] Kayis-Topaksu A *et al* (CHORUS) 2007 *Eur. Phys. J.* C **51** 775
[25] Honda M, Kajita T, Kasahara K and Midorikawa S 2011 *Phys. Rev.* D **83** 123001
[26] Honda M, Kajita T, Kasahara K, Midorikawa S and Sanuki T 2007 *Phys. Rev.* D **75** 043006
[27] Airapetian A *et al* (HERMES Collaboration) 2013 *Phys. Rev.* D **87** 074029
[28] Menden F M 2001 *PhD Thesis* Albert-Ludwigs-Universität Freiburg im Breisgau
[29] Rubin J G 2009 *PhD Thesis* University of Illinois, Urbana-Champaign (doi:10.3204/DESY-THESIS-2009-045)
[30] Hillenbrand A 2005 *PhD Thesis* Uneivrstät Erlangen-Nürnberg (doi:10.3204/DESY-THESIS-2005-035)
[31] Airapetian A *et al* (HERMES Collaboration) 2010 *J. High Energy Phys.* JHEP08(2010)130
[32] Allen P *et al* (Aachen-Bonn-CERN-Munich-Oxford Collaboration) 1981 *Nucl. Phys.* B **181** 385
[33] Kuzmin K S and Naumov V A 2013 *Phys. Rev.* C **88** 065501
[34] Juszczak C, Nowak J A and Sobczyk J T 2006 *Nucl. Phys.* B **159** 211
[35] Buss O *et al* 2012 *Phys. Rep.* **512** 1
[36] Hayato Y 2002 *Nucl. Phys.* B **112** 171
[37] Nowak J A 2006 *Phys. Scr.* **T127** 70
[38] Nowak J A and Sobczyk J T 2006 *Acta Phys. Pol.* B **37** 2371
[39] Derick M *et al* 1982 *Phys. Rev.* D **25** 624
[40] Allen P *et al* (Aachen-Bonn-CERN-Munich-Oxford Collaboration) 1983 *Nucl. Phys.* B **214** 369
[41] Wittek W *et al* (BEBC WA59 Collaboration) 1988 *Z. Phys.* C **40** 231
[42] Ivanilov A *et al* 1985 *Yad. Fiz.* **41** 1520
[43] Grassler H *et al* (Aachen-Birmingham-Bonn-CERN-London-Munich-Oxford Collaboration) 1983 *Nucl. Phys.* B **223** 269
[44] Ammosov V *et al* 1979 *Nuovo Cim.* A **51** 539
[45] Joosten S J 2013 *PhD Thesis* University of Illinois, Urbana-Champaign
[46] Katori T (MicroBooNE) 2011 *AIP Conf. Proc.* **1405** 250
[47] Gallmeister K and Mosel U 2008 *Nucl. Phys.* A **801** 68
[48] Sobczyk J and Zmuda J 2015 *Phys. Rev.* C **91** 045501
[49] Aartsen M *et al* (IceCube) 2013 *Science* **342** 1242856
[50] Aartsen M *et al* (IceCube Collaboration) 2013 *Phys. Rev. Lett.* **111** 081801
[51] Ribordy M and Smirnov A Y 2013 *Phys. Rev.* D **87** 113007

Bibliography

1. Pauli, W. *Letter to Tübingen conference participants* Web document. 1930.
2. Chadwick, J. Intensitätsverteilung im magnetischen Spectrum der β-Strahlen von radium B + C. *Verhandl. Dtsc. Phys. Ges.* **16,** 383 (1914).
3. Chadwick, J. Possible Existence of a Neutron. *Nature* **129,** 312 (1932).
4. Fermi, E. An attempt of a theory of beta radiation. 1. *Z. Phys.* **88,** 161–177 (1934).
5. Cowan, C. L., Reines, F., Harrison, F. B., Kruse, H. W. & McGuire, A. D. Detection of the free neutrino: A Confirmation. *Science* **124,** 103–104 (1956).
6. Davis Jr., R., Harmer, D. S. & Hoffman, K. C. Search for neutrinos from the sun. *Phys. Rev. Lett.* **20,** 1205–1209 (1968).
7. Pontecorvo, B. Neutrino Experiments and the Problem of Conservation of Leptonic Charge. *Sov. Phys. JETP* **26.** [Zh. Eksp. Teor. Fiz.53,1717(1967)], 984–988 (1968).
8. Maki, Z., Nakagawa, M. & Sakata, S. Remarks on the unified model of elementary particles. *Prog. Theor. Phys.* **28.** [,34(1962)], 870–880 (1962).
9. Bionta, R. M. *et al.* Observation of a Neutrino Burst in Coincidence with Supernova SN 1987a in the Large Magellanic Cloud. *Phys. Rev. Lett.* **58,** 1494 (1987).
10. Hirata, K. *et al.* Observation of a Neutrino Burst from the Supernova SN 1987a. *Phys. Rev. Lett.* **58.** [,727(1987)], 1490–1493 (1987).
11. Alekseev, E. N., Alekseeva, L. N., Volchenko, V. I. & Krivosheina, I. V. Possible Detection of a Neutrino Signal on 23 February 1987 at the Baksan Underground Scintillation Telescope of the Institute of Nuclear Research. *JETP Lett.* **45.** [,739(1987)], 589–592 (1987).
12. Alekseev, E. N., Alekseeva, L. N., Krivosheina, I. V. & Volchenko, V. I. Detection of the Neutrino Signal From SN1987A in the LMC Using the Inr Baksan Underground Scintillation Telescope. *Phys. Lett.* **B205,** 209–214 (1988).
13. Fukuda, Y. *et al.* Evidence for oscillation of atmospheric neutrinos. *Phys. Rev. Lett.* **81,** 1562–1567 (1998).

14. Ahmad, Q. R. *et al.* Measurement of the rate of $\nu_e + d \rightarrow p + p + e^-$ interactions produced by ^8B solar neutrinos at the Sudbury Neutrino Observatory. *Phys. Rev. Lett.* **87,** 071301 (2001).

15. Ahmad, Q. R. *et al.* Direct evidence for neutrino flavor transformation from neutral current interactions in the Sudbury Neutrino Observatory. *Phys. Rev. Lett.* **89,** 011301 (2002).

16. Messerly, B., Lister, A., Ellison, J., Friant, D. & Mandalia, S. *The Neutrino "Livingston" plot* `https://github.com/admlw/neutrinoDetectorsPlot`.

17. Kayser, B. On the Quantum Mechanics of Neutrino Oscillation. *Phys. Rev.* **D24,** 110 (1981).

18. Akhmedov, E. K. & Smirnov, A. Yu. Paradoxes of neutrino oscillations. *Phys. Atom. Nucl.* **72,** 1363–1381 (2009).

19. Visinelli, L. & Gondolo, P. Neutrino Oscillations and Decoherence. arXiv: `0810.4132 [hep-ph]` (2008).

20. Akhmedov, E. K. & Kopp, J. Neutrino Oscillations: Quantum Mechanics vs. Quantum Field Theory. *JHEP* **04.** [Erratum: JHEP10,052(2013)], 008 (2010).

21. Giunti, C. & Kim, C. W. *Fundamentals of Neutrino Physics and Astrophysics* ISBN: 9780198508717 (2007).

22. Beringer, J. *et al.* Review of Particle Physics (RPP). *Phys. Rev.* **D86,** 010001 (2012).

23. Esteban, I., Gonzalez-Garcia, M. C., Maltoni, M., Martinez-Soler, I. & Schwetz, T. Updated fit to three neutrino mixing: exploring the accelerator-reactor complementarity. *JHEP* **01,** 087 (2017).

24. Esteban, I., Gonzalez-Garcia, M. C., Hernandez-Cabezudo, A., Maltoni, M. & Schwetz, T. Global analysis of three-flavour neutrino oscillations: synergies and tensions in the determination of θ_{23}, δ_{CP}, and the mass ordering. *JHEP* **01,** 106 (2019).

25. Wolfenstein, L. Neutrino Oscillations in Matter. *Phys. Rev.* **D17.** [,294(1977)], 2369–2374 (1978).

26. Mikheyev, S. P. & Smirnov, A. Yu. Resonant neutrino oscillations in matter. *Prog. Part. Nucl. Phys.* **23,** 41–136 (1989).

27. Smirnov, A. Yu. Solar neutrinos: Oscillations or No-oscillations? arXiv: `1609.02386 [hep-ph]` (2016).

28. Streater, R. F. & Wightman, A. S. *PCT, spin and statistics, and all that* ISBN: 0691070628, 9780691070629 (1989).

29. Gaisser, T. K., Engel, R. & Resconi, E. *Cosmic Rays and Particle Physics* ISBN: 9780521016469. http://www.cambridge.org/de/academic/subjects/physics/cosmology-relativity-and-gravitation/cosmic-rays-and-particle-physics-2nd-edition?format=HB (Cambridge University Press, 2016).

30. Fukuda, Y. *et al.* Atmospheric muon-neutrino / electron-neutrino ratio in the multi-GeV energy range. *Phys. Lett.* **B335,** 237–245 (1994).

31. Louis, B. *et al.* The Evidence for Oscillations. *Los Alamos Sci* **25,** 16 (1997).

32. Fedynitch, A., Engel, R., Gaisser, T. K., Riehn, F. & Stanev, T. Calculation of conventional and prompt lepton fluxes at very high energy. *EPJ Web Conf.* **99,** 08001 (2015).

33. Gaisser, T. K. Spectrum of cosmic-ray nucleons, kaon production, and the atmospheric muon charge ratio. *Astropart. Phys.* **35,** 801–806 (2012).

34. Ahn, E.-J., Engel, R., Gaisser, T. K., Lipari, P. & Stanev, T. Cosmic ray interaction event generator SIBYLL 2.1. *Phys. Rev.* **D80,** 094003 (2009).

35. Riehn, F. *et al.* The hadronic interaction model SIBYLL 2.3c and Feynman scaling. *PoS* **ICRC2017.** [35,301(2017)], 301 (2018).

36. Picone, J. M., Hedin, A. E., Drob, D. P. & Aikin, A. C. NRLMSISE-00 empirical model of the atmosphere: Statistical comparisons and scientific issues. *Journal of Geophysical Research: Space Physics* **107,** SIA 15–1–SIA 15–16 (2002).

37. Kappes, A., Hinton, J., Stegmann, C. & Aharonian, F. A. Potential Neutrino Signals from Galactic Gamma-Ray Sources. *Astrophys. J.* **656.** [Erratum: Astrophys. J.661,1348(2007)], 870–896 (2007).

38. Aartsen, M. G. *et al.* Observation of High-Energy Astrophysical Neutrinos in Three Years of IceCube Data. *Phys. Rev. Lett.* **113,** 101101 (2014).

39. Aartsen, M. G. *et al.* Evidence for Astrophysical Muon Neutrinos from the Northern Sky with IceCube. *Phys. Rev. Lett.* **115,** 081102 (2015).

40. Aartsen, M. G. *et al.* Multimessenger observations of a flaring blazar coincident with high-energy neutrino IceCube-170922A. *Science* **361,** eaat1378 (2018).

41. Aartsen, M. G. *et al.* Neutrino emission from the direction of the blazar TXS 0506+056 prior to the IceCube-170922A alert. *Science* **361,** 147–151 (2018).

42. Marc *et al. marcharper/python-ternary: Version 1.0.6* version 1.0.6. Apr. 2019. doi:10.5281/zenodo.2628066. https://doi.org/10.5281/zenodo.2628066.

43. Andreopoulos, C. *et al.* The GENIE Neutrino Monte Carlo Generator. *Nucl. Instrum. Meth.* **A614,** 87–104 (2010).

44. Gandhi, R., Quigg, C., Reno, M. H. & Sarcevic, I. Neutrino interactions at ultrahigh-energies. *Phys. Rev.* **D58,** 093009 (1998).

45. Bodek, A & Yang, U. K. Higher twist, xi(omega) scaling, and effective LO PDFs for lepton scattering in the few GeV region. *J. Phys.* **G29,** 1899–1906 (2003).

46. Cooper-Sarkar, A., Mertsch, P. & Sarkar, S. The high energy neutrino cross-section in the Standard Model and its uncertainty. *JHEP* **08,** 042 (2011).

47. Frank, I. M. & Tamm, I. E. Coherent visible radiation of fast electrons passing through matter. *Compt. Rend. Acad. Sci. URSS* **14.** [Usp. Fiz. Nauk93,no.2,388(1967)], 109–114 (1937).

48. Tanabashi, M. *et al.* Review of Particle Physics. *Phys. Rev.* **D98,** 030001 (2018).

49. Bethe, H. Theory of the Passage of Fast Corpuscular Rays Through Matter. *Annalen Phys.* **5.** [Annalen Phys.397,325(1930)], 325–400 (1930).

50. Aartsen, M. G. *et al.* The IceCube Neutrino Observatory: Instrumentation and Online Systems. *JINST* **12,** P03012 (2017).

51. Abbasi, R. *et al.* The Design and Performance of IceCube DeepCore. *Astropart. Phys.* **35,** 615–624 (2012).

52. Abbasi, R. *et al.* Calibration and Characterization of the IceCube Photomultiplier Tube. *Nucl. Instrum. Meth.* **A618,** 139–152 (2010).

53. Aartsen, M. G. *et al.* All-sky Search for Time-integrated Neutrino Emission from Astrophysical Sources with 7 yr of IceCube Data. *Astrophys. J.* **835,** 151 (2017).

54. Weaver, C. *Evidence for Astrophysical Muon Neutrinos from the Northern Sky* PhD thesis (Wisconsin U., Madison, 2015). https://docushare.icecube.wisc.edu/dsweb/Get/Document-73829/.

55. Aartsen, M. G. *et al.* Energy Reconstruction Methods in the IceCube Neutrino Telescope. *JINST* **9,** P03009 (2014).

56. Aartsen, M. G. *et al.* Evidence for High-Energy Extraterrestrial Neutrinos at the IceCube Detector. *Science* **342,** 1242856 (2013).

57. Hallen, P. *On the Measurement of High-Energy Tau Neutrinos with IceCube* PhD thesis (RWTH Aachen University, 2013). https://www.institut3b.physik.rwth-aachen.de/global/show_document.asp?id=aaaaaaaaaapwhzq.

58. Xu, D. L. *Search for astrophysical tau neutrinos in three years of IceCube data* PhD thesis (The University of Alabama, 2015). http://acumen.lib.ua.edu/content/u0015/0000001/0001906/u0015_0000001_0001906.pdf.

59. Ishihara, A. *The IceCube Upgrade – Design and Science Goals 36th International Cosmic Ray Conference (ICRC 2019) Madison, Wisconsin, USA, July 24-August 1, 2019* (2019). arXiv: 1908.09441 [astro-ph.HE].

60. Aartsen, M. G. *et al.* IceCube-Gen2: A Vision for the Future of Neutrino Astronomy in Antarctica. arXiv: 1412.5106 [astro-ph.HE] (2014).

61. Aartsen, M. G. *et al.* Letter of Intent: The Precision IceCube Next Generation Upgrade (PINGU). arXiv: 1401.2046 [physics.ins-det] (2014).

62. Nagai, R. & Ishihara, A. *Electronics Development for the New Photo-Detectors (PDOM and D-Egg) for IceCube-Upgrade* (2019). arXiv: 1908.11564 [astro-ph.IM].

63. Classen, L., Kappes, A. & Karg, T. *A multi-PMT Optical Module for the IceCube Upgrade* (2019). arXiv: 1908.10802 [astro-ph.HE].

64. Fruck, C., Henningsen, F. & Spannfellner, C. *The POCAM as self-calibrating light source for the IceCube Upgrade 36th International Cosmic Ray Conference (ICRC 2019) Madison, Wisconsin, USA, July 24-August 1, 2019* (2019). arXiv: 1908.09600 [astro-ph.IM].

65. Kostelecky, V. A. & Samuel, S. Spontaneous Breaking of Lorentz Symmetry in String Theory. *Phys. Rev.* **D39,** 683 (1989).

66. Carroll, S. M., Harvey, J. A., Kostelecky, V. A., Lane, C. D. & Okamoto, T. Noncommutative field theory and Lorentz violation. *Phys. Rev. Lett.* **87,** 141601 (2001).

67. Groot Nibbelink, S. & Pospelov, M. Lorentz violation in supersymmetric field theories. *Phys. Rev. Lett.* **94,** 081601 (2005).

68. Kostelecky, V. A. & Russell, N. Data Tables for Lorentz and CPT Violation. *Rev. Mod. Phys.* **83,** 11–31 (2011).

69. Liberati, S. Tests of Lorentz invariance: a 2013 update. *Class. Quant. Grav.* **30,** 133001 (2013).

70. Coleman, S. R. & Glashow, S. L. High-energy tests of Lorentz invariance. *Phys. Rev.* **D59,** 116008 (1999).

71. Ashie, Y. *et al.* Evidence for an oscillatory signature in atmospheric neutrino oscillation. *Phys. Rev. Lett.* **93,** 101801 (2004).

72. Aartsen, M. G. *et al.* Neutrino Interferometry for High-Precision Tests of Lorentz Symmetry with IceCube. *Nature Phys.* **14,** 961–966 (2018).

73. Amelino-Camelia, G. *The Three perspectives on the quantum gravity problem and their implications for the fate of Lorentz symmetry On recent developments in theoretical and experimental general relativity, gravitation, and relativistic field theories. Proceedings, 10th Marcel Grossmann Meeting, MG10, Rio de Janeiro, Brazil, July 20-26, 2003. Pt. A-C* (2003), 2214–2216. arXiv: `gr-qc/0309054 [gr-qc]`.

74. Hooper, D., Morgan, D. & Winstanley, E. Lorentz and CPT invariance violation in high-energy neutrinos. *Phys. Rev.* **D72,** 065009 (2005).

75. Colladay, D. & Kostelecky, V. A. CPT violation and the standard model. *Phys. Rev.* **D55,** 6760–6774 (1997).

76. Colladay, D. & Kostelecky, V. A. Lorentz violating extension of the standard model. *Phys. Rev.* **D58,** 116002 (1998).

77. Nagel, M. *et al.* Direct Terrestrial Test of Lorentz Symmetry in Electrodynamics to 10^{-18}. *Nature Commun.* **6,** 8174 (2015).

78. Komatsu, E. *et al.* Five-Year Wilkinson Microwave Anisotropy Probe (WMAP) Observations: Cosmological Interpretation. *Astrophys. J. Suppl.* **180,** 330–376 (2009).

79. Kostelecký, V. A. & Mewes, M. Constraints on relativity violations from gamma-ray bursts. *Phys. Rev. Lett.* **110,** 201601 (2013).

80. Kostelecký, V. A., Melissinos, A. C. & Mewes, M. Searching for photon-sector Lorentz violation using gravitational-wave detectors. *Phys. Lett.* **B761,** 1–7 (2016).

81. Maccione, L., Taylor, A. M., Mattingly, D. M. & Liberati, S. Planck-scale Lorentz violation constrained by Ultra-High-Energy Cosmic Rays. *JCAP* **0904,** 022 (2009).

82. Allmendinger, F. *et al.* New Limit on Lorentz-Invariance- and CPT-Violating Neutron Spin Interactions Using a Free-Spin-Precession ^{3}He - ^{129}Xe Comagnetometer. *Phys. Rev. Lett.* **112,** 110801 (2014).

83. Smiciklas, M., Brown, J. M., Cheuk, L. W. & Romalis, M. V. A new test of local Lorentz invariance using ^{21}Ne-Rb-K comagnetometer. *Phys. Rev. Lett.* **107,** 171604 (2011).

84. Heckel, B. R. *et al.* New CP-violation and preferred-frame tests with polarized electrons. *Phys. Rev. Lett.* **97,** 021603 (2006).

85. Bennett, G. W. *et al.* Search for Lorentz and CPT violation effects in muon spin precession. *Phys. Rev. Lett.* **100,** 091602 (2008).

86. Pruttivarasin, T. *et al.* A Michelson-Morley Test of Lorentz Symmetry for Electrons. *Nature* **517,** 592 (2015).

87. Kostelecký, V. A. & Tasson, J. D. Constraints on Lorentz violation from gravitational Čerenkov radiation. *Phys. Lett.* **B749,** 551–559 (2015).

88. Kostelecky, A. & Mewes, M. Neutrinos with Lorentz-violating operators of arbitrary dimension. *Phys. Rev.* **D85,** 096005 (2012).

89. Katori, T., Kostelecky, V. A. & Tayloe, R. Global three-parameter model for neutrino oscillations using Lorentz violation. *Phys. Rev.* **D74,** 105009 (2006).

90. Gonzalez-Garcia, M. C., Halzen, F. & Maltoni, M. Physics reach of high-energy and high-statistics icecube atmospheric neutrino data. *Phys. Rev.* **D71,** 093010 (2005).

91. Dziewonski, A. M. & Anderson, D. L. Preliminary reference earth model. *Phys. Earth Planet. Interiors* **25,** 297–356 (1981).

92. Enberg, R., Reno, M. H. & Sarcevic, I. Prompt neutrino fluxes from atmospheric charm. *Phys. Rev.* **D78,** 043005 (2008).

93. Aartsen, M. G. *et al.* Searches for Sterile Neutrinos with the IceCube Detector. *Phys. Rev. Lett.* **117,** 071801 (2016).

94. Argüelles, C. A. *New Physics with Atmospheric Neutrinos* PhD thesis (The University of Wisconsin - Madison, 2015).

95. Jones, B. J. P. *Sterile Neutrinos in Cold Climates* PhD thesis (MIT, 2015). doi:10.2172/1221354. http://lss.fnal.gov/archive/thesis/2000/fermilab-thesis-2015-17.pdf.

96. Fedynitch, A., Becker Tjus, J. & Desiati, P. Influence of hadronic interaction models and the cosmic ray spectrum on the high energy atmospheric muon and neutrino flux. *Phys. Rev.* **D86,** 114024 (2012).

97. Casella, G. & Berger, R. *Statistical Inference* ISBN: 9780534243128. `https://books.google.co.uk/books?id=0x\_vAAAAMAAJ` (Thomson Learning, 2002).

98. Neyman, J. & Pearson, E. S. On the Problem of the Most Efficient Tests of Statistical Hypotheses. *Phil. Trans. Roy. Soc. Lond.* **A231,** 289–337 (1933).

99. Wilks, S. S. The Large-Sample Distribution of the Likelihood Ratio for Testing Composite Hypotheses. *Annals Math. Statist.* **9,** 60–62 (1938).

100. Bayes, R. An essay toward solving a problem in the doctrine of chances. *Phil. Trans. Roy. Soc. Lond.* **53,** 370–418 (1764).

101. Jeffreys, H. *The Theory of Probability* ISBN: 9780198503682, 9780198531937, 0198531931. `https://global.oup.com/academic/product/the-theory-of-probability-9780198503682?cc=au&lang=en&#` (1939).

102. Robert, C. & Casella, G. *Monte Carlo Statistical Methods* ISBN: 9781475730715. `https://books.google.co.uk/books?id=lrvfBwAAQBAJ` (Springer New York, 2013).

103. Hastings, W. K. Monte Carlo sampling methods using Markov chains and their applications. *Biometrika* **57,** 97–109. ISSN: 0006-3444 (Apr. 1970).

104. Goodman, J. & Weare, J. Ensemble samplers with affine invariance. *Communications in Applied Mathematics and Computational Science, Vol. 5, No. 1, p. 65-80, 2010* **5,** 65–80 (2010).

105. Skilling, J. Nested Sampling. *AIP Conference Proceedings* **735,** 395–405 (2004).

106. Collin, G. L. *Neutrinos, neurons and neutron stars : applications of new statistical and analysis techniques to particle and astrophysics* PhD thesis (Massachusetts Institute of Technology, 2018). `http://hdl.handle.net/1721.1/118817`.

107. Abe, K. *et al.* Test of Lorentz invariance with atmospheric neutrinos. *Phys. Rev.* **D91,** 052003 (2015).

108. Aartsen, M. G. *et al.* Determining neutrino oscillation parameters from atmospheric muon neutrino disappearance with three years of IceCube DeepCore data. *Phys. Rev.* **D91,** 072004 (2015).

109. Abbasi, R. *et al.* Determination of the Atmospheric Neutrino Flux and Searches for New Physics with AMANDA-II. *Phys. Rev.* **D79,** 102005 (2009).

110. Abbasi, R. *et al.* Search for a Lorentz-violating sidereal signal with atmospheric neutrinos in IceCube. *Phys. Rev.* **D82,** 112003 (2010).

111. Abraham, J. *et al.* Observation of the suppression of the flux of cosmic rays above 4×10^{19}eV. *Phys. Rev. Lett.* **101,** 061101 (2008).

112. Aab, A. *et al.* Evidence for a mixed mass composition at the 'ankle' in the cosmic-ray spectrum. *Phys. Lett.* **B762,** 288–295 (2016).

113. Chalmers, M. Interview: Steven Weinberg. *CERN Courier* **57,** 31–35 (Nov. 2017).

114. Foreman-Mackey, D., Hogg, D. W., Lang, D. & Goodman, J. o. emcee: The MCMC Hammer. **125,** 306 (2013).

115. Feroz, F., Hobson, M. P. & Bridges, M. MultiNest: an efficient and robust Bayesian inference tool for cosmology and particle physics. *Mon. Not. Roy. Astron. Soc.* **398,** 1601–1614 (2009).

116. Vieregg, A. *et al.* Fundamental Physics with High-Energy Cosmic Neutrinos. *Bulletin of the American Astronomical Society* **51,** 215 (May 2019).

117. Argüelles, C. A. *et al. Fundamental physics with high-energy cosmic neutrinos today and in the future 36th International Cosmic Ray Conference (ICRC 2019) Madison, Wisconsin, USA, July 24-August 1, 2019* (2019). arXiv: 1907.08690 [astro-ph.HE].

118. Athar, H., Jezabek, M. & Yasuda, O. Effects of neutrino mixing on high-energy cosmic neutrino flux. *Phys. Rev.* **D62,** 103007 (2000).

119. Beacom, J. F., Bell, N. F., Hooper, D., Pakvasa, S. & Weiler, T. J. Measuring flavor ratios of high-energy astrophysical neutrinos. *Phys. Rev.* **D68.** [Erratum: Phys. Rev.D72,019901(2005)], 093005 (2003).

120. Barenboim, G. & Quigg, C. Neutrino observatories can characterize cosmic sources and neutrino properties. *Phys. Rev.* **D67,** 073024 (2003).

121. Kashti, T. & Waxman, E. Flavoring astrophysical neutrinos: Flavor ratios depend on energy. *Phys. Rev. Lett.* **95,** 181101 (2005).

122. Xing, Z.-Z. & Zhou, S. Towards determination of the initial flavor composition of ultrahigh-energy neutrino fluxes with neutrino telescopes. *Phys. Rev.* **D74,** 013010 (2006).

123. Lipari, P., Lusignoli, M. & Meloni, D. Flavor Composition and Energy Spectrum of Astrophysical Neutrinos. *Phys. Rev.* **D75,** 123005 (2007).

124. Pakvasa, S., Rodejohann, W. & Weiler, T. J. Flavor Ratios of Astrophysical Neutrinos: Implications for Precision Measurements. *JHEP* **02,** 005 (2008).

125. Esmaili, A. & Farzan, Y. An Analysis of Cosmic Neutrinos: Flavor Composition at Source and Neutrino Mixing Parameters. *Nucl. Phys.* **B821,** 197–214 (2009).

126. Lai, K.-C., Lin, G.-L. & Liu, T. C. Determination of the Neutrino Flavor Ratio at the Astrophysical Source. *Phys. Rev.* **D80,** 103005 (2009).

127. Choubey, S. & Rodejohann, W. Flavor Composition of UHE Neutrinos at Source and at Neutrino Telescopes. *Phys. Rev.* **D80,** 113006 (2009).

128. Bustamante, M., Gago, A. M. & Jones Perez, J. SUSY Renormalization Group Effects in Ultra High Energy Neutrinos. *JHEP* **05,** 133 (2011).

129. Xu, X.-J., He, H.-J. & Rodejohann, W. Constraining Astrophysical Neutrino Flavor Composition from Leptonic Unitarity. *JCAP* **1412,** 039 (2014).

130. Fu, L., Ho, C. M. & Weiler, T. J. Aspects of the Flavor Triangle for Cosmic Neutrino Propagation. *Phys. Rev.* **D91,** 053001 (2015).

131. Argüelles, C. A., Katori, T. & Salvado, J. New Physics in Astrophysical Neutrino Flavor. *Phys. Rev. Lett.* **115,** 161303 (2015).

132. Bustamante, M., Beacom, J. F. & Winter, W. Theoretically palatable flavor combinations of astrophysical neutrinos. *Phys. Rev. Lett.* **115,** 161302 (2015).

133. Gonzalez-Garcia, M. C., Maltoni, M., Martinez-Soler, I. & Song, N. Non-standard neutrino interactions in the Earth and the flavor of astrophysical neutrinos. *Astropart. Phys.* **84,** 15–22 (2016).

134. Nunokawa, H., Panes, B. & Zukanovich Funchal, R. How Unequal Fluxes of High Energy Astrophysical Neutrinos and Antineutrinos can Fake New Physics. *JCAP* **1610,** 036 (2016).

135. De Salas, P. F., Lineros, R. A. & Tórtola, M. Neutrino propagation in the galactic dark matter halo. *Phys. Rev.* **D94,** 123001 (2016).

136. Rasmussen, R. W., Lechner, L., Ackermann, M., Kowalski, M. & Winter, W. Astrophysical neutrinos flavored with Beyond the Standard Model physics. *Phys. Rev.* **D96,** 083018 (2017).

137. Lai, K.-C., Lai, W.-H. & Lin, G.-L. Constraining the mass scale of a Lorentz-violating Hamiltonian with the measurement of astrophysical neutrino-flavor composition. *Phys. Rev.* **D96,** 115026 (2017).

138. Bustamante, M. & Agarwalla, S. K. Universe's Worth of Electrons to Probe Long-Range Interactions of High-Energy Astrophysical Neutrinos. *Phys. Rev. Lett.* **122,** 061103 (2019).

139. Capozzi, F., Shoemaker, I. M. & Vecchi, L. Neutrino Oscillations in Dark Backgrounds. *JCAP* **1807,** 004 (2018).

140. Klop, N. & Ando, S. Effects of a neutrino-dark energy coupling on oscillations of high-energy neutrinos. *Phys. Rev.* **D97,** 063006 (2018).

141. Argüelles, C. A. *et al.* Probe Of Sterile Neutrinos Using Astrophysical Neutrino Flavor. arXiv: `1909.05341 [hep-ph]` (2019).

142. Bustamante, M. & Ahlers, M. Inferring the flavor of high-energy astrophysical neutrinos at their sources. *Phys. Rev. Lett.* **122,** 241101 (2019).

143. Pagliaroli, G., Palladino, A., Villante, F. L. & Vissani, F. Testing nonradiative neutrino decay scenarios with IceCube data. *Phys. Rev.* **D92,** 113008 (2015).

144. Conrad, J. M., Ignarra, C. M., Karagiorgi, G., Shaevitz, M. H. & Spitz, J. Sterile Neutrino Fits to Short Baseline Neutrino Oscillation Measurements. *Adv. High Energy Phys.* **2013,** 163897 (2013).

145. Ahlers, M., Bustamante, M. & Mu, S. Unitarity Bounds of Astrophysical Neutrinos. *Phys. Rev.* **D98,** 123023 (2018).

146. De Gouvea, A. & Murayama, H. Neutrino Mixing Anarchy: Alive and Kicking. *Phys. Lett.* **B747,** 479–483 (2015).

147. Schneider, A. *Characterization of the Astrophysical Diffuse Neutrino Flux with IceCube High-Energy Starting Events 36th International Cosmic Ray Conference (ICRC 2019) Madison, Wisconsin, USA, July 24-August 1, 2019* (2019). arXiv: `1907.11266 [astro-ph.HE]`.

148. Stachurska, J. *First Double Cascade Tau Neutrino Candidates in IceCube and a New Measurement of the Flavor Composition 36th International Cosmic Ray Conference (ICRC 2019) Madison, Wisconsin, USA, July 24-August 1, 2019* (2019). arXiv: 1908.05506 [astro-ph.HE].

149. Farrag, K. *Highlights from the 7 year High Energy Starting Event sample in Icecube 8th Meeting on CPT and Lorentz Symmetry (CPT'19) Bloomington, Indiana, USA, May 12-16, 2019* (2019). arXiv: 1906.09623 [hep-ex].

150. Argüelles, C. A. & Dujmovic, H. *Searches for Connections Between Dark Matter and Neutrinos with the IceCube High-Energy Starting Event Sample 36th International Cosmic Ray Conference (ICRC 2019) Madison, Wisconsin, USA, July 24-August 1, 2019* (2019). arXiv: 1907.11193 [hep-ph].

151. Yuan, T. *Measurement of the high-energy all-flavor neutrino-nucleon cross section with IceCube 36th International Cosmic Ray Conference (ICRC 2019) Madison, Wisconsin, USA, July 24-August 1, 2019* (2019). arXiv: 1908 . 07027 [astro-ph.HE].

152. Yuan, T. *New results with high-energy neutrinos in IceCube* Fermilab Neutrino Seminar. https://npc.fnal.gov/wp-content/uploads/2018/09/180830_fermilab2.pdf (2018).

153. Usner, M. *Search for Astrophysical Tau-Neutrinos in Six Years of High-Energy Starting Events in the IceCube Detector* PhD thesis (Humboldt U., Berlin (main), 2018-09-21). doi:10.18452/17016. https://edoc.hu-berlin.de/handle/18452/20228.

154. Gazizov, A. & Kowalski, M. P. ANIS: High energy neutrino generator for neutrino telescopes. *Comput. Phys. Commun.* **172,** 203–213 (2005).

155. Honda, M., Kajita, T., Kasahara, K., Midorikawa, S. & Sanuki, T. Calculation of atmospheric neutrino flux using the interaction model calibrated with atmospheric muon data. *Phys. Rev.* **D75,** 043006 (2007).

156. Bhattacharya, A., Enberg, R., Reno, M. H., Sarcevic, I. & Stasto, A. Perturbative charm production and the prompt atmospheric neutrino flux in light of RHIC and LHC. *JHEP* **06,** 110 (2015).

157. Van Santen, J. *Neutrino Interactions in IceCube above 1 TeV: Constraints on Atmospheric Charmed-Meson Production and Investigation of the Astrophysical Neutrino Flux with 2 Years of IceCube Data taken 2010–2012* PhD thesis (Wisconsin U., Madison, 2014-11-18). http://search.proquest.com/docview/1637727437/abstract/CE0FBEF172B24F9APQ/1.

158. Heck, D., Knapp, J., Capdevielle, J. N., Schatz, G. & Thouw, T. CORSIKA: A Monte Carlo code to simulate extensive air showers (1998).

159. Glashow, S. L. Resonant Scattering of Antineutrinos. *Phys. Rev.* **118,** 316–317 (1960).

160. Argüelles, C. A., Schneider, A. & Yuan, T. A binned likelihood for stochastic models. *JHEP* **06,** 030 (2019).

161. Hall, L. J., Murayama, H. & Weiner, N. Neutrino mass anarchy. *Phys. Rev. Lett.* **84,** 2572–2575 (2000).

162. Haba, N. & Murayama, H. Anarchy and hierarchy. *Phys. Rev.* **D63,** 053010 (2001).

163. De Gouvea, A. & Murayama, H. Statistical test of anarchy. *Phys. Lett.* **B573,** 94–100 (2003).

164. Aartsen, M. G. *et al.* PINGU: A Vision for Neutrino and Particle Physics at the South Pole. *J. Phys.* **G44,** 054006 (2017).

165. Aartsen, M. G. *et al.* Measurement of Atmospheric Tau Neutrino Appearance with IceCube DeepCore. *Phys. Rev.* **D99,** 032007 (2019).

166. *Fermilab Test Beam Facility* https://ftbf.fnal.gov/.

167. Rominsky, M. *et al.* Fermilab Test Beam Facility Annual Report FY17. doi:10.2172/1418446 (2018).

168. Aidala, C. A. *et al.* Design and Beam Test Results for the sPHENIX Electromagnetic and Hadronic Calorimeter Prototypes. *IEEE Trans. Nucl. Sci.* **65,** 2901–2919 (2018).

169. Wendt, C. Private Communication. 2019.

170. Hamamatsu. *Photomultiplier Tubes and Assemblies for Scintillation Counting and High Energy Physics* Hamamatsu. https://www.hamamatsu.com/resources/pdf/etd/High_energy_PMT_TPMZ0003E.pdf (2019).

171. Hamamatsu. *Large Photocathode Area Photomultiplier Tubes* Hamamatsu. https://www.hamamatsu.com/resources/pdf/etd/LARGE_AREA_PMT_TPMH1376E.pdf (2019).

172. *Tank Depot Schematics* https://www.tank-depot.com/Drawings%2face%2fop1010-64.pdf.

173. Duvernois, M. Generation-2 IceCube Digital Optical Module and DAQ. *PoS* **ICRC2015,** 1148 (2016).

174. Sandstrom, P. Digital optical module design for PINGU. *AIP Conf. Proc.* **1630,** 180–183 (2015).

175. Abbasi, R. *et al.* The IceCube Data Acquisition System: Signal Capture, Digitization, and Timestamping. *Nucl. Instrum. Meth.* **A601,** 294–316 (2009).

176. *Intel Cyclone V FPGA* https://www.intel.co.uk/content/www/uk/en/products/programmable/fpga/cyclone-v.html.

177. Kaether, F. & Langbrandtner, C. Transit Time and Charge Correlations of Single Photoelectron Events in R7081 PMTs. *JINST* **7,** P09002 (2012).

178. Agostinelli, S. *et al.* GEANT4: A Simulation toolkit. *Nucl. Instrum. Meth.* **A506,** 250–303 (2003).

179. Abe, K. *et al.* Observation of Electron Neutrino Appearance in a Muon Neutrino Beam. *Phys. Rev. Lett.* **112,** 061802 (2014).

180. Adamson, P. *et al.* First measurement of electron neutrino appearance in NOvA. *Phys. Rev. Lett.* **116,** 151806 (2016).

181. Kouchner, A. Next-generation atmospheric neutrino experiments. *Phys. Dark Univ.* **4,** 60–74 (2014).

182. Indumathi, D. India-based neutrino observatory (INO): Physics reach and status report. *AIP Conf. Proc.* **1666,** 100003 (2015).

183. Kearns, E. *et al. Hyper-Kamiokande Physics Opportunities Proceedings, 2013 Community Summer Study on the Future of U.S. Particle Physics: Snowmass on the Mississippi (CSS2013): Minneapolis, MN, USA, July 29-August 6, 2013* (2013). arXiv: 1309.0184 [hep-ex]. http://www.slac.stanford.edu/econf/C1307292/docs/submittedArxivFiles/1309.0184.pdf.

184. Adams, C. *et al. The Long-Baseline Neutrino Experiment: Exploring Fundamental Symmetries of the Universe Snowmass 2013: Workshop on Energy Frontier Seattle, USA, June 30-July 3, 2013* (2013). arXiv: 1307.7335 [hep-ex]. http://lss.fnal.gov/archive/2014/pub/fermilab-pub-14-022.pdf.

185. Sjostrand, T., Mrenna, S. & Skands, P. Z. PYTHIA 6.4 Physics and Manual. *JHEP* **0605,** 026 (2006).

186. Hayato, Y. NEUT. *Nucl. Phys. Proc. Suppl.* **112.** [,171(2002)], 171–176 (2002).

187. Sjostrand, T., Mrenna, S. & Skands, P. Z. A Brief Introduction to PYTHIA 8.1. *Comput. Phys. Commun.* **178,** 852–867 (2008).

188. Brun, R. & Rademakers, F. ROOT: An object oriented data analysis framework. *Nucl.Instrum.Meth.* **A389,** 81–86 (1997).

189. Gallagher, H. The NEUGEN neutrino event generator. *Nucl.Phys.Proc.Suppl.* **112,** 188–194 (2002).

190. Katori, T., Lasorak, P., Mandalia, S. & Terri, R. First look at PYTHIA8 hadronization program for neutrino interaction generators. *JPS Conf. Proc.* **12,** 010033 (2016).

191. Yang, T., Andreopoulos, C., Gallagher, H., Hoffmann, K. & Kehayias, P. A Hadronization Model for Few-GeV Neutrino Interactions. *Eur.Phys.J.* **C63,** 1–10 (2009).

192. Koba, Z., Nielsen, H. B. & Olesen, P. Scaling of multiplicity distributions in high-energy hadron collisions. *Nucl.Phys.* **B40,** 317–334 (1972).

193. Zieminska, D. *et al.* Charged Particle Multiplicity Distributions in neutrino n and neutrino p Charged Current Interactions. *Phys. Rev.* **D27,** 47–57 (1983).

194. Barlag, S. *et al.* Charged Hadron Multiplicities in High-energy Anti-muon Neutrino n and Anti-muon Neutrino p Interactions. *Z.Phys.* **C11,** 283 (1982).

195. Wittek, W. *et al.* Production of π^0 Mesons and Charged Hadrons in Anti-neutrino Neon and Neutrino Neon Charged Current Interactions. *Z.Phys.* **C40,** 231 (1988).

196. Gustafson, G. *THE LUND MODEL, MULTIPLE SCATTERING, AND FINAL STATES* eng. *ACTA PHYSICA POLONICA B* **39** (ACTA PHYSICA POLONICA B, JAGELLONIAN UNIV, INST PHYSICS, Copanello, ITALY, 2008), 2173–2192.

197. Andersson, B., Gustafson, G., Ingelman, G. & Sjöstrand, T. Parton fragmentation and string dynamics. *Physics Reports* **97,** 31 –145. ISSN: 0370-1573 (1983).

198. Katori, T. & Mandalia, S. PYTHIA hadronization process tuning in the GENIE neutrino interaction generator. *J. Phys.* **G42,** 115004 (2015).

199. Airapetian, A. *et al.* Multiplicities of charged pions and kaons from semi-inclusive deep-inelastic scattering by the proton and the deuteron. *Phys. Rev.* **D87,** 074029 (2013).

200. Andreopoulos, C. Private Communication. 2019.

201. Andreopoulos, C. *The GENIE Hadronization Model* NuSTEC Workshop on Shallow- and Deep-Inelastic Scattering. `https://indico.cern.ch/event/727283/contributions/3159400/` (2018).